JRJC 2019. Book of Proceedings

Celine Armand, Halim Ashkar, Bowen Bai, Ophelie Bugnon, Reina Camacho Toro, Robin Albert Andre Caron, Etienne Chardonnet, David E. Cohen, João A.B. Coelho, Nicolas Dray, et al.

JRJC 2019

Journées de Rencontres Jeunes Chercheurs

Société Française de Physique

BOOK of PROCEEDINGS

Centre nautique de **Moulin-Mer**

Route du centre nautique,
29460 Logonna-Daoulas,
Finistère

Energie nucléaire
Structure du noyau
Astrophysique nucléaire
Physique médicale
Physique hadronique
Cosmologie
Instrumentation
Physique théorique
Modèle standard électrofaible
Au-delà du modèle standard
Neutrinos
Astroparticules
Physique des saveurs

site web

Secrétariat
Isabelle Cossin, LPNHE
isabelle.cossin@lpnhe.in2p3.fr
Tel: +33 (0)1 44 27 68 95

Comité d'organisation :

Pauline Ascher	(CENBG)
Aoife Bharucha	(CPT)
François Brun	(CEA Saclay)
Nicolas Chanon	(IP2I)
Emmanuel Chauveau	(CENBG)
Rachel Delorme	(IMNC)
Romain Gaior	(LPNHE)
Julien Masbou	(SUBATECH)
Laure Massacrier	(IJCLab)
Antonio Uras [(*)]	(IP2I)
Dimitris Varouchas	(IJCLab)

[(*)] Editor of these proceedings

Secrétariat :

Isabelle Cossin	(LPNHE)

Contents

Part I

Astrophysics and Cosmology

session chaired by Romain GAIOR

The hunt for VHE gamma-rays in the Gravitational Waves era

Halim Ashkar

IRFU, CEA, Université Paris-Saclay, F-91191 Gif-sur-Yvette, France

Abstract — In multi-messenger astrophysics, we combine different astrophysical messengers in order to study different aspects of an object or a process in the Universe. The first direct discovery of gravitational waves (GW) emitted from the inward spiral of two black holes in 2015 took multi-messenger astrophysics to the next level, adding direct detection of GWs to the list of messengers coming from the sky. Almost two years later, the first detection of GWs from a binary neutron star merger alongside electromagnetic (EM) counterparts in several bands started a new era in multi-messenger astrophysics triggering worldwide search programs for GW counterparts. Nowadays, four astronomical messengers exist: EM waves, cosmic rays, neutrinos and GWs. Very High Energy (VHE) gamma-rays cover the highest band in the electromagnetic spectrum and provides valuable information for the characterization of astrophysical phenomena. This is why the search for VHE gamma-ray from GW events is in the heart of these search campaigns. In this contribution, I report on the GW follow-up program with the H.E.S.S. Imaging Atmospheric Cherenkov Telescopes, focusing on the coverage algorithms, that I helped develop and implement in the H.E.S.S. GW follow-up strategy and on its outcome until now.

1 Introduction

The four astrophysical messengers that we know as of today are electromagnetic (EM) radiation, cosmic rays, neutrinos, and gravitational waves (GW). Astrophysical messenger are produced by different physical processes and carry valuable information on the emitter source. Combined, these information provide a wider understanding of the studied source and could help disentangle unexplained problems, such as the distinction between hadronic and leptonic emission processes in astrophysical sources. However, each messenger has its own limitations and detection challenges. In this contribution I focus on EM radiation and GWs, more specifically, the EM follow-up of GWs in the Very High Energy (VHE) gamma-ray band with the High Energy Stereoscopic System (H.E.S.S.).

Although GWs have been detected in the past [1], the first direct observation of GWs happened in 2015 by the LIGO interferometers that detected a GW signal emitted by the inward spiral of two black holes (BH) at a distance of $410^{+160}_{-180} Mpc$ [2]. This event named GW150914 took GW multi-messenger astrophysics to a new level by adding direct detection of GWs to the list of messengers. While most models do not predict a sizable EM emission associated to BH mergers, it is different for mergers of binary neutron stars (NS), as illustrated two years later by the detection of GWs from a NS merger, GW170817, complemented by a short gamma-ray burst (GRB) [3]. This event triggered one of the most extensive multi-wavelength observation campaigns in recent history, which led to the detection of radio, optical and X-ray counterparts, and started a new era in multi-messenger astrophysics.

H.E.S.S., is an array of Imaging Atmospheric Cherenkov Telescopes located in the Khomas highlands in Namibia and sensitive to gamma and cosmic rays in the range of 30 GeV to 100 TeV. Covering the VHE band of the EM spectrum, H.E.S.S. participated in the GW170817 multi-wavelength global search and played an important role as the first ground based instrument to observe the target several hours before the detection of the optical counterpart [4], in the lookout for a potential VHE GRB.

GW localizations generally span tens to thousands of square degrees in the sky which requires specific follow-up strategies for EM telescopes. In this proceeding, I describe the observational strategies adopted by H.E.S.S. for the follow-up of GW and present a quick summary of the H.E.S.S. GW observations and analysis results.

2 Observation scheduling and preparations

Upon the detection of GWs from a compact binary coalescence, localization probability maps of the event are issued either by a rapid localization [5] or by a slower but more precise approach [6]. The maps are in the Healpix format and each pixel in the map contains a probability of hosting the GW event and possibly information on the distance of the event [8]. In order to cover the reconstructed GW localisation region with a relatively small field of view telescope (e.g. 5deg diameter) an observational strategy is required. Taking into consideration telescope constraints like the Field of View (FoV), the visibility, the maximum allowed zenith angle, in addition to Moon constraints [12] and standard 28 minutes H.E.S.S. observation windows, two approaches are used to optimize coverage. If distance information is not provided or the galaxy catalog is unre-

liable in the location of the event a 2D approach is used. If distance information can be used, a 3D approach correlating localization information from the GW map with the distribution of the galaxies in the local universe, as explained in [11], is favoured.

- **2D approach**: Initially the 2D algorithm is used to search for the highest pixel for each window in the localisation map and chooses it as a target for H.E.S.S. observation. It got modified for the LIGO and Virgo third observation run (O3) and is now searching for the highest integrated probability within the FoV. To do this, the map is reduced to a heaplix resolution with NSIDE = 512. This value was chosen as a compromise between reducing computation time and maintaining efficient coverage. Each resulting pixel is chosen as a seed for the FoV pointings, then the seed with the highest integrated GW probability is chosen as an observation target for a given window and the observed pixels are subtracted for the next iteration.

- **3D approach**: In addition to the information provided by the localisation sky map, the local distribution of galaxies in our Universe is taken into account through the use of the GLADE galaxy catalog [7]. The sky localisation of the gravitational wave is correlated with the galaxy distribution and each galaxy is assigned a normalised probability of hosting the event. The algorithm then ranks the galaxies according to their probability to host the event and for each window, it chooses the visible galaxies as pointing seeds and integrates the total probability from the galaxies inside each one of the H.E.S.S. FoV in an iterative way. A final zenith angle weighting is done before choosing the pointing with the highest integrated probability for observation during the given window. The observed galaxies are then subtracted for the next observational window to avoid overlapping [11]. In a non-homogeneous local universe, a 3D approach seems to be more coherent. This method is proved to be efficient during the follow-up of GW170817 as shown in Fig. 1. I also investigated a new approach for 3D coverage that uses the map pixels as pointing seeds like in the 2D algorithms and integrates the galaxy probabilities in the FoVs. To reduce the number computation time, we reduce the number of seeds by choosing NSIDE=64. Any smaller NSIDE will affect the performance of the algorithm due to gaps in the coverage when the pixel size approaches the H.E.S.S. FoV size. However the galaxy probabilities are computed from the original non-reduced map to maintain accuracy. The performance of this approach was tested on simulated GW maps from [**?**] and was found more suitable for large localization uncertainties when it comes to computation time. This is due to the increasing number of potential host galaxies versus the number of pixels in large uncertainty volumes. This approach is still being developed and it is not yet implemented in the H.E.S.S. response scheme.

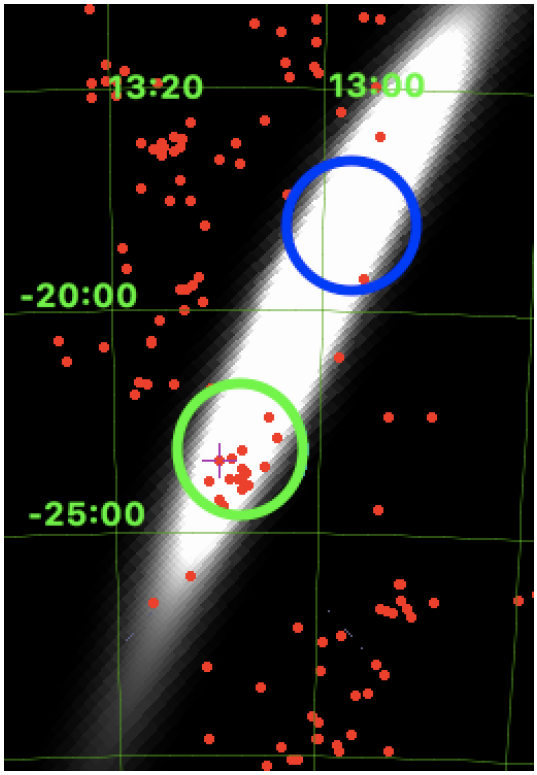

Figure 1: GW map of GW170817. The red dots are galaxies from the GLADE catalog at the distance of the event (32 - 48 Mpc). The green circle represent the first scheduled observation using a 3D approach for this event and it contains the electromagnetic counterpart SSS17a [13]. The blue circle represents the observation that a 2D approach would have scheduled covering the brightest area in the probability map.

These algorithms are integrated within the H.E.S.S. automatic response scheme. The scheme handles all alerts foreseen by LIGO/Virgo, filters out the less interesting ones depending and makes automatic decisions for prompt and afterglow observations depending on the nature of the GW event. The H.E.S.S. response time to GW events is reduced to a few seconds and for the most interesting events, like mergers including at least one NS, the filtering requirements are looser than for other events since high energy emission is anticipated by such events [4].

3 Observations and results summary

In August 2017, the Virgo interferometer joined the two LIGO detectors in their second observation run (O2) and in 14 August, GW170814 was the first BH merger to be detected by all three LIGO and Virgo interferometers and it was until then the best localized event with a final 90% credible area of 60° [9]. This well localized event was used to test the H.E.S.S. observational strategies and a good coverage was achieved. Results of these

observations can be found in [10]. Although no significant VHE gamma-rays were detected, the first upper limits for VHE gamma-ray emission were computed for a GW event detected by three interferometers.

Three days later, GW170817 was detected and using a 3D approach, H.E.S.S. was the first ground based instrument to get on target 5.3 hours after the merger. The first scheduled observation covered a region containing the optical counterpart that was discovered several hours later. After this discovery, observations were focused on the optical transient. This follow-up is well described in [4] and permitted to constrain the VHE gamma-ray emission from a NS merger at $t < 5$ days with stringent upper limits. After ~ 9 days the non-thermal radio and X-ray signal started rising and plateaued around after ~ 160 days. An indication of a good environment for high energy emissions by synchrotron self-Compton (SSC) and a suitable H.E.S.S. sensitivity for probing such emissions [14] motivated a long-term H.E.S.S. follow-up of this event allowing to constrain the VHE gamma-ray emission, hence the magnetic field in the remnant [15]. Long term H.E.S.S. follow-up observations took place from 124 to 272 days after the merger.

The third LIGO/Virgo observation run (O3) started officially in April 2019 and until the end of the same year 42 GW candidates were detected with a confirmed binary NS [16] with no counterparts. Among these candidates, and due to large localization uncertainties, visibility constraints and weather conditions, only two binary BH candidates were observed by H.E.S.S.: S190512at and S190728q. Data analysis is still ongoing. Early 2020, H.E.S.S. also followed on S200115j, an GW event falling in the mass gap category between binary NS and NS-BH merger.

4 Prospects

In this contribution I briefly discussed the ongoing H.E.S.S. GW follow-up program. The next step is to improve the use of galaxy catalogs by using galaxy stellar masses as an additional probability weighting factor as described in [17] . This program is building the basis for the low-latency GW follow-up program of the future Cherenkov Telescope Array (CTA). The idea is to build a pipeline that uses the algorithms described above and simulates all the workflow from the reception of a GW alert and observation scheduling to the real time analysis of the data and potential GRB detection [18]. This will allow to compute accurate expectations and detection rates for CTA. With its increased sensitivity, wider FoV and fast slewing time, CTA will provide a faster scanning of the GW probability maps and will drastically increase the chances of detection of VHE gamma ray emission from GW events.

References

[1] J. H. Taylor, J. M. Weisberg (1982). ApJ. 253, 908

[2] Abbott, B. P., et al. (2016). PRL, 116, 061102

[3] B. P. Abbott et al. (LIGO Scientific Collaboration and Virgo Collaboration, Fermi-GBM, INTEGRAL) (2017). ApJL 848, L13.

[4] H. Abdalla et al. (H.E.S.S. Collaboration) (2017). ApJL 850, L22

[5] Singer L. P., Price L. R. (2016). Physical Review D93, 4013

[6] Veitch J. et al. (2015). Physical Review D91, 2003.

[7] Dalya G. et al. (2016). VizieR Online Data Catalog 7275

[8] Singer L. P. et al. (2016). ApJL 829, L15.

[9] Abbott B. P. et al. (2017). PRL, 119, 141101

[10] H. Ashkar, F. Schüssler, M. Seglar-Arroy (2019). MmSAI, Arxive 1906.10426, https://arxiv.org/abs/1906.10426

[11] M. Seglar-Arroyo, F. Schüssler (2017). Proceedings Rencontres de Moriond 2017, VHEPU, 1705.10138

[12] M. Seglar-Arroyo et al. (2019).ICRC 2019, Proceedings of Science: `https://pos.sissa.it/358/789/pdf`

[13] Coulter et al. (1M2H Collaboration)GCN Circ. 21529

[14] X. Rodrigues et al. (2019). 409 Astroparticle Physics, 106, 10, 1806.01624.

[15] S. Ohm. (2019).ICRC 2019, Proceedings of Science: `https://pos.sissa.it/358/756/pdf`

[16] LIGO Scientific Collaboration and Virgo Collaboration (2020). `https://www.ligo.org/detections/GW190425.php`

[17] Ducoin et al. (2019). ICRC 2019. 1991.05432: `https://arxiv.org/abs/1911.05432`

[18] M. Seglar-Arroyo et al. (2019). ICRC 2019, Proceedings of Science: `https://pos.sissa.it/358/790/pdf`

Optimisation of the optical follow up of gravitationnal waves events

Jean-Grégoire Ducoin

Université Paris-Saclay, CNRS/IN2P3, IJCLab, 91405 Orsay, France

Abstract — In this proceeding I present a new strategy to optimize the electromagnetic follow-up of gravitational wave triggers. This method is based on the widely used galaxy targeting approach where we add the stellar mass of galaxies in order to prioritize the more massive galaxies. We cross-matched the GLADE galaxy catalog with the AllWISE catalog up to 400 Mpc with an efficiency of $\sim$ 93%, and derived stellar masses using a stellar-to-mass ratio using the WISE1 band luminosity. We developed a new grade to rank galaxies combining their 3D localization probability associated to the gravitational wave event with the new stellar mass information. The efficiency of this new approach is illustrated with the GW170817 event, which shows that its host galaxy, NGC4993, is ranked at the first place using this new method. The catalog, named Mangrove, is publicly available and the ranking of galaxies is automatically provided through a dedicated web site for each gravitational wave event.

1 Introduction

Gravitational waves from binary neutron star (BNS) coalescence, in association to short gamma-ray burst, opened a new era of multi-messenger astronomy [18]. The identification of the counterpart and its multi-wavelength observations improved our understanding of the physics of strong-field gravity and put some constraints on astrophysical models related to matter during the merger and post-merger phase. With improved sensitivity of the LIGO-Virgo detectors, the year-long third observing run (O3) promises many merging binaries detection with an expected number of BNS mergers in the range 1-50 [16]. Therefore an intensive multi-wavelength follow-up of those events with ground and space instruments is performed all around the world (see for example [17]). But the identification of the electromagnetic counterpart of such event is very challenging knowing the wide sky localization area provided by LIGO-Virgo (from few tens of degrees to thousands of degrees^2) and requires complex observation strategies implying many telescopes. In this proceeding I will present our recent development on galaxies targeting strategies, the building of the Mangrove galaxies catalog and the publicly available tools dedicated to improve the follow up of gravitational waves events [1].

2 Galaxy targeting method

2.1 Standard approach

Many efforts were done recently to optimize the observations for these large sky areas provided by LIGO-Virgo [2, 3]. For large field of view ($\gtrsim 1$ deg^2) telescope the standard approach consists in observing the localization error box provided by LIGO-Virgo using an optimized tiling of the sky [4]. In such standard strategy, the scheduling of the tile observation is provided by the 2D probability distribution from LIGO-Virgo skymaps. In case of compact binary merger, there are analytical formulas which allows one to estimate the distance to the source. In such case LIGO-Virgo provides an estimation of the 3D localization of the source. In such cases as suggested by [5] adding the galaxy catalog allows one to improve the efficiency of the search, also to include galaxy's population to the strategy allow to provide a scheduling of observation for narrow field of view telescopes ($\lesssim 1$ deg^2). Indeed, with such information we can provide a list of interesting galaxies (i.e. ranked by their 3D position probability inside the LIGO-Virgo skymap) to be observed by these small field of view telescopes. With LIGO-Virgo skymap we are able to fetch the probability density per unit of volume at a given position. This is used to infer the probability of a given galaxy to be the host of the merger according to its celestial position P_{pos} with the following relation:

$$P_{pos} = \frac{P_{pixel}}{Pixel\ area}\, N_{pixel}\, e^{-\frac{1}{2}\left(\frac{D_{galaxy}-\mu_{pixel}}{\sigma_{pixel}}\right)^2} \quad (1)$$

Where P_{pixel} is the 2D probability included in the given pixel, N_{pixel} is the normalization factor for the given pixel, μ_{pixel} is the mean distance value at the given pixel, σ_{pixel} is the standard deviation at the given pixel and D_{galaxy} is the luminosity distance of the galaxy fetched from the galaxy catalog. The outputs of the LIGO-Virgo localization pipelines are HEALPix (Hierarchical Equal Area isoLatitude Pixelization) all-sky images, the skymap we are dealing with is composed of pixels defined by the HEALPix format.
Note that for the selection of the galaxies, we classified as "compatible" with the skymap, a galaxy which fulfills the two following conditions:

- Its 2D position in the sky has to be in the 90% of the 2D skymap probability distribution.

- Its distance has to fall within the 3 sigma distance error localization at the given pixel of the galaxy.

To use the information related to galaxies, one must rely on a galaxy catalog that is sufficiently complete compared to the interferometers sensitivity range. The current binary neutron star range [1] are at 130 Mpc, 110Mpc and 50Mpc for LIGO Livingston, LIGO Hanford and Virgo respectively. Therefore, for the purpose of our work, we rely on the publicly available GLADE galaxy catalog [6] which is all-sky and complete up to 100Mpc, and nearly complete up to 150Mpc.

2.2 Grade reformulation with stellar masses

Given the large size of error boxes, the number of galaxies compatible with an event can be very large (>few thousands). In such cases, the classification using the 3D probability only is limited because it will produce similar values for a large number of galaxies. Adding galaxy properties to the ranking is a way to reduce the sample size of interesting galaxies. Among the various galaxies properties that could influence the rate of BNS merger, such as star formation rate (SFR), stellar mass and metallicity, several works pointed out a significant dependence to the stellar mass [7, 8, 9]. Furthermore, short GRB host galaxies are known to be associated to BNS merger since GW170817, and are found in massive galaxies. The short GRB host galaxies are more massive than the long GRBs host galaxies, pointing to the importance of the stellar mass in determining the rate of short GRBs [10]. So far, the only one known (by gravitational waves) host galaxy of BNS merger is NGC4993 from GW170817 event. This galaxy present a very high mass and a low star formation rates. The host galaxy of GRB150101B presented as an analogue of GRB170817A [11] is also a vary massive galaxy. In the light of those information we chose to focus on the stellar mass for the selection of gravitational waves host galaxy candidates.

Assuming that we are able to get the stellar masses information of the galaxies we introduce a new term G_{mass} defined as:

$$G_{mass} = \frac{M_{*,galaxy}}{\sum M_{*,galaxy}} \tag{2}$$

where $M_{*,galaxy}$ is the stellar mass of a given galaxy and the sum is over all of the galaxies compatibles with a given skymap. In order to keep galaxies without stellar mass information, and still use their 3D localization probability, P_{pos} from equation (1), we propose to redefine the grade as:

$$G_{tot} = P_{pos}\,(1 + \alpha\beta G_{mass}) \tag{3}$$

where α and β are positive real parameters. With such definition, G_{mass} is set to 0 when the stellar mass information is not available to fall back on P_{pos}. The parameter β is used to weight the importance of G_{mass} in the total grade, it is skymap independent. Ideally, β should be fitted on a statistically significant sample of gravitational wave host galaxies, but as only one event has been detected so far, we simply chose to put β equal to one. The parameter α is defined such that the two terms in equation (3) contribute equally to the total grade, G_{tot}:

$$\frac{\sum P_{pos}}{N} = \frac{\sum P_{pos}\,\alpha\,G_{mass}}{N} \tag{4}$$

$$\Rightarrow \alpha = \frac{\sum P_{pos}}{\sum P_{pos}\,G_{mass}} \tag{5}$$

where N is the total number of galaxies compatible for a given skymap having a determined stellar mass, and the sum is also over all galaxies compatible for a given skymap having a determined stellar mass.

Any details on this reformulation of the grade allowing the ranking of the galaxies and comparison with previous work expression can be found in [1]. As an example we chose to test this new version of the ranking on the GW170817 event. We chose this event in particular because this is the only known gravitational waves event for which the host galaxy has been determined at the moment. Our results show that our new reformulation of the grade provide better results than any previous works by ranking the host galaxy of the event at the first position. An important improvement of our grade expression is also the fact that galaxies without determined stellar masses are still present in the ranking using only their P_{pos} defined (1). Any detail on this test can be found in [1].

3 Publicly available tools

3.1 The Mangrove catalog

Homogeneity in the stellar mass estimation is crucial for our purpose as it is used to rank the galaxies. Unfortunately,the GLADE galaxy catalog we rely on provides the B, J, H and K band magnitudes for some of the galaxies but not the stellar mass. We did not chose to compile the stellar masses from various works for homogeneity reasons as it would bring systematics in the ranking process due to possibly quite different methods in the stellar mass estimation.

The near-infrared luminosity emitted by the old stellar population is fairly insensitive to dust extinction, and is thus considered as a reliable indicator of the total stellar mass of a galaxy. Previous works [13, 14] showed that the stellar mass of galaxies can be esti-

[1] The distance at which the merger of a BNS system gives a matched filter signal-to-noise ratio (SNR) of 8; the distance is averaged over all the possible sky localizations and binary orientations. Each neutron star in the binary is assumed to have mass equal to 1.4 solar masses [16]

mated with a constant mass to light ratio: $\Upsilon_*^{3.4\mu m} \sim 0.60 M_\odot / L_{\odot,3.4\mu m}$ where $M_\odot / L_{\odot,3.4\mu m}$ is the mass-to-light ratio in units of solar masses over the solar luminosity in the WISE 3.4μm band ($m_\odot, 3.4\mu m = 3.24 mag; L_\odot, 3.4\mu m = 1.58 \times 10^{32} ergs^{-1}$ [15]). This approach derives stellar mass with an error of 0.10 in log scale.
In order to provide the stellar masses information we chose to merge the GLADE catalog [6] up to 400Mpc and the AllWISE catalog [12] and use this mass-to-light ratio method. We obtained a merging efficiency of ∼93%. Any detail on this merging work can be found in [1]. The resulting catalog, which includes GLADE, AllWISE and stellar mass information is named Mangrove (Mass AssociatioN for GRavitational waves ObserVations Efficiency) and it is fully publicly available at `https://mangrove.lal.in2p3.fr`. As presented in the previous section, this catalog providing the stellar mass information of the galaxies allow us to highly optimize the galaxies targeting approach.

3.2 The Mangrove web interface

We chose to publicly provide our new method.

Firstly, if anyone wants to use our improved grade presented in this work to produce their own observation plan, it is implemented in the widely used *gwemopt*[2] python package, developed to optimize the efforts of electromagnetic follow-up of gravitational wave events.

Secondly, we have built a dedicated web interface (`https://mangrove.lal.in2p3.fr`) which provide for any gravitational wave alert bellow 400Mpc a ranked list of galaxies according to our new method. It is possible define an observational configuration and limitation (latitude, longitude, elevation, horizon, distance to the moon, maximum airmass) to produce a list of ranked galaxies effectively observable from any observatory.

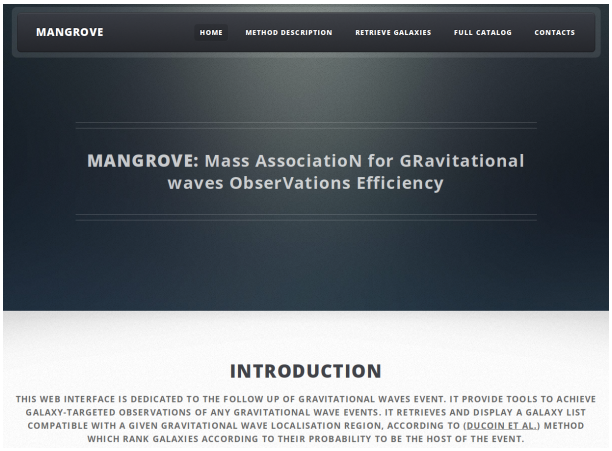

Figure 1: Screenshot of the Mangrove web interface

[2] https://github.com/mcoughlin/gwemopt

4 Conclusions

The electromagnetic follow-up of gravitational wave events is very challenging, the poor localization of the source provided by LIGO-Virgo forces telescopes around the world to observe large areas of the sky. As the electromagnetic counterpart is expected to decay rapidly in luminosity, an optimization is required to perform a rapid and efficient follow-up of the skymap. Recent developments in both catalog of galaxies and galaxy targeting strategy already optimized significantly the follow-up of such event. Our work provides an efficient tool to upgrade in one hand a catalog of galaxies by adding the stellar mass information and on the other hand the galaxy targeting approach with a new expression of the grade using this stellar mass information to select and rank the galaxies. This work plainly encourages further developments of the galaxy targeting strategy including other physical properties of the galaxies, for instance by focusing low SFR galaxies, but such development are slowed down by the poor number of information available in the publicly available galaxy catalogs.

Acknowledgements

We acknowledge the JRJC organizing committee for the invitation. We acknowledge the Virtual data of labex P2IO for the supply of IT resources. This work made use of the NASA/IPAC Extragalactic Database (NED). We acknowledge the GRANDMA (Global Rapid Advanced Network Devoted to the Multi-messenger Addicts) collaboration for its technical support and assistance in the development of the mangrove web interface.

References

[1] Ducoin, J.-G., Corre, D., Leroy, N., Floch, E. L. 2019, arXiv preprint arXiv:1911.05432

[2] Ghosh S., Bloemen S., Nelemans G., Groot P. J., Price L. R., 2016a,AA,592, A82

[3] Coughlin M. W., Dietrich T., Heinzel J., Khetan N., Antier S., Christensen N., Coulter D. A., Foley R. J., 2019a, arXiv e-prints, p. arXiv:1908.00889

[4] Coughlin M. W., et al., 2018, MNRAS, 478, 692

[5] Gehrels N., Cannizzo J. K., Kanner J., Kasliwal M. M., Nissanke S., Singer L. P., 2016, ApJ, 820, 136

[6] Dalya G., et al., 2018, MNRAS, 479, 2374

[7] Artale M. C., Mapelli M., Giacobbo N., Sabha N. B., Spera M., Santoliquido F., Bressan A., 2019, MNRAS, 487, 1675

[8] Toffano M., Mapelli M., Giacobbo N., Artale M. C., Ghirlanda G., 2019, MNRAS, p. 2085

[9] Mapelli M., Giacobbo N., Toffano M., Ripamonti E., Bressan A., Spera M., Branchesi M., 2018, MNRAS, 481, 5324

[10] Berger E., 2014, ARAA, 52, 43

[11] Troja E., et al., 2018, Nature Communications, 9, 4089

[12] Cutri R. M., et al. 2014, VizieR Online Data Catalog, p. II/328

[13] Kettlety T., et al., 2018, MNRAS, 473, 776

[14] Norris M. A., Meidt S., Van de Ven G., Schinnerer E., Groves B., Querejeta M., 2014, ApJ, 797, 55

[15] Jarrett T. H., et al., 2013, AJ, 145, 6

[16] Abbott B. P., et al., 2018a, Living Reviews in Relativity, 21, 3

[17] Coughlin, M. W., Dietrich, T., Antier, S., et al. 2019, arXiv e-prints, arXiv:1910.11246

[18] Abbott B. P., et al., 2017a, Phys. Rev. Lett., 119, 161101

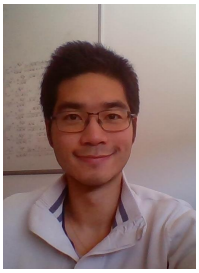

A model of the coating thermo-elastic and thermorefractive noises in gravitational wave detectors

Hui Victor

Laboratoire d'Annecy de Physique des Particules (LAPP)

Abstract — The first gravitational wave detection occurred with the LIGO detector in the United states and the Virgo detector in Europe, opening the way to the field of gravitational astronomy and providing information on black holes, neutron stars and relativity theory of Einstein that were inaccessible before. It is essential to improve the sensitivity of these detectors to progress in this area. One of the main limitation to the sensitivity comes from the thermal fluctuation that occurs within the mirrors used in these giant laser interferometers. The fluctuation-dissipation theorem asserts that any mechanical oscillator is affected by a motion of thermal origin directly related to its thermodynamic temperature. The Virgo and LIGO detectors use mirrors and their suspensions which are examples of such mechanical oscillators. As a consequence their position is affected by this thermal vibration and the sensitivity of the gravitational wave detector is said to be thermal noise limited over a wide range of frequencies. Detailed studies show that these thermal fluctuations are dominant in the reflective multilayered coating deposited on the surface of the mirror. In this proceeding, we present a model that we developed to calculate the spectral density of two specific thermal noises that are relevant for the interferometer: the thermorefractive noise and the thermoelastic noise.

1 Introduction

The gravitational wave detectors Virgo and LIGO use long baseline laser Michelson interferometers to measure the vibration of space-time induced by a gravitational wave. Currently, gravitational wave detectors have reached a sensitivity of slightly more than $10^{-23}/\sqrt{\text{Hz}}$. This is equivalent to mirror displacements of the order of $10^{-19}\text{m}/\sqrt{\text{Hz}}$. Figure 1 shows the planned strain sensitivity of Advanced Virgo reaching a level of about $5.10^{-24}/\sqrt{\text{Hz}}$ for frequencies around 100 Hz.

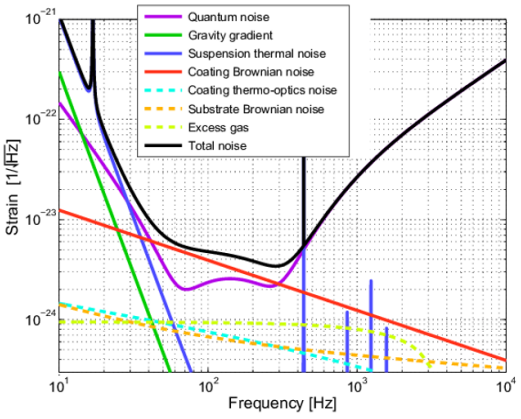

Figure 1: Noises limiting Advanced Virgo sensitivity as a function of frequency

We can observe that the detector's sensitivity is mainly limited by the thermal noise in the coating, especially the Brownian noise which will be explained later. The spectrum of thermal noise is known through the fluctuation-dissipation theorem once we know the dissipation that affects the system. As a consequence, it is crucial to have a detailed knowledge of the dissipation mechanism in order to predict and possibly reduce thermal noise amplitude. In the following of the article, we will briefly explain the fluctuation-dissipation theorem in section 2 while in section 3, we will discuss the ways to reduce coating thermal noise. We will then discuss the case of the coating thermoelastic and thermorefractive noise in section 4 and explain how we obtain our model in section 5. The results will be presented and discussed in section 6.

2 The Fluctuation-Dissipation theorem

Let's consider a linear physical system with an impedance Z in thermodynamic equilibrium at temperature T. The Fluctuation-Dissipation Theorem asserts that when this system is affected by some form of dissipation, it will be subject to a fluctuation whose amplitude is related to its thermodynamic temperature.

By explaining the Johnson noise in electrical resistors, H. Nyquist formulated in 1928 the theoretical general form of the so called Fluctuation-Dissipation Theorem which we will note FDT. It provides a relation between the power spectrum of the fluctuating thermal force applied on an observable $x(\omega)$ of the system and the system's impedance $Z(\omega)$, which is defined as the ratio between the speed $v(\omega) = i\omega x(\omega)$ and the generalized force $F(\omega)$ applied to the observable x:

$$Z(\omega) = \frac{F(\omega)}{v(\omega)} \tag{1}$$

where ω is the angular frequency. We can then write the power spectrum of the fluctuation of x using the admittance $Y(\omega) = \frac{1}{Z(\omega)}$:

$$S_x(\omega) = \frac{4k_BT}{\omega^2} Re\big(Y(\omega)\big) \tag{2}$$

where k_B is the Boltzmann constant, ω the angular frequency and T the mean temperature of the system. Its numeric value will be 300 K in all the rest of the discussion. The expression for the real part of the admittance can be derived [1] using the relation between the generalized force $F(t)$ and the velocity v which gives the dissipated power:

$$W_{diss} = \left\langle \int F(\vec{t}).v(\vec{t})dt \right\rangle = F_0^2 Re(Y(\omega))\frac{1}{2} \tag{3}$$

where F_0 is the amplitude of the force. Hence

$$|Re\big(Y(\omega)\big)| = \frac{W_{diss}}{\frac{F_0^2}{2}}. \tag{4}$$

Finally, the spectral density of the fluctuations of x is then written as:

$$S_x(\omega) = \frac{8k_BT}{\omega^2}\frac{W_{diss}}{F_0^2} \tag{5}$$

3 Coatings

Coatings are made of couples of layers that are laminated alternately on the substrate. Each doublet is made of two different materials. Its structure is similar to the Bragg's reflector structure, made of superposed thin layers. In Virgo, the mirrors coatings are made in amorphous material. The couple of materials used for the alternating layers is Titanium doped tantala oxide and Silica ($Ti{:}Ta_2O_5/SiO_2$).

Since Brownian noise is the dominant thermal noise in the interferometer, we want to reduce it. Preliminary studies have shown that coatings material properties have an impact on Brownian noise. Especially if we use crystalline materials, the mechanical losses will be lower, hence Brownian thermal noise will decrease [2]. But for this type or coating, other thermal noises that occur in the coating can become significant, namely the thermo-optic noise (in blue-dotted line in fig 1) who consists of two noises: the thermorefractive and thermoelastic noises. These are discussed in the next session.

4 Thermoelastic and thermorefractive noise

Thermoelastic noise

The thermoelastic noise is due to temperature fluctuations that change the coating layers' thickness because of their thermal expansion coefficient. It will locally create a deformation at the surface of the coating. So when the beam illuminates the mirror, it will result in a phase shift in the reflected beam. The expression of the thermoelastic noise is

$$S_{TE} = \frac{2\sqrt{2}k_BT^2}{\pi r_0^2\sqrt{\omega\kappa_s C_s}}(\alpha_c d)^2 \tag{6}$$

where C_s and κ_s are respectively the volume heat capacity and the thermal conductivity of the substrate. α_c is the coating coefficient of thermal expansion and d the coating's thickness.

Thermorefractive noise

The thermorefractive noise is another effect due to temperature fluctuations but with a different physical origin. It is related to the refraction index of the material of which the mirror's coating is made of.

Although we consider high reflective mirror's, the laser is actually not completely reflected at the surface but part of it is propagating inside the layers of the coating.

Since the indices n1 and n2 of the couples of layers that constitutes the coating depend on the temperature T, then thermodynamical fluctuation of temperature lead to fluctuations of optical thickness of these layers, hence to the phase noise in the reflected beam. The expression of the thermorefractive noise is

$$S_{TR} = \frac{2\sqrt{2}k_BT^2}{\pi r_0^2\sqrt{\omega C_s\kappa_s}}(\beta\lambda)^2 \tag{7}$$

where β is the coefficient of thermorefraction of the coating and λ the wavelength of the laser (λ=1064 nm).

5 Construction of the model for thermoelastic and thermorefractive noise

Motivation

We want to build a model of the thermorefractive and thermoelastic noise in different types of coating. However, due to the fact that we cannot confront the simulation by direct measurements on the Virgo site, we have to impose some experimental restrictions. We do the measurements on optical benches, so we use smaller laser beams than the one used for Virgo. In particular, that means that the spotsize r_0 of the laser has to be smaller. Whereas in Virgo, the spot size is about 5 cm, on optical benches, we will use laser with a spot size around 100 microns. This has the advantage to make the effect of thermal noise larger thus making its measurement easier. Nevertheless, in these conditions, the expressions of thermal noises presented in the previous section are not valid anymore. Indeed, those expressions are computed using approximations, namely the adiabatic approximation which neglect thermal diffusion in the mirror. For small r_0 this approximation is not valid anymore at low frequencies. That's why we need to build a new model for small laser spotsizes

which does not assume any approximations on the thermal diffusion.

General steps

First, in order to obtain the thermal noise, one need to determine the dissipated power. Its expression is given by

$$W_{diss} = \frac{\kappa}{T}\Big\langle \int (\nabla T(\vec{r}))^2 \mathrm{d}^3 r \Big\rangle \tag{8}$$

where $T(\vec{r})$ is the distribution of temperature in the mirror as a function of space variables. Its expression can be obtained from the thermal diffusion equation:

$$\frac{\rho C}{\kappa}\frac{\partial T(\vec{r},t)}{\partial t} - \nabla^2 T(\vec{r},t) = \frac{Q(z,t)}{\kappa} \tag{9}$$

Depending on the nature of the studied noise, the heat injected Q(z,t) will have a different expression. In the space and time transformed Fourier space, we define $k_\perp = (k_x, k_y)$. Using Fourier transform, we then have

$$(k^2 + k_\perp^2)T - \frac{\partial^2 T(k_\perp,\omega)}{\partial z^2} = \frac{\tilde{Q}(k_\perp,\omega)}{\kappa} \tag{10}$$

We define $k = \sqrt{\frac{i\omega\rho C}{\kappa}}$ and k is related to the thermal length: $l_{th} \to l_{th} = \frac{1}{|k|}$. The expression of the injected heat Q will depend on the intensity of the laser beam that arrives on the mirror' surface. So we can write

$$Q(k_\perp,\omega) = e^{-\frac{k_\perp^2 r_0^2}{8}} Q_0(\omega) \tag{11}$$

Where $Q_0(\omega) = \tilde{Q}_{TR}(\omega)$ for the thermorefractive model and $Q_0(\omega) = \tilde{Q}_{TE}(\omega)$ for the thermoelastic model. Second, we determine the expression of $\tilde{Q}_{TR}(\omega)$ and $\tilde{Q}_{TR}(\omega)$. They depend on the properties of the heat source injected in the mirror [3]. We will explain the case for the thermorefractive noise. The approach for the thermoelastic noise is similar. Let's consider a mirror with a multi-layer coating. We observe the incident light coming on the mirror and the reflected light and we also consider a local change of temperature δT in the coating. The light's intensity profile is described by the function $|\Psi(\vec{r})|^2$. The plot below show the field phase shift upon reflection as a function of the layer whose temperature is changed by $\Delta T = 1K$ and affected by the thermorefractive mechanism.

On the plot we can observe that the reflected light phase rapidly falls to zero which means it penetrates the coating over a small length l (a maximum of 10 layers thickness). We can then assume that layers which play a role in the thermorefractive effect are the ones near the surface of the mirror. The reflected light's phase at a local point $\vec{r}$ is given by

$$\phi(\vec{r}) = \int \delta T(\vec{r},t) f(\vec{r}) \mathrm{d}^3 r \tag{12}$$

We are looking for the form factor function $f(\vec{r})$ which links the phase of the reflected light to the temperature fluctuation. Since the laser wave penetrates the mirror

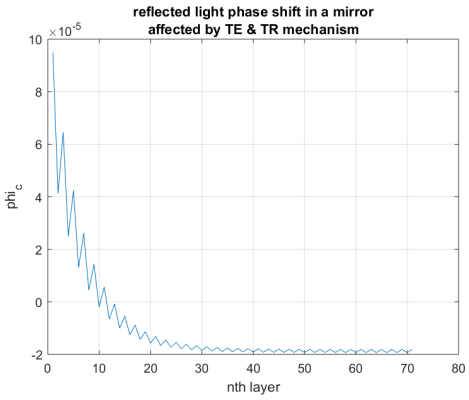

Figure 2: Evolution of phase shift with nth layer in TR noise model

over a small distance along the z direction, the intensity profile pondering the average phase is multiplied by a function $G(z) = A\frac{e^{-\frac{z}{l}}}{l}$, where l is the penetration depth of the laser wave and A a factor which will depend on the physical parameters. So we have a form factor which expression is $f(\vec{r}) = \big|\Psi(\vec{r})\big|^2 A e^{-\frac{z}{l}}$. So we can write the phase $\phi(\vec{r})$ as follows

$$\phi(\vec{r}) = \int \delta T(\vec{r},t) A \big|\Psi(\vec{r})\big|^2 e^{-\frac{z}{l}} \mathrm{d}^3 r \tag{13}$$

Assuming that the light amplitude profile is normalized and that we consider a temperature variation of 1 Kelvin, we have

$$\begin{aligned}\phi(\vec{r}) &= \int A\big|\Psi(\vec{r})\big|^2 e^{-\frac{z}{l}} \mathrm{d}S\mathrm{d}r \\ &= \int A e^{-\frac{z}{l}} dz = A e^{-\frac{z_k}{l}}\end{aligned} \tag{14}$$

where z_k is the z position of the layer where the temperature change occurs. If we try to fit the curve from the plot of figure 2, we can find $A = 4\pi\beta = 0.0001$. If we want to write the phase in the same form as in the thermoelastic model we have

$$\phi(\vec{r}) = \frac{4\pi}{\lambda}\iiint \mathrm{d}^3 r |\Psi(\vec{r})|^2 \beta\lambda e^{-\frac{z}{l}} \delta T(\vec{r},t) \tag{15}$$

Then after integration over z we obtain

$$\phi(\vec{r},t) = \frac{4\pi}{\lambda} e^{-\frac{z_k}{l}} \int \beta\lambda |\Psi(\vec{r})|^2 \delta T(\vec{r},t) \mathrm{d}x\mathrm{d}y \tag{16}$$

We can then deduce from that the form factor $f(\vec{r})$ that shape the heat injected in the coating for this model: $f_{TR}(\vec{r}) = \beta\lambda|\Psi_m(\vec{r})|^2$. Since the layers that really impact the phenomenon are close to the surface, we can assume that the profile of the heat injected is a surface profile. This comes from the $e^{\frac{z_k}{l}}$ term which falls rapidly to 0 as z_k increases. We give its expression: $Q(r,t) = F_0\cos(\omega t) f(\vec{r})$ The form factor is given by $f(\vec{r}) = \beta\lambda I(\vec{r})$ where $I(\vec{r})$ is the in-

tensity of the laser beam. Combining this form factor with the expression of the heat $Q(k_\perp, \omega)$ in Fourier time and space domain we obtain the expression of $Q_0(\omega)$: $Q_0(\omega) = \beta\lambda\omega T F_0 \sin(\omega t) = \tilde{Q}_{TR}(\omega)$. Third, solving the thermal diffusion equation, one gets the temperature distribution in the coating and the substrate and taking the gradient of it, one can obtain the dissipated power:

$$W^{TE,TR}_{diss_{coat}} = \frac{\kappa_c}{T}\int_0^\infty\int_0^{z_{coat}} \left\langle \left|\nabla\tilde{T}^{TE,TR}_c(k_\perp, z)\right|^2\right\rangle \mathrm{d}z\mathrm{d}k_\perp$$
$$W^{TE,TR}_{diss_{subst}} = \frac{\kappa_s}{T}\int_0^\infty\int_0^{z_{coat}} \left\langle \left|\nabla\tilde{T}^{Te,TR}_s(k_\perp, z)\right|^2\right\rangle \mathrm{d}z\mathrm{d}k_\perp \tag{17}$$

Finally, we get the expression of the thermal noises from equation (5).

6 Results

The resulting spectra for the thermorefractive and thermoelastic noises are shown in figure 3 and 4 respectively We compare these thermal noises for two types of coatings, a coating made of Ti:Ta_2O_5/SiO_2 as the one used in Virgo, and a crystalline coating made of layers of AlGaAs/GaAs. For the material properties, we used the values in table II of Evans paper [4] and Table I of Chalermsongsak et al. article [5].

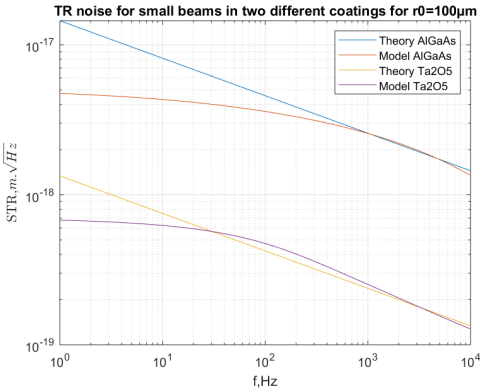

Figure 3: Comparison of thermorefractive noise in two types of coatings

In each plot we compare the noise calculated with the basic theoretical approach to our model, where the adiabatic approximation is dropped. One can observe that there is a cutoff frequency below which our model is drifting apart from the model that is valid for big laser spotsizes. This frequency is linked to the conditions where the adiabatic approximation is not valid anymore. Indeed, when the frequency decreases, the mirror is heated and cooled at a slower rate and, compared to r_0, the thermal diffusion length is not negligible anymore.

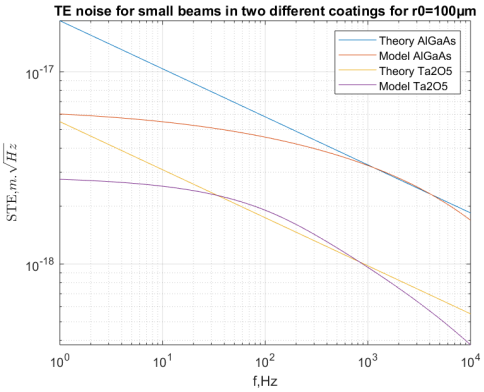

Figure 4: Comparison of thermoelastic noise in two types of coatings

7 Conclusion and future prospects

We presented a model of thermorefractive and thermoelastic noise in specific experimental conditions. We did the complete calculation without approximations and in the whole space of the mirror. There are still some on-going investigations especially around the high-frequency area where our model is dropping from the theoretical one. We are also exploring the thermo-optic noise, which is the coherent combination of thermorefractive and thermoelastic noise. Such a combination is expected to be smaller than each of the two contributions, making crystalline coatings a promising solution for future gravitational wave detectors.

References

[1] VB. Braginsky et al., Thermorefractive noise in gravitationnal wave antennae, Physics Letters A 271, 2000.

[2] G. Cole et al., Tenfold reduction of Brownian noise in high-reflectivity optical coatings, Nature Photonics, 2013.

[3] Y. Levin, Fluctuation-dissipation theorem for thermorefractive noise, Pysics Letters A 372, 2008.

[4] M. Evans et al., Thermo-optic noise in coated mirrors for high-precision measurements, Physical Review D78, 2008.

[5] Tara Chalermsongsak et al 2016 Metrologia 53 860.

Development of an advanced Compton telescope for MeV–range gamma–ray astronomy

Adrien Laviron, V. Gourlaouen, C. Hamadache, C. Hiver, J. Kiener, J. Peyre, V. Tatischeff

Université Paris-Sud, CNRS/IN2P3, CSNSM, 91405 Orsay, France

Abstract — An advanced Compton telescope appears to be the best instrument concept for the next generation gamma–ray space observatory in the MeV range. A first prototype of advanced Compton telescope is being developed to match the constraints of a nano satellite mission, with the scientific objective of measuring gamma–ray burst prompt emission polarization. Instrumental developments at CSNSM for this project are focusing on the position–sensitive calorimeter module, made of a monolithic inorganic $CeBr_3$ scintillator read by a pixelated photodetector. 3D position reconstruction is obtained by deep–learning algorithms that have been optimized down to an uncertainty of 2 mm for each spatial direction.

1 Introduction

MeV–range gamma–ray astronomy contains a large number of science themes such as the nucleosynthesis and chemical evolution of the universe, cosmic rays physics, or multi–messenger astronomy. The best concept for next generation instruments is thought to be a space–borne advanced Compton imager.

Compton imaging relies on the dominant process of interaction of gamma rays with matter in this energy range, Compton scattering. In a next generation MeV–range gamma–ray space telescope as proposed in [1], the incoming photon undergoes an inelastic scattering in one or several layers of position–sensitive silicon strip detector before being absorbed in a position–sensitive calorimeter based on inorganic scintillators. The measurement of both positions and energy deposits enables the determination of the photon's source direction [2]. It also enables measurement of the linear polarization of the incident gamma rays, which can provide a powerful diagnostic of the emission processes.

These measurements may be performed either in a large space observatory with a modular design or with a fleet of nano–satellites that enables all–time full–sky coverage, preferable for studying transient phenomena such as gamma–ray bursts.

2 Current instrumental developments

The main task of the CSNSM research team on this project is to develop a calorimeter module, that could be used either as a calorimeter in a nano–satellite or as a part of a large observatory's calorimeter. This study follows the work of [3] and [4].

The selected design for this calorimeter module is a monolithic square $51 \times 51 \times 10$ mm Cerium Bromide ($CeBr_3$) inorganic hygroscopic crystal (manufactured by SCIONIX company) read by a 64 channels multi–anode photomultiplier tube (MAPMT) or by an array of 8×8 silicon photomultipliers (SiPM). Those pixelated photodetectors are read by a commercial, self–triggered electronic system ROSMAP (designed by IDEAS company). Such a module can be seen on Figure 1.

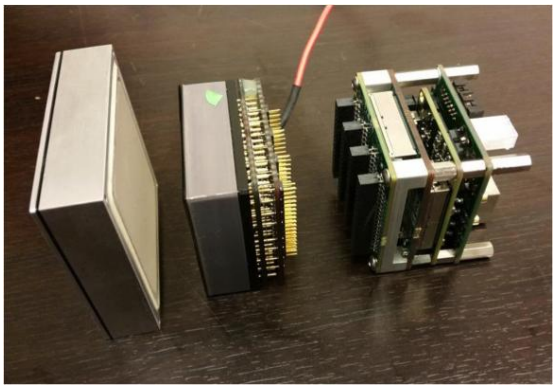

Figure 1: Photograph of the three parts of a module. From left to right : Hygroscopic $CeBr_3$ scintillator in its aluminium casing, Hamamatsu MAPMT, and ROSMAP front–end electronics.

In case of interaction of a gamma ray in the crystal, this scintillator produces an amount of light proportional to the energy deposit. This light is collected by the pixelated photodetector, and the sum of the signals read for each pixel enables energy measurements. Figure 2 shows an energy spectrum of a ^{137}Cs radioactive source acquired with this module.

The use of a pixelated photodetector also enables the analysis of the shape of the scintillation light distribution, in order to reconstruct the 3D position of first interaction of the gamma ray in the calorimeter. This principle is illustrated on Figure 3.

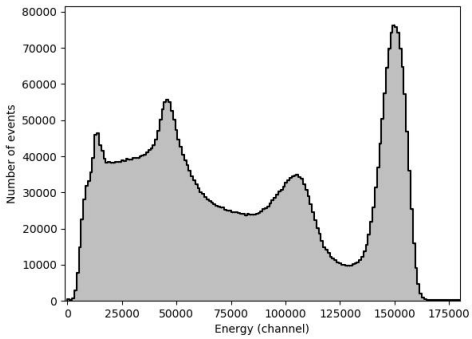

Figure 2: Spectrum of a ^{137}Cs radioactive source (662 keV line centered on channel $\approx$ 150000)

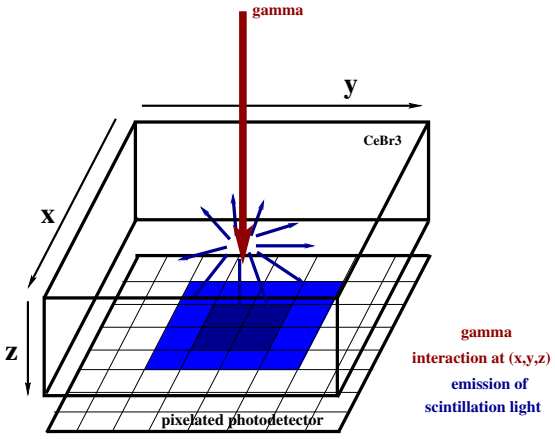

Figure 3: Schema of the calorimeter module. The gamma ray interacts in the $CeBr_3$ that emits scintillation light. This light is detected by a pixelated photodetector optically coupled to the scintillating crystal to analyze the shape of the scintillation light distribution.

3 Data analysis

To assess the position reconstruction ability of the module, we have developed a test bench consisting of a collimated radioactive source generating a gamma–ray beam of width 2 mm, and a module that can be automatically moved along two axes perpendicular to the direction of the gamma–ray beam. The source can irradiate either the xy or the yz plane of the scintillator (see Fig. 3). That way, either the (x, y) coordinates or the (y, z) coordinates of the gamma–ray first interaction are known.

In this part, we will briefly discuss the morphology of the events, before presenting the deep–learning algorithms that we use to reconstruct the position first in the xy plane and then in 3D.

Events morphologies

We define an event as one or several interactions of a single gamma ray that deposits enough energy to trigger the read–out electronics. Figure 4 shows the scintillation light distribution of an event. Because of the dominant physics processes at these energies, gamma rays may interact several times by Compton scattering in the scintillator. This leads sometimes to an event with several distinct energy deposits, as shown on Figure 5.

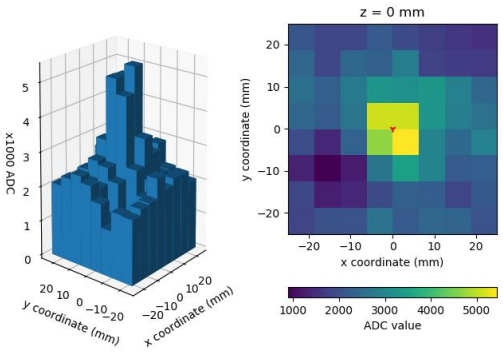

Figure 4: Example of a light distribution of an event recorded by the module. Both parts of the figure show the same data, one in parallel perspective and the other in colorscale.

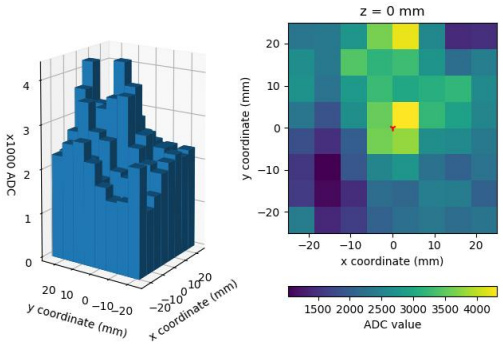

Figure 5: Example of a light distribution composed of several energy deposits recorded by the module.

These events can be identified automatically using an algorithm that checks whether the pixels that received the more scintillation light are packed together or separated. It relies on a 2D convolution of a shape representing the maximum authorized spread of the event with the scintillation light distribution.

This analysis showed that about 15% of events have a scintillation light distribution that is either spread or multiple.

The reconstruction of the first interaction position is done by machine learning algorithms that analyze the shape of the scintillation light distribution. Events with a spread or multiple scintillation light distribution are less well reconstructed by the algorithms, and they may or may not be used for position reconstruction

depending on the intensity of the astrophysical source and the targeted sensitivity and angular resolution of the telescope.

Artificial neural networks

An artificial neural network (ANN) is a network of simple algorithms that aims at mimicking the operation of a biological neuron. Those algorithms execute a weighted sum of several inputs, and apply to this number an $\mathbb{R} \to \mathbb{R}$ function called activation function. We use ANNs to reconstruct the position of interaction of a gamma ray from the measured scintillation light distribution.

The machine learning used in this study is supervised learning. It means that ANNs are first trained to output the correct coordinates using data with known output, by minimizing an error function. Once the training is completed, reconstructing unknown events consists in executing the neural network program with the parameters calculated during the training process. The weights of the neurons are free parameters adjusted during the training of the ANN.

ANNs used in this work are multi–layer perceptrons: neurons are organised into one or several layers, that are executed sequentially. The number of layers and their size (number of neurons) are meta–parameters of the ANN, chosen by the programmer. The activation function is also a meta–parameter, as well as the algorithm used for training. All this work has been done using the python Keras framework [5] with Theano [6] backend.

2D position reconstruction

To check the effect of varying meta–parameters on the performance of neural networks, a systematic exploration of the meta–parameters space has been conducted. The analysis has been performed for the following set of meta–parameters:

- 0 to 4 hidden layers
- 6 to 35 neuron per hidden layers
- `sigmoid`, `hard sigmoid`, `tanh`, `elu`, `relu`, `softplus`, `softmax`, `softsign`, and `linear` activation functions [5]
- `adam`, `nadam` and `adamax` training algorithms

Figure 6 shows an output example of such an exploration. The colorscale represents the performance of an ANN which is defined as the square root of the mean squared distance from the reconstructed coordinates to the known ones,

$$\sigma_{\mathrm{XY}} = \sqrt{\frac{1}{N}\sum_{i=1}^{N}\left[\left(x_i^{\mathrm{known}} - x_i^{\mathrm{rec}}\right)^2 + \left(y_i^{\mathrm{known}} - y_i^{\mathrm{rec}}\right)^2\right]}, \quad (1)$$

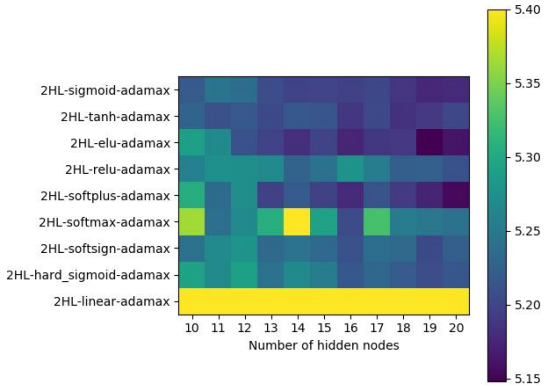

Figure 6: Output example of a systematic meta–parameters space exploration. On the x axis is represented the number of neurons per layer. On the y axis are indicated the nine tested activation functions. Here the ANN uses two hidden layers (HL) and the adamax training algorithm. Colorscale represents the performance of the ANN σ_{XY} as defined in the text (lower is better).

where x_i^{known} (respectively y_i^{known}) is the known x (resp. y) coordinate of event i and x_i^{rec} (resp. y_i^{rec}) is the x (resp. y) coordinate reconstructed using the ANN. Equation 1 is calculated on a set of $N = 14450$ events evenly distributed on the xy plane of the detector.

It should be noted that this definition of the performance of an ANN includes in the calculation some events from the background radioactivity. Their position of interaction is not in general that of the gamma rays from the source, leading to an apparent worsening of the ANN performance from $\sigma_{\mathrm{XY}} \approx 5.2\,\mathrm{mm}$ to $\sigma_{\mathrm{XY}} \approx 2.8\,\mathrm{mm}$. In measurements with the ^{137}Cs source, the background amounts to 2% of the total number of counts in the selected energy window.

The analysis has been conducted for various event selection procedures. All of them have in common a fine selection of the energy of the events around the full–energy peak of the source.

Since the calorimeter must be able to detect and reconstruct the position of gamma rays of any energy, some datasets were acquired using the 59.5 keV line of a collimated ^{241}Am radioactive source. An example of event at this energy can be seen on Figure 7.

This study concluded that the most robust way of training an ANN for our application is using `adamax` and all event morphologies.

Since there is very little improvement with more than 2 hidden layers and 20 neurons per hidden layer and since those numbers have an effect on the execution time of the reconstruction algorithm, these numbers have been found to be a good compromise. Considering the results shown on Figure 6 amongst others, we choose to use either the `elu` or `softplus` activation function. Finally, this study showed that using two

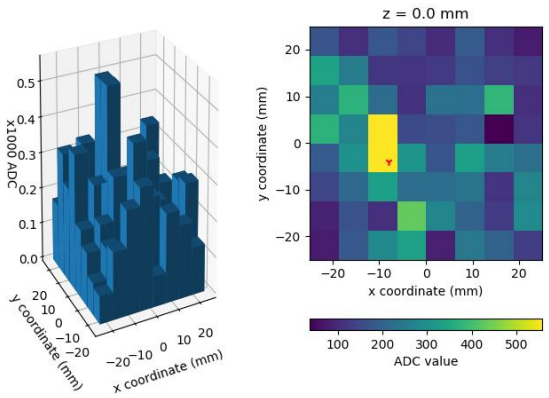

Figure 7: Example of an event of energy 59.5 keV recorded by the module.

neural networks, each trained on a single 59.5 keV or 662 keV energy window, does not perform significantly better than using a single neural network trained on both energy windows, with $\sigma_{XY} \approx 2.8$ mm.

Depth of interaction reconstruction

The depth of interaction reconstruction algorithm has been designed using the knowledge acquired from the reconstruction of the xy position. The principle driving the position reconstruction along the z axis is that the measured scintillation light distribution is expected to be narrower for gamma–ray interactions occurring closer to the photodetector. However, this effect is faint and therefore requires a deeper neural network. For that purpose we choose to focus the optimization on a 4 hidden layers, 80 neurons per layer ANN and optimize only the activation function and the training algorithm.

To train the neural networks, data was acquired by irradiating the yz plane of the detector with a ^{137}Cs radioactive source. These trainings rely only on the z coordinate. To generate events of different energies, four energy ranges were defined, one in the full–energy peak at 662 keV, the three others in the Compton front around 60 keV, 130 keV and 300 keV. These last three types of events approximate a localised full–energy event of a lower energy gamma–ray by the scintillation light of a Comptonized electron.

To assess the performance of these ANNs, we use the standard deviation

$$\sigma_Z = \sqrt{\frac{1}{N}\sum_{i=1}^{N}\left(z_i^{\text{known}} - z_i^{\text{rec}}\right)^2}\,, \qquad (2)$$

where the terminology is the same as in Equation 1.

This part of the study concluded that ANNs are best trained for our purpose using `adamax`. The most performing activation functions in this case are `elu` and `relu`. The energies at which depth of interaction is best reconstructed are around 662 keV and 300 keV, with $\sigma_Z \approx 2$ mm. In the 130 keV energy range, ANNs are significantly worse with $\sigma_Z \approx 2.4$ mm, and in the 60 keV energy domain they perform even worse with $\sigma_Z \approx 2.6$ mm. This could be explained by the shape of the scintillation light distribution at lower energies, as shown in Figure 7: The width of such a distribution is hard to measure and its peak is close to the noise level. For these lower energy gamma rays, the attenuation length in $CeBr_3$ is < 2 mm, therefore using a neural network of larger uncertainty is sub–optimal. Assigning to each of these events a depth of interaction equal to the mean depth of interaction of gamma rays with the same energy (calculated from NIST XCOM cross–section database [7]) gives $\sigma_Z < 2$ mm.

Finally, as for the 2D position reconstruction, training ANNs with all events from the 662 keV, 300 keV and 130 keV energy domains led to σ_Z results similar to those obtained with specific ANNs trained with events from each energy domain.

4 Conclusions

We developed a calorimeter module for next generation MeV–range gamma–ray observatories. We focused on reconstructing as best as possible the 3D position of the first impact of an incident gamma–ray within the detector, as this property is vital for the performance of a Compton telescope. We chose for that purpose deep learning algorithms. 2D position reconstruction algorithms were optimized to attain an uncertainty $\sigma_{XY} \approx 2.8$ mm using 2 hidden layers, 20 neurons per layer, `elu` or `softplus` activation function and `adamax` training algorithm. 3D position is obtained by reconstructing the depth of interaction with a separate neural network using 4 hidden layers, 80 neurons per layer, `elu` or `relu` activation function and `adamax` training algorithm. The uncertainty of this reconstruction is $\sigma_Z \approx 2$ mm. Those results apply to any gamma–ray energy from 60 keV to 662 keV.

Finally, using an energy correction dependant on the position of interaction [4], the spectral resolution of the module is found to be 5.1% at 662 keV.

References

[1] A. De Angelis, V. Tatischeff, M. Tavani et al. The e-ASTROGAM mission. Exploring the extreme Universe with gamma rays in the MeV–GeV range, Experimental Astronomy 44 (1) (2017) 25–82. arXiv:1611.02232, doi:10.1007/s10686-017-9533-6.

[2] A. C. Zoglauer, First light for the next generation of Compton and pair telescopes : Development of new techniques for the data analysis of combined Compton and pair telescopes and their application to the MEGA prototype, Ph.D. thesis, - (Jan 2006).

[3] A. Gostojic, V. Tatischeff, J. Kiener et al. Application of artificial neural network in 3D imaging

with lanthanum bromide calorimeter. Nuclear Instruments and Methods in Physics Research A 787 (2015) 140–143. doi:10.1016/j.nima.2014.11.076.

[4] A. Gostojic, V. Tatischeff, J. Kiener et al. Characterization of $LaBr_3$:Ce and $CeBr_3$ calorimeter modules for 3D imaging in gamma-ray astronomy. Nuclear Instruments and Methods in Physics Research A 832 (2016) 24–42. doi:10.1016/j.nima.2016.06.044.

[5] F. Chollet et al. Keras. https://keras.io (2015)

[6] The Theano Development Team. Theano: A Python framework for fast computation of mathematical expressions. arXiv:1605.02688

[7] Berger, M.J., Hubbell, J.H., Seltzer, S.M., et al. (2010), XCOM: Photon Cross Section Database (version 1.5). [Online] Available: http://physics.nist.gov/xcom [2020, January 23]. National Institute of Standards and Technology, Gaithersburg, MD.

The Search for Light Dark Matter with DAMIC and DAMIC-M

Ariel Y. Matalon, for the DAMIC and DAMIC-M Collaborations

Kavli Institute for Cosmological Physics and The Enrico Fermi Institute, The University of Chicago, Chicago, USA

Laboratoire de Physique Nucléaire et des Hautes Energies, Sorbonne Université, CNRS-IN2P3, Paris, France

Abstract — The DAMIC (Dark Matter in CCDs) experiment employs the bulk silicon of scientific-grade charge coupled devices (CCDs) to detect dark matter particles. Since 2017, DAMIC has operated a seven-CCD detector (40-gram target mass) installed in a low radiation environment in the SNOLAB underground laboratory. The CCDs have excellent energy and spatial resolutions, low-energy thresholds, and a unique capability to identify surface and bulk radioactive backgrounds. DAMIC-M, the next phase of the program, will be installed at the Laboratoire Souterrain de Modane in France. It will feature a kg-size silicon target consisting of ultra low-noise CCDs, and will probe a broad range of low-mass dark matter particles. DAMIC-M CCDs feature a new specialized Skipper readout and have unprecedented single electron resolution, resulting in a detection threshold as low as 2 ionized electrons. We present results from the DAMIC Experiment at SNOLAB, and review key development efforts of DAMIC-M, including obtaining single electron resolution for our first batch of Skipper CCDs, the largest ever built.

1 Introduction

There is overwhelming astrophysical and cosmological evidence for Dark Matter (DM) as a major constituent of the universe, in particular by how its gravitational presence effects dynamics of galaxy clusters [1], galactic rotation curves [2], and features of the Cosmic Microwave Background [3]. DM comprises about 25% of the energy matter density of the universe; ordinary matter comprises 5%. This DM component has influenced cosmic structure and galaxy formation. Determining the so-far-elusive nature of DM remains one of the most important scientific efforts today.

One of the most attractive paradigms to describe DM is a set of exotic particles, described by the WIMP, or Weakly Interacting Massive Particle. WIMPs, thermal relics from the early universe, have kinetic energy on the order of tens of keV, and are expected to scatter elastically off a nucleus of target material. Searches for WIMPs at heavier masses (≈ 100 GeV/c^2) have placed sensitive limits [4][5], but so far have been unsuccessful in directly detecting DM. As such, there has been a shift to search for WIMPs across a broader mass range, and to probe for the existence of a hidden sector of lighter DM particles that interact with electrons.

2 DAMIC at SNOLAB

The DAMIC (Dark Matter in CCDs) experiment [6]–[10] employs the bulk silicon of scientific-grade charge-coupled devices (CCDs) to detect coherent elastic scattering of WIMPs. By virtue of the low readout noise of the CCDs and the relatively low mass of the silicon nucleus, DAMIC is especially sensitive to low mass ($<$20 GeV/c^2) WIMPs. DAMIC is located 2 km underground in the SNOLAB laboratory. A tower of seven, 16Mpix CCDs has been acquiring data since 2017.

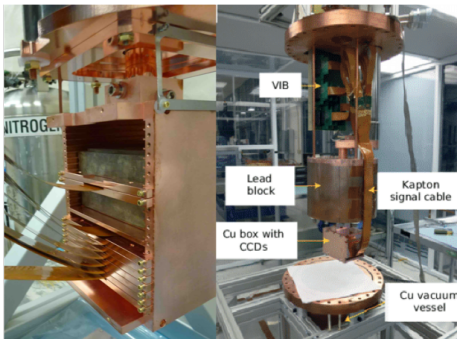

Figure 1: The DAMIC setup at SNOLAB.

CCDs were installed into a copper box using OHFC and electroformed copper modules; they are shielded by lead and polyethylene. The CCDs were developed at LBNL MicroSystems Lab, and feature a 3-phase polysilicon gate structure with a buried p-channel [11]. Each pixel is 15μm $\times$ 15μm. The active region is fabricated from n-type, high-resistivity ($>$10 kΩ cm) silicon, enabling low substrate-donor-density, leading to full depletion at low bias voltages. At full depletion, ionization is drifted along the direction of the electric field. The charge carriers (holes) are collected and held $<$1 μm below the gates until readout. The charge spatial variance is proportional to carrier transit time.

During readout, charge is transferred vertically from pixel to pixel by modulating the electrodes ("parallel clocks") of each pixel's gate structure. Higher frequency "serial" clocks move charge from the serial register to the CCD's output node, where it is measured by a correlated double-sampling circuit. Charge transfer inefficiency is on the order of 10^{-6}; the pixel charge r.m.s. is $<$ 2 electrons, leading to a very low energy threshold. DAMIC CCDs have the lowest dark current ever measured in a semiconductor detector: $\leq 10^{-21}$A/cm^2.

2.1 Measurements of radioactive backgrounds in DAMIC CCDs

The sensitivity of DM direct-detection experiments is determined by the ability to identify and mitigate backgrounds, namely from cosmogenic and natural radioactivity (e.g. ^{238}U, ^{232}Th). The isotopes ^{32}Si, produced by cosmic ray spallation of ^{40}Ar, and ^{210}Pb, a daughter of ^{222}Rn, are of particular concern for DAMIC.

Acquisition of background data was completed between February and September 2017 using six active DAMIC CCDs (35.4 g equivalent) at SNOLAB. The energy response of each CCD was obtained during the commissioning phase by using an LED installed in the cryostat. Images in this data had 30 ks exposure, and were read so that physical pixels correspond to image pixels, optimizing spatial resolution. Images were processed using the same procedure as described in Ref. [7], including steps for pedestal subtraction, correlated noise subtraction, masking regions with high leakage current or defects, and extracting calibration response.

We distinguish and reject background events, utilizing exquisite spatial resolution of CCDs to identify bulk (^{32}Si) and surface (^{210}Pb) spatially-correlated decay sequences over long periods. The characteristics of α and β clusters enable efficient discrimination. In particular, β's have lower energy and "worm"-like tracks compared to α's (Fig. 3). Furthermore, α's can be separated into two types: "plasma" and "bloomed". Plasma α's correspond to highly-diffuse and round clusters due to the plasma effect [12]; they originate in the bulk or the back of the CCD. Bloomed α's originate on the front of the CCD, and produce vertical tracks due to charge spilling over potential barriers between vertical pixels. To differentiate, we determine the fraction of pixels (f_{pix}) in the smallest box drawn around the cluster, the number of pixels (N_{pix}), and the spatial RMS values of a cluster's x and y position (σ_x, σ_y). The value of f_{pix} is larger for α's than β's; bloomed α's are more vertical than plasma α's, and can be separated using the variable $N_{pix}(\sigma_x/\sigma_y)$, as in Fig. 2.

Table 1: Decay sequences of ^{32}Si and ^{210}Pb.

Decay Sequence	$\tau_{1/2}$	Q-value
$^{32}\text{Si} \longrightarrow {}^{32}\text{P} + \beta^-$	150 y	225 keV
$^{32}\text{P} \longrightarrow {}^{32}\text{S} + \beta^-$	14.3 d	1.71 MeV
$^{210}\text{Pb} \longrightarrow {}^{210}\text{Bi} + \beta^- + \text{IC}/\gamma$	22.3 y	63.5 keV
$^{210}\text{Bi} \longrightarrow {}^{210}\text{Po} + \beta^-$	5.01 d	1.16 MeV
$^{210}\text{Po} \longrightarrow {}^{206}\text{Po} + \alpha$	138 d	5.41 MeV

Searches were conducted to identify spatially-correlated decay sequences in order to directly measure radioactive contamination of CCDs, covering ^{32}Si, ^{210}Pb (Tab. 1), as well as ^{238}U, ^{232}Th, and the subcomponents of their respective decay chains. The decay characteristics, specifically the half-life and Q-value of each isotope, guided the searches (Tab. 2). For a decay sequence to be considered a candidate: (1) events had to occur in the same CCD, (2) isotope daughter clusters had to occur in later images than their parents, (3) clusters had to match appropriate α, β classification, (4) clusters had to be spatially coinciding (minimum one-pixel overlap) and not be in masked regions, and (5) sequences had to fall within energy (E) and separation time (Δt) cuts. The search for ^{32}Si was split to disentangle any event overlap with the ^{210}Pb β-β search. Separation Δt was constrained to within $\approx 5\tau_{1/2}$.

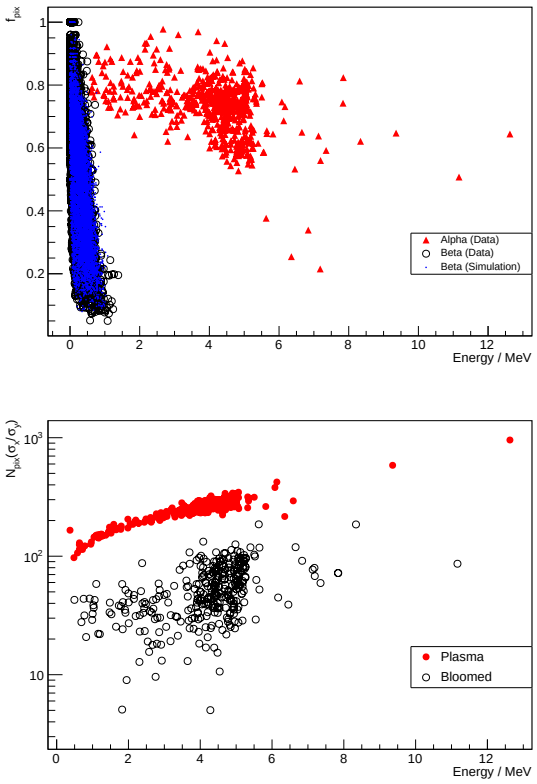

Figure 2: Discrimination of α's and β's (top); discrimination of plasma and bloomed α's (bottom).

Table 2: ^{32}Si and ^{210}Pb searches, constrained by E, Δt.

Isotope	E Cut 1 [keV]	E Cut 2 [keV]	Separation [d]
^{32}Si	$E_{\beta 1} > 70$	$E_{\beta 2} < 230$	$\Delta t < 70$
^{32}Si	$E_{\beta 1} > 0.5$	$E_{\beta 2} < 70$	$25 < \Delta t < 70$
^{210}Pb	$E_{\beta 1} > 0.5$	$E_{\beta 2} < 70$	$\Delta t < 25$
^{210}Pb	$E_{\beta 1} < 70$	$E_{\alpha} < 5400$	$\Delta t < 715$
^{210}Pb	$E_{\beta 2} < 1200$	$E_{\alpha} < 5400$	$\Delta t < 690$

The number of sequences were adjusted for accidentals by applying search criteria to iterations of spatially-randomized data. Geant4 simulations with detailed CCD geometry enabled calculation of pair selection efficiencies. Despite DAMIC's high duty-cycle, there were breaks in data acquisition due to image readout and equipment maintenance. Time efficiency of each search was obtained analytically by solving for probabilities of seeing subsequent decays after identifying initial candidates, and cross-checked with Monte-Carlo simulations.

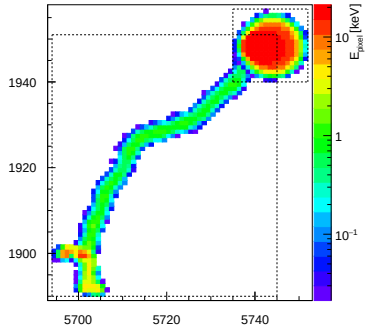

Figure 3: Spatially-correlated β, α clusters of a ^{210}Pb decay: E_β = 717 keV, E_α = 3.62 MeV, Δt = 32.3 d.

2.2 Results

We measure a decay rate of 133.3 ± 27.8 μBq/kg for ^{32}Si, and 83.1±11.8 nBq/cm^2 for ^{210}Pb. Given the non-observation of α-β sequences, we place an upper limit on ^{238}U contamination: 0.53/kg/d, or 1.5 ppt (95% CI). Similarly, we do not observe any α sequences totaling E = 18.7 MeV, and thus place an upper limit on ^{232}Th contamination: 0.35/kg/d, or 1 ppt (95% CI).

This result has major implications for current and next-generation silicon-based DM experiments. It shows a demonstrable need for better CCD packaging and handling protocol in order to lower ^{222}Rn levels. It provides the first-ever comparison to the ^{32}Si contamination level in detector-grade silicon (see Ref. [6]), and confirms that ^{32}Si levels can vary locally, as suggested in Ref. [13]. Both the future of the DAMIC program (Sec. 3) and other leading silicon-based experiments [14] rely on DAMIC's measurement of contamination, and this technique could enable optimization of silicon ingot selection for detector fabrication. The aforementioned results, coupled with ICP-MS measurements, germanium γ-counting, and Geant4 simulations, play a critical role in constraining the background model in DAMIC's ongoing WIMP search analysis (Fig. 4, 5).

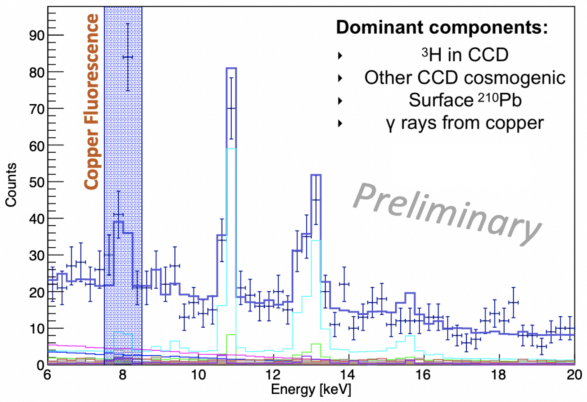

Figure 4: 2-D fit to data projected onto energy.

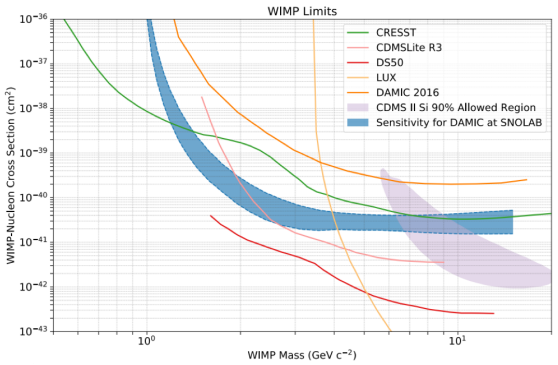

Figure 5: Preliminary DAMIC WIMP 13.4 kg-d result.

3 DAMIC-M

DAMIC leads efforts for detection of DM-induced nuclear/electron recoils in CCDs. Following the success of the DAMIC experiment at SNOLAB, a next-generation, kg-scale detector with 50 record-mass (20 g, 36 Mpix) CCDs, is being developed (Fig. 6). DAMIC-M will feature innovative technology, in particular by implementing novel "Skipper" readout in its CCDs to reach sub-electron noise. Skipper CCDs utilize a non-destructive, multiple charge measurement of pixel charge; the readout noise decreases by $1/\sqrt{N}$ for N charge measurements. Such a system was first demonstrated for a smaller-scale detector [15]. The effect of 1/f noise is also significantly reduced, as the integration time to measure each pixel is shorter than in conventional CCD readout. DAMIC-M readout will be facilitated by custom electronics, including a 4-channel programmable CCD ReadOut Chip (CROC), Clocks and Biases ASIC for CCDs (CABAC), ADC, and FPGA.

DAMIC-M will be housed in the Laboratoire Souterrain de Modane (LSM). LSM is one of the best facilities in Europe for shielding cosmic rays; it also has something no other lab can offer: a radon-trapping facility that produces radon-free air. DAMIC-M will be able to strategically use this facility for underground packaging and testing. Extensive detector shielding, careful material selection, minimizing cosmogenic activation of detector components, and implementation of contamination measurement (Sec. 2) will enable DAMIC-M to achieve a background of ≈0.1 event/(keV·kg·day), a ×100 decrease relative to DAMIC at SNOLAB.

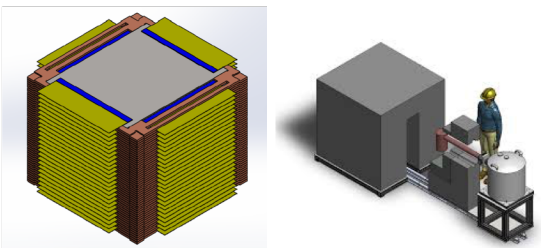

Figure 6: Conceptual design for DAMIC-M 50-CCD tower, cryostat, and shielding insfrastructure.

3.1 Construction of a high-performance CCD test chamber for DAMIC-M

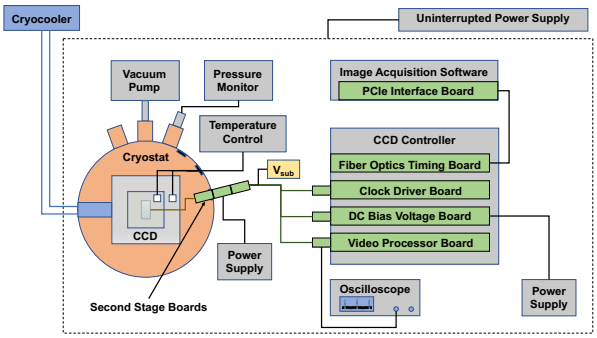

Figure 7: Apparatus for a CCD test chamber.

DAMIC-M will need to test the performance and design features of CCDs across multiple fabrication cycles. Studies prior to the final production of DAMIC-M CCDs will be critical to the success of the experiment. In order to guide the development of DAMIC-M, an automated, high-performance test chamber was constructed at Laboratoire de Physique Nucléaire et des Hautes Energies (LPNHE), Paris. The test chamber features a cryostat to operate CCDs in cryogenic conditions (T < 130 K), and is located in a modular, ISO-7 cleanroom. It utilizes a commercial CCD controller developed by Astronomical Research Cameras, Inc. that delivers bias and clocks voltages to the CCD and reads the CCD signal. The substrate bias ($V_{\rm sub}$) is ramped with an RC circuit. Custom software was developed to facilitate automated image acquisition.

A standard 8Mpix DAMIC CCD was deployed and calibrated using an ^{241}Am source – the readout noise for the system was measured at a level < 6 electrons. Following this, the apparatus and operating parameters were used to help enable the first image acquisition achieved using the CABAC.

3.2 Characterization of the first DAMIC-M Skipper CCDs

The first batch of DAMIC-M CCDs has already been completed. It includes 1k × 6k CCDs that feature Skipper amplifier circuits [16]. The CCDs were packaged in a low-radon cleanroom at the University of Washington, covering steps of epoxy-curing the CCD kapton flex cable, wire bonding, and thermal contact insertion. One of the CCDs from this batch was installed in the LPNHE test chamber. Following a sweep in bias and clock voltages and sequencing, optimal parameters were obtained. Single electron resolution was achieved for the first time in a DAMIC-M CCD. The spectrum for this result and $1/\sqrt{N}$ trend can be seen in Fig. 8.

This work will play a major role in preparing for the upcoming commissioning of a prototype to be installed in the low-background environment of LSM. The prototype will feature 6k × 4k Skipper CCDs operated by the same controller as the LPNHE test chamber.

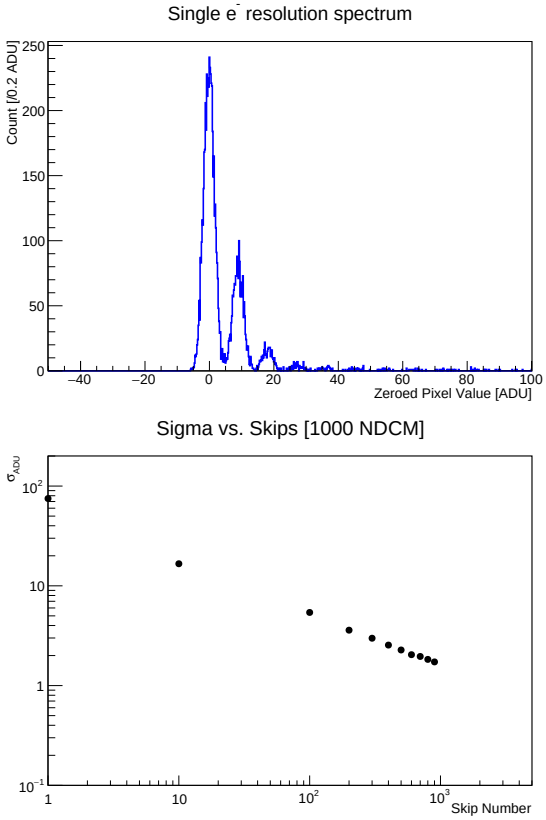

Figure 8: DAMIC-M CCD single electron resolution.

4 Conclusions

DAMIC has demonstrated CCDs as successful detectors to search for DM. We have described the DAMIC experiment at SNOLAB, and in Sec. 2.1 we reported results on the measurement of radioactive contamination in CCDs. In Sec. 3 we outlined the construction of a test chamber to guide DAMIC-M, a next-generation DM experiment. By deploying a Skipper CCD in this chamber, we were able to achieve single electron resolution. The development of DAMIC-M is rapidly progressing: a prototype detector at LSM will enable measurement of leakage current and radioactive background, verification of packaging, and integration of novel electronics. DAMIC-M's innovative technology and ambitious but attainable goals will lead to monumental advancements in the search for DM.

Acknowledgments

This work was realized under the supervision of Professor Paolo Privitera and Dr. Antoine Letessier Selvon. This material is based upon work supported by the National Science Foundation Graduate Research Fellowship Program under Grant DGE-1144082, and by the National Science Foundation Graduate Research Opportunities Worldwide Program. This material is based upon research supported by the Chateaubriand Fellowship of the Office for Science and Technology of the Embassy of France in the United States.

References

[1] F. Zwicky, "Spectral displacement of extra galactic nebulae," Helv. Phys. Acta 6 (1933) 110.

[2] V.C. Rubin and W.K. Ford, Jr., "Rotation of the Andromeda Nebula from a Spectroscopic Survey of Emission Regions," Astrophys. J. 159 (1970) 379

[3] N. Aghanim et al., "Planck 2018 results. VI. Cosmological parameters," arXiv preprint arXiv:1807.06209 (2018).

[4] D.S. Akerib et al. (LUX Collaboration), "Results from a Search for Dark Matter in the Complete LUX Exposure," Phys. Rev. Lett. 118 (2017) 021303.

[5] E. Aprile et al. (XENON Collaboration), "Dark Matter Search Results from a One Ton-Year Exposure of XENON1T," Phys. Rev. Lett. 121 (2018) no.11, 111302.

[6] A. Aguilar-Arevalo et al. (DAMIC Collaboration), "Measurement of radioactive contamination in the high-resistivity silicon CCDs of the DAMIC experiment," J. Instrum. 10 (2015) P08014.

[7] A. Aguilar-Arevalo et al. (DAMIC Collaboration), "Search for low-mass WIMPs in a 0.6 kg day exposure of the DAMIC experiment at SNOLAB," Phys. Rev. D 94 (2016) 082006.

[8] A. Aguilar-Arevalo et al. (DAMIC Collaboration), "First Direct-Detection Constraints on eV-Scale Hidden-Photon Dark Matter with DAMIC at SNOLAB," Phys. Rev. Lett. 118 (2017) 141803.

[9] A.E. Chavarria et al., "Measurement of the ionization produced by sub-keV silicon nuclear recoils in a CCD dark matter detector," Phys. Rev. D 94 (2016) 082007.

[10] A. Aguilar-Arevalo et al. (DAMIC Collaboration), "Constraints on Light Dark Matter Particles Interacting with Electrons from DAMIC at SNOLAB," Phys. Rev. Lett. 123 (2019), 181802.

[11] S. Holland et al., "Fully depleted, back-illuminated charge-coupled devices fabricated on high-resistivity silicon," IEEE Trans. Electron Devices 50 (2003), no. 1 225â238.

[12] J. Estrada, J. Molina, J. J. Blostein, and G. Fernandez, "Plasma effect in silicon charge coupled devices (CCDs)," Nucl. Instrum. Meth. Phys. Res. A 665 (2011) 90â93, [arXiv:1105.3229].

[13] J. L. Orrell et al. "Naturally occurring ^{32}Si and low-background silicon dark matter detectors," Astroparticle Physics 99 (2018): 9-20.

[14] R. Agnese et al. "Projected Sensitivity of the SuperCDMS SNOLAB experiment," Phys. Rev. D 95.8 (2017): 082002.

[15] J. Tiffenberg et al., "Single-electron and single-photon sensitivity with a silicon Skipper CCD," Phys. Rev. Lett. 119, 131802, arXiv:1706.00028 (2017).

[16] S. Haque et al., "Design of low-noise output amplifiers for P-channel charge-coupled devices fabricated on high-resistivity silicon," Proc. SPIE 8298, Sensors, Cameras, and Systems for Industrial and Scientific Applications XIII, 82980X (2012); https://doi.org/10.1117/12.905460.

Development and characterization of novel electronics for the search of dark matter for DAMIC-M

Giorgos Papadopoulos

LPNHE, Sorbonne University, Paris

Abstract — Despite plenty of evidence for the existence of Dark Matter (DM), no experiment has ever managed to capture it directly. In the last decades, the search of the Weakly Interacting Massive Particle (WIMP) paradigm, the most popular among the DM models, has proven unsuccessful experimentally in a variety of detection methods in the GeV-TeV mass range. DAMIC-M [1] (DArk Matter In CCDs at Modane) will aim to directly search for light WIMPs (<10 GeV) and hidden-sector DM using scientific-grade Charge-Coupled Devices (CCDs) of a kg-size total target mass. In addition, by implementing the Skipper readout technique, a sub-electron energy resolution can be achieved. A fundamental feature of this undertaking will be the development of an acquisition system for the overall control and readout of the CCDs. I will present preliminary results from the evaluation of novel readout electronics including the front-end CCD ReadOut Chip (CROC), which will provide a pre-amplification on the output signal and improve the Signal-to-Noise Ratio, and a new Analog-to-Digital Converter (ADC) board, allowing for a fast and high-resolution readout.

1 Introduction

The CCDs find wide use in everyday life, like digital cameras. In physics, when low energy events is the object of research, a temperature-dependent white noise introduced by thermally generated electrons in the bulk of the semiconductor, also know as dark current, needs to be suppressed. For this reason, the CCD is placed in a cryostat from which the air is pumped out, down to a low pressure of $\sim 10^{-6}$ mBa. Isolated from the surrounding environment, the CCD is cooled down to ~100-140 K. At very cold temperatures (<70 K), there is a physical limit known as "freeze out" in which the dopant atoms recombine rather than exist in the lattice in an ionized state and the CCD ceases to work [2]. There are two main operation phases: the exposure and the readout. During the exposure phase, the CCD is in a static state where the generated charge from incident particles is collected in the pixels. The dark current is a time-dependent noise, so the exposure time is usually limited by this factor for an acceptable Signal to Noise Ratio (SNR). In at least one corner of the CCD frame there is a readout circuit where every pixel-charge is driven by alternating properly the electrodes above the pixels (vertical and horizontal clocks). With the Skipper technique [3] one can measure the charge multiple times in a non-destructive way, hence the output error will decrease by the square root of the number of samples.

The DAMIC-M experiment plans to use 50 scientific CCDs of 36 Mpixels of pure silicon and about 20 g each, with the Skipper readout implementation in all four corners of the frame. It will achieve a sub-electron resolution by measuring the pixel-charge with the lowest possible electronic noise and a high number of non-destructive charge measurements (NDCM). Novel electronics designed in the collaboration will make fusible the goals of the experiment. Figure 1, shows a brief CCD setup analogous to the final experiment. The whole control of the CCD will be done by the 4CABAC board, providing bias voltages and clocks. Implemented on the Odile motherboard is the ADC board as well. Right in the output of the CCD, there will be the CROC operating at low temperature.

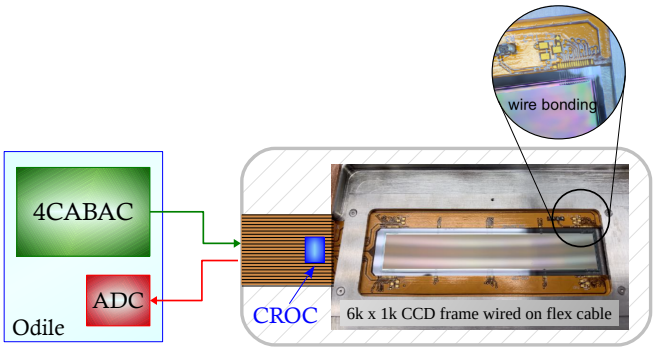

Figure 1: Setup schematic analogous to DAMIC-M

2 CCD output signal

The principle of measuring the charge of a pixel is rather simple. First, the Reset Gate (RG) (see Figure 2 sets the floating gate at a voltage reference value (Vref). This will cause a bump in the output signal, as can be seen in Figure 3 top. This bump will decay quickly and result in an outcome reference level around Vref. The charge Q is injected to the floating gate changing the voltage by $V_Q = Q/C_{SN}$, where C_{SN} is the capacity of the sense node which is known. In practice though, it gets more complicated. The reference level is not always exactly the same due to the reset or kT/C (or kTC) noise, a thermal noise generated by the resistance

of the reset FET (MR) introducing an uncertainty in the reference level. The uncertainty depends on the inverse of the C_{SN} which is in the order of fF. In order to measure the V_Q accurately, both reference and signal levels need to be measured and subtracted. This method is called Correlated Double Sampling (CDS) and is used to deduct the reset noise.

The Skipper technique allows to move the charge back to the Output Gate (OG) and Summing Well Gate (SG) and repeat the measurement. After completing the requested samples, the charge is transferred to the Dump Gate (DG) and it is discarded. A new pixel measurement can begin until the whole CCD is read out.

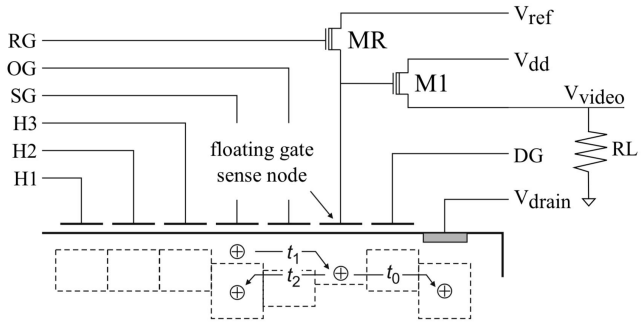

Figure 2: CCD readout circuit

3 CROC: CCD ReadOut Chip

The actual measurement of the CCD signal can be performed in two ways: Dual Slope Integration (DSI) and Digital Correlated Double Sampling (DCDS) (see next section). The CROC is a single ended input to differential output amplifier, able to perform DSI and operate in Transparent mode to perform DCDS. The reason why it is located as close as possible to the CCD output is to improve the ratio of the signal to any introduced noise until the ADC. When the signal is measured by the ADC, it will be divided by the amplification factor and so the noise will be suppressed. This programmable gain can allow the search in different regions in terms of deposited energy in the silicon bulk. A first version of CROC is already under evaluation.

Transparent mode

In Transparent mode, the CROC operates as a simple single-to-differential gain amplifier. The CCD output signal shape will remain untouched besides being amplified. The principle is to oversample the output signal and digitally determine the reference and signal levels by averaging a sufficient number of samples (see Figure 3 middle). The Digital CDS is achieved by subtracting the two levels. Having individual samples allows for further digital analysis like in the frequency domain, if necessary. In addition, this mode offers a coupling capacitor in the order of nF right in the output of the CCD. The reset noise of C_{SN} will be replaced by the

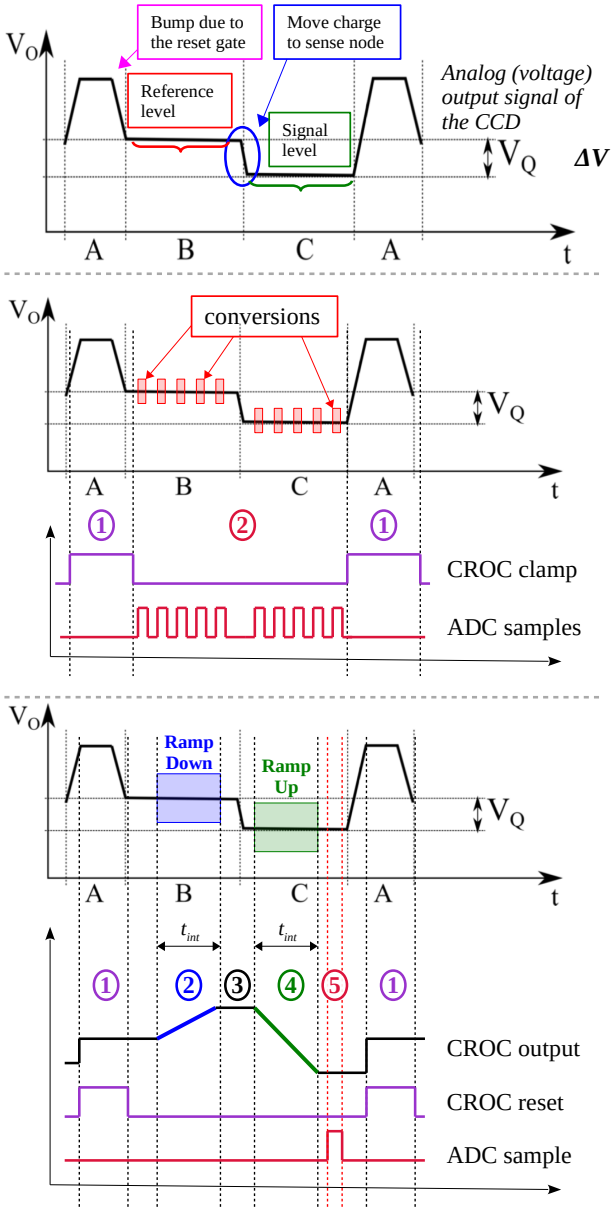

Figure 3: CCD output signal (top), CROC in Transparent mode (middle), CROC in DSI mode (bottom)

reset noise of the coupling capacitor minimizing the uncertainty of the reference level. This mode allows for a fast readout sampling, eliminating the flicker or 1/f noise which is dominant up to 1 MSps. An ADC candidate is the LTC2387-18 [4] with 18-bits in an input range of 8.192 V_{p-p} and 15 MSps. Some preliminary results of the first version of this ADC are presented in the next section.

DSI mode

The DSI is at the moment the dominating readout mode for DAMIC-M. The DSI method combines a correlated double sampling and a CCD signal integration. The main steps can be seen in Figure 3 middle.

1. While the RG sets the SN under a reference, a reset pulse will set the input of the CROC in a reference

voltage, as well.

2. As soon as the reference level of the CCD is stable, the CROC amplifies and integrates it for a given time t_{int}.
3. There must be a window during the charge transfer to the SN where the CROC input is isolated.
4. When again the output is stable, the signal level is integrated for the same integration time with reversed polarity than the first integration. The final level will be the measurement of the signal level but with respect to the reference level, in other words the $\Delta V \times gain$.
5. Since the CDS is already achieved, the ADC samples the output of the CROC and that value will be the $V_Q \times gain$.

The longer the integration time, the better the accuracy of the measurement. In regular CCDs, The noise of a single sample reaches a plateau of a few electrons above 10 μs where the 1/f noise dominates. In Skipper CCDs, the integration time must be lower around 1 μs in order to achieve fast readout. The major objective is to achieve a sub-electron resolution by increasing the number of samples per pixel. However, the total readout time will increase linearly and it must remain reasonable compared to the expose time of the CCD. The single sample readout time needs to be short for a fast readout but also sufficiently long to minimize the electronic noise. An ADC must be capable of performing optimally the readout in terms of speed and resolution and the two candidates to support this mode are the AD4020, 20-bits in $10V_{p-p}$ and 1.8 MSps and the MAX11905, 20-bits in $6V_{p-p}$ and 1.6 MSps

4 Rapide ADC board

The so called Rapide board consists of four identical channels using the differential input LTC2387-18 ADC chip. A brief schematic of the evaluation setup is shown in Figure 4.

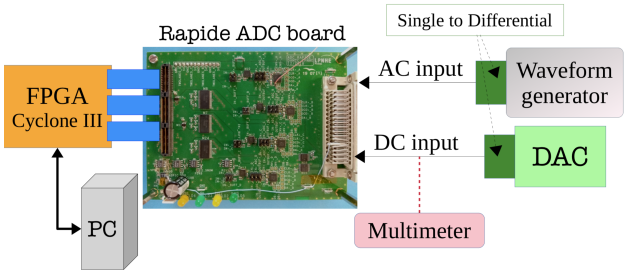

Figure 4: Schematic of the ADC evaluation setup

An FPGA board (Field-Programmable Gate Array) controls the ADC board. Even though the ADC can achieve a readout speed of 15 MHz, the FPGA that was used cannot exceed the limit of 10 MHz. The tests were realised with a sampling frequency of 9.091 MHz. The signal sources to test the ADC are provided by an AD5791 20-bit low noise Digital to Analog Converter (DAC) [5] for DC signals and a waveform generator for AC signals. Both are single-ended output sources so a single to differential (StD) converter is necessary. Moreover, a high resolution, down to 1 μV, digital multimeter was used to characterize the DAC and StD converter board. The DAC evaluation found to be in good agreement with the datasheet of the chip, with a Least Significant Bit (LSB) equal to 19.07 μV and both Integral and Differential Non-Linearity below 1 LSB. The converter board introduces some effect to the signal. An attempt to understand the shape of this effect was done in order to subtract it later in the data analysis.

The ADC board is being evaluated under four aspects: Intrinsic (or transition) noise, DC and AC inputs and Cross-talk. One of the four channels is not functional so the results that are presented concern the rest three channels.

Intrinsic noise

For this test, the positive and negative inputs of the ADC need to be shorted under a low noise voltage reference. The ADC chip itself produces such a reference at ~2 V. A large amount of samples of about 10000 is recorded for good statistics. A typical histogram of the output of the ADC is given in Figure 5. The intrinsic noise is determined by the sigma of the Gaussian fit on the histogram. The noise was measured:

- channel 0 → 1.598 ± 0.012 ADU
- channel 1 → 1.591 ± 0.011 ADU
- channel 3 → 1.483 ± 0.011 ADU

while 1.4 ADU is expected. The maximum noise 1.6 ADU corresponds to 50 μV (see next section).

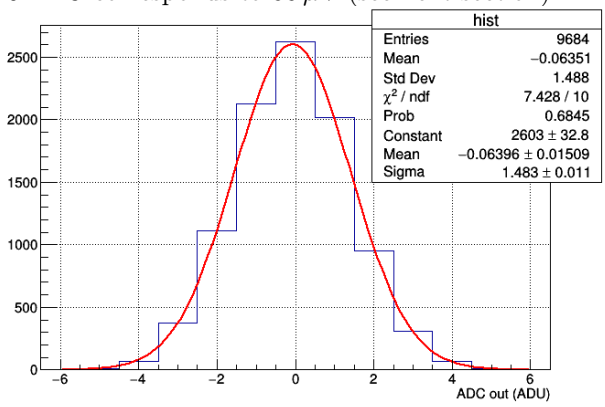

Figure 5: Typical histogram for intrinsic noise measurement

DC input - Linearity

Using the DAC, low noise DC signals are injected to the ADC covering the whole input range with a fixed step. With the linearity plot as the ADC output vs the ADC input, one can calculate the voltage equivalent of the Analog to Digital Unit (ADU). Knowing DAC's 1 LSB, the 1 ADU equals to 31.24 μV, while theoretically was expected to be $8.192\,\mathrm{V}/2^{18} = 31.25\,\mu\mathrm{V}$. The residuals of the measured points from the fit line will provide further detailed information for the linearity of

the ADC. As mentioned before, a correction was applied to remove the effect of the converter board. A maximum deviation of 4-5 ADU on the full input range was calculated for all three channels, with an expected typical value of ±0.3 ADU and a maximum of ±3 ADU.

AC input

To test the ADC for AC input, sinusoidal signals of programmable amplitude, frequency and offset are injected from a waveform generator. For various parameters the ADC has shown a generally good response with consistent reconstructed amplitude and frequency, see Figure 6. Yet, no correction was applied for the converter board and the non-linearity plots shown a deviation of a few 10s of ADU.

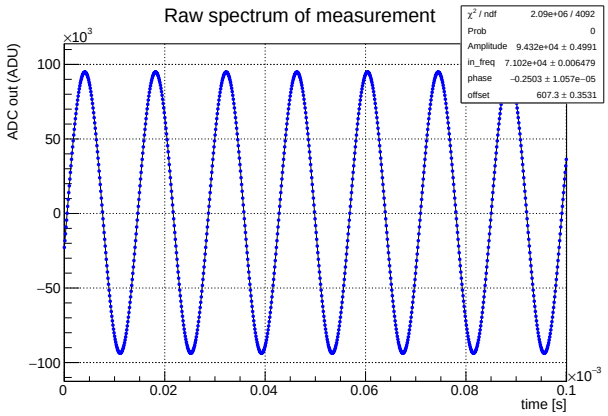

Figure 6: ADC output for sinusoidal input signal - zoomed time axis

Cross talk

The cross talk concerns the impact of an input signal to a certain channel of the ADC board to the rest of the channels. To do so, a sinusoidal signal of maximum possible amplitude is sent to a channel while the other two are under a reference voltage. The noise is measured from the channels to the reference similarly to the intrinsic noise case. The table of Figure 7 shows the cross talk values that were measured for the three channels. Comparing them with the intrinsic noise values, there is a relative good agreement, preventing the quantification of the cross talk effect.

		Signal sent to:		
		Channel 0	Channel 1	Channel 3
Signal read from	Channel 0	x	1.527±0.017	1.521±0.016
	Channel 1	1.605±0.018	x	1.622±0.019
	Channel 3	1.469±0.016	1.509±0.018	x

Figure 7: Cross talk table

5 Conclusions

The two main components that the CCD output are under design, production and evaluation with further upgrades expected. The first version of the CROC chip is functional and under evaluation. The two operational modes give different opportunities with DSI and DCDS methods waiting to be compared for the final decision for the DAMIC-M experiment. Based on the mode, different requirements are demanded from the ADC. All the ADC candidates are also under evaluation. A first view on the fast ADC appears to be promising to support the setup in the DCDS mode. Later versions of these components and tests with everything integrated in a CCD setup will be crucial to result in more thorough and reliable conclusions.

References

[1] DAMIC-M Experiment: Thick, Silicon CCDs to search for Light Dark Matter, Castello-Mor, 2020

[2] Scientific Charge-coupled Devices, James R. Janesick, SPIE Press, 2001

[3] Single-electron and single-photon sensitivity with a silicon Skipper CCD, Javier Tiffenberg et al, 2017

[4] Linear Technology: LTC2387-18 18-bit 15MSps ADC data sheet

[5] Analog Devices: AD5791 20-bit DAC data sheet

StarTrack predictions of the stochastic gravitational-wave background from compact binary coalescences

Carole Périgois

LAPP, CNRS, 9 Chemin de Bellevue, 74941 Annecy-le-vieux, France

Abstract — In this study we evaluate the contribution of binary coalescences to the stochastic gravitational-wave background from population I, II and III, according to the Hertzsprung-Russel classification. We assume that the observed coalescences are formed through stellar evolution in the field of galaxies with no dynamical interactions. We use the new population synthesis `StarTrack` to generate realistic population of merging binaries (binary black holes, binary neutron stars and neutron-star black-holes), and calculate the energy density spectrum of the background. We account for the evolution of the orbit and of the redshift, which is expected to play a significant role at low frequencies accessible by the space antenna LISA. In addition, for the first time, we include binaries that do not merge in a Hubble time. For all the populations, we compute the energy density contributions and derive the residual contribution to the stochastic background by subtracting the detected sources of the following four detector networks: HLV (AdLIGO Hanford and Livingston and AdVirgo), HLVIK (HLV and LIGO India and Kagra), ET (Einstein Telescope), and ET+2CE (ET and two Cosmic Explorer located at the actual place of Hanford and Livingston). All of this study is detailed in the paper by C.Périgois et al. 2020 [1].

1 Introduction to the stochastic gravitational-wave background

Gravitational waves are space-time perturbations, propagating at the speed of light through the universe. They were predicted by the general relativity theory of Albert Einstein in 1916 [2].

Gravitational-wave astronomy began in 2015 with the first detection of a gravitational signal from a binary black hole coalescence [3] by the LIGO detectors [4]. Two years later, the European detector Virgo [5] joined the network and the first BNS coalescence was observed, simultaneously detected through gravitational waves and EM [6]. This event mark the entry of gravitational waves into multi-messenger astronomy together with neutrinos, cosmic-rays and gamma-rays. During the two runs O1 and O2 [7] (between Sep.2015 and Aug.2017) LIGO-Virgo observed 7 binary black-holes events and one binary neutron star. Since April 2019 and until April 2020, the network LIGO-Virgo is taking data, and expect an average of one event per week. After the current run, the new Japanese detector Kagra [8] will join the network. The same year will start the building of the ultra-high vacuum environment interferometer for the LIGO collaboration in Maharashtra (India) [9]. The gravitational-waves community plans also a space antenna, LISA [10], for which the pathfinder mission finished successfully in 2017 [11]. In addition, 3G terrestrial detectors ET [12] and CE [13] are under design study. A comprehensive study of the impact of these new detectors for the gravitational stochastic background becomes relevant for further astrophysical and cosmological investigations.

The stochastic gravitational wave background is defined as the superposition of every gravitational wave signals which are not resolved by the detectors. We classify the gravitational wave sources in two categories: the ones from post-stellar activity phenomena (astrophysical background) and the ones from pre-stellar activity phenomena (cosmological background). We characterize the background energy density with the dimensionless quantity $\Omega_{GW}(f)$:

$$\Omega_{GW}(f) = \frac{1}{\rho_c}\frac{\mathrm{d}\rho_{GW}}{\mathrm{d}(\ln(f))}\,, \tag{1}$$

where the critical energy density ρ_c assumes a closed and flat universe, f is the observed frequency and ρ_{GW} is the gravitational waves energy density. In this study we characterize the contribution of binary coalescences to the stochastic background for a large frequency band (1 μHz - 2.5 kHz) to include LISA most sensitive frequencies. We first have simulated the compact binary population using the synthesis code `StarTrack` [14]. Because the sources are observed over a long time range, we include the redshift and the orbital evolution in our calculations. We then derived the residual stochastic background obtained by subtracting detectable sources for each terrestrial detector network. Moreover, we also evaluate the contribution from sources which do not merge within a Hubble time.

2 Compact binary coalescence contributions to the stochastic background

To evaluate the stochastic background contribution we generate a realistic population of binaries with `StarTrack`.

Model `StarTrack` is a simulation of binary stars evolution from the birth of the stars to the compact objects

formation, including mass exchange between the two stars, stellar wind and the common envelop phase [15]. In our study we assume two stars born in binary system from the same galactic field, with no dynamical interactions.

Stochastic background from compact binary coalescences A binary coalescence is the process by which two compact objects (black holes or neutron stars) merge to form a single black-hole. This phenomenon exhibits three phases: The inspiral phase during which both objects are getting closer, the merger phase, and finally the ringdown phase, when the resulting object stabilizes. During the process the emitted gravitational waves can be modelized with the phenomenological waveforms [16]. From there, we can express the energy density as function of the observed frequency

$$\frac{\mathrm{d}E_{\mathrm{GW}}}{\mathrm{d}f} \propto \begin{cases} f^{-1/3} & \text{si } f < f_{\mathrm{merg}}\,, \\ f^{2/3} & \text{si } f_{\mathrm{merg}} \leq f < f_{\mathrm{ring}} \\ \mathcal{L}(f, f_{\mathrm{ring}}, \sigma) & \text{si } f_{\mathrm{ring}} \leq f < f_{\mathrm{cut}}\,, \end{cases} , \tag{2}$$

where $\mathcal{L}$ is the Lorentzian function and f_{merg}, f_{ring}, f_{cut} and σ are the emission parameters depending on the masses of the two components m_1 and m_2.

We distinguish three types of binaries: binaries of two black-holes (BBH), binaries of two neutron stars (BNS) and binaries with a black-hole and a neutron star (NSBH).

Calculation of the contribution In order to evaluate the total contribution of all sources, we first compute the contribution for each individual ones. This is achieve by scanning around all observe frequencies and evaluate for each of them the sum of the energy density of the four first harmonics emission n=2 to 6 according to [17, 18]

$$\frac{\mathrm{d}E^n_{GW}}{\mathrm{d}f}(f,n) = \frac{\mathrm{d}E_{GW}}{\mathrm{d}f}\,\frac{g(n,e)}{\Psi(e)}\left(\frac{4}{n^2}\right)^{1/3}, \tag{3}$$

where $g(n,e)$ is a sum of Bessel functions and $\Psi(e)$ is a function of the eccentricity e.

We calculate the contribution for one source, given the observe frequency f and the harmonic n according to

$$\Omega^{i,n}_{GW}(f) = \frac{1}{\rho_c}\frac{f}{H_0}\frac{\mathrm{d}z}{E(\Omega,z)}s_i\frac{\mathrm{d}E^{n,i}_{\mathrm{GW}}}{\mathrm{d}f}(f,\mathcal{M}^i_{\mathrm{c}},z), \tag{4}$$

where we used the last Planck measurements [19] for the total energy density $E(\Omega,z) = \sqrt{\Omega_\Lambda + \Omega_m(1+z)^3}$ and the Hubble constant H_0. $\mathcal{M}_c = (m_1 m_2)^{3/5}/(m_1+m_2)^{1/5}$ is the chirp mass. Finally, we derive the background energy density

$$\Omega_{GW}(f) = \sum_{n=2}^{6}\sum_i \Omega^{i,n}_{GW}(f)\,. \tag{5}$$

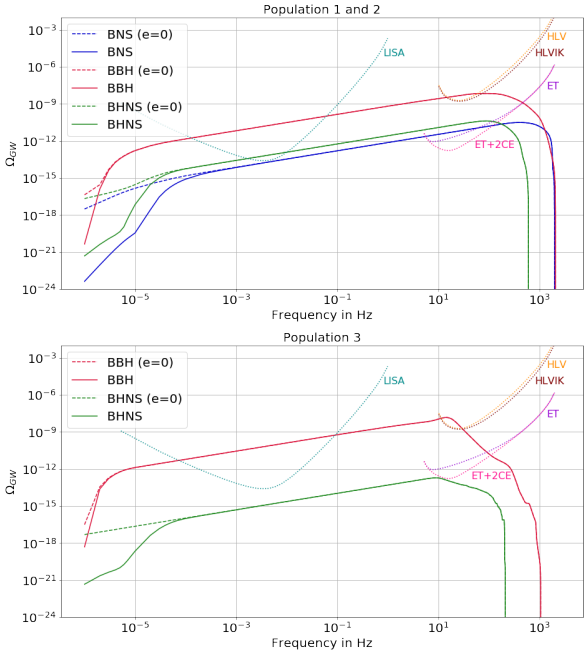

Figure 1: Energy density for the total population of sources that coalesce within the Hubble time. The upper panel is for Population I/II stars and the lower panel for Population III stars. The three different type of binaries BBH, BHNS and BNS are shown separately in red, green and blue, with a null eccentricity (dashed line) and accounting for harmonics $n = 2-5$ (continuous). The dotted lines represent the Power Integrated curves of the different networks of terrestrial detectors (see text) and LISA.

3 Results

Total background from merging sources The spectra for the different types of binaries (BNS, NSBH and BBH) that coalesce within the Hubble time, including all the sources, are shown in Fig.1 for population I and II stars (top) and for population III stars (bottom). Here we account for the eccentricity (continuous line) and we consider the first four harmonics ($n = 2-5$). For comparison we also show the case without eccentricity (dashed line). The dotted lines in the figure show the projected sensitivities, the so-called Power Integrated (PI) curves, for the space antenna LISA and for different terrestrial detector networks: HLV: Advanced LIGO Hanford (H) and Livingston (L), and Advanced Virgo at design sensitivity. HLVIK: HLV with in addition a new detector in India (I), whose sensitivity will be similar to the two LIGO detectors, and the Japanese detector KAGRA (K), also at design sensitivity. ET: third generation European detector Einstein Telescope, currently under design study. ET+2CE: ET and two third generation Cosmic Explorer (CE), also under design study.

A power-law stochastic background that is tangent to a PI curve is detectable with a signal-to-noise-ratio of 2 by the given network. For LISA we assume an effective integration time of 3 years (corresponding to the 10 years mission with a duty cycle of about 50%) [10]

and for terrestrial detectors we assume an effective integration time of 1 year following [20].

For the three types, and for both Populations I/II and III one can recognize the evolution as $\Omega_{GW}(f) \sim f^{2/3}$, which is characteristic of compact binary models in the inspiral phase. The sharp increase at low frequencies, about $\sim 10^{-5}$ Hz for BBHs, $\sim 10^{-4}$ Hz for BH-NSs and $\sim 10^{-3}$ Hz for BNSs, corresponds to frequencies were not all the sources have started to emit (before the initial frequency). Similarly, there is a decrease around a few hundred Hz because some sources have merged and stopped emitting. In the case of Population III, we observe a first maximum at about 20 Hz and then a second lower peak at a few hundred Hz corresponding to lower mass sources ($0<M_{tot}<70$ in $M_\odot$) at lower redshift, less numerous and whose merger occurs at higher frequencies.

Residual background As the sensitivity of the detectors will improve in the future, they will be able to detect more sources and therefore decrease the background, assuming one can successfully subtract individual signals from the data [21]. In order to calculate the residual background we need to remove the sources that can be detected individually. For a network of N terrestrial detectors the coherent signal-to-noise ratio (SNR) ρ, assuming optimal matched filtering and uncorrelated Gaussian noise in the detectors is given by:

$$\rho^2 = \sum_{i=1}^{N} 4 \int_0^\infty \frac{|F_{+,i}(f)H_+(f) + F_{\times,i}(f)H_\times(f)|^2}{S_{n,i}} \, \mathrm{d}f, \tag{6}$$

where $F_{+,i}$ and $F_{\times,i}$ are the antenna response functions to the + and × polarizations, and $S_{n,i}(f)$ is the one-sided noise power spectral density (PSD) of the i^{th} detector. We assume that only sources with a SNR below a given threshold ρ_T contribute to the residual confusion background. Figure 2 shows the residual background for the different networks presented in the previous section. Here a source is assumed to be detected when its combined signal to noise ratio (see Eq. 6) is larger than a threshold $\rho_T = 12$. In order to quantify the reduction of the background, we calculate the ratio of energy densities r_Ω and number of contributing sources r_{Count} between the residual background and the total background :

$$r_\Omega = \frac{\Omega_{GW,res}(f_{\rm ref})}{\Omega_{GW,tot}(f_{\rm ref})}, \quad r_{Count} = \frac{N_{res}(f_{\rm ref})}{N_{tot}(f_{\rm ref})}. \tag{7}$$

where the reference frequency $f_{\rm ref}$ at which the calculation is done corresponds to the most sensitive frequency of the network.

Figure 3 compares the ratios r_Ω (blue bars) and r_{Count} (orange bars) for the three types of binaries BNS, BBH and BHNS, and for the different terrestrial detector networks considered in this study i.e HLV, HLVIK, ET and ET+2CE. Because the sources that are detected at the lowest redshifts are also those whose contribution to Ω_{GW} is the largest, the ratio r_{Count} is higher than $r_{\Omega_{GW}}$ for every types of binary and detector networks (except for BBHs in ET+2CE). In second generation detector networks we have very few resolved sources (less than 0.1%), which are decreasing the background between 1-3(0.7for BNSs in HLV and 2.7for BBHs in HLVIK). Whith the third generation the number of resolved sources is reducing, and the diminution is following the binary masses : In the BBHs case only several percent of sources left in the residual background (18.9in ET and 0.8in ET+2CE), while BNSs are exhibiting a slight reduction (98.3in ET and 72.6in ET+2CE. Because of their intermediate masses BHNSs stays between these two extremes (73.7of source left in ET and 14.6in ET+2CE). The ratios in number of sources in ET+2CE exhibits a great improvement comparing to the ET ones, we expected to resolves at least 35more. This is an argument for the necessity to build a third generation detectors network. In the mean time the background energy density decrease dramatically by a factor of a most 33 for BBH (99.1in HLV against 3in ET+2CE). Regarding the sensitivity improvement this will not be a problem for the background detection. Following the detectors design sensitivity we expect to win a factor ≈700 between HLV and ET(ratio of PICs at 25 Hz).

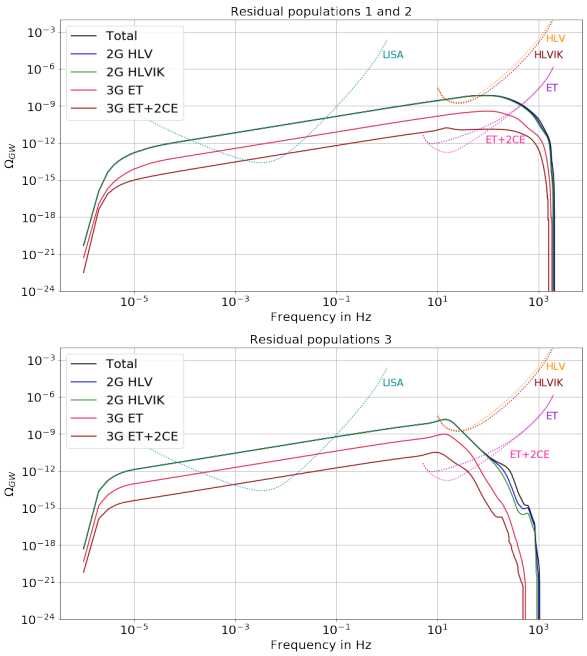

Figure 2: Energy density for the residual population of sources that coalesce within the Hubble time. The upper panel is for Population I/II stars and the lower panel for Population III stars. The three different types of binaries BBH, BH-NS and BNS are shown separately in red, green and blue, with a null eccentricity (dashed line) and accounting for harmonics $n = 2 - 5$ (continuous). The dotted lines represent the Power Integrated curves of the different networks of terrestrial detectors (see text) and LISA.

Sources that do not merge within the Hubble time Finally, we also calculate the contribution of sources that do not coalesce within a Hubble time, which can be either long-lived sources with a lifetime

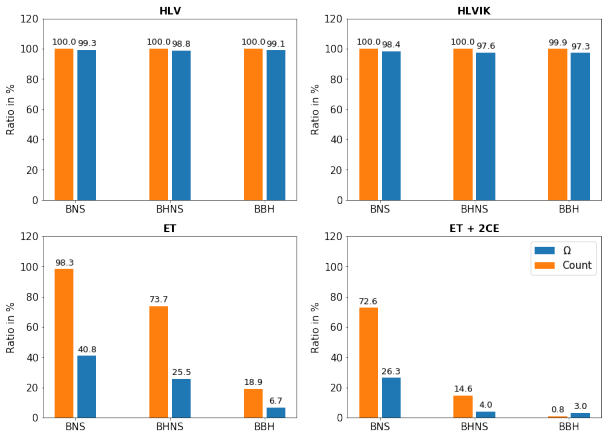

Figure 3: Ratio for residual backgrounds for the total population I/II and III. The blue bars exhibits the ratio in energy density, while the orange ones shows the ratio by counting sources in the residual background.

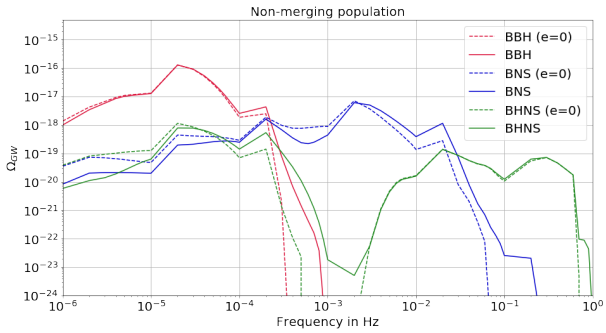

Figure 4: Energy density from binaries which do not merge in a Hubble time including the seven first mode of emission. The solid lines describe the energy densities for each types of binaries with eccentricity evolution while the red dashed one represents the BBH contribution with e = 0.

longer than the Hubble time or sources that were born too recently and will merge in the future. The energy density is shown in Figure 4. We assumed that all the sources are emitting at their initial frequency and we consider the first seven harmonics ($n = 2-8$) . The continuous lines represent the energy density of the different types of binaries, while the dashed line corresponds to BBHs with an an eccentricity e=0.

Total binary contribution The last Figure 5 summarizes the previous results. We represent all residual populations studied here by adding sources which merge within a Hubble time and the ones which do not. In solid lines we represents the results including the orbital evolution while by the dashed one the energy density for e=0. As a conclusion, the eccentricity do not play a role even in LISA sensitive frequencies band. The dashdotted lines exhibits the level of the contribution of non-merging sources since they are invisible in the total population. At 10 Hz we recognize the typical bump of the population III, which dominate the energy density contributions at f <10 Hz. For frequencies higher than 10 Hz, the population I and II is dominating because of their higher/larger merger frequencies. due to their lower masses.

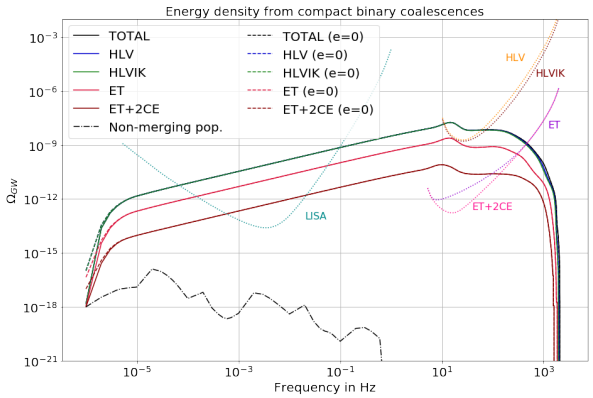

Figure 5: Energy density for the residual total populations. The solid lines describe the residual energy densities for different networks of terrestrial detectors (see text) including the orbital evolution, while the dashed one assuming e=0. The dashdotted line exhibits the total non-merging population (including BBHs, BNSs and NSBHs). The dotted lines represent the Power Integrated Curves of 2G and 3G networks and LISA

4 Conclusions and discussion

In this study we have calculated the contribution of compact binary coalescences from Population I/II and III, to the gravitational wave stochastic background, using the population synthesis code `StarTrack`. We have used Monte Carlo techniques in order to model the evolution of the eccentricity and the redshift, which can play a role at low frequencies. We obtain that the background is dominated by the population of BBHs and should be detected with the second generation of terrestrial detectors after they have reached design sensitivity, in agreement with previous estimates [20]. With future detectors, such as Einstein Telescope, Cosmic Explorer or LISA, the goal will be to be able to subtract the background from compact binary coalescences, in order to see the cosmological or other astrophysical backgrounds below. With terrestrial detectors it will be possible to reduce the background by 2 order of magnitudes. In the LISA band, where the signal last longer, the sources overlap and it may be very difficult to separate them. However, one may be able to remove the waveform detected with terrestrial detectors at high frequencies, down to low frequencies. The challenge may be that the information on the eccentricity is lost when entering the frequency band of terrestrial detectors, but we have shown in this study that the effect of the eccentricity was small in the LISA band, giving hope the subtraction of the background would be possible.

References

[1] C. Périgois, C. Belczynski, T. Bulik and T. Regimbau, StarTrack predictions of the stochastic gravitational-wave background from compact binary mergers [arXiv:2008.04890 [astro-ph.CO]].

[2] A. Einstein. Die Grundlage der allgemeinen RelativitÃtstheorie. *Ann. Phys*, 354:769–822, 1916.

[3] B. P. Abbott et al. Observation of Gravitational Waves from a Binary Black Hole Merger. *Phys. Rev. Lett.*, 116(6):061102, 2016.

[4] J. Aasi et al. Advanced LIGO. *Class. Quant. Grav.*, 32:074001, 2015.

[5] F. Acernese et al. Advanced Virgo: a second-generation interferometric gravitational wave detector. *Class. Quant. Grav.*, 32(2):024001, 2015.

[6] B.âP. Abbott et al. GW170817: Observation of Gravitational Waves from a Binary Neutron Star Inspiral. *Phys. Rev. Lett.*, 119(16):161101, 2017.

[7] B. P. Abbott et al. GWTC-1: A Gravitational-Wave Transient Catalog of Compact Binary Mergers Observed by LIGO and Virgo during the First and Second Observing Runs. 2018.

[8] Yoichi Aso, Yuta Michimura, Kentaro Somiya, Masaki Ando, Osamu Miyakawa, Takanori Sekiguchi, Daisuke Tatsumi, and Hiroaki Yamamoto. Interferometer design of the KAGRA gravitational wave detector. *Phys. Rev.*, D88(4):043007, 2013.

[9] Souradeep T. Unnikrishnan C. S. Dhurandhar S. Raja S. Iyer, B. and A. Sengupta. LIGO-India, Proposal of the Consortium for Indian Initiative in Gravitational-wave Observations (IndIGO). 2011.

[10] P. Amaro-Seoane et al. Laser interferometer space antenna. 2017.

[11] H. Audley et al. LISA Pathfinder. In *28th International Symposium on Lepton Photon Interactions at High Energies (LP17) Guangzhou, Guangdong, China, August 7-12, 2017*, 2019.

[12] M Punturo et al. The einstein telescope: a third-generation gravitational wave observatory. *Classical and Quantum Gravity*, 27(19):194002, sep 2010.

[13] David Reitze et al. Cosmic Explorer: The U.S. Contribution to Gravitational-Wave Astronomy beyond LIGO. 2019.

[14] Krzystof Belczynski, Vassiliki Kalogera, Frederic A. Rasio, Ronald E. Taam, Andreas Zezas, Tomasz Bulik, Thomas J. Maccarone, and Natalia Ivanova. Compact object modeling with the startrack population synthesis code. *Astrophys. J. Suppl.*, 174:223, 2008.

[15] K. Belczynski et al. The origin of low spin of black holes in LIGO/Virgo mergers. 2017.

[16] P. Ajith, M. Hannam, S. Husa, Y. Chen, B. Brügmann, N. Dorband, D. Müller, F. Ohme, D. Pollney, C. Reisswig, L. Santamaría, and J. Seiler. Inspiral-Merger-Ringdown Waveforms for Black-Hole Binaries with Nonprecessing Spins. *Physical Review Letters*, 106(24):241101, June 2011.

[17] P. C. Peters. Gravitational radiation and the motion of two point masses. *Phys. Rev.*, 136:B1224–B1232, Nov 1964.

[18] P. C. Peters and J. Mathews. Gravitational radiation from point masses in a keplerian orbit. *Phys. Rev.*, 131:435–440, Jul 1963.

[19] N. Aghanim et al. Planck 2018 results. VI. Cosmological parameters. 2018.

[20] Benjamin P. Abbott et al. GW170817: Implications for the Stochastic Gravitational-Wave Background from Compact Binary Coalescences. *Phys. Rev. Lett.*, 120(9):091101, 2018.

[21] T. Regimbau, M. Evans, N. Christensen, E. Katsavounidis, B. Sathyaprakash, and S. Vitale. Digging deeper: Observing primordial gravitational waves below the binary black hole produced stochastic background. *Phys. Rev. Lett.*, 118(15):151105, 2017.

Using simulated quasar catalogs for the Baryon Acoustic Oscillation in Lyman-α analysis of the eBOSS and DESI experiments

Julianna Stermer

Sorbonne Université, Université de Paris, CNRS/IN2P3, Laboratoire de Physique Nucléaire et de Hautes Energies, LPNHE, 4 Place Jussieu, F-75252 Paris, France

Abstract — The accelerated expansion of the universe caused by the presence of dark energy was first observed in 1998 by measurement of the luminosity of type Ia supernovae. In 2005, a new probe for dark energy, the Baryon Acoustic Oscillation (BAO) was introduced. This probe is based on the imprint left in the matter density field by sound waves propagating in the primordial universe. Following the initial detection of this BAO signal, several surveys, including eBOSS and its successor DESI, have been designed to measure this signal in the quasar and galaxy distribution through the computation of their correlation function. Quasars with redshift higher than 2 have in their spectra a collection of absorption lines called the Lyman-α forest. These absorptions stem from the presence of neutral hydrogen clouds along the line of sight of the quasar. Each of these absorption lines is a mass tracer that can be used to calculate the correlation function. Neutral hydrogen clouds with column density above $2 \cdot \log(20)$ cm^{-2} are called Damped Lyman-α Absorbers (DLAs). Their presence in quasar spectra skews the calculation of the correlation function and has to be addressed. Hitherto DLAs in data are identified by a DLA finder algorithm and masked out of the forest. My work focuses on studying the impact masking the DLAs has on the measured cosmological parameters. I will present results using simulated quasar spectra catalogs with different masking strategies to determine the efficiency of this method.

1 Introduction

1.1 The Baryon Acoustic Oscillation

During inflation, quantum fluctuations generated inhomogeneities in the content distribution of the universe, creating over- and underdense regions. With time, the gravitational pull - that was stronger than the expansion - made overdense regions grow denser, depleting the already underdense regions. The then hot and dense universe had its photons and baryonic matter tightly coupled into a plasma like fluid. The competition between contractions in the plasma and radiative pressure generated a cosmic sound wave propagating through the photon-baryon plasma at a the speed of sound ($c_s \sim c/\sqrt{3}$). As the Universe expanded, the temperature dropped, allowing for the recombination of electrons and protons. As the photons saw their mean free path rocket to reach lengths larger than the size of the horizon, they flew away from the plasma. After decoupling, no radiation pressure was left to fuel the sound wave, effectively freezing the propagation of the baryons, thus leaving a baryonic matter overdensity shell at $r_d = 100$ Mpc$/h$ in comoving space around the primordial density perturbation, with $h = \frac{H_0}{100 \text{ km/s/Mpc}}$. This phenomenon is called the Baryon Acoustic Oscillation (BAO). The distance traveled by the sound wave until decoupling r_d links the speed of sound c_s and the Hubble parameter $H(z)$. The gravitational pull between the dark matter and the baryons dispersed the dark matter perturbation around the center of the shell and attracted the baryons back towards its center. Overdense regions are seeds for structure formation and evolve into galaxies or quasars for example. Structures, then, formed preferentially with a separation of 100 Mpc$/h$.

Looking at the distribution of matter today, this preferred separation can be seen as an excess probability of 1% in the two-point correlation function - the BAO peak. Because of the faintness of the signal that has to be measured, large amounts of data are necessary.

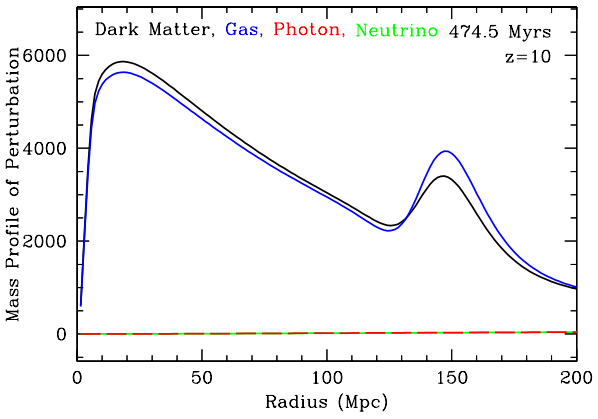

Figure 1: Mass Profile of an overdense region as a function of separation from the origin in Mpc for dark matter, baryonic matter (gas), photons and neutrinos once the BAO shell has been imprinted in the matter distribution, from [2]. The BAO peak is visible at 150 Mpc from the initial matter perturbation, with $h = 0.72$.

1.2 The Lyman-α forest

Several mass tracers can be used to measure the BAO peak. At redshifts up to $z \sim 0.8$, galaxies are excellent mass tracers but are too faint at higher redshift. Other tracers, like quasars and their Lyα forest absorption are then used. Here, we focus on high redshift studies, and thus on quasar Lyα forests. Quasars are active galaxy nuclei that emit luminous relativistic jets allowing them to be seen deeper than galaxies.

The Lyα forest is observed on quasar spectra because of the presence of matter on the line of sight. Quasars emit a strong Lyα line at 121.6 nm in the restframe, but as the light propagates towards the detectors, it passes through neutral hydrogen clouds that absorb it. The further the quasar is, the more numerous clouds on the line of sight are, the more absorption lines are visible on the spectrum. The redshift for each cloud is: $z = \frac{\lambda}{\lambda_{abs}} - 1$, with λ_{abs} the absorbed rest frame wavelength and λ the observed wavelength on the spectrum.

1.3 Cosmological parameters

The position of the BAO peak in the 2-point correlation function measures the angular $\Delta\theta$ and redshift Δz separations between two mass tracers. These quantities relate the comoving angular diameter distance $H_A(z)$ and the Hubble distance $D_H(z)$ with r_d. From there, one can obtain a value for the Hubble parameter at the relevant redshift.

1.4 Cosmological surveys

The extended Baryon Oscillation Spectroscopic Survey (eBOSS) is one of four experiments on the Sloan Digital Sky Survey telescope, a 2.5 m telescope at Apache Point, NM, USA. Its goal is to precisely measure the BAO scale using spectra from galaxies and quasars. Retired in 2019 it obtained more than 200 000 quasar spectra with resdshifts up to 3.

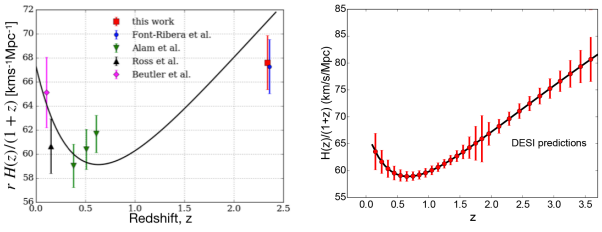

Figure 2: *Left:* the comoving expansion rate as a function of redshift, from [8]. *Right:* DESI predictions from [4]. The black line is the model for a flat ΛCDM cosmology, [6].

Its successor, the Dark Energy Spectroscopic Instrument (DESI), has started commissioning late 2019. It has been installed on the Mayall telescope (4 m) at Kitt Peak National Observatory, AZ, USA. It should observe 2.5 million quasars, 700 00 of which Lyman-α quasars, ten times more than eBOSS, allowing for a more complete study of the BAO for $0.5 < z < 3.5$.(Fig. 2)

2 The auto-correlation function

Computing the correlation function goes as follows:

- Extracting the Lyman-α absorption field
- Converting distances
- Calculating the correlation function

The details of the estimation of the absorption field δ will be addressed in section 5. The auto-correlation function is calculated on a grid of radial and perpendicular directions. The grid is obtained by converting the angular separation and the comoving distances between two absorbing clouds. This conversion requires the input of a fiducial cosmological model, here [6]. The auto-correlation function in each bin of the grid is then calculated by averaging the product of the absorption field at a position x and of the absorption field at a position $x + r$, the average is weighted with the inverse variance for each pixel:

$$\xi_A = \langle \delta(x)\ \delta(x + r) \rangle \tag{1}$$

The position of the BAO peak is then obtained by fitting the correlation with a model that can be completed by the addition of astrophysical and non linear effects, such as metals, high density columns, UV corrections, and peculiar velocities. Figure 3 shows the correlation function for the latest eBOSS data release [7] for one wedge in μ[1]. The position of the BAO peak stays very

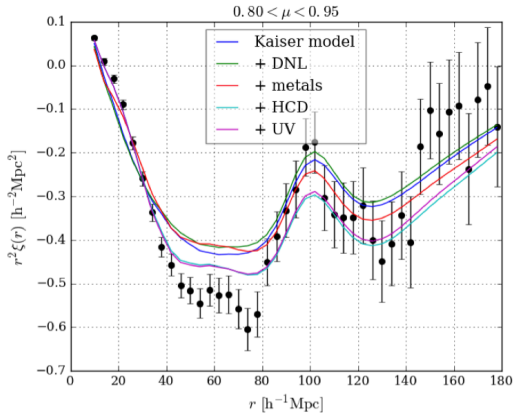

Figure 3: Auto-correlation function of the Lyα forest close to the line of sight ($0.8 < \mu < 0.95$), from eBOSS data with different fit models. The correlation function is multiplied by r^2 for visibility of the BAO peak at 100 Mpc/h, from [8]

robust regardless of the model corrections that are applied. However other cosmological parameters such as the Lyα bias parameters are more dependent on the model considered. In order to verify validity of the analysis, tests can be run on simulations.

[1] $\mu = 1$ is for the radial direction i.e. looking along the line of sight

3 Mocks

Simulations can be used to test the analyses systematics as well as the effects different astrophysical phenomena have on the correlation function and thus the measured cosmological parameters.

Two teams, in London[2] and Saclay[3], are developing sets of quasar transmission field simulations - or mocks. I focus here on the Saclay mocks. Those mocks are generated from random gaussian fields tuned to have the proper 1D and 3D power spectrum, refer to [3].

The transmission fields are then converted into quasar spectra with a mock expander (quickquasars[4]) where a random redshift and magnitude are assigned to each quasar. From there the same analysis done on the data can be applied to the mocks, see Fig. 4.

At first order, the agreement between the data and the mocks is very good. The BAO peak has the same amplitude and position. In contrast, the region between 25 and 75 Mpc/h is not well reproduced by the mocks. This can be explained by the lack of astrophysical effects in this analysis of the mocks. Indeed, neither metals nor Damped Lyman-α Absorbers (DLAs) have been incorporated in the basic Lyα+continuum mocks. In section 4, the effects of DLAs on the correlation function are addressed.

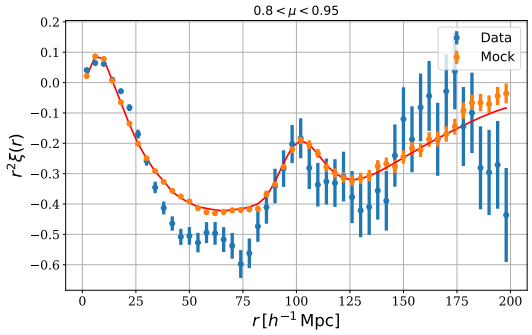

Figure 4: Auto-correlation function of the Ly-α forest. In blue: the data from the latest eBOSS data release [7]. In orange: one realization of the Saclay mocks, with its fit in red.

4 Damped Lyman-α Absorbers

Damped Lyman-α Absorbers (DLAs) are a subset of High Column Density (HCD) systems (neutral hydrogen clouds) with column density ($n_{HI} \geq 2.10^{20} cm^{-2}$) [5]. If present along the line of sight of a quasar, a significant portion of the quasar light is absorbed. This loss of light skews the estimation of the absorption field δ_q for the affected wavelengths. To remedy this, a DLA finder algorithm is run to identify and mask out the DLAs.

[2] https://github.com/igmhub/LyaCoLoRe
[3] https://github.com/igmhub/SaclayMocks
[4] https://github.com/desihub/desisim/

Contrary to data, in mocks, the true HCD catalog is known and HCDs can be added to the mock expander. Once they have been added, tests can be run with different masking options.

Figure 5 shows the effects of the presence of DLAs and their masking on the auto-correlation function. Although the position of the BAO peak remains unchanged, its amplitude and the overall shape of the correlation function is affected by the presence of DLAs. It is expected that the overall shape of the correlation function is modified by the inclusion of DLAs, indeed, the loss of light in the Lyman-α region affects the calculation of the absorption field, retrieving exactly the same shape then proves impossible.

HCDs that are not DLAs (i.e. $n_{HI} \leq 2.10^{20}$ cm^{-2}) cannot be reliably detected by the finder thus only DLAs (true or found) are masked. However, the DLA finder performs poorly in measuring the column density of the HCD it has found, frequently overestimating it. The catalog of found DLAs is then more populated than the true catalog. This explains the relative positions of the green and red curves. A more precise measurement the the column density for found DLAs is paramount to be able to rely on it when applied to the data. However the similarities between the unmasked and the 2 masked correlation functions does question the necessity of masking the DLAs altogether. Another option for taking DLAs into account is to model their effect on the correlation function on mocks and apply this model to the fitting procedure.

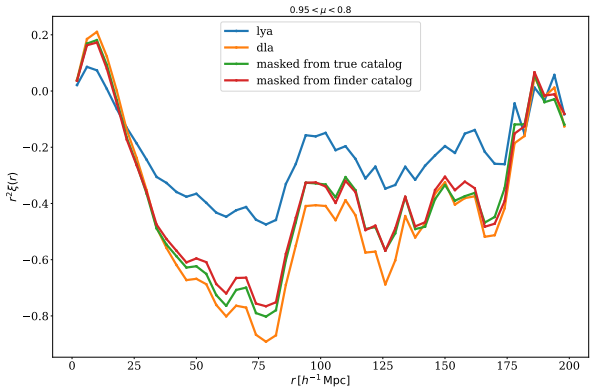

Figure 5: Correlation function of mocks for different runs of the analysis. In blue, the base analysis with no DLAs, in orange the DLAs have been added but not masked, in green all DLAs from the truth catalog with $\log(n_{HI}) \geq 20.3$ have been masked out, and in red all DLAs from the finder catalog with the same condition on n_{HI} have been masked out.

5 The effects of continuum fitting

The first step to calculate the two-point correlation function is the extraction of the absorption field.

5.1 The absorption field

The light that is received from quasars is a combination of the unabsorbed flux density or continuum $C_q(\lambda)$ of the quasar and of the absorption field $\delta_q(\lambda)$ created by the neutral hydrogen clouds present on the line of sight. This absorption field can be used as a mass tracer. It is obtained from equation 2.

$$\delta_q(\lambda) = \frac{f_q(\lambda)}{C_q(\lambda)\bar{F}(z)} - 1 \tag{2}$$

Where q denotes each quasar and $\bar{F}(z)$ is the mean transmitted flux fraction, the flux averaged over all quasars in the catalog. With there being no way of knowing the true continuum, it has to be estimated. The procedure to obtain the absorption field for each quasars (Eq. 2) relies on the estimation of the continuum $C_q(\lambda)$. To evaluate it, the first step is to average all quasar fluxes and multiply it by a linear function so as to account for spectral diversity and potential calibration errors: $C_q(\lambda) = C(\lambda_{\text{ref}})\ (a_q + b_q\ \log(\lambda))$. Here, λ_{ref} is the reference frame wavelength: $\lambda_{\text{ref}} = \frac{\lambda}{1+z_q}$.

The fit performed to obtain the parameters a_q and b_q introduces a new correlation between nearby pixels of a forest. Refer to [1] for further details. The measured correlation function is distorted compared to the true correlation function.

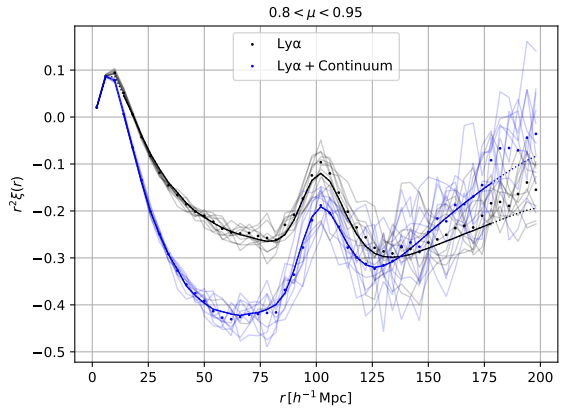

Figure 6: Correlation function of mocks for the same range in μ. In black mocks have not undergone continuum fitting and in blue the continuum fitting has been added. The light curves correspond to ten individual realizations of the mocks and the points represent the 10 stacked realizations with the fit in heavy lines (where the distortion matrix has been added to the blue model curve).

5.2 Distortion matrix

A distortion matrix D_{AB} can then be used to link the measured $\hat{\xi}$ correlation function and the true ξ one:

$$\hat{\xi_A} = D_{AB}\ \xi_B \tag{3}$$

The distortion matrix is then included in the fitting procedure. With mocks, the validity of this method can be verified. "raw" or "Lya" mocks are quasar transmission files that haven't been expanded into spectra. Their absorption fields can be calculated without continuum fitting, hence they do not possess the additional correlation. The two methods can then be compared.

Fig. 6 shows the effect of the continuum fitting. The agreement between the mocks and their fit indicates in both cases the first order overall validity of the distortion matrix procedure. It is then expected that applying the same distortion matrix to the raw mocks would yield the same results as when the continuum fitting is implemented. But in Fig. 7, although it is a small effect, applying the distortion matrix doesn't allow the raw mocks to recover the cooked values. Indeed some residual correlation can still be observed. This indicates that the distortion matrix doesn't fully model the distortion introduced by continuum fitting. How this affects the values of the fitted cosmological parameters still remains to be studied. However, this effect is more prominent for this analysis than it was for [1]. This discrepancy might stem from the resolution applied to the transmission files by the mock expander.

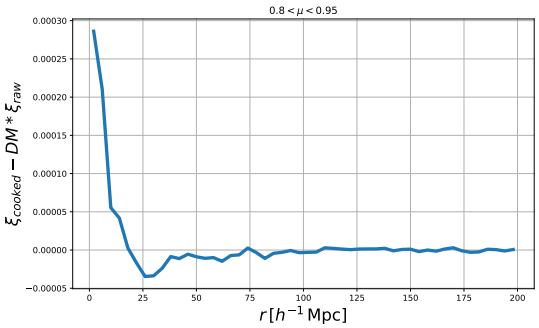

Figure 7: Difference between the cooked (with continuum fitting) and the raw (no continuum) mocks when the distortion matrix (DM) is applied to the raw mocks for one mock realization in the same μ range. The redshift evolution corrections have also been taken into account.

6 Conclusions

The Lyman-α forest in quasar spectra is a very efficient mass tracer: not only does it allow for high redshift measurements but it also provides more statistics than quasars themselves. The final eBOSS data release [7] will present the most complete BAO in Lyman-α analysis using the analysis and simulations described above.

Mocks are being used to verify and refine parts of the analysis such as the impact of DLAs or continuum fitting on the cosmological parameters that are measured. More extensive testing still has to be done such as fitting the different analyses to understand the evolution of the fitted parameters with each case. The incorporation of metals and other astrophysical phenomena in mocks is also necessary to have a full understanding of the systematics of the analysis.

References

[1] Bautista, J. E., Busca, N. G., Guy, J., et al. 2017, A&A, 603, A12

[2] Eisenstein, D. J., Seo, H.-J., & White, M. 2007, ApJ, 664, 660

[3] Etourneau, T., et al. in prep., 2020

[4] Flaugher, B. & Bebek, C. 2014, in Proc. SPIE, Vol. 9147, Ground-based and Airborne Instrumentation for Astronomy V, 91470S

[5] Font-Ribera, A., Miralda-Escudé, J., Arnau, E., et al. 2012, J. Cosmology Astropart. Phys., 2012, 059

[6] Planck Collaboration, Ade, P. A. R., Aghanim, N., et al. 2016, A&A, 594, A13

[7] du Mas des Bourboux, H. et al. in prep., 2020

[8] de Sainte Agathe, V., Balland, C., du Mas des Bourboux, H., et al. 2019, A&A, 629, A85

Part II

Beyond Standard Model

session chaired by Loïc VALÉRY

Search for additional neutral Higgs bosons decaying to τ leptons pairs in the CMS experiment at the LHC

Lucas Torterotot

Institut de Physique des Deux Infinis – Lyon

Abstract — This document presents a search for additional neutral Higgs bosons decaying to τ leptons pairs in the CMS experiment at the LHC in the context of the minimal supersymmetric extension of the standard model. In order to rely as much as possible on data instead of simulation, an embedding technique is used to estimate the contributions of processes having a pair of τ leptons in the final state, along with a data-driven background estimation of fake tau backgrounds. This study is based on the LHC Run-II data collected with the CMS detector in 2017 at a center-of-mass energy of 13 TeV, corresponding to an integrated luminosity of 41.5 fb^{-1}. A smart parallelization tool for Python scripts used for this study is also introduced.

1 Introduction

The discovery of the Higgs boson in 2012 at CERN LHC [1, 2] gave evidence that spontaneous symmetry breaking, as proposed by the Brout-Englert-Higgs mechanism [3, 4, 5], may be realized in nature. The LHC data confirm, within the experimental accuracy, that this boson is consistent with the standard model (SM) Higgs boson [6, 7].

However, several questions remain about the SM. Heavy particles contributing to the Higgs boson propagator give diverging corrections to the Higgs mass. To balance such divergences, a solution is to add a so-called superpartner for each particle. For a fermion, the superpartner is a boson and vice-versa. Indeed, bosons and fermions corrections to the Higgs mass have opposite signs. Supersymmetry is an example of a Beyond-the-Standard-Model theory based on this principle.

In the minimal supersymmetric extension of the standard model (MSSM), the Higgs sector consists of two complex Higgs doublets, $\mathrm{H_u}$ and $\mathrm{H_d}$, providing masses for up- and down-type fermions. In the CP-conserving MSSM, this leads to five physical Higgs bosons:

- a light Higgs boson h of mass m_h;
- a heavy Higgs boson H of mass $m_H > m_h$;
- a heavy pseudo scalar Higgs boson A of mass m_A;
- two charged Higgs bosons, H^+ and H^-.

Given current data, m_A seems likely to be greater than 300 GeV [6, 7, 8]. In this case, the MSSM is close to the decoupling limit, in which h takes the role of the SM Higgs boson ($m_h = 125$ GeV) and the heavy Higgs bosons are nearly degenerate in mass.

A search for additional neutral MSSM Higgs bosons in the $\tau\tau$ final state has been carried out with the 2016 LHC data recorded by the CMS detector [9]. In this document, the search is based on the LHC Run-II data collected with the CMS detector in 2017 at a center-of-mass energy of 13 TeV, corresponding to an integrated luminosity of 41.5 fb^{-1}. The choice of the channel is introduced in section 2. Section 3 summarizes the event selection. Background estimation techniques are described in sections 4 and 5. Section 6 contains results obtained with the 2017 dataset. A smart parallelization tool for Python scripts used in this study is introduced in section 7.

2 Neutral MSSM Higgs bosons phenomenology

At leading order in the MSSM, the coupling of H and A bosons to down-type fermions (down, strange and bottom quarks and charged leptons) is proportional to a factor $\tan\beta$, defined as the ratio of the vacuum expectation values of the neutral components of the two Higgs doublets,

$$\tan\beta = \frac{\langle \mathrm{H_u}^0 \rangle}{\langle \mathrm{H_d}^0 \rangle} = \frac{v_\mathrm{u}}{v_\mathrm{d}}\,. \tag{1}$$

When $\tan\beta$ is large, the coupling of H and A bosons to up-type fermions and vector bosons is suppressed, while being enhanced for down-type fermions. Therefore, the decays of the Higgs bosons to down-type fermions are particularly interesting in the high $\tan\beta$ regime.

Due to their high masses, the b quark has the largest branching ratio (BR) among down-type fermions, followed by the τ lepton. However, τ leptons provide better experimental accessibility as proton collisions lead to intense hadronic activity and b-quark production.

As they are not stable particles, τ leptons decay before entering the sensitive parts of the CMS detector. Therefore, only the decay products of the τ lepton can be detected. The τ leptons decay proceeds through the diagrams displayed in figure 1 and decay modes of tau leptons are listed in table 1.

These three different categories of tau decays (electron e, muon μ or hadronic tau τ_h), for the two τ leptons coming from the Higgs boson decay, lead to six

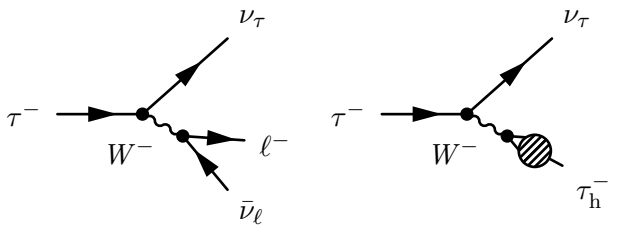

Figure 1: Tau leptons decaying leptonically (left) and hadronically (right). The lepton ℓ can be either an electron or a muon. In the hadronic decay, a pair of quarks is produced. A hadronisation process follows, resulting in a hadronic tau, τ_h, composed of charged hadrons and eventual neutral pions.

Decay mode	BR (%)
$\tau^- \to e^- \bar{\nu}_e \nu_\tau$	17.8
$\tau^- \to \mu^- \bar{\nu}_\mu \nu_\tau$	17.4
$\tau^- \to h^- \nu_\tau$	11.5
$\tau^- \to h^- \pi^0 \nu_\tau$	26.0
$\tau^- \to h^- \pi^0 \pi^0 \nu_\tau$	10.8
$\tau^- \to h^- h^+ h^- \nu_\tau$	9.8
$\tau^- \to h^- h^+ h^- \pi^0 \nu_\tau$	4.8
Others hadronic modes	1.8
All hadronic modes	64.8

Table 1: Tau lepton decay modes.

different channels ($\tau_h\tau_h$, $\mu\tau_h$, $e\tau_h$, $\mu\mu$, $e\mu$, ee). In this study, only the semi-leptonic channels, $\mu\tau_h$ and $e\tau_h$, are analyzed.

3 Event selection

An online, i.e. at collision time, selection is applied, based on the presence of at least one muon (respectively electron) with a transverse momentum $p_T \geq 24$ GeV (27 GeV) at trigger level for the $\mu\tau_h$ ($e\tau_h$) channel. This selection is complemented with events containing one muon (electron) with $p_T \geq 20$ GeV (24 GeV) associated with a τ_h with $p_T \geq 27$ GeV (30 GeV), all of these objects having a pseudorapidity η respecting $|\eta| \leq 2.1$.

Requirements on the p_T and η of the reconstructed τ lepton decay products are applied offline, as listed in table 2. In addition to these kinematic selections, identification requirements are applied to the tau decay products.

The lepton ℓ (muon or electron) has to pass a multi-variable identification requirement. Contributions from background processes are reduced by requiring ℓ to be isolated from hadronic activity in the detector, as explained in [9]. The hadronic tau τ_h is required to pass tight τ_h identification discriminant and further requirements are made to avoid muons and electrons misidentified as τ_h.

Channel	Lepton ℓ	Hadronic tau τ_h
$\mu\tau_h$	$p_T \geq 21$ GeV, $\lvert\eta\rvert \leq 2.1$	$p_T \geq 23$ GeV, $\lvert\eta\rvert \leq 2.3$
$e\tau_h$	$p_T \geq 25$ GeV, $\lvert\eta\rvert \leq 2.1$	$p_T \geq 23$ GeV, $\lvert\eta\rvert \leq 2.3$

Table 2: Kinematic selection applied to the tau decay products.

The ℓ and τ_h passing these selections are then required to be associated to the primary vertex within a distance of 0.045 cm in the transverse plane for ℓ and 0.2 cm along the beam axis for ℓ and τ_h.

Then, pairs are constructed with all ℓ and τ_h passing previous selections to reconstruct a $H \to \tau\tau$ decay candidate. To do so, ℓ and τ_h are required to be of opposite charges and separated by more than 0.5 in $\Delta R = \sqrt{(\Delta\eta)^2 + (\Delta\phi)^2}$, where $\Delta\eta$ ($\Delta\phi$) is the difference in pseudorapidity (azimuth) between ℓ and τ_h. Should several pairs of $\ell\tau_h$ be possible for an event, further selection criteria are applied to keep only one pair, based on the ℓ and τ_h isolation and p_T. Any event with extra leptons passing selection criteria for other channels is removed to avoid overlapping between channels.

In addition, the transverse mass of the lepton, defined as

$$m_T^\ell = m_T(\ell, \text{MET}) = \sqrt{2 p_T{}^\ell p_T{}^{\text{MET}} (1 - \cos\Delta\phi)} \quad (2)$$

where $p_T{}^{\text{MET}}$ is the missing transverse energy (MET) and $\Delta\phi$ difference in azimuth between $\vec{p}_T^{\,\ell}$ and $\vec{p}_T^{\,\text{miss}}$, is required to be below 70 GeV.

4 Embedding technique

The embedding technique estimates from data the contribution of the standard model background processes that lead to two τ leptons in the final state, with minimal input from simulation [10]. This technique relies on a recorded sample of di-muon events. The two muons are removed from the event and replaced by simulated τ leptons with the same kinematic properties.

A set of hybrid data-simulation events is obtained, where most of the event comes from data, and where simulation is only used to model the decay of the τ leptons. Challenges in describing the underlying event or the production of associated jets in the simulation are thus avoided.

The embedded samples make it possible to avoid using simulated samples for $Z \to \tau\tau$ and the parts of $t\bar{t}$, di-boson and electroweak events where the reconstructed muon (electron) is matched to a prompt muon (electron) and the τ_h to a genuine tau at generator level in the $\mu\tau_h$ ($e\tau_h$) channel.

5 Fake factor method

The fake factor method is almost only based on data and is used to estimate the amount of events in the signal region containing a jet misidentified as a τ_h, called fake taus, $n_{j\to\tau_h}$. The main idea is illustrated in figure 2.

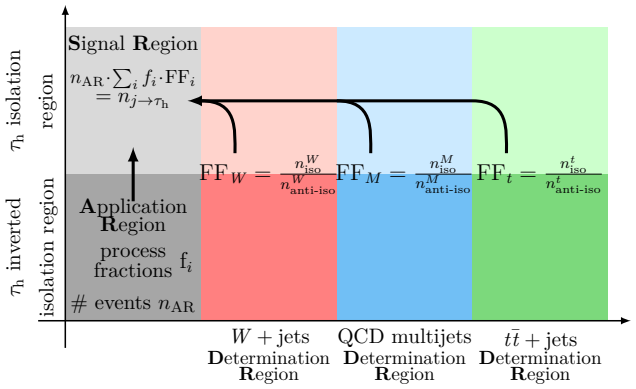

Figure 2: Principle of the fake factor method.

An application region (AR) is defined by only inverting the cut on the τ_h candidate isolation and contains n_{AR} events. The AR contains almost exclusively events with fake taus. Actual τ_h may populate the AR but do not represent more than a few percent of the events. In parts of the phase space, e.g. close to the Z boson mass peak, up to 20 % of the events in the AR may only contain real τ_h. Corrections using simulated samples are applied to account for such contamination. By using determination regions (DR), the fake factor FF to be applied to n_{AR} to obtain $n_{j \to \tau_h}$ is derived.

Three processes give fake τ_h. One DR is defined for each of them:

$t\bar{t}$ + jets for which simulated event samples are used. The same selections as in the SR and AR are used;

W + jets is coming from data and the selections are the same as for SR and AR, except for the lepton transverse mass defined in equation (2), which is above 70 GeV (orthogonality with SR and AR) and no b-jet allowed (orthogonality with $t\bar{t}$ + jets);

QCD multijet is coming from data and the selections are the same as for SR and AR, except for the charges of the two tau decay products, which have to be the same while being opposite to each other in the other regions.

The fake factor FF to apply to the AR is defined as the weighted sum of the partial fake factors FF_i derived for each process i, weighted by the process fractions f_i observed in the AR. Then,

$$n_{j \to \tau_h} = n_{AR} \cdot FF = n_{AR} \cdot \sum_i f_i \cdot FF_i \qquad (3)$$

where FF_i is defined as the ratio of the number of events in the isolated to anti-isolated regions for process i. The fake factors are measured as functions of the τ_h constituents, p_T and η. Further corrections using simulated samples are applied to FF_i to account for background impurities, e.g. QCD events passing the W + jets DR selection.

6 Results

The discriminating variable used is the total transverse mass m_T^{tot}, defined as

$$m_T^{tot} = \sqrt{m_T^2(\ell, \tau_h) + m_T^2(\ell, \text{MET}) + m_T^2(\tau_h, \text{MET})} \qquad (4)$$

where $m_T(A, B)$ is the transverse mass of A and B as defined in (2). The last results obtained for the 2017 data with the $\mu\tau_h$ channel are shown in figure 3.

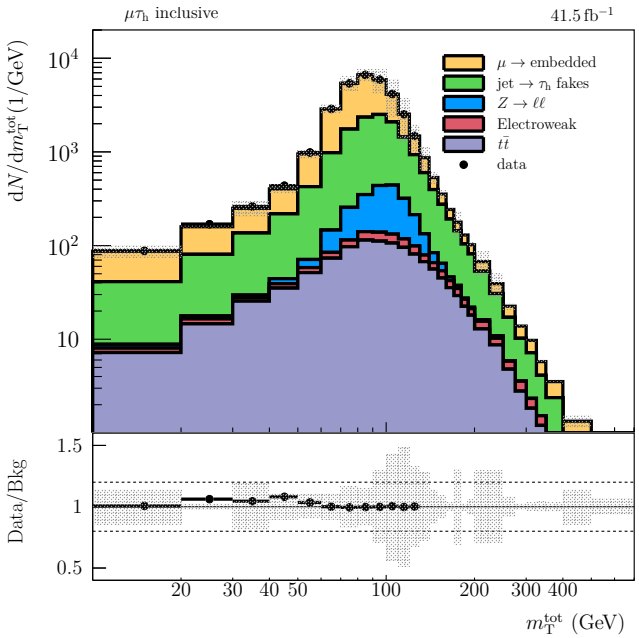

Figure 3: Expected (filled, stacked histograms) and observed (black points) distributions of m_T^{tot} in the $\mu\tau_h$ channel. The shadow bands associated to the sum of the stacked histograms is the combined uncertainty obtained by taking into account yield, normalization and shapes uncertainties in all background processes with associated correlations, as obtained from the fit performed. On the lower part, the ratio of data to backgrounds is shown.

The considered background processes are the following:

$\mu \to$ embedded corresponds to the embedded events described in section 4;

jet $\to \tau_h$ fakes corresponds to the estimated amount of events containing jets misidentified as τ_h, as described in section 5, and this amount is subtracted from the corresponding samples to avoid double-counting;

$Z \to \ell\ell$ are simulated event samples, in which a Z boson decays into a pair of electrons or muons, one of them misidentified as a τ_h;

Electroweak are simulated event samples corresponding to diboson and single-top processes;

$t\bar{t}$ are simulated events, in which a pair of top quarks decay into electrons or muons, one of them misidentified as a τ_h.

Work is, at this date, still ongoing. Some background events are missing due to a computation issue. Though the corresponding processes are renormalized, this increases uncertainties. Good agreement is obtained between data and background estimation for $50 < m_{\mathrm{T}}^{\mathrm{tot}} < 130$ GeV. Above this value, a blinding is applied while the low $m_{\mathrm{T}}^{\mathrm{tot}}$ area is not fully analyzed.

7 Smart parallelization tool

To carry this analysis out, thousands of files need to be processed. Their contents are merged in different ways to obtain the histograms represented in figure 3. As a consequence, a sequential script is far from optimal.

Dask [11] is an already existing Python module allowing users to easily parallelize their scripts. The idea is to redefine Python objects used in the code as being Dask delayed objects, which are related to one another based on their inter-dependence as shown in figure 4.

```
#!/usr/bin/python3
import time, dask

def add(a,b):
    time.sleep(1)
    return dask.delayed(a+b)

x = add(1,2)
y = add(3,4)
z = add(x,y)
a = add(x,z)
b = add(y,z)
c = add(a,y)

to_compute = [a, b, c]
dask.visualize(*to_compute)
dask.compute(*to_compute)
```

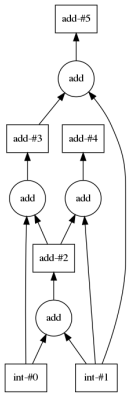

Figure 4: Example of Dask use (left) and relations between Dask delayed objects (right).

Then, the Dask module knows which delayed objects can be processed in parallel, which ones need to wait for others to be computed and handles processing priority for these objects consequently to optimize the CPU usage. Its use in the case of the figure 4 reduces computing time from 6 to 4 seconds. The running time of our analysis script is reduced by a factor of 10.

8 Conclusions and prospects

An introduction to search for additional neutral Higgs bosons decaying to τ leptons pairs in the context of the MSSM has been presented. This search is performed in the $\mu\tau_{\mathrm{h}}$ and $e\tau_{\mathrm{h}}$ final states for the τ leptons pair.

This analysis relies as much as possible on data. All the processes leading to a τ leptons pair in the final state are estimated using the embedding technique, which only requires to simulate the two τ leptons decay products. An estimate of the amount of events containing jets faking τ_{h} is obtained by the fake factor method, which is almost only based on data. Remaining backgrounds contributions, corresponding to less than few percent of the events in each range of the discriminating variable, are obtained using simulated event samples.

At this date, good agreement between data and background estimation is obtained in signal-depleted regions in the $\mu\tau_{\mathrm{h}}$ channel. Once the low $m_{\mathrm{T}}^{\mathrm{tot}}$ region is correctly modeled, the high $m_{\mathrm{T}}^{\mathrm{tot}}$ region will be unblinded and searches for a signal will be possible. For the $e\tau_{\mathrm{h}}$ channel, the same procedure will be followed. These two channels could then be combined, along with the $\tau_{\mathrm{h}}\tau_{\mathrm{h}}$ channel, in a global study.

Identifying τ_{h} more efficiently is a way of improving this analysis. For this purpose, the use of deep learning techniques will be explored. These new techniques have made possible improvements in many fields and may help identifying τ_{h} with a lower misidentification rate.

Such study can benefit a lot from parallelization. For Python scripts, Dask is easy to implement and offers direct improvements in terms of computing time.

References

[1] ATLAS Collaboration, *Observation of a new particle in the search for the Standard Model Higgs boson with the ATLAS detector at the LHC*, Phys. Lett. **B 716** (2012).

[2] CMS Collaboration, *Observation of a new boson at a mass of* 125 *GeV with the CMS experiment at the LHC*, Phys. Lett. **B 716** (2012).

[3] P.W. Higgs, *Broken symmetries, massless particles and gauge fields*, Phys. Lett. **12** (1964).

[4] G.S. Guralnik, C.R. Hagen and T.W.B. Kibble, *Global conservation laws and massless particles*, Phys. Rev. Lett. **13** (1964).

[5] F. Englert and R. Brout, *Broken symmetry and the mass of gauge vector mesons*, Phys. Rev. Lett. **13** (1964).

[6] ATLAS, CMS collaborations, *Combined measurement of the Higgs boson mass in pp collisions at* $\sqrt{s} = 7$ *and* 8 *TeV with the ATLAS and CMS experiments*, Phys. Rev. Lett. **114** (2015).

[7] ATLAS, CMS collaborations, *Measurements of the Higgs boson production and decay rates and constraints on its couplings from a combined ATLAS and CMS analysis of the LHC pp collision data at* $\sqrt{s} = 7$ *and* 8 *TeV*, JHEP **08** (2016).

[8] CMS Collaboration, *Search for neutral MSSM Higgs bosons decaying to a pair of tau leptons in pp collisions*, JHEP **10** (2014).

[9] CMS Collaboration, *Search for additional neutral MSSM Higgs bosons in the* $\tau\tau$ *final state in proton-proton collisions at* $\sqrt{s} = 13$ *TeV*, JHEP **9** (2018).

[10] CMS Collaboration, *An embedding technique to determine genuine* $\tau\tau$ *backgrounds from CMS data*, JINST **14** (2019).

[11] *Dask: Scalable analytics in Python*, `https://dask.org/`.

Part III

Flavor Physics

session chaired by João Coelho

Introduction to the Flavor Physics Session

João Coelho

Université Paris-Saclay, CNRS/IN2P3, IJCLab, 91405 Orsay, France

Abstract — A short review of the main concepts and the current status of the flavor physics is presented.

1 Introduction

The Standard Model of particle physics describes almost all the data we have collected so far, however we know it is incomplete. Gravity is not included in the model, we have very little understanding of the dark sector, neutrino mass is not explained, and a number of theoretical issues exist, including the fact that the model contains 19 free parameters with no explanation for their structure. Out of these 19 parameters, 15 are related to particle masses and at least an extra 7 would be needed to describe neutrino masses and mixing.

2 Open questions

Mass generation in the Standard Model arises from spontaneous symmetry breaking due to the non-zero vacuum expectation value of the Higgs field [1]. The importance of the discovery of the Higgs boson in 2012 [2] cannot be overstated, as it confirmed this central aspect of the theory and deservedly resulted in the Nobel Prize in physics being awarded to Higgs and Englert in 2013. A very interesting aspect of this mass generation mechanism in the Standard Model is the relationship between the Yukawa couplings and the flavor structure of the model. Yukawa couplings are couplings between two fermions and a scalar field, which in the Standard Model is given by the Higgs field. These terms are responsible for the masses of all fermions. Because the Standard Model contains 3 copies (families) of each of the quark and lepton fields which share the same gauge charges, Yukawa interactions can couple fermions from different families without breaking gauge invariance. This breaks the flavor symmetry of the model and gives rise to flavor mixing.

From these considerations on the origin of mass we can contemplate the extent of our ignorance. Why are there different families of fermions? Where does the structure of the Yukawa couplings come from? In essence, what can we learn from these mass and flavor connections about the underlying high energy theory that gives rise to the Standard Model at low energies?

Answering these questions is one of the goals of flavor physics. Heavy flavor experiments such as LHCb, Belle and BaBar have explored these questions by studying b hadrons, looking in particular for decays that are rare in the Standard Model. These rare decays are often

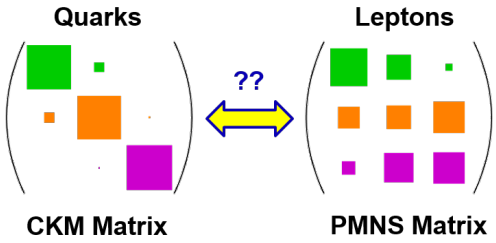

Figure 1: Comparison between the structures of the Cabibbo-Kobayashi-Maskawa (CKM) matrix, describing quark flavor mixing, and the Pontecorvo-Maki-Nakagawa-Sakata (PMNS) matrix, describing neutrino flavor mixing. While the quark matrix seems strongly diagonal, the neutrino matrix is almost random. The reason for these structures or the relationship between them is still unknown.

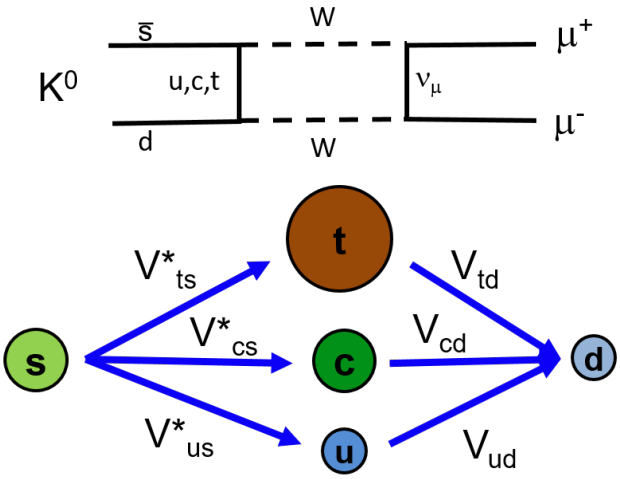

Figure 2: Example of the GIM mechanism in action. Transitions between strange and down quarks are FCNCs and can occur via mixing through three paths as shown in the bottom figure. Due to the unitary nature of the CKM matrix, this leads to almost complete destructive interference between the amplitudes. One example is the $K^0 \to \mu^+\mu^-$ decay, which is extremely suppressed and led to the prediction of the charm quark in the GIM paper [3].

subject to what is known as the Glashow-Iliopoulos-Maiani (GIM) mechanism [3], where transitions between quarks of the same charge, i.e. Flavor-Changing Neutral-Currents (FCNCs), are suppressed by a combination of the small mixing between quark families and the lack of tree-level FCNCs in the Standard Model. Because this suppression originates from a flavor symmetry of the Standard Model, one may expect that possible new physics phenomena that may break these symmetries would avoid the suppression and their contribution to the decay amplitudes may become comparable to the Standard Model components even if their tree-level coupling is small. In this way, flavor physics can become sensitive to new physics at energy scales much larger than direct searches can currently reach.

Additionally, the existence of three families of quarks with mixing gives rise to CP violation, which is an essential condition to explain the baryon asymmetry in the universe. However, the current observed amount of CP violation in the Standard Model is at least 6 orders of magnitude smaller than what's required to explain the measured baryon/photon ratio in the universe [4]. New sources of CP violation must be present and flavor physics may be an important window into these new phenomena.

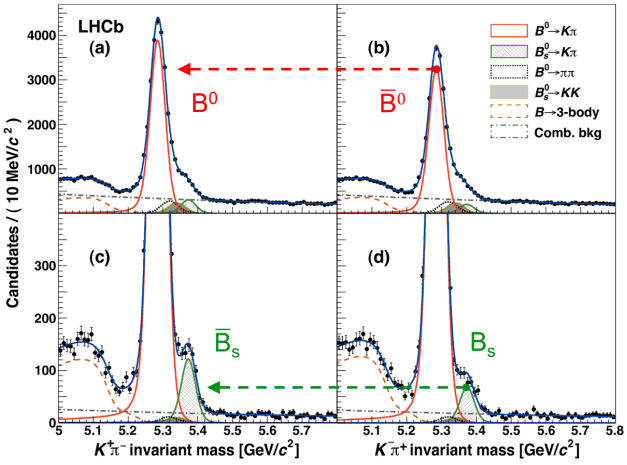

Figure 3: Example of CP violation in B^0 and B_s^0 decays [5]. While the existence of CP violation in the Standard Model is well established, it is not enough to account for the observed baryon/photon ratio in the universe, due to the small mixing between quarks and the tiny neutrino masses.

3 Experimental constraints

At present, no significant deviations from the Standard Model have been found either in CP violating measurements or in rare decays. However, some hints are currently on the horizon. In particular, some weak evidence (less than 5σ) now exists that B decays may violate the flavor universality principle of the Standard Model, in which all fermion families experience the same coupling to the weak force. Measurements from BaBar, Belle and LHCb [6] of the branching fractions of the semileptonic decay $B \to D^{(*)}\tau\nu$ seem to be significantly larger than expected from the Standard Model when compared to similar decays such as $B \to D^{(*)}\mu\nu$. Similarly, an asymmetry between the rare decays $B \to K^{(*)}\mu\mu$ and $B \to K^{(*)}ee$ has been hinted at by LHCb [7], where non is expected from the Standard Model. These results are not yet conclusive, but new data from the LHCb and Belle II experiments should settle these questions in the near future.

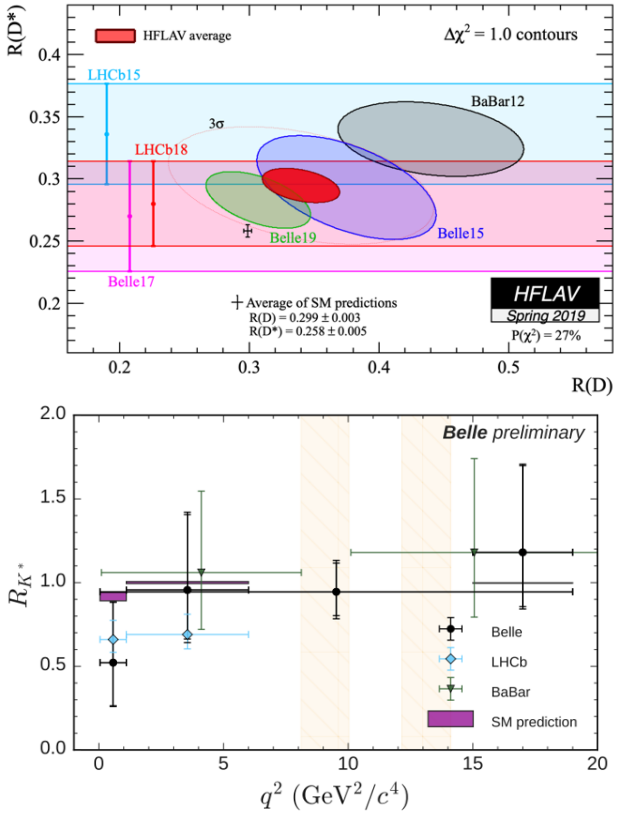

Figure 4: Current hints of lepton flavor universality violation in B decays from the LHCb, Belle and BaBar experiments. The top plot shows the measured ratios R(D) and R(D*) corresponding to $B \to D^{(*)}\tau\nu/B \to D^{(*)}\mu\nu$ [8, 6]. The bottom plot shows similar measurements of the ratio R(K*) corresponding to $B \to K^*\mu\mu/B \to K^*ee$ [7].

Contributions at JRJC 2019

At JRJC 2019, the heavy flavor session had a contribution from Jacopo Cerasoli, from CPPM, who presented his work on the searches for $B^0 \to K^{*0}\tau^+\tau^-$. This channel is of the same type as the $B^0 \to K^{*0}l^+l^-$ which form the R(K*) anomaly. While the anomaly is observed between muon and electron flavors, many models indicate strong enhancements in the tau channel branching ratio with respect to the Standard Model. His contribution focuses on the challenges of reconstructing events with two tau leptons, where missing energy from neutrinos drastically degrade mass resolu-

tion. More details of his research are presented in the next few pages.

References

[1] F. Englert and R. Brout, Phys. Rev. Lett. 13, 321 (1964); Peter W. Higgs, Phys. Rev. Lett. 13, 508 (1964).

[2] ATLAS Collaboration, Phys. Lett. B716 (2012) 1-29; CMS Collaboration, Phys. Lett. B716 (2012) 30-61.

[3] S.L. Glashow, J. Iliopoulos and L. Maiani, Phys. Rev. D2 (1970) 1285-1292.

[4] Andrew G. Cohen, Proceedings of the 29th SLAC Summer Institute on Particle Physics (2001).

[5] LHCb Collaboration, Phys. Rev. Lett. 110, 221601 (2013).

[6] BaBar Collaboration, Phys. Rev. Lett. 109, 101802 (2012); Belle Collaboration, arXiv:1904.08794; LHCb Collaboration, Phys. Rev. D 97, 072013 (2018).

[7] LHCb Collaboration, Phys. Rev. Lett. 122, 191801 (2019); JHEP 08 (2017) 055; Belle Collaboration, Phys. Rev. Lett. 103, 171801 (2009); arXiv:1904.02440; BaBar Collaboration, Phys. Rev. D 86, 032012 (2012)

[8] Amhis, Yasmine Sara et al., arXiv:1909.12524, updated results and plots available at `https://hflav.web.cern.ch/`

Part IV

Hadronic Physics

session chaired by Maxime GUILBAUD

Measurement of an excess in the yield of J/ψ at very low p_{T} in Pb–Pb collisions with ALICE

Ophélie Bugnon

Subatech Nantes

Abstract — In heavy-ion collisions, quarkonia provide a unique probe to study the properties of quark-gluon plasma so their production is widely studied by the ALICE collaboration. In 2015, an excess in the yield of J/ψ at very low transverse momentum ($p_{\mathrm{T}} < 0.3$ GeV/c) in the forward rapidity region ($2.5 < y < 4$) in peripheral Pb–Pb collisions at $\sqrt{s_{\mathrm{NN}}} = 2.76$ TeV was reported for the first time. The coherent photoproduction was proposed as the potential underlying physics mechanism. This mechanism is the main responsible for low-p_{T} J/ψ production in ultra-peripheral collisions but was never observed in more central collisions that are dominated by hadronic interactions. The coherent photoproduction of vector mesons in ultra-peripheral collisions and the analysis performed on peripheral Pb–Pb collisions at $\sqrt{s_{\mathrm{NN}}} = 2.76$ TeV will be presented. We will discuss the new theoretical motivations assuming that the coherent photoproduction is at the origin of the excess and the new experimental measurements that can be accessed with the larger data sample from Pb–Pb collisions at $\sqrt{s_{\mathrm{NN}}} = 5.02$ TeV.

1 Introduction

In extreme conditions of energy density, the Quantum Chromodynamic (QCD) predicts a new deconfined state of partonic matter where quarks and gluons can freely evolve, the Quark-Gluon Plasma (QGP). Since the last two decades, ultra-relativistic heavy-ion collisions (HIC) at the CERN Large Hadron Collider (LHC) and the BNL Relativistic Heavy Ion Collider (RHIC) aim at creating the QGP.

The QGP properties are not directly accessible due to its very small lifetime ($\tau \sim 10$ fm/c). Experimentally, it requires observables that carry information on the medium properties even after the end of the deconfined phase. The production of quarkonia, charm and anti-charm ($c\bar{c}$) and beauty anti-beauty ($b\bar{b}$) bound states, was proposed as a unique probe of the QGP. Due to their large mass, heavy quarks are expected to be produced at the initial stages of the collision and experience the whole evolution of the hot QCD medium.

It was predicted that in presence of a strongly interacting medium, the formation of charmonia is expected to be partially prevented by the color-charge screening mechanism. This screening will affect the various quarkonia states at different temperatures since they have different binding energy. Thus, the sequential suppression of charmonium states was suggested to be used as a temperature probe for the QGP [1]. At the same time, other mechanisms affect the charmonium production in presence of the QGP. In particular, a charmonium enhancement occurs during or at the end of the deconfined phase due to the recombination of initially uncorrelated c and $\bar{c}$ quarks [2, 3]. The recombination probability is expected to increase with the charm density and thus with the collision energy and the centrality of the collision. The quarkonium production in heavy-ion collision can also be affected by effects unrelated with the QGP formation. Indeed, a free proton will act differently as a proton inside an nucleus. Such effects, known as cold nuclear matter (CNM) effects can be experimentally studied in proton-lead (p–Pb) collisions [4]. To conclude, the study of the QGP properties requires many probes in different collisions systems to understand the various production mechanisms.

The ALICE collaboration reported an excess in the yield of J/ψ (the charmonia vector state with the lower mass) at very low transverse momentum in Pb–Pb collisions at $\sqrt{s_{\mathrm{NN}}} = 2.76$ TeV [5]. This observation added a complication to the physics interpretation of J/ψ production in Pb-Pb collisions. The most plausible candidate as the underlying mechanism is the coherent photoproduction of J/ψ. This mechanism is well known in ultra-peripheral HIC, but it was not foreseen in peripheral events that are dominated by hadronic interactions. A detailed study of this photoproduction in peripheral collisions is necessary, as it constitute a background for the QGP study. On the other hand, the phenomenon is interesting on its own since it opens more fundamental questions on how the coherence with an entire nucleus can survive in collisions with nuclear overlap assuming that coherent photoproduction of J/ψ is at the origin of the excess. The second part of this article is dedicated to a description of vector meson photoproduction in UPC. This will be followed by a presentation of the analysis steps and a brief description of the different ALICE detectors used in the analysis. Finally, the results from Pb–Pb collisions at $\sqrt{s_{\mathrm{NN}}} = 2.76$ TeV will be discussed since no public results at $\sqrt{s_{\mathrm{NN}}} = 5.02$ TeV are currently available. Nevertheless, some expectations and new outlooks for Pb–Pb collisions at $\sqrt{s_{\mathrm{NN}}} = 5.02$ TeV will be mentioned.

2 Vector meson photoproduction in heavy ion collisions

The coherent photoproduction is the main production mechanism of vector mesons in ultra-peripheral collisions (UPC). These collisions are characterized by an impact parameter larger than the sum of the radii of the two nuclei ($b > R_1 + R_2$) and thus hadronic interactions are strongly suppressed. The intense electromagnetic field of ultra-relativistic heavy ions can be treated by the Weiszäcker-Williams approximation [6, 7] as a virtual-photon flux proportional the the square of the nuclear charge (Z^2) and the charge distribution. The photoproduction cross section is the product of the photon flux $n_\gamma(\pm y, b)$ described by the QED and a photonuclear cross section $\sigma_{\gamma A}(\pm y)$ described by the QCD. The virtual-photon emitted by one nucleus fluctuates into a quark anti-quark pair that will scatter off the second nucleus to emerge as a vector meson. Treated at Leading-Order (LO) perturbative QCD (pQCD), this process implies at least two gluons in a singlet color state [8]. Therefore, the $\sigma_{\gamma A}$ should be proportional to the square of the gluon density in the nucleus at a value of Bjorken-x with $x(\pm y) = (m_{\mathrm{J}/\psi}/\sqrt{s_{\mathrm{NN}}})exp(\pm y)$, $m_{\mathrm{J}/\psi}$ being the J/ψ mass.

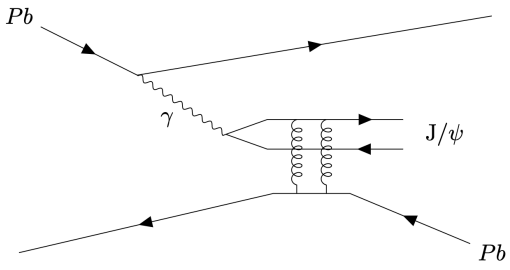

Figure 1: Feynman diagram for vector meson photoproduction at leading order.

In A–A collisions, the total cross section is a combination of two contributions, with one nucleus emitting the photon and the other that acts as a gluon source. Consequently, two values of Bjorken-x are probed covering from $x = 10^{-2}$ to $x = 10^{-5}$ at LHC energies. In this region, a CNM effect called gluon saturation modifies the gluon distribution in the initial state in A–A collisions [9].

Experimentally, the photoproduction has a clear signature of an exclusive vector meson with very low p_{T} such as $\langle p_{\mathrm{T}} \rangle < 1/R_{\mathrm{nucleus}}$. Figure 2 shows the latest results of the p_{T} distribution for opposite sign dimuons in ultra-peripheral Pb–Pb collisions at $\sqrt{s_{\mathrm{NN}}} = 5.02$ TeV measured with ALICE around the J/ψ mass [10]. We should make a distinction between the coherent and the incoherent photoproduction of J/ψ. In the first case, the photon interacts coherently with the gluon field of the entire nucleus. The resulting J/ψ transverse momentum is $\langle p_{\mathrm{T}} \rangle \simeq 60$ MeV/c and the target nucleus doesn't break up. In the second case, the photon interacts to a single nucleon inside the nucleus. The coherence condition leads to a higher $\langle p_{\mathrm{T}} \rangle \simeq 500$ MeV/c. Other production mechanisms contribute to low p_{T} dimuons in UPC collisions as the J/ψ from the decay of photoproduced ψ(2S) and the electromagnetic continuum process $\gamma\gamma \to \mu^+\mu^-$.

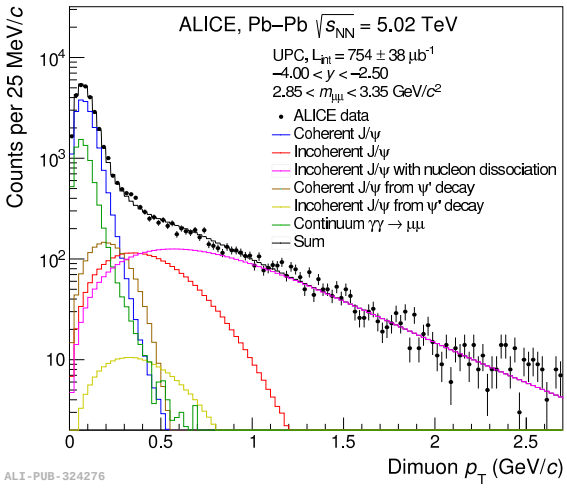

Figure 2: Transverse momentum distribution of OS dimuons for $2.85 < m_{\mu\mu} < 3.35$ GeV/c^2 and $-4 < y < -2.5$ in UPC Pb–Pb collisions at $\sqrt{s_{\mathrm{NN}}} = 5.02$ TeV [10].

3 Experimental apparatus and data sample

In the ALICE experiment [11, 12], quarkonia are reconstructed in their dimuon decay channel with the muon spectrometer located at forward rapidity. The muon spectrometer identifies, reconstructs and triggers muon tracks in the pseudo-rapidity range $-2.5 < \eta < -4$ in full azimuth. The tracking system consists of 10 plane of multi-wire proportional chambers, arranged two-by-two in five stations, the third of which is embedded inside a dipole magnet to measure the muon momentum. The trigger system is made up of two stations and selects events with muons above a programmable threshold. Finally, the spectrometer comprises several absorbers that filter out muons from the decay of light particles and hadrons as well as particles from beam-gas interactions. The vertex reconstruction is performed with the Silicon Pixel Detector (SPD), the innermost layer of the Inner Tracking System (ITS). The V0 detectors, two arrays of scintillator counters located on both sides of the interaction point, are used to measure the luminosity and the centrality of the collision. Events are classified as a percentage of the total inelastic hadronic cross section which is obtained with predictions from the Glauber model fit to the signal amplitude in the V0 detectors. The centrality goes from 0% for central collisions to 90% for the most peripheral ones. They also provide a Minimum Bias (MB) trigger, defined by the coincidence of signals in the two V0 detectors.

The presented analysis exploits data collected in

2011 in Pb–Pb collisions at $\sqrt{s_{\rm NN}} = 2.76$ TeV. Only events with two opposite-sign (OS) muons, each with a $p_{\rm T} > 1\,{\rm GeV}/c$, in coincidence with a MB trigger are selected. The data sample corresponds to an integrated luminosity $\mathcal{L}_{\rm int} \approx 70\ \mu{\rm b}^{-1}$.

4 Analysis and results

J/ψ candidates are obtained by combining all pairs of OS muon tracks in the muon spectrometer acceptance. The figure 8 shows the transverse momentum distribution of OS dimuons around the J/ψ mass ($2.8 < m_{\mu\mu} < 3.4$ GeV/c^2) in the most peripheral events (70-90%) before background subtraction. It shows a large excess at very low $p_{\rm T}$ with a shape similar to the one observed for coherent photoproduction in UPC. The red line represents J/ψ from coherent photoproduction in Pb–Pb UPC obtained with the STARLIGHT Monte-Carlo generator [13].

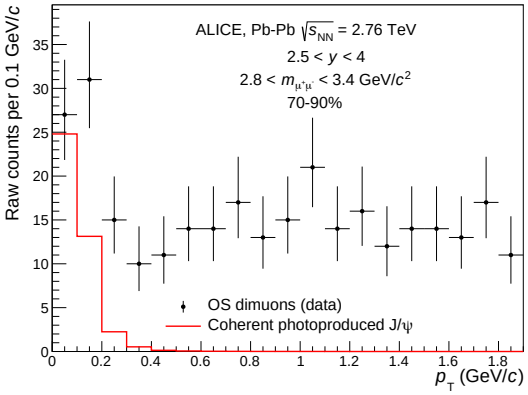

Figure 3: Transverse momentum distribution of OS dimuons for $2.85 < m_{\mu\mu} < 3.35$ GeV/c^2 and $-4 < y < -2.5$ in peripheral Pb–Pb collisions at $\sqrt{s_{\rm NN}} = 2.76$ TeV and coherently photoproduced J/ψ calculations performed with STARLIGHT.

The raw number of J/ψ ($N_{\rm raw}^{\rm J/\psi}$) is extracted by fitting the OS dimuons invariant mass distribution. Two functions with different sets of tail parameters are used to describe the signal. These functions comprise a Gaussian core with power law tails that take into account different detector effects [14]. The signal is extracted in three $p_{\rm T}$ ranges : $0-0.3$, $0.3-1$ and $1-8$ GeV/c where the coherent photoproduction, the incoherent photoproduction and the hadroproduction are dominant, respectively. Additionally, the analysis is performed in five centrality classes (0-10%, 10-30%, 30-50%, 50-70% and 70-90%) to test the centrality dependence of the cross section. The top (bottom) panel of figure 4 shows the signal extraction for OS dimuons with $p_{\rm T} < 0.3$ GeV/c in the 0-10% (70-90%) centrality class.

The next step in the analysis consists in estimating the number of J/ψ from hadroproduction ($N_{\rm AA}^{h\ {\rm J/\psi}}$) and subtracting it from the raw number of J/ψ. This quantity is obtained by integrating the following parametrisation for $p_{\rm T} < 0.3$ GeV/c in each centrality class.

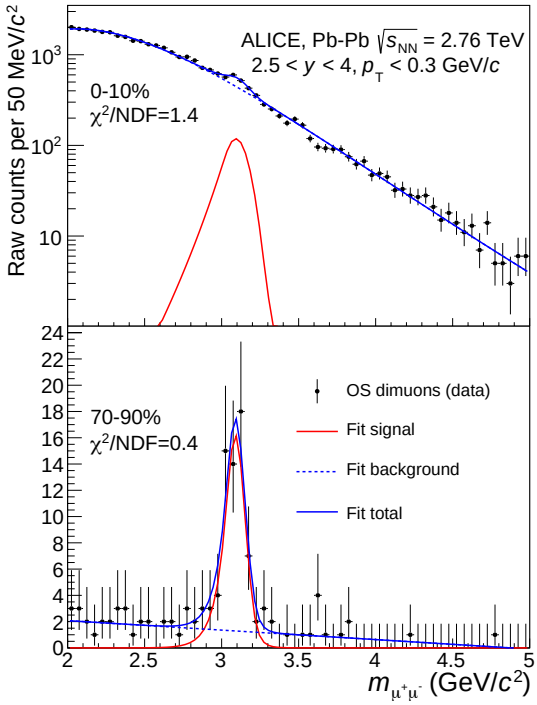

Figure 4: Invariant mass distribution of OS dimuons for $p_{\rm T} < 0.3$ GeV/c and $-4 < y < -2.5$ in peripheral Pb–Pb collisions at $\sqrt{s_{\rm NN}} = 2.76$ TeV. The top (bottom) panel shows the distribution in the 0-10% (70-90%) centrality class.

$$\frac{{\rm d}N_{\rm AA}^{\rm h\ J/\psi}}{{\rm d}p_{\rm T}} = \mathcal{N} \times \frac{{\rm d}\sigma_{\rm pp}^{\rm h\ J/\psi}}{{\rm d}p_{\rm T}} \times R_{\rm AA}^{\rm h\ J/\psi} \times (\mathcal{A} \times \epsilon)_{\rm AA}^{\rm h\ J/\psi}$$

The first term is a normalization factor corresponding to the number of J/ψ in the $p_{\rm T}$ range $1-8$ GeV/c where the hadronic component is expected to be dominant. The second term is the $p_{\rm T}$ differential cross section measured by ALICE in pp collisions at the same energy [15]. The third term is a parametrization of the J/ψ nuclear modification factor from ALICE measurement in Pb–Pb collisions at $\sqrt{s_{\rm NN}} = 2.76$ TeV [16, 17]. Finally, the last term is the hadronic J/ψ acceptance times efficiency obtained via MC simulations.

After subtracting the hadronic number of J/ψ to obtain the excess of J/ψ, one has to correct it with the fractions of incoherently produced J/ψ ($f_{\rm coh}^{\rm J/\psi}$) and J/ψ from the decay of coherently produced ψ' ($f_{\rm incoh}^{\psi'}$) to get the number of coherently photoproduced J/ψ ($N_{\rm coh}^{\rm J/\psi}$). These quantities are obtained from the UPC analysis at the same energy [18]. As a last step, the J/ψ coherent photoproduction cross section is computed using the following formula :

$$\frac{{\rm d}\sigma_{\rm coh}^{\rm J/\psi}}{{\rm d}p_{\rm T}} = \frac{N_{\rm coh}^{\rm J/\psi}}{BR_{\rm J/\psi\to\mu^+\mu^-} \times (\mathcal{A} \times \epsilon)_{\rm coh}^{\rm J/\psi} \times \mathcal{L}_{\rm int} \times \Delta y}$$

Where $BR = 5.961 \pm 0.033$ [19] is the branching ratio

Centrality (%)	0–10	10–30	30–50	50–70	70–90
$\frac{\mathrm{d}\sigma^{\mathrm{J}/\psi}_{\mathrm{coh}}}{\mathrm{d}p_{\mathrm{T}}}$ (μb)	< 318	< 290	$73 \pm 44^{+26}_{-27} \pm 10$	$58 \pm 16^{+8}_{-10} \pm 8$	$59 \pm 11^{+7}_{-10} \pm 8$

Table 1: J/ψ coherent photoproduction cross section in Pb–Pb collisions at $\sqrt{s_{\mathrm{NN}}} = 2.76$ TeV with their statistical, uncorrelated and correlated systematic uncertainties, respectively. For the most central classes, an upper limit at 95% CL on the cross section is given. More details on the uncertainties evaluation can be found in [5].

of J/ψ decaying into dimuon; $(\mathcal{A} \times \epsilon)_{\mathrm{coh}}$ is the coherent J/ψ acceptance times efficiency, which differs from the hadronic one due to the assumed transverse polarization of the photoproduced J/ψ; $\mathcal{L}_{\mathrm{int}}$ is the integrated luminosity and Δy is the width of the rapidity range in order to be compared to other experiment results. Results of the cross section as a function of the centrality are reported table 1.

5 Conclusion and outlook

ALICE measured the p_{T}-differential J/ψ production down to $p_{\mathrm{T}} = 0$. The results show an excess at very low p_{T} ($p_{\mathrm{T}} < 0.3$ GeV/c), that was quantified with a significance of 5.4σ and 3.4σ in the 70–90% and 50-70% centrality class, respectively. The coherent photoproduction of J/ψ is a plausible explanation but since it was not predicted in peripheral hadronic Pb–Pb collisions, no theoretical calculations existed at the time of the measurement.

The next step is to perform the analysis on the new and larger data sample from Pb–Pb collisions at $\sqrt{s_{\mathrm{NN}}} = 5.02$ TeV. The cross section is expected to increases by a factor ~ 2.5 with respect to $\sqrt{s_{\mathrm{NN}}} = 2.76$ TeV. With a large enough data sample (30 times larger than 2.76 TeV), we could study the J/ψ $\langle p_{\mathrm{T}} \rangle$ as a function of the centrality and extend the analysis to more central collisions. Since the coherence leads to a $\langle p_{\mathrm{T}} \rangle < 1/R_{\mathrm{nucleus}}$, the $\langle p_{\mathrm{T}} \rangle$ should stay stable if the coherence occurs with the entire nucleus whereas it is expected to increase in more central collisions if only spectators play a part in the process. In addition, if it is confirmed that the coherent photoproduction is at the origin of the excess, a differential study in rapidity could help extracting the nuclear photo cross section $\sigma_{\gamma A}(\pm y)$ and probing the gluonic content of the nucleus at very low Bjorken-x. Finally, it is worth noting that the vector mesons photoproduction, which occurs at the early stages of the collision, could become a new probe of the QGP, provided that a solid theoretical model is developed for its description.

References

[1] Matsui T. and Satz H., "J/ψ Suppression by Quark-Gluon Plasma Formation", Phys. Lett. B178 (1986) 416

[2] Thews R. L., Schroedter M. and Rafelski J., "Enhanced J/ψ production in deconfined quark matter", Phys. Rev. C63 (2001) 054905

[3] Braun-Munzinger P. and Stachel J., "(Non)thermal aspects of charmonium production and a new look at J/ψ suppression", Phys. Lett. B490 (2000) 196

[4] ALICE Collaboration, Acharya S. et al, "Inclusive J/ψ production at forward and backward rapidity in p–Pb collisions at $\sqrt{s_{\mathrm{NN}}} = 8.16$ TeV", JHEP07 (2018) 160

[5] ALICE Collaboration, Adam J., "Measurement of an excess in the yield of J/ψ at very low p_{T} in Pb-Pb collisions at $\sqrt{s_{\mathrm{NN}}} = 2.76$ TeV", Phys. Rev. Lett. 116 (2016) 22

[6] von Weizsacker C. F., "Radiation emitted in collisions of very fast electrons", Z. Phys. 88 (1934) 612

[7] Williams E. J., "Applications of the Method of Impact Parameter in Collisions", Proceedings of the Royal Society of London Serie A, 139 (1933) 163

[8] Ivanov I. P., Nikolaev N. N. and Savin A. A., "Diffractive vector meson production at HERA: From soft to hard QCD", Phys. Part. Nucl. 37 (2006) 1

[9] Contreras J. G., "Gluon shadowing at small x from coherent J/ψ photoproduction data at energies available at the CERN Large Hadron Collider", Phys. Rev. C96 (2017) 015203

[10] ALICE Collaboration, Acharya S. et al, "Coherent J/ψ photoproduction at forward rapidity in ultra-peripheral Pb-Pb collisions at $\sqrt{s_{\mathrm{NN}}} = 5.02$ TeV", Phys. Lett. B798 (2019) 134926

[11] ALICE Collaboration, Aamodt K. et al, "The ALICE experiment at the CERN LHC", JINST 3 (2008) S08002

[12] ALICE Collaboration, Abelev B. et al, "Performance of the ALICE Experiment at the CERN LHC", Int. J. Mod. Phys. A29 (2014) 1430044

[13] Klein S.R., Nystrand J., Seger J., Gorbunov Y. and Butterworth J., "STARlight: A Monte Carlo simulation program for ultra-peripheral collisions of relativistic ions", Comput. Phys. Commun. 212 (2017) 258

[14] ALICE collaboration, "Quarkonium signal extraction in ALICE", ALICE-PUBLIC-2015-006

[15] ALICE Collaboration, Abelev, B. et al, "Inclusive J/ψ production in pp collisions at $\sqrt{s_{\rm NN}}$ = 2.76 TeV", Phys. Lett. B718 (2012) 295

[16] ALICE Collaboration, Abelev, B. et al, "Centrality, rapidity and transverse momentum dependence of J/ψ suppression in Pb–Pb collisions at $\sqrt{s_{\rm NN}}$ = 2.76 TeV", Phys. Lett. B734 (2014) 314

[17] ALICE Collaboration, Adam, J. et al, "Differential studies of inclusive J/ψ and ψ(2S) production at forward rapidity in Pb–Pb collisions at $\sqrt{s_{\rm NN}}$ = 2.76 TeV", JHEP 05 (2016) 179

[18] ALICE Collaboration, Abelev B. et al, "Coherent J/ψ photoproduction in ultra-peripheral Pb–Pb collisions at $\sqrt{s_{\rm NN}}$ = 2.76 TeV", Phys. Lett. B718 (2013) 1273

[19] Particle Data Group, Tanabashi M. et al, "Review of Particle Physics", Phys. Rev. D98 (2018) 3

Quarkonium anisotropic flow in ultra-relativistic heavy-ions collisions

Robin Caron

Département de Physique Nucléaire (CEA/Irfu), Université Paris-Saclay

Abstract — The ALICE experiment at LHC studies, through ultra-relativistic heavy-ion collisions, a deconfined state of matter, the QuarkâGluon Plasma (QGP). This state raises many questions about the mechanisms of strong interaction and the cohesion of matter. The QGP is an extremely hot and dense state that behaves as a nearly ideal, strongly interacting fluid (and it can represents the universe at the first microseconds). According to Quantum Chromodynamics, the theory that describes the strong interaction, the heavy quark bound pair (quarkonium) represents an ideal probe to study such a state. The collective hydrodynamic expansion in the early stage of the fireball is accessible by the measurement of the azimuthal anisotropy in the particle production. Thus, the measurement of quarkonium azimuthal anisotropy gives information about the degree of thermalization of heavy quarks and is a powerful observable to study the emergence of quarkonium suppression and regeneration processes inside the QGP. We will present the measurement of anisotropic flow for the quarkonium states and in Pb−Pb collisions at a centre-of-mass energy per nucleon pair of $\sqrt{s_{\mathrm{NN}}} = 5.02$ TeV.

1 Introduction

At the extreme energy densities and temperatures produced in ultra-relativistic heavy-ion collisions, hadronic matter undergoes a transition into a state of deconfined quarks and gluons, the QuarkâGluon Plasma (QGP). This state behaves like a nearly ideal and strongly interacting fluid, in the sense that its shear viscosity to entropy density ratio approaches the smallest possible values [1]. The spatial initial-state anisotropy of the overlap region of the two colliding nuclei is transformed by the fluid pressure gradients into a momentum anisotropy of the produced final-state particles [15]. This effect corresponds to the hydrodynamic anisotropic flow [2]. It is quantified in terms of the harmonic coefficients of the Fourier decomposition of the azimuthal particle distribution in the final state:

$$\frac{\mathrm{d}N}{\mathrm{d}\varphi} \propto 1 + 2\sum_{n=1}^{+\infty} v_n \cos\left[n(\varphi - \Psi_n)\right] \qquad (1)$$

where Ψ_n represents the symmetry plane angle which gives an estimation of the reaction plane, spanned by the beam axis z and the distance separating the two nuclei, the impact parameter b. In particular, in high energy heavy-ions collision the two colliding objects can be seen like two flat disks, due to Lorentz contraction. Then, the centrality variable can be define simply by the impact parameter value. The central collisions are associated with a b close to zero and the non-central ones correspond to a significant b compare to the diameter of the nuclei. Therefore, centrality is expressed in terms of percentage from 0−10% for central collisions, to 60−90% for peripheral ones.

The dominant coefficient of the Fourier series in non-central collisions is the second harmonic, denoted by and called elliptic flow, since this coefficient directly arises from the ellipsoid shape of energy density in the transverse plane. Moreover, it is approximately proportional to the eccentricity ϵ_2 of the initial collision geometry [3] and related to the response of the system associated to κ_n since the hydrodynamic calculations show (only for $n = 2, 3$):

$$v_n \approx \kappa_n \epsilon_n \qquad (2)$$

Charm and beauty quarks are important probes of the QGP. They are created predominantly in hard-scattering processes at the early collision stage and therefore experience the entire evolution of the QGP through interactions with its constituents. Thus, the measurement of bound states of heavy quarks − quarkonia (charmonia $c\bar{c}$ or bottomonia $b\bar{b}$) − is expected to provide sensitive information of the strongly interacting medium formed in the early stages of the collision [4].

The heavy quarkâantiquark pair of a quarkonium state are bound together by strong interaction and can be see in a classical view as orbiting at a relative distance of about 0.5 fm and 0.28 fm for the ground states and $\Upsilon(1S)$, respectively [5]. All the excited states have larger sizes and smaller binding energies. However, if the quarkonium were to be placed inside a QGP, then its binding could be screened by the large number of color charges (quarks and gluons), that make up the QGP surrounding or flowing around it freely. Therefore, the binding of the quark-antiquark pair become weaker to the point that it may dissociate â it is "suppressed". This scenario of suppression by color screening was proposed as a signature of the QGP [5]. In addition, the theory has shown that the probability of dissociation depends on the temperature of the QGP, which lead to the naive picture of the quarkonium suppression

as a way to place a "thermometer" in the medium itself.

This suppression mechanism has long been a strong interest in quarkonium production studies at the SPS and RHIC energies, as it was demonstrated for the J/ψ [8]. However, at LHC energies the energy density is larger and the number of $c\bar{c}$ pairs is much higher, both leading to the emergence of another production mechanism, regeneration by recombination of individual charm quarks from the medium. Through a coalescence behavior or by statistical recombination [16, 6], additional can be formed in the later stage of the collision. This regeneration effect is more relevant for charmonium than for bottomonium states due to smaller number of $b\bar{b}$ pairs than $c\bar{c}$ pairs created in the collision. These two production mechanisms (suppression and regeneration) have an opposing behavior as a function of the collision energy, their contributions need to be judiciously considered in the theoretical models to reproduce the experimental observations.

As heavy quarks couple to the expanding QGP, the same behavior than for light particles could be observed in the quarkonium azimuthal particle distribution. Measuring the flow of quarkonia gives directly the access to the deconfinement between $c\bar{c}$ pair since the c quark should initiate a thermalization process to be able to acquire flow from the medium [16]. The observed significant D-meson in nucleusânucleus collisions suggests that the charm quarks participate in the collective anisotropic flow of the QGP fluid [10, 11]. In this case, the light-flavor quarks also contribute to the D-meson flow, thus we can not draw firm conclusions about charm quark flow.

Within the regeneration scenario, the elliptic flow of charmonia is directly inherited from the velocity field of the individual charm quarks within the medium and results in a positive coefficient, mainly at low-p_{T}. Recent ALICE measurement [9] favors this scenario of regeneration and the idea of charm quark flow. However, the $\Upsilon(1S)$ state − corresponding to the most tightly bound state of $b\bar{b}$ pairs − has larger mass, higher binding energies and smaller radius. Dissociate such a state need a very high temperature in the medium. Hence, the $b\bar{b}$ pairs should recombine at larger temperature and thus at early stage in the lifetime of the expanding QGP, where the momentum anisotropy is much smaller than at the end of the expansion [17].

The suppression of $\Upsilon(1S)$ has been measured [12] and found to be equivalent to that of [13]. At the difference of $c\bar{c}$ pair, as we say previously the $b\bar{b}$ pair recombination is expected to be negligible and thus the elliptic flow of $\Upsilon(1S)$ should be much smaller than for the case. Furthermore, the measurement of $\Upsilon(1S)$ in the final state and their v_2 will give essential information of their production mechanisms evolved in Pb−Pb collisions at the LHC and it will be presented, additionally with the J/ψ, in the following parts.

2 Experimental apparatus

Quarkonia encode the information throughout the entire evolution of the medium and finally decay into different channel of particles. In this paper, quarkonia are reconstructed in the forward rapidity region using the dimuon decay channel, where J/ψ or Υ states will decay into $\mu^+\mu^-$.

The muon spectrometer of the ALICE experiment, which covers the pseudo-rapidity range $-4 < \eta < -2.5$, is used to reconstruct muon tracks. It consists of a front absorber followed by five tracking stations with the third station placed inside a dipole magnet. Two trigger stations located downstream of an iron wall complete the spectrometer. The Silicon Pixel Detector (SPD) consists of two cylindrical layers covering the full azimuthal angle and $|\eta| < 2.0$ and $|\eta| < 1.4$, respectively. The SPD is employed to determine the position of the primary vertex and to reconstruct tracklets (track segments formed by the clusters in the two SPD layers and the primary vertex). Two arrays of 32 scintillator counters each, covering $2.8 < \eta < 5.1$ (V0A) and $-3.7 < \eta < 1.7$ (V0C), are used for triggering, the event selection and the determination of the collision centrality and the event flow vector Q_n (3).

The results presented were obtained using Pb−Pb collisions at 5.02 TeV in the ALICE experiment during the full Run 2 at LHC. The total data sample analyzed correspond to a integrated luminosity approximately equivalent to 0.75 nb^{-1}. The muons are selected using standard cuts as [12, 13]. The dimuons are reconstructed in the acceptance of the muon spectrometer ($2.5 < y < 4.0$).

3 Analysis details

First, there is a need to characterize the Pb−Pb collision event. Non-uniform acceptance effects of the detectors are corrected through an equalization procedure which consists of multiple corrections of the Q_n vector in order to have a flat ψ_n distribution [7]. The resolution on the is calculated with the three sub-event technique [3] consisting in the reconstruction of the event-plane from different detectors (SPD, V0A, V0C) having pseudo-rapidity gaps between each of them. The event-plane azimuth is defined as the azimuthal angle of the flow vector Q_n. This vector is constructed by summing over all unitary vectors of charged particles (tracklets) in an event, for the harmonic n :

$$Q_n = \sum_{j=1}^{N} \cos(n\varphi_j) + i\sin(n\varphi_j) = |Q_n| e^{in\Psi_n} \qquad (3)$$

where φ_j is the azimuthal angle of the particle j, N is the number of charged particles in an event (corresponding to the multiplicity).

Secondly, the and dimuon candidates need to be reconstructed. The raw number of reconstructed quarko-

nia were obtained by fitting the dimuon mass spectra with a superposition of signal and background functions. Then, the elliptic flow of each dimuon can be estimated using the azimuthal angle of the pair φ and the angle Ψ_n as the following the formula

$$v_n = \langle \cos[n(\varphi - \Psi_n)] \rangle \tag{4}$$

which can be derived from (1) solely by using the orthogonality properties of trigonometric functions. The brackets $\langle ... \rangle$ denote the average over all events and all particles. In the absence of fluctuations all symmetry planes Ψ_n are identical and equal to the hypothetical reaction plane. This plane is estimated by computing an event plane angle Ψ_n calculated from the Q_n flow vector. An example of the v_2 extraction is illustrated in Figure 1, the extraction of v_2 is done using the same method.

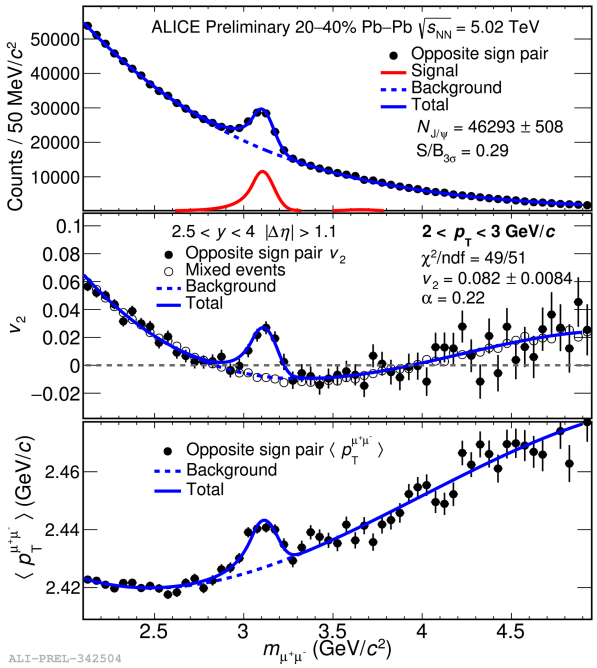

Figure 1: (Top) signal extraction using the dimuon invariant mass spectrum. (Middle) Total dimuon as function of $m_{\mu\mu}$ and the corresponding fitting functions as the formula (5), each black circle corresponds to the average value of all dimuons in one bin of $m_{\mu\mu}$. (Lower) Extraction of the $\langle p_T \rangle^{J/\psi}$ corresponding to the fit on total dimuon $\langle p_T \rangle$.

After computing the mean over all dimuon pairs in each bin of $m_{\mu\mu}$ as the formula (4), a total fit on dimuon v_n can be realized using the following formula

$$v_n = v_n^{bkg}(1-\alpha) + v_n^{sig}\alpha \tag{5}$$

where v_n^{sig} is extracted by fitting the total dimuon v_n, the signal fraction $\alpha = \frac{S}{S+B}$ extracted from the invariant mass distribution fit and v_n^{bkg} is parametrized by standard functions to reproduce the shape of the background dimuon flow.

4 Results

This section will present the results of and in Pb−Pb collisions at 5.02 TeV. The muon spectrometer can not separate the coming from primary or secondary vertex corresponding to prompts or non-prompts (decaying from B mesons). The of inclusive is measured as function of p_T and it is compared to those of light flavor particles pions ($\pi^{\pm}$), protons ($p + \bar{p}$), and ϕ meson in the Figure 2. This measurement has been done using non-central collisions corresponding to 20−40% where the number of $c\bar{c}$ pairs is enough to produce regenerated and the is expected to be significant due to the collision geometry. We can see that the elliptic flow has clearly a different behavior compared to those of light particles.

Light flavor particles have long been studied and their properties in heavy ions collisions are well known. QGP is composed principally by light flavors u, d and also s quarks, which participate to the hydrodynamic flow at low-p_T and their motions at high-p_T is well described by energy loss mechanisms, radiative (by emitted gluons) or collisional (collisions with other partons). The central barrel of ALICE detector has a excellent particle identification (PID) which gives access to properties of many soft particles produced at the chemical freeze out. When temperature decrease below T_C, all deconfined partons will produced many hadrons species. Since, they are composed from light particles at the phase boundary, this hadrons inherit directly their from the collective medium expansion. Also, they respect the Number of Constituent Quark (NCQ) scaling [19] at intermediate-p_T.

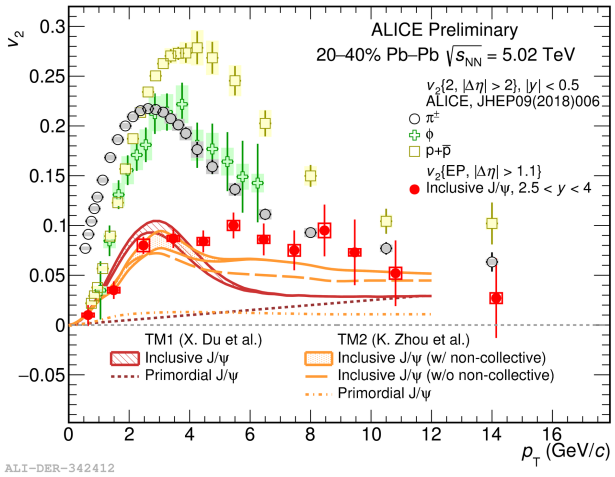

Figure 2: Inclusive as function of transverse momentum p_T and comparison to those of light flavor charged particles (pions, protons, ϕ meson) for non-central Pb−Pb collisions corresponding to 20−40% centrality class.

Additional comparison to current Transport Models (based on a Boltzmann equation) is shown. Both models assume a very fast equilibrium ($\Delta\tau \approx 0.5$ fm/c) of the collision zone. A good agreement with both TM1

[16] and TM2 [18] at low-p_{T} confirms the scenario of regeneration, since both models include a large from the recombination of uncorrelated c and $\bar{c}$ pair. Nevertheless, at high p_{T} the models underestimate the in particular for TM1 where the contribution from primordial (explained by path-length dependent suppression where particle crosses longer distances out of plane than in-plane) does not reproduce such large v_2.

The TM2 includes other non-collective mechanisms corresponding to a strong initial magnetic field effect create by electric charge asymmetry between proton spectators in the two nuclei, only possible for non-central collision. This measurement confirms the importance of regeneration process as an additional production mechanism in heavy-ion collisions. Also, at high-p_{T}, the of light flavor and heavy flavor particles seems to converge to same value which can be interpreted as universal partons energy loss mechanisms.

The first measurement of elliptic flow as function of p_{T} is presented in Figure 3, it correspond to non-central Pb−Pb collisions for 5−60% centrality class and using the dimuon decay channel at forward rapidity. The comparison with in exactly the same kinematics region is also shown. The central and peripheral collisions (corresponding to 0−5% and 60−90% centrality intervals) are excluded due to a lower event plane resolution. The measured is consistent with zero and with the small positive values predicted by transport models within uncertainties. In addition, the recombination of (partially) thermalized bottom quarks gives a negligible contribution to the coefficient due to the small number of available b quarks.

The beauty quark has larger mass compared to charm quark but much heavier compare to light flavor particles. The models predicts a very low for the state, since they implement a large binding energy and a very small radius. They use a temperature dependent binding energy and the medium effects are taken from lattice-QCD, based on equation of state for bulk evolution. Taking into account this effects, the dissociation of the should only limited to the early stage of QGP evolution where temperature is the largest, since temperature decreases very quickly. In this sense, the can only have a very small at low p_{T}, slowly increasing for higher p_{T} due to the path-length dependence suppression.

These results, combined with earlier suppression measurements, are in agreement with a scenario in which the production in PbâPb collisions at LHC energies is dominated by dissociation limited to the early stage of the collision. While in the other case, for the there are experimental evidence of a additional regeneration component. In addition, the can be measured significantly lower than the by a factor of 2.6 σ corresponding to an integrated measurement in 5−60% centrality class and $2 < p_{\mathrm{T}} < 15$ GeV/c. In this case, the very low-p_{T} region ($p_{\mathrm{T}} < 2$ GeV/c) is excluded because the of is too small.

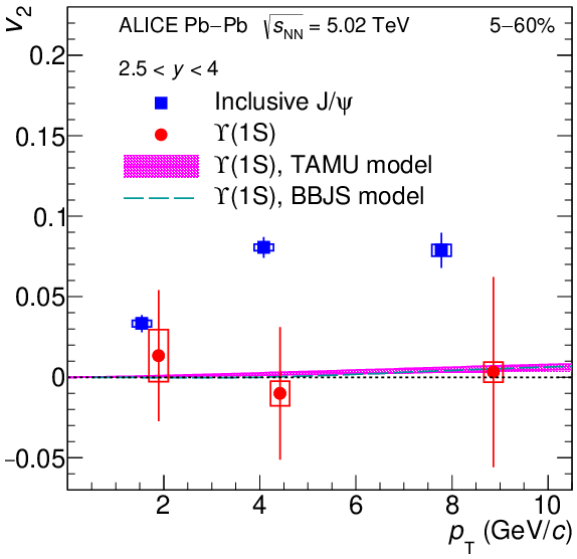

Figure 3: $\Upsilon(1S)$ as function of transverse momentum p_{T} for centrality class 5−60% and comparison to inclusive $v_2(J/\psi)$ from published 2015 data. The p_{T} ranges correspond to $0-3$, $3-6$, $6-15$ GeV/c. The major contributions for the TAMU model [17] corresponds to $\Upsilon(1S)$ generated by path length dependent suppression and the regeneration. The BBJS model [20] use a 3+1D quasi particle anisotropic escape mechanism based on a hydro-dynamical description with no recombination.

5 Conclusions

Quarkonium production is a excellent probe to study the interaction of heavy quarks with a extremely high temperature and energy density deconfined medium. The initial production of heavy quark pairs is a process well known however their eventual hadronization and when it happens compare to the equilibrium processes is not fully clear. The measurements of and elliptic flow in Pb−Pb collision give a direct access to the degree of thermalization of charm or beauty quark in the medium and thus also to the temperature of the QGP. The measurement of confirms the importance of regeneration process at low-p_{T} from uncorrelated c and $\bar{c}$ as an additional production mechanism in heavy-ion collisions at LHC energies. The behavior of at high-p_{T} reveals a convergence phenomenon from light to heavy flavor which can possibly originate from an universal parton energy loss mechanisms. This observation, coupled to the different measured centrality and p_{T} dependence of the and suppression in PbâPb collisions at the LHC can be interpreted within the models used for comparison as a sign that unlike $\Upsilon(1S)$, production has a significant regeneration component.

References

[1] P. Kovtun, D. T. Son, and A. O. Starinets, *Viscosity in strongly interacting quantum field theories from black hole physics*, `Phys. Rev. Lett. 94 (2005) 111601`

[2] P. Kovtun, D. T. Son, and A. O. Starinets, *Anisotropy as a signature of transverse collective flow*, Phys. Rev. D46 (1992) 229â245

[3] S. Voloshin and Y. Zhang, *Flow study in relativistic nuclear collisions by Fourier expansion of Azimuthal particle distributions*, Z. Phys. C70 (1996) 665â672.

[4] Andronic, A. and others, *Heavy-flavour and quarkonium production in the LHC era: from protonâproton to heavy-ion collisions*, Eur. Phys. J. C76, 107 (2016), 1506.03981

[5] T.Matsui, H.Satz, *$J\psi$ Suppression by Quark Gluon Plasma formation*, Phys. Let. B 178, 416 (1986)

[6] Braun-Munzinger, P. and Stachel, J., *(Non)thermal aspects of charmonium production and a new look at $J\psi$ suppression*, Phys. Lett. B490 196 (2000)

[7] Selyuzhenkov, Ilya and Voloshin, Sergei, *Effects of non-uniform acceptance in anisotropic flow measurement*, Phys. Rev. C77 (2008) 034904, 0707.4672

[8] STAR Collaboration, L. Adamczyk et al., *Measurement of Azimuthal Anisotropy in Au+Au Collisions at $\sqrt{s_{\rm NN}} = \mathbf{200}$ GeV*, Phys. Rev. Lett. 111 no. 5, (2013) 052301, arXiv:1212.3304)

[9] ALICE Collaboration, S. Acharya et al., *$J\psi$ elliptic flow in Pb−Pb collisions at $\sqrt{s_{\rm NN}}$ = 5.02 TeV*, Phys. Rev. Lett. 119 no. 24, (2017) 242301

[10] Sirunyan, Albert M and others, CMS Collaboration *Measurement of prompt D^0 meson azimuthal anisotropy in Pb−Pb collisions at $\sqrt{s_{NN}}$ = 5.02 TeV*, Phys. Rev. Lett. 120, 20 (2018), 1708.03497

[11] Acharya, Shreyasi and others, ALICE Collaboration *D-meson azimuthal anisotropy in midcentral Pb−Pb collisions at $\sqrt{s_{\rm NN}} = \mathbf{5.02}$ TeV*, Phys. Rev. Lett. 120, 10 (2018), 1707.01005

[12] Acharya, Shreyasi and others",ALICE Collaboration Υ *suppression at forward rapidity in Pb−Pb collisions at $\sqrt{s_{\rm NN}}$ = 5.02 TeV*, Phys. Lett. B790 (2019) 1805.04387

[13] ALICE Collaboration, J. Adam et al. *$J\psi$ suppression at forward rapidity in Pb−Pb collisions at $\sqrt{s_{\rm NN}}$ = 5.02 TeV*, Phys. Lett. B766 (2017) 212â224

[14] Andronic, A. and Braun-Munzinger, P. and Redlich, K. and Stachel, J., *Statistical hadronization of heavy quarks in ultra-relativistic nucleus-nucleus collisions*, Nucl. Phys. A789 (2007)

[15] Snellings, Raimond, *Elliptic Flow: A Brief Review*", New J. Phys. 13 (2011) 055008, 1102.3010

[16] Du, Xiaojian and Rapp, Ralf, *Sequential Regeneration of Charmonia in Heavy-Ion Collisions*, Nucl. Phys. A943 (2015) 147-158, 1504.00670

[17] Du, Xiaojian and Rapp, Ralf and He, Min, *Color screenning and regeneration of bottomonia in high-energy heavy-ion collisions*, Phys. Rev. C 96 (2017) 054901

[18] K. Zhou and al., *Medium effects on charmonium production at relativistic energies available at the CERN LHC*, Phys. Rev. C 89 (2014) 054911, 1504.00670

[19] Liang Zheng, Hui Li, Hong Qin, Qi-Ye Shou, Zhong-Bao Yin, *Investigating the NCQ scaling of elliptic flow at LHC with a multiphase transport model*, Eur. Phys. J. A (2017) 53: 124

[20] Bhaduri, Partha Pratim and Borghini, Nicolas and Jaiswal, Amaresh and Strickland, Michael *Anisotropic escape mechanism and elliptic flow of bottomonia*, arXiv (2018) 1809.06235

Probing the quark-gluon plasma with the B_c meson in CMS

Guillaume Falmagne

Laboratoire Leprince-Ringuet, École Polytechnique, CNRS/IN2P3, Institut Polytechnique de Paris, 91128, Palaiseau, France

Abstract — Studying the interaction of beauty and charm quarks with the quark-gluon plasma sheds light on the behavior of quantum chromodynamics in extreme temperature and pressure conditions. In this context, the B_c meson is an interesting and new probe, that gives new insights both on heavy quark energy loss, and on the charm recombination mechanism. These proceedings show the progress of the first study of the B_c meson in heavy ion collisions, in 2018 lead-lead (PbPb) data from CMS experiment at $\sqrt{s_{\mathrm{NN}}} = 5.02$ TeV, in the leptonic channel $B_c^+ \to J/\psi(\to \mu\mu)\mu^+\nu_\mu$. The equivalent study in 2017 proton-proton (pp) reference data at 5.02 TeV is more advanced, and used as a benchmark for the PbPb analysis. Muon acceptance studies are done to push down in transverse momentum the B_c acceptance. Multiple backgrounds are thoroughly studied to confirm the feasibility of a template fit to extract the yields in pp and PbPb collisions.

1 Motivations and principle

In the very high energy density and temperature created in heavy-ion collisions, quarks and gluons move freely in a deconfined state of matter called Quark-Gluon Plasma (QGP) [1]. Charm and beauty quarks are excellent probes of QGP formation, as they are produced in hard scatterings before the expansion of the medium, and form hadrons that decay long after its cool-down. They also interact strongly with the medium, resulting in energy loss (leading to jet quenching [2]), which probes the scattering properties of the QGP.

Energy loss might be reduced for heavier quarks, due to the dead-cone effect [3]; experimental evidence of this mass dependence is still ambiguous, because b-meson suppression is often studied via inclusive decay products, which have 'smeared' the kinematics (as for non-prompt J/ψ, from b-decays [4]). Studying the B_c meson in an exclusive decay can give an original view on this question, as it is a bound state of $\bar{b}$ and c quarks.

The most energetic lead-lead (PbPb) collisions at 5 TeV can produce up to 1000 charm quark pairs, which could lead to recombination of low transverse momentum (p_{T}) charm quarks. Many models compete to explain the J/ψ data with this effect: statistical hadronization [5], transport model [6], comovers [7], etc. Meanwhile, the B_c has a particularly low cross-section in proton-proton (pp) collisions, because two heavy quark pairs ($b\bar{b}$ and $c\bar{c}$) need to be produced. If there is significant recombination of heavy quarks produced in different hard scatterings, then the B_c might be dramatically augmented compared to pp (up to a factor of 10^{3-4} [8]). A caveat is that this concerns the total cross-section, while CMS can only measure the B_c of relatively high transverse momentum (p_{T}), where recombination is less relevant.

A measurement of the modification of the B_c meson in PbPb collisions could help understanding energy loss and hadronisation dynamics in the QGP. In this analysis, the yields are determined from pp 2017 data taken with the Compact Muon SolenoÃ¯d (CMS) experiment at the CERN Large Hadron Collider (LHC)at $\sqrt{s_{\mathrm{NN}}} = 5.02$ TeV, and from PbPb 2018 data at the same energy. The leptonic channel $B_c^+ \to J/\psi\,\mu^+\nu_\mu$ (charge conjugation is implicit throughout this text) is used because its branching fraction is about 20 times higher than the fully reconstructed hadronic channel $B_c^+ \to J/\psi\,\pi^+$ [9]. Only the three muons are reconstructed, so the measured signal should be a displaced trimuon of total charge ± 1 whose invariant mass is a broad distribution between $m_{J/\psi} + m_\mu = 3.20$ GeV and $m_{B_c} = 6.28$ GeV.

The CMS detector features a solenoid of field 3.8 T, within which a silicon tracker [11] can measure charged particles in the pseudo-rapidity range $|\eta| < 2.5$. Downstream of the magnet and calorimeters, drift tubes, cathode strip chambers, and resistive-plate chambers reconstruct and identify muons [12]. CMS is specialized in detecting muons, with its silicon tracker and muon chambers giving an excellent p_{T} resolution, muon identification, and secondary vertex reconstruction – the latter being essential because the B_c lifetime ($c\tau_{B_c} = 150\,\mu$m) is three times smaller than most b-mesons. It also collected a high luminosity (1.6 nb^{-1} in PbPb and 330 pb^{-1} in pp). However, CMS has a quite high p_{T} threshold for the muon acceptance (around 1.5 GeV in the forward region, and 3.5 GeV for central muons of $|\eta| < 1.2$), which translates into a low acceptance for signal trimuons of $p_{\mathrm{T}} \lesssim 6$ GeV.

A Boosted Decision Tree (BDT) is used to optimize the signal significance, after a basic pre-selection of the candidates. Once the yields are measured, they can be corrected by the acceptance and efficiency, obtained from BCVEGPY [10], a B_c-specific MonteCarlo (MC). The resulting cross-sections in pp and PbPb will eventually allow for the measurement of the nuclear modification factor $R_{\mathrm{PbPb}}(B_c)$ as a function of p_{T}. Prompt

and non-prompt J/ψ MC, used to study the backgrounds, are produced in a classic simulation chain.

2 Reconstruction and preselection

Muons in CMS can be reconstructed as 'tracker', i.e. a track from the inner tracker that has matching hits in the first muon station, or as 'global', which is a standalone track from the muon stations matched to a track from the tracker. Tracker muons contain more fakes, especially in PbPb data, but can be reconstructed to lower p_{T}. In this analysis, the *soft-muon* selection [12] is used for the tracker muons that are not global, and the looser *hybrid-soft-muon* selection for global muons. Selected trimuon candidates must have two global muons passing *hybrid-soft*, while the third can be only tracker if it passes the full *soft-muon* selection.

The events were selected with a dimuon trigger, with hardware-level muons in pp, but with software-level muons and very loose J/ψ cuts in PbPb. The trimuon selection requires two muons to fire the trigger.

The generated B_c peak at $p_{\mathrm{T}} \simeq 3$ GeV. The three muons typically do not share equally the available p_{T}, one of them often having $p_{\mathrm{T}} < 2$ GeV, as shows Fig.1. Lowering the muon p_{T} thresholds, and allowing a softer acceptance for one of the muons, is therefore crucial to increase the observable yields. The single muon reconstruction, selection, and trigger efficiencies were studied in pp and PbPb, in order to define $(p_{\mathrm{T}}, |\eta|)$ acceptance cuts keeping only regions with total efficiency above 10%. The trigger efficiency is determined with a simplified tag-and-probe method [12], needed when measuring a single muon efficiency for a double-muon trigger. Two acceptance cuts (shown in Fig.2) are set, for the two triggering muons, and for the one that is not required to trigger.

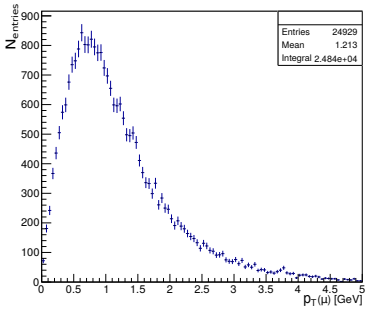

Figure 1: p_{T} of the softest muon from generated trimuons from B_c, when the two other muons are already reconstructed as global

The mass signal region and background sidebands for the J/ψ dimuon are chosen of equal size (to operate a simple sideband subtraction) and tighter when the muons are closer to the central barrel, because the muon p_{T} (hence dimuon mass) resolution is better in this region [12]. So the signal and sidebands regions are respectively:

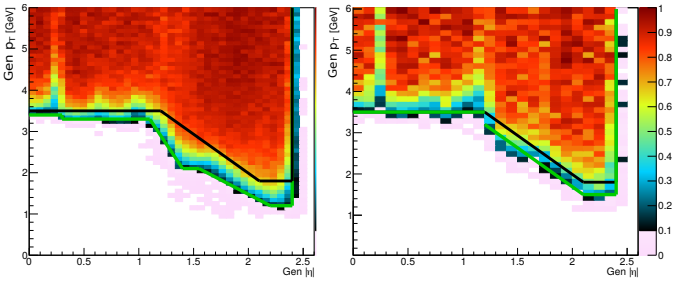

Figure 2: $(p_{\mathrm{T}}, |\eta|)$ maps of the efficiencies of reconstruction + hybrid-soft without Global requirement *(left)*, and of reconstruction + selection + trigger *(right)*, in PbPb. The green line is the chosen acceptance cuts, compared the ones used with 2015 data in black.

- $m_{\mu\mu} - m_{\mathrm{PDG}}(J/\psi) \in [-150, 110]$ MeV and $m_{\mu\mu} - m_{\mathrm{PDG}}(J/\psi) \in [-330, -200] \cup [150, 280]$ MeV, when all three muons have $|\eta| < 1.5$;
- $m_{\mu\mu} - m_{\mathrm{PDG}}(J/\psi) \in [-100, 80]$ MeV and $m_{\mu\mu} - m_{\mathrm{PDG}}(J/\psi) \in [-240, -150] \cup [120, 210]$ MeV otherwise.

For a trimuon of charge ± 1, there are two choices of opposite-sign (OS) dimuons. In order not to bias the mass shape of the chosen J/ψ dimuon, the J/ψ is *not* chosen as the closest to $m_{\mathrm{PDG}}(J/\psi)$. Instead, a trimuon is considered to be in the J/ψ signal region if at least one of the OS dimuons is in the signal region, and no OS pair is in the sidebands; and vice-versa for a trimuon in the J/ψ sidebands. In case two pairs are in the same region, the few J/ψ-specific cuts are applied to a random OS pair. If one pair is in the J/ψ peak region, and the other in the sidebands (which concerns 8% of the signal), then the trimuon candidate is kept, but split between the two regions, with two appropriate weights of sum 1.

Trimuon candidates are also required to have:

- probability of the trimuon vertex fit $> 1\%$, and of the J/ψ vertex $> 0.5\%$;
- distance of closest approach between the J/ψ muons < 0.3 mm;
- trimuon lifetime significance (i.e. the displacement of the trimuon vertex from the primary vertex (PV) divided by its error); > 1.5 both in 2D (transverse plane) and in 3D;
- $\cos\alpha > 0.7$ (where α is the pointing angle, between the trimuon momentum and its displacement from the PV) both in 2D and 3D.

3 Backgrounds

The leptonic channel is partially reconstructed, so the signal extraction is done with a template fit of the trimuon mass. The trimuon mass distribution is studied in the $[3.3, 7.3]$ GeV region, for data, for the expected signal given by a MC, and for the different background sources, given by MC or data-driven methods. The $[6.3, 7.3]$ GeV region above the B_c mass is used as a control region. The signal yield is fitted alongside

some background normalisations, keeping fixed shapes. This means the background shapes must be understood in detail, as well as their normalisation for data-driven estimates.

The most straightforward background comes from fake J/ψ. A simple dimuon mass sideband subtraction is performed, assuming a linear dimuon mass background. The events in the sidebands (of same size as the J/ψ peak region) are estimated to have similar properties and normalisation as the fake J/ψ events under the J/ψ peak. The trimuon mass of J/ψ sideband events are shown in Fig.3.

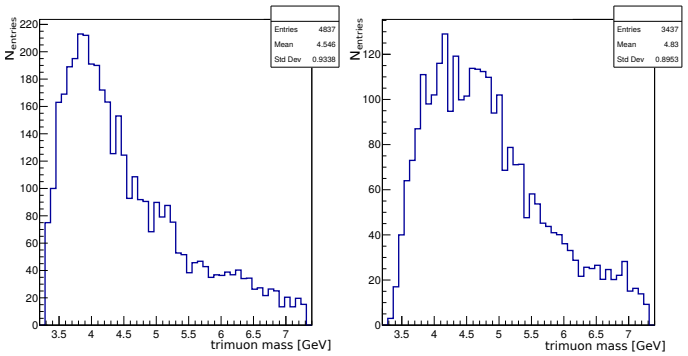

Figure 3: Trimuon mass for events from the lower *(left)* and higher *(right)* sidebands

Care has been taken in keeping unbiased the J/ψ candidates mass shape, by using no mass criteria to select the J/ψ dimuon; otherwise artificial peaks appear in the trimuon mass, due to excessive kinematic constraints. Despite conservative kinematic corrections for the shifted dimuon mass, the shapes in the two sidebands are different; hence, both shapes are to be fitted with an error function plus decreasing exponential, and the weighted-averaged shape is to be taken as extrapolation under the J/ψ peak, normalized by the number of sidebands events. In the shown results, the shape is for now taken as the sum of the two sidebands histograms.

The backgrounds containing a true J/ψ are harder to describe. The MC for prompt and non-prompt (coming from b-decays) J/ψ, where the J/ψ combines with a third muon, should describe it, but it is found to underestimate the high-mass control region in pp 2017 preselected data. The track multiplicity appears in agreement in data and MC, but discrepancies are observed in generic dimuon samples for some vertex quality and displacement variables. These discrepancies and how they could be corrected is still investigated, but a data-driven strategy is conducted in parallel.

In pre-selected data, the third muon is in most cases a fake (i.e. a pion or kaon), because tracks are numerous, and the $K \to \mu$ and $\pi \to \mu$ misidentification rates (misID) are resp. about 0.5% and 0.2% (the proton one being negligible). The term 'muon' in the following hence describes any track that was identified as a muon. Another criterion than muon misID is however used to categorize the background trimuons containing a true J/ψ. When the J/ψ and the third muon come from the same b-vertex, we use the $B \to J/\psi\, X$ decays from the non-prompt J/ψ MC, where the J/ψ and muon are matched to a common generated b-meson parent. This 'correlated' background results in trimuon masses up to 5.4 GeV, close to the B_s mass, meaning it does not contribute to the data/MC discrepancy seen in the high-mass control region. The MC is considered reliable for this background source.

On the other hand, when the J/ψ and muon do not come from the same displaced vertex, the muon might come from a decay of the $\bar{b}$ that recoiled against the b-parent of the J/ψ, which we call 'loosely correlated'; or it might come from a random muon from the underlying event, that happens to be consistent with the J/ψ vertex. The latter category is called "combinatorial", and includes the rare passing candidates where the J/ψ and muon are both prompt.

A data-driven method is needed to get the trimuon mass shape from these two categories, and possibly their normalization, though it can be normalized to the control region. The used method, called *flipJpsi*, is to take all J/ψ in data, flip the direction of their momentum and displacement from the PV by a given angle, then let them combine with muons from the same event. Moving the J/ψ emulates a displaced J/ψ combining with random muons from a similar-looking event, while killing the correlated background. However, if the J/ψ flipping angle does not change the original η, the flipped J/ψ could emulate the background of muons from the recoiling b, whose angle correlations are very loose.

Seven flipping angles are tried: same azimuthal angle ϕ, $\phi \pm \frac{\pi}{2}$, and $\phi + \pi$ when reversing the η; and $\phi \pm \frac{\pi}{2}$ and $\phi + \pi$ when keeping the same η. The yields in the control region for each angle are shown for pp and PbPb in Fig.4, after simple background subtraction and basic cuts. Twice more events are observed in pp when the J/ψ is flipped only in ϕ. This higher activity on the side of the original J/ψ could be understood as a boost of the partonic center-of-mass. In PbPb collisions, as the hard scattering is swamped in the underlying event, there are only $\simeq 15\%$ more events for same-η flipping, which makes this method more reliable.

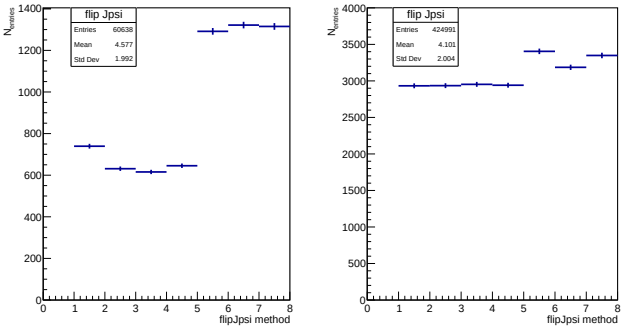

Figure 4: Number of events in the high-mass control region for the seven J/ψ flipping angles, the first four featuring a η reversal, and the last three featuring only a ϕ rotation. *Left*: pp, *right*: PbPb.

The trimuon mass shapes for the different flipping angles were compared, as well as other variables, and the observed differences are small, giving rise to a rea-

sonable systematic error. The yield for the same-η flipping is only slightly lower than the control region yield, which also gives confidence in the method. The normalization are be matched to the control region in the coming results.

4 Signal extraction

The signal and background sample are used as input for a Boosted Decision Tree (BDT, using ROOT TMVA), to build one optimal variable discriminating signal and background, from the discriminant variables given as input. These variables are the ones used for pre-selection (vertex probability, lifetime significance, pointing angle α, the number of global muons), but also more topological variables, such as the sum of the $\Delta R = \sqrt{(\Delta\eta)^2 + (\Delta\phi)^2}$ between the three muon pairs, the imbalance between $p_{\mathrm{T}}(J/\psi)$ and p_{T} of the third muon, or the trimuon mass corrected for the momentum of the neutrino transverse to the flight direction.

A priori normalization of the signal and backgrounds are needed for the BDT, and are used for the pre-fit signal extraction, which is shown in this work. The signal normalization is taken as a weighted average of previous measurements of the pp B_c cross section times branching fraction, from CMS [13] and LHCb ([14] in the hadronic channel and [9] for the ratio of hadronic to leptonic channel). BCVEGPY generated distributions were used to scale these cross sections to the appropriate phase space and center-of-mass energy. This scaling should correctly estimate the pp yields, but not the PbPb yield, as the nuclear modification factor is unknown. The prompt and non-prompt J/ψ MC is scaled using pp and PbPb cross sections from a CMS measurement [4] in the same kinematic range, extrapolated for $p_{\mathrm{T}}(J/\psi) < 6.5$ GeV.

The BCVEGPY signal sample is given to the BDT, as well as the background samples from:

- The J/ψ sidebands;
- The wrong-sign sample, containing candidates of charge ± 3. This sample describes purely combinatorial background, which should be present in the sidebands sample, but it is still used as a complement. A weight of 3 is given to the events, because three random muons are three times more likely to have charge ± 1 than charge ± 3;
- The full scaled prompt and non-prompt J/ψ MC;
- The high-mass control region candidates, with kinematic corrections approximately shifting them to a mass of 5 to 6 GeV;
- The J/ψ flipping sample, averaged over the seven rotation angles.

The last and prior-to-last samples are given resp. weights of 0.65 and 0.5, considering they roughly describe the same background, and correcting the too low normalization of the J/ψ flipping with opposite η. As having wrong normalizations in the input samples could result in a sub-optimal BDT, it was preferred to add all background sources, possibly redundant, to cover for all possible background properties. The input samples are randomly separated in two, and two separate BDTs are trained: one uses the first half as training sample and the second half as the evaluation sample, and vice-versa for the second BDT. The BDT cuts are applied on the evaluation samples and on the signal region data. The resulting trimuon mass distributions for pp are shown before and after optimal cuts in Fig.5.

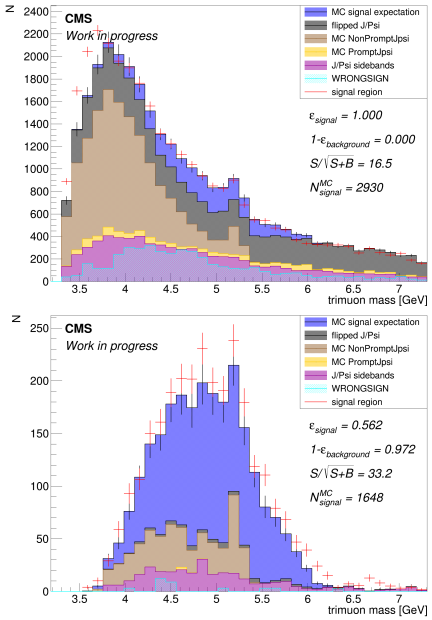

Figure 5: Trimuon mass for data versus the sum of expected signal and backgrounds, before template fit, in pp. Only true $B \to J/\psi X$ events are kept in the non-prompt MC, with a factor 2 for the wrong modelling of the muon misID. The wrong-sign sample is only shown for illustration and not added in the summed background. *Top*: only preselection. *Bottom*: after BDT cuts, optimized with $S/\sqrt{S+B}$ in the signal region.

There are discrepancies between the discriminant variables in the control region data, and the flipped J/ψ events in the same region; this leads to an excess in data in the control region after BDT cuts, that can propagate to the signal region. A weighting procedure to correct these distributions is still being investigated.

The PbPb result is not shown, because a fully reliable procedure in pp must be found before applying it to PbPb data, which has an equivalent luminosity four times smaller than pp, contains more background (requiring tighter BDT cuts), and where the B_c might be strongly modified. However, the combinatorial background will dominate the correlated one, which gives confidence that the J/ψ flipping method will give a good background description.

5 Conclusions

The B_c meson can shed light on the heavy quark hadronization and charm recombination dynamics in

the QGP. A pp analysis at $\sqrt{s} = 5.02$ TeV with CMS is on its way, only lacking a fully reliable background description and the acceptance and efficiency corrections. The study of the B_c in heavy ion collisions is also on-going, and first results with PbPb data at $\sqrt{s} = 5.02$ TeV are promising.

References

[1] R. Pasechnik and M. Å umbera. Phenomenological Review on QuarkâGluon Plasma: Concepts vs. Observations. *Universe*, 3(1):7, 2017.

[2] J. D. Bjorken. Energy Loss of Energetic Partons in Quark - Gluon Plasma: Possible Extinction of High p(t) Jets in Hadron - Hadron Collisions. FERMILAB-PUB-82-059-THY, 1982.

[3] R. Thomas, B. Kampfer, and G. Soff. Gluon emission of heavy quarks: Dead cone effect. *Acta Phys. Hung.*, A22:83, 2005.

[4] CMS Collaboration. Measurement of prompt and nonprompt charmonium suppression in PbPb collisions at 5.02 TeV. *Eur. Phys. J.*, C78(6):509, 2018.

[5] P. Braun-Munzinger and J. Stachel. (Non)thermal aspects of charmonium production and a new look at J/ψ suppression. *Physics Letters B*, 490(3-4):196, 2000.

[6] P. Zhuang, L. Yan, and N. Xu. J/ψ continuous regeneration and suppression in quark–gluon plasma. *Journal of Physics G: Nuclear and Particle Physics*, 34(8):S487, 2007.

[7] E.G. Ferreiro. Charmonium dissociation and recombination at LHC: Revisiting comovers. *Physics Letters B*, 731, 10 2012.

[8] M. Schroedter, R. L. Thews, and J. Rafelski. B_c meson production in nuclear collisions at RHIC. *Phys. Rev.*, C62:024905, 2000.

[9] LHCb Collaboration. Measurement of the ratio of B_c^+ branching fractions to $J/\psi\pi^+$ and $J/\psi\mu^+\nu_\mu$ final states. *Phys. Rev. D*, 90:032009, 2014.

[10] C.-H. Chang, J.-X. Wang, and X.-G. Wu. BCVEGPY2.0: A upgrade version of the generator BCVEGPY with an addendum about hadroproduction of the p-wave B_c states. arXiv:hep-ph/0504017 2005.

[11] CMS Collaboration. Description and performance of track and primary-vertex reconstruction with the CMS tracker. *JINST*, 9 (2014) no.10, P10009 doi:10.1088/1748-0221/9/10/P10009

[12] CMS Collaboration. Performance of the CMS muon detector and muon reconstruction with proton-proton collisions at $\sqrt{s} = 13$ TeV. *JINST*, 13(06):P06015, 2018.

[13] CMS Collaboration. Measurement of production cross sections times branching fraction of $B_c^+ \to J/\psi\pi^+$ and $B^+ \to J/\psi K^+$ in pp collisions at $\sqrt{s} =$ 7 TeV at CMS. CMS Physics Analysis Summary CMS-PAS-BPH-13-002, 2013.

[14] LHCb Collaboration. Measurement of B_c^+ production in proton-proton collisions at $\sqrt{s} = 8$ TeV. *Phys. Rev. Lett.*, 114:132001, Apr 2015.

Inclusive J/ψ production in pp and Pb-Pb collisions at $\sqrt{s_{\rm NN}}$= 5.02 TeV with ALICE at the LHC

Chun Lu Huang

Université Paris-Saclay, CNRS/IN2P3, IJCLab, 91405 Orsay, France

Abstract — A Large Ion Collider Experiment (ALICE) focuses on studying the matter at extremely high temperature and density created by heavy-ion collisions in the laboratory. This state of matter is called the quark-gluon plasma (QGP) and is made of deconfined quarks and gluons. The QGP is thought to have existed for the first few microseconds after the Big Bang. There are many observables proposed to probe the QGP properties. Studying charmonium production is one of those tools. In this proceeding, we report on the J/ψ nuclear modification factor $R_{\rm AA}$ measurement as a function of transverse momentum ($p_{\rm T}$) in Pb-Pb collisions at $\sqrt{s_{\rm NN}}$= 5.02 TeV. The J/ψ production cross section in pp collisions is measured at the same energy and serves as a reference for the Pb-Pb measurements. Measurements are performed in the dimuon decay channel with the ALICE muon spectrometer. These new data in Pb-Pb and pp collisions, corresponding to the LHC Run-2 statistics, extend the previous $R_{\rm AA}$ and pp cross section measurements up to $p_{\rm T}$ = 20 GeV/c.

1 Introduction

The QGP is a deconfined state of nuclear matter, created under extreme conditions such as high temperatures or high matter density, where quarks and gluons can move freely. These conditions are believed to be met either in the early Universe after the Big Bang (high temperature) or in the core of neutron stars (high density). Figure 1 shows the phase diagram of the nuclear matter where the high temperature and the high density conditions are illustrated, as well as the phase transition from ordinary matter to the QGP phase. In order to create nuclear matter at high temperature in the laboratory, the Large Hadron Collider (LHC) collides ultra-relativistic heavy ions at high energy. The ALICE experiment was designed to study such collisions. During the collision, many particles are produced and the QGP is expected to exist for a very short time [7]. There have been many observables proposed to probe the QGP, such as hard jet losing energy while passing through the medium, the hydrodynamic flow of charged particles or charmonia (charm quark and charm anti-quark bounded states: $c\bar{c}$). In particular, the J/ψ, one of the most abundantly produce charmonium states, is considered as a probe of the QGP properties.

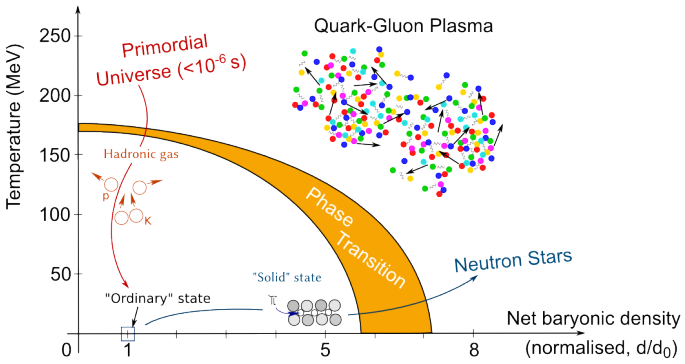

Figure 1: Phase diagram of quantum chromodynamics (QCD) matter. Figure from [6].

2 Physics motivations

In the early stages of the collision before the QGP phase formation, $c\bar{c}$ pairs are produced during the hard scattering of partons and can bound to form a J/ψ. In the QGP phase and if the temperature is large enough, the J/ψ is predicted to be dissociated because of a mechanism called color screening [8]. Indeed the high density of color charges in the deconfined medium can screen the interquark potential and prevent the formation of the bound state. This is known as J/ψ melting. On the other hand, at LHC colliding energies, another mechanism of J/ψ production can be considered. Since the production cross section of $c\bar{c}$ pairs is large, charmonia (including J/ψ) can be formed in the deconfined medium or at the end of the QGP phase, from uncorrelated deconfined charm and anticharm quarks. This is called the regeneration mechanism [9]. On top of that, $c\bar{c}$ pairs, through the hot medium, can lose their energies by multiple scattering with the surrounding partons or by gluon radiation. Energy loss effect could also arise from quarks or gluons rather than from the $c\bar{c}$ pairs [10]. To study the J/ψ yield modifications due to hot medium effects in heavy-ion collisions with respect to nucleon-nucleon collisions, the nuclear modification factor $R_{\rm AA}$ is used. It is defined as,

$$R_{\rm AA} = \frac{Y^{J/\psi}_{\rm AA}}{\langle T_{\rm AA} \rangle \cdot \sigma^{J/\psi}_{pp}}, \quad (1)$$

where $Y_{\rm AA}^{J/\psi}$ is the invariant yield of J/ψ in heavy-ion collisions, and $\langle T_{\rm AA} \rangle$ is the nuclear overlap function which quantifies the average nucleon luminosity in the collision process [11]. The $\sigma_{pp}^{J/\psi}$ denotes the production cross section of J/ψ in proton-proton collisions ant it is defined as:

$$\sigma_{pp}^{J/\psi} = \frac{N_{\rm J/\psi \to \mu\mu}}{BR(\rm J/\psi \to \mu\mu) \times L_{\rm int} \times A\epsilon}, \qquad (2)$$

where BR is the J/ψ to dimuon branching ratio, $L_{\rm int}$ is the integrated luminosity, $N_{\rm J/\psi \to \mu\mu}$ is the inclusive J/ψ yield, and Aϵ is the acceptance times efficiency correction factor of the detector.

If the $R_{\rm AA}$ is larger than one, it means that the J/ψ production is enhanced in Pb-Pb collisions with respect to nucleon-nucleon collisions (as expected if J/ψ regeneration is the dominant mechanism at play). If $R_{\rm AA}$ is less than one, the J/ψ production is suppressed (as expected from color screening or energy loss mechanisms).

3 ALICE experiment

The ALICE experiment [2] is designed to study QGP properties in heavy-ion collisions. In addition, pp and p-Pb collisions are studied in order to estimate the contribution of cold nuclear matter effects in the quarkonium production. The ALICE detectors measure the particles produced in the collisions in the mid- and forward-rapidity region. In this article, the J/ψ production is measured in pp and Pb-Pb collisions at forward-rapidity hence only the relevant sub-detectors are described below. The muon spectrometer is used to identify muons at forward-rapidity. The spatial information of muons is recorded using muon tracking chambers (MCH), made of Multi-Wire Proportional Chambers (MWPC). A dipole magnet sits in the middle of these chambers and provides an integral field of 3 Tm to deflect charged particles. It allows to determine the particle momentum and electric charge of the tracks reconstructed by the MCH. In addition, events that contain muon candidates above a programmable $p_{\rm T}$ threshold are selected using the muon trigger chambers (MTR), which consist of Resistive Plate Chambers (RPC). Finally, an absorber is placed in between the interaction point (IP) and the muon spectrometer to suppress the background events such as low-momentum muons coming from pion and kaon decays.

The Silicon Pixel Detector (SPD) is located in the center of the ALICE central barrel close to the IP and it determines the vertex of a collision. The V0 detector is composed of two scintillator counters located on each side of the IP and provides the minimum bias (MB) trigger. It is also used as a centrality [1] estimator in heavy-ion collisions. The T0 detector is made of two Cherenkov counters and serves as an alternative MB trigger to estimate the luminosity in nucleon-nucleon collisions. The Zero-Degree Calorimeter (ZDC) are quartz-fiber spaghetti calorimeters with sliced optical fibers embedded in an absorber. It is used in this analysis for background rejection purposes.

[1] The centrality is a percentage quantity that describes the collision geometry based on the number of nucleon participants. Its values range from 0 to 100 %. A collision with an high number of participants (ions collide head-on) is called a central collision and the centrality value is typically below 20 %. On contrary, a collision with very few participants is named a peripheral collision and the centrality value is usually above 70 %.

4 Analysis and results

The inclusive J/ψ analysis in pp collisions is performed with the data at $\sqrt{s} = 5.02$ TeV recorded in 2017. Event and track selections are used in the data sample in order to select muon candidates from the J/ψ muon decay channel. Events are selected if they trigger the opposite-sign dimuon trigger and if they pass standard event selections, which among others, permit to reject beam-gas events.

The track selections require tracks to be in the pseudo-rapidity range of $2.5 < \eta < 4$, and to have a polar angle at the end of the absorber in the range $2 < \theta_{abs} < 10$ degree. Tracks in MCH should also match a track in MTR, whose $p_{\rm T}$ is required to be above the online trigger low-$p_{\rm T}$ threshold. A selection on the $p \times DCA$ is also used to reject beam-gas tracks where p is the total momentum of the track and DCA is the Distance of Closest Approach corresponding to the distance in the transverse plane between the primary vertex and the straight extrapolation of the track exiting the front absorber to the IP. In addition, dimuons are requested to fall within the rapidity range $2.5 < y < 4$ and to be formed by two muons of opposite charge.

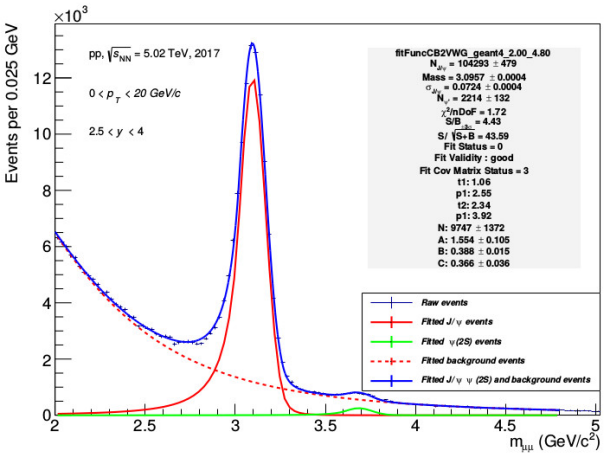

Figure 2: Inclusive J/ψ signal extraction for $0 < p_{\rm T} < 20$ GeV/c at forward rapidity in pp collisions.

The dimuon invariant mass is calculated according to the formula:

$$m_{\mu^+\mu^-} = \sqrt{2m_{\mu^\pm}^2 + 2(E_{\mu^+}E_{\mu^-} - \vec{p}_{\mu^+} \cdot \vec{p}_{\mu^-})},$$

where $m_{\mu^\pm}$ is the mass of muon particles, E_{μ^+} and E_{μ^-} are the energies of the positive-charge and the negative-charge muon particles, $\vec{p}_{\mu^+}$ and $\vec{p}_{\mu^-}$ are the momentum-vector of the positive-charge and the negative-charge muon particles. To extract the number of J/ψ from the dimuon invariant mass spectra, a fit method is adopted.

Figure 2 shows an example of the J/ψ signal extraction for $0 < p_{\rm T} < 20$ GeV/c in pp collisions. The global fit in blue describes the dimuon invariant mass spectrum well for $2 < m_{\mu\mu} < 4.8$ GeV/c^2. The fit components are the J/ψ yield in red, ψ(2S) yield in green and background signal in dashed red. The J/ψ and ψ(2S) yields are described by the Crystal Ball[2] and NA60[3] functions. The background signal is described by a Variable Width Gaussian function [5] and a ratio of first order to second order polynomial. To correct for detector effects and geometrical acceptance, the acceptance and efficiency correction factor ($A\epsilon$) was estimated using Monte Carlo (MC) simulations. The event and the track selections in the MC simulation are the same as in real data. The evaluation of the integrated luminosity corresponding to the data sample is necessary to compute the cross section in pp collisions. Different methods using minimum bias (MB) triggers and dimuon triggers are used to estimate the luminosity and its uncertainty. Luminosity of 1219 nb^{-1} is found. With the above ingredients, the J/ψ cross section is computed and is found to be 5.88 $\pm$ 0.03 (stat.) $\pm$ 0.34 (syst.) μb integrated over $p_{\rm T}$ for $2.5 < y < 4$. The $p_{\rm T}$ differential cross section as a function of $p_{\rm T}$ is shown in Figure 3. This new measurement extend the $p_{\rm T}$ reach to 20 GeV/c. It is compared to an earlier measurement at the same energy and a good agreement is obtained.

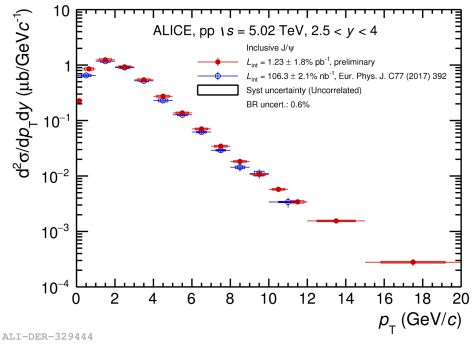

Figure 3: Inclusive J/ψ differential cross section as a function of $p_{\rm T}$ at forward rapidity in pp collisions at $\sqrt{s_{\rm NN}}$= 5.02 TeV. The new measurement with 2017 data is shown (red) and compared to the published results of 2015 (blue).

The inclusive J/ψ analysis in Pb-Pb collisions follows procedure similar to the pp analysis. The 2015 and 2018 Pb-Pb data samples are analyzed with the same event and track selections described in the previous section. The J/ψ signal is extracted by fitting the dimuon invariant mass spectra. Additionally, an event mixing technique [4] is employed to subtract the uncorrelated background in the dimuon invariant mass spectra. Figure 4 shows the new $R_{\rm AA}$ measurement which is compared to the published results in the 0-20% centrality class. Good agreement between the two analysis results has been seen. The new $R_{\rm AA}$ measurement uses the new J/ψ cross section measurement obtained above. The 2015 and 2018 Pb-Pb data samples are merged to increase the luminosity, measurements are more precise and reach larger $p_{\rm T}$ up to 20 GeV/c.

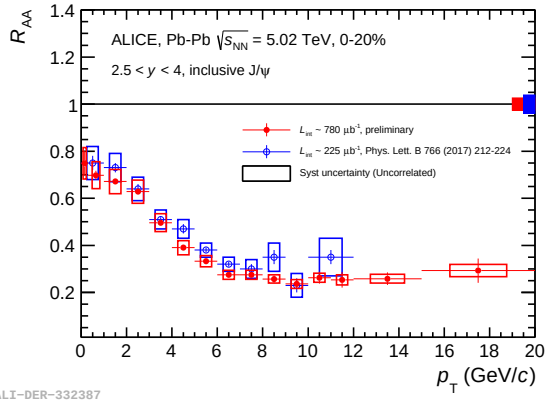

Figure 4: Inclusive J/ψ nuclear modification factor as a function of $p_{\rm T}$ in most central collisions at forward rapidity in Pb-Pb collisions at $\sqrt{s_{\rm NN}}$= 5.02 TeV. The new measurement with 2015 and 2018 data is shown (red) and compares to the previous published results (blue).

5 Comparison to models and discussion

We have measured the inclusive J/ψ differential cross section in pp collisions at $\sqrt{s_{\rm NN}}$= 5.02 TeV and the $R_{\rm AA}$ in Pb-Pb at the same energy. In this section, the discussion will focus on the comparison between the measurements and the theoretical models. Figure 5 shows the $p_{\rm T}$ distribution of the inclusive J/ψ production cross section in pp collisions, compared to existing theoretical calculations. Non-relativistic quantum chromodynamics (NRQCD) models [14, 15] considers color octet diagrams that dominate at high $p_{\rm T}$ and color singlet diagrams that dominate at low $p_{\rm T}$. Color glass condensate (CGC) model describes the saturation of the small-x gluon in the proton [13]. Fixed-order next-to-leading logarithms (FONLL) [12] model describes the J/ψ contribution from the B meson decay (non-prompt J/ψ). As the measurements are performed for inclusive J/ψ, the contribution from NRQCD and CGC

[2]This function was first used by Crystal Ball Collaboration [3].

[3]NA60 function was first used for the charmonium signal extraction by NA60 Collaboration[4].

[4]This technique is about the estimation of the dimuon background events. It is estimated by mixing opposite-sign muons sharing similar global properties in different events.

models (prompt J/ψ only) is added with the calculation based on the FONLL model. All the calculations including NRQCD, CGC and FONLL reproduce the data for $p_{\rm T} < 8$ GeV/c. In the high $p_{\rm T}$ region, the two calculations from NRQCD and FONLL describe the data well.

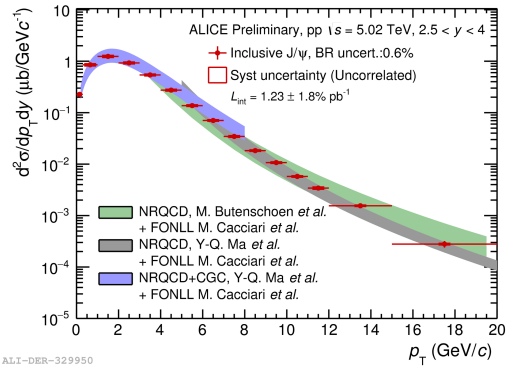

Figure 5: Inclusive J/ψ differential cross section as a function of $p_{\rm T}$ in pp collisions at forward rapidity at $\sqrt{s_{\rm NN}}$= 5.02 TeV. The data are compared to theoretical calculations based on NRQCD, CGC and FONLL (see text for details and references).

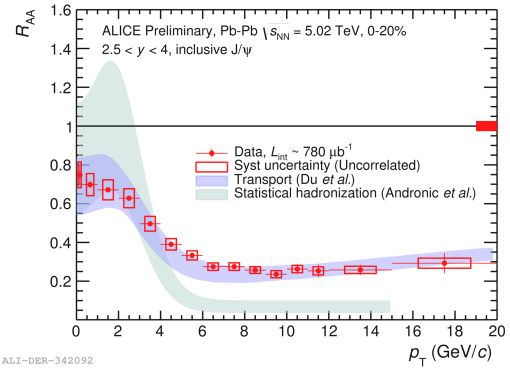

Figure 6: Inclusive J/ψ nuclear modification factor as a function of $p_{\rm T}$ in most central collisions at forward rapidity in Pb-Pb collisions at $\sqrt{s_{\rm NN}}$= 5.02 TeV. Calculations from the transport model and statistical model are also shown.

Figure 6 shows the $R_{\rm AA}$ comparison with a transport model [16] and a statistical hadronization [17] model. The transport model gives a good description of the data for the full $p_{\rm T}$ range. In this model, The J/ψ yield is dominated by the regeneration from the $c\bar{c}$ pair in the QGP phase for $p_{\rm T} < 6$ GeV/c. For $p_{\rm T}$ above 6 GeV/c, the J/ψ yield is dominated by primordial J/ψ that survive in the QGP. The statistical hadronization model describes well the $R_{\rm AA}$ for $p_{\rm T} < 4$ GeV/c. In this region, the initially produced J/ψ in the nucleus core are fully suppressed and the J/ψ yield is dominated by the regeneration from $c\bar{c}$ pairs at the phase transition. For $p_{\rm T} > 4$ GeV/c, the initially produced J/ψ survive in the nucleus corona where there is no QGP. It contributes to a non-zero $R_{\rm AA}$, but it underestimates the data.

6 Conclusions

We have measured the inclusive J/ψ $p_{\rm T}$-differential cross section at forward rapidity in pp collisions at $\sqrt{s_{\rm NN}}$= 5.02 TeV with the ALICE experiment. This measurement is important to study the J/ψ production mechanisms. Besides, it is also an important reference for $R_{\rm AA}$ measurements in Pb-Pb collisions. We have compared our measurement with calculations based on NRQCD, CGC and FONLL. A good agreement is found in this comparison. We have also measured the inclusive J/ψ $R_{\rm AA}$ as a function of $p_{\rm T}$ in most central events at forward rapidity in Pb-Pb collisions at $\sqrt{s_{\rm NN}}$= 5.02 TeV. The Run 2 statistics allow to reach higher $p_{\rm T}$ for the $R_{\rm AA}$ measurements in Pb-Pb collisions. The $R_{\rm AA}$ measurements are compared to the calculations from the transport model and the statistical hadronization model. The transport model describes the $R_{\rm AA}$ data well for the full $p_{\rm T}$ range. The statistical hadronization model describes the data for $p_{\rm T} < 4$ GeV/c however, it underestimates the data for $p_{\rm T} > 4$ GeV/c.

References

[1] M. Tanabashi et al., Phys. Rev. D 98 (2018) 030001.

[2] ALICE Collaboration, JINST 3 (2008) S08002.

[3] J. E. Gaiser, Ph.D. Thesis, Standford, SLAC-R-225 (1982).

[4] R. Shahoyan, PhD. Thesis, Lisbon, IST (2001).

[5] Alice Collaboration, ALICE-PUBLIC-2015-006 (2015).

[6] A. Maire, ALICE PhD, CERN-THESIS-2011-263, https://cds.cern.ch/record/2025215.

[7] M. Strickland, Acta Phys. Polon. B45 (2014) no. 12, 2355-2394.

[8] T. Matsui et al., Phys. Lett. B178, (1986) 416-422.

[9] R. L. Thews, M. Schroedter, and J. Rafelski, Phys. Rev. C 63 (2001) 054905.

[10] F. Arleo, Phys. Rev. Lett. 119 (2017) 062302.

[11] ALICE Collaboration, ALICE-PUBLIC-2018-011, https://cds.cern.ch/record/2636623.

[12] M. Cacciari, JEHP 1210 (2012) 137.

[13] Y-Q Ma, et al., Phys. Rev. Lett. 113 (2014) 192301.

[14] M. Butenschoen, Phys. Rev. Lett. 106 (2011) 022003.

[15] Y.-Q. Ma, et al., Phys. ReV. Lett. 106 (2011) 042002.

[16] X. Zhao and R. Rapp, Nucl. Phys. A859 (2011) 114.

[17] A. Andronic et al., Phys. Lett. B797 (2019) 134836.

Z^0- and $W^{\pm}$-boson production in p–Pb collisions at $\sqrt{s_{NN}}$= 8.16 TeV with ALICE

Guillaume Taillepied

Laboratoire de Physique de Clermont, Clermont-Ferrand, France

Abstract — The current status of the measurement of weak bosons in proton-lead collisions at $\sqrt{s_{NN}}$= 8.16 TeV with ALICE is reported. Preliminary cross sections for the Z production at forward and backward rapidity are presented and compared to theoretical predictions from the most recent parametrizations of nuclear partonic distributions. The ongoing analysis of the W production is presented.

1 Introduction

Heavy-ion collisions aim at bringing QCD matter to extreme thermodynamical conditions where a plasma phase called the Quark-Gluon Plasma (QGP) [1] is created and can be studied. A precise knowledge of the initial state of the collision is of utmost importance to disentangle QGP-induced phenomena from other nuclear effects. In this regard, the weakly interacting Z and W bosons, when detected through their leptonic decay channels, provide a medium-blind reference that allows probing of initial-state effects such as the nuclear modification of Partonic Distribution Functions (PDF). The nuclear PDF sets (nPDF) currently available are suffering from a lack of experimental constraints in the x-range probed at the LHC [2].

Thanks to the high energies and luminosities delivered by the LHC, the measurement of the production of weak bosons is now accessible in heavy-ion collisions [3, 4, 5, 6, 7, 8, 9, 10]. The four main LHC experiments have complementary kinematic coverages which give access to a wide range of Bjorken-x values (from 10^{-4} to almost unity) in a region of high virtuality ($Q^2 \sim M_{W,Z}$) where the nPDFs are weakly constrained by other experiments.

2 The ALICE detector

ALICE[1] is one of the four main LHC experiments, the only one dedicated to heavy-ion physics. It is composed of 18 sub-detectors regrouped in three sets: a central barrel at midrapidity optimised for the reconstruction of hadrons, electrons and photons; a muon spectrometer at large rapidity for the reconstruction of heavy-flavour hadrons, quarkonia and electroweak bosons through their muonic decays; and a set of detectors for the measurement of general quantities such as the collision centrality[2] and the particle multiplicity. A complete description of the ALICE detector can be found in [11]. As this analysis is based on the latter two subsets, a short description is given in the following.

The muon spectrometer [12] is a conical-shape detector covering the pseudorapidity interval $-4 < \eta < -2.5$. In proton–lead (p–Pb) collisions, the proton and lead beams have different energies, the nucleon-nucleon centre-of-mass is thus boosted with respect to the one in the laboratory frame by $\Delta y = 0.465$ in the direction of the proton beam. The rapidity acceptance of the spectrometer is therefore $2.03 < y_{\rm cms} < 3.53$ ($-4.46 < y_{\rm cms} < -2.96$)[3] when the proton (Pb) beam travels toward the spectrometer, hereafter referred to as p–going (Pb–going). The spectrometer contains a tracking system made of ten multi-wire proportional chambers with cathode pads readout, arranged two-by two in five stations. The third station sits inside a dipole magnet with a 3 Tm integrated field. The tracking stations are placed downstream from a conical front absorber made of carbon, concrete and steel for a total length of 4.1 m, that filters out hadrons coming from the interaction point. The tracker is associated with a triggering system made of two stations of two planes of resistive plate chambers each. The trigger stations lie after a 1.2 m thick iron wall that absorbs secondary hadrons escaping from the front absorber and low-momentum muons, mainly coming from the decay of light hadrons. Finally, a beam shield covering the beam pipe protects the spectrometer from particles produced in the interaction of large-η particles with the pipe itself.

The vertex position is measured by the Silicon Pixel Detector (SPD), consisting in the two innermost layers of the Inner Tracking System (ITS). The first and second layers respectively cover the $|\eta| < 2$ and $|\eta| < 1.4$ pseudorapidity intervals. The Minimum Bias (MB) trigger is provided by the V0 detector, two arrays of 32 scintillator tiles each, located on both sides of the interaction point, at 340 cm and -90 cm, covering the $2.8 < \eta < 5.1$ and $-3.7 < \eta < -1.7$ pseudorapidity ranges respectively.

[1] A Large Ion Collider Experiment.

[2] The centrality of a collision is related to the impact parameter, the distance between the center of the colliding nuclei. It is expressed as the percentage of the total hadronic interaction cross section.

[3] By convention, the proton beam is assumed to travel towards positive rapidities.

3 Data sample, event and track selection

The data analyzed are coming from two proton-lead periods and were collected in November and December 2016. Different trigger classes are used for the event selection. The MB trigger corresponds to a logical AND between signals from the two arrays of the V0 detector. For the Z-boson analysis, the Muon-Unlike-sign-Low (MUL) class requires a muon pair of opposite sign, each with $p_{\mathrm{T}} \gtrsim 0.5$ GeV/c, in addition to the MB trigger. In the W case, the Muon-Single-High (MSH) class requires a single muon track reconstructed in the trigger system, with a p_{T} threshold of about 4.2 GeV/c, in addition to the MB trigger. The integrated luminosity computed in the two analyses are found to be the same, which is expected as both analyses are based on the same MB conditions. It amounts to $8.40 \pm 0.01 \pm 0.16$ nb^{-1} in the p–going period and $12.74 \pm 0.01 \pm 0.24$ nb^{-1} in the Pb–going one, where the quoted errors are statistical and systematic, respectively.

In order to ensure a clean data sample, a selection is performed on the single muon tracks reconstructed in the tracker, requiring them to have pseudorapidity $-4 < \eta < -2.5$ and polar angle $170° < \theta_{\mathrm{abs}} < 178°$ measured at the end of the front absorber. This aims at removing tracks at the edge of the spectrometer acceptance, as well at rejecting tracks crossing the high-Z material part of the detector, undergoing multiple scattering. The background from tracks not pointing to the interaction vertex is removed by applying a selection on the product of the track momentum to its distance of closest approach (i.e. the distance to the primary vertex of the track extrapolated to the plane transverse to the beam axis and containing the collision vertex itself). Finally, a track is identified as a muon if the segment reconstructed in the tracking system matches a segment formed by two clusters in the trigger stations.

4 Z analysis

Analysis procedure

The Z-boson signal extraction is performed by combining muons of high transverse momentum in pairs of opposite sign. Only muons with $p_{\mathrm{T}} > 20$ GeV/c are used in order to reduce the contribution from low mass resonances and semileptonic decay of charm and beauty hadrons. An invariant mass range, $60 < m_{\mu\mu} < 120$ GeV/c^2, centered on the Z mass, is defined as to reject most of the remaining background after the event and track selection (mostly coming from Drell-Yan processes through the exchange of off-shell photons). The signal extraction is therefore performed in the fiducial region:

$$\begin{cases} -4 < \eta^{\mu} < -2.5, \\ p_{\mathrm{T}}^{\mu} > 20 \text{ GeV}/c, \\ 60 < m_{\mu\mu} < 120 \text{ GeV}c^2. \end{cases}$$

Figure 1 shows the invariant mass distribution of the unlike-sign dimuons selected in the two considered periods, compared to POWHEG simulations of the $\mathrm{Z} \to \mu^+\mu^-$ process.

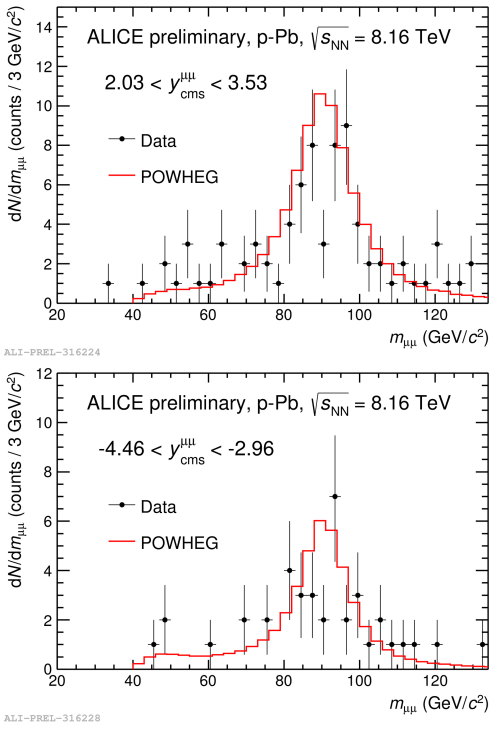

Figure 1: Invariant mass distribution of $\mu^+\mu^-$ pairs for p–Pb collisions at $\sqrt{s_{\mathrm{NN}}}$= 8.16 TeV for the p–going (top panel) and Pb–going (bottom panel) data samples. The distributions are obtained from muons with $-4 < \eta < -2.5$ and $p_{\mathrm{T}} > 20$ GeV/c (black points) and compared to POWHEG simulations (red curve).

The simulations are performed using the POWHEG[4] [13] generator, a Next-to-Leading-Order (NLO) generator of processes where Higgs boson, heavy quarks and electroweak bosons are involved. As POWHEG is only a hard event generator, it is interfaced with PYTHIA6 [14] for parton showering. The generation are performed using CT10nlo [15] as free-proton PDF and EPS09NLO [16] for the nuclear modifications. Finally, the propagation of the particles through the detector is simulated with the GEANT3 [17] code. In order to take into account the isospin effect, the final simulated distributions are obtained with a weighted average of pp and pn binary collisions. The simulations are corrected for the relative displacement of the detector elements with respect to one another, which is measured by photometry before data taking, as well as for a global displacement of the detector with a data-driven method.

Several processes can contribute to the invariant mass spectrum of unlike-sign dimuons. The combinatorial background arising from the random pairing of muons in an event is evaluated by means of the invariant mass distribution of same-sign dimuons, applying the same selections as for the signal extraction. In the two considered periods, no entries are left in the region

[4] POsitive Weight Hard Event Generator

of interest. A conservative estimate of this source can also be evaluated by releasing the transverse momentum selection, fitting the remaining distribution at low p_{T}, and extrapolating to the region of interest. Even with such a conservative method, the contribution of the combinatorial background is found to be negligible.

Contributions from $c\bar{c}$, $b\bar{b}$, $t\bar{t}$ and the muonic decay of τ pairs through the process $Z \rightarrow \tau^+\tau^- \rightarrow \mu^+\mu^-$ were evaluated with Monte Carlo (MC) simulations using POWHEG, obtaining a cross section distribution as a function of the invariant mass for each process. For the charm and bottom contributions, the distributions are normalized by the luminosity of the considered period to get a realistic estimation of the production. The top and tau contributions were compared to the Z one considering the ratio of their respective cross section in the region of interest. The sum of all those contributions is found to be equal to 1% of the signal in the p–going period, and to be negligible in the Pb–going one. The low amount of background allows to perform the signal extraction by simply counting the entries in the distributions in Figure 1 in the 60 to 120 GeV/c^2 mass region. 64 ± 8 entries are found in p–going period, 34 ± 6 in the Pb–going one, the errors being statistical only. The 1% background background contribution evaluated in the p–going period is taken as the systematic uncertainty on the signal extraction.

For the computation of the production cross section, the measured yield needs to be corrected for the efficiency ϵ of the detector. This is done with MC simulations, using POWHEG. The efficiency is defined as the ratio of the number of reconstructed dimuons, applying the same selection as for the signal extraction, to the number of generated ones with $-4 < \eta^{\mu} < -2.5$ and $p_{\mathrm{T}}^{\mu} > 20$ GeV/c. A selection on the dimuon invariant mass, $60 < m_{\mu\mu} < 120$ GeV/c^2 is applied to both reconstructed and generated distributions. The simulation set-up is the same as the one presented above.

Results

The Z-boson production cross section, by convention uncorrected for the branching ratio, is evaluated as:

$$\sigma_{\mathrm{Z}\rightarrow\mu^+\mu^-} = \frac{N_{\mathrm{Z}}}{\mathcal{L} \cdot \epsilon} \qquad (1)$$

where N_Z is the number of Z bosons extracted from the data, $\mathcal{L}$ is the luminosity of the period, and ϵ is the efficiency of the detector. For the two considered periods, one obtains:

$$\begin{cases} \sigma_{\mathrm{Z}\rightarrow\mu^+\mu^-}^{2.03<y_{\mathrm{cms}}<3.53} & = 10.12 \pm 1.27 \pm 0.67 \text{ nb} \\ \sigma_{\mathrm{Z}\rightarrow\mu^+\mu^-}^{-4.46<y_{\mathrm{cms}}<-2.96} & = 3.67 \pm 0.65 \pm 0.19 \text{ nb} \end{cases}$$

where the quoted errors are statistical and systematic, respectively.

Figure 2 displays the measured cross sections at forward and backward rapidity, compared to those measured in p–Pb collisions at $\sqrt{s_{\mathrm{NN}}} = 5.02$ TeV [4]. The same forward-backward asymmetry is observed, which mainly comes from the rapidity shift that pushes the rapidity range towards regions where the production cross section is higher (p–going) or lower (Pb–going). The increase in the number of events leads to a reduction of the relative uncertainty on the final measurement.

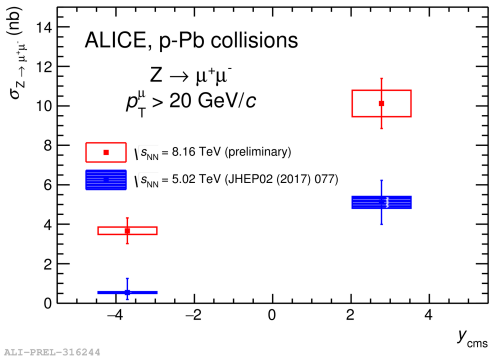

Figure 2: Z-boson production cross section as a function of rapidity in p–Pb collisions at $\sqrt{s_{\mathrm{NN}}} = 8.16$ TeV and 5.02 TeV. The bars and boxes around the points correspond to statistical and systematic uncertainties respectively.

The measured cross sections are compared to theoretical calculations in Figure 3. The predictions were computed with the EPPS16 [18] nPDF set, using CT14nlo [19] as baseline PDF, and with nCTEQ15 [20]. The measurements are well reproduced by the predictions, but the statistical limitations and the small magnitude of the nuclear effects in p–Pb collisions prevent any firm conclusion to be derived on nuclear modifications.

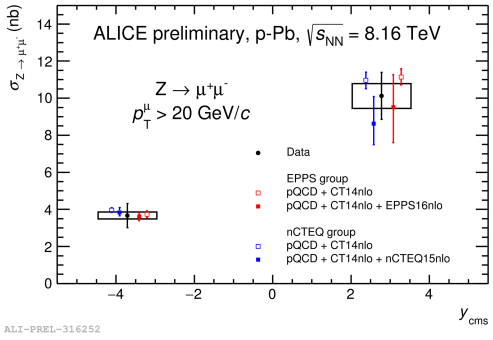

Figure 3: Z-boson production cross section as a function of rapidity in p–Pb collisions at $\sqrt{s_{\mathrm{NN}}} = 8.16$ TeV compared to theoretical calculations using the EPPS16 and nCTEQ15 nPDF sets. The bars and boxes around the data points correspond to statistical and systematic uncertainties, respectively. The theoretical points are horizontally shifted for readability, the close (open) symbols correspond to predictions with (without) nuclear modification of the PDF.

5 W analysis

The W bosons are detected through the $W^{\pm} \rightarrow \mu^{\pm}\nu$ process. Experimentally, one does not have access to the decay neutrino, so no invariant mass analysis is applicable. The W signal extraction is therefore performed from the p_T distribution of single muons.

At transverse momenta above 10 GeV/c, the main contributions to the inclusive single muon p_T spectrum are the muonic decays of W and Z bosons, and muonic decays of heavy-flavored (HF) hadrons. All those contributions need to be reproduced in order to isolate the W one. This is done by fitting the distribution with a combination of MC templates using the formula:

$$f(p_T) = N_{bkg} f_{bkg}(p_T) + N_W \cdot (f_W(p_T) + R \cdot f_Z(p_T)) \quad (2)$$

where f_i are the templates accounting for muons coming from the contribution i (i = W, Z or HF), N_W and N_{bkg} are the numbers of muons from W and HF respectively, being the free parameters of the fit, and R is a fixed parameter, defined as the ratio of the cross sections of muons from Z to W as predicted by the POWHEG generator. The W and Z templates are obtained by simulations with POWHEG, while the template for HF is built with PYTHIA, using as input QCD calculations in the Fixed-Order-Next-to-Leading-Log (FONLL) [21] approach. The inclusive transverse momentum distribution of single muons passing the selection presented above is then fitted according to Equation 2, from which the parameter N_W is extracted. The analysis is done independently for each charge of the muons in the two beam configurations, resulting in the evaluation of four cross sections. An example of such a fit, performed on data from p–Pb collisions at $\sqrt{s_{NN}}$= 5.02 TeV [4], is shown in Figure 4.

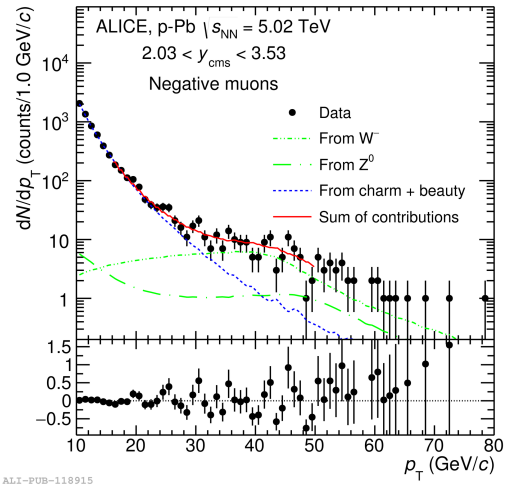

Figure 4: Inclusive distribution of negatively charged muons candidates measured in p–Pb collisions at $\sqrt{s_{NN}}$= 5.02 TeV, in the p–going configuration. The result of the fit with a sum of MC templates is also shown. The figure is taken from [4].

As to account for the dependence of the signal extraction on the simulation parameters, the fits are performed several times with variations of the simulation inputs, such as the PDF and nPDFs in POWHEG, the factorization and renormalization scales used for the FONLL calculations, the transport code, the detector misalignment conditions, or the boundaries of the p_T range on which the fit is done. Overall, hundreds of fits are performed for each charge and beam configuration. The final value for N_W is evaluated as the average of the outputs of all the fits, while their dispersion, estimated as the root mean square, is taken as the systematic uncertainty on the signal extraction. Finally, and as for the Z-boson analysis, the measured yield is corrected for the efficiency of the detector in order to evaluate the production cross section.

In the W case, another quantity of interest will be measured, namely the lepton charge asymmetry. It is defined as:

$$A = \frac{N_{\mu^+ \leftarrow W^+} - N_{\mu^- \leftarrow W^-}}{N_{\mu^+ \leftarrow W^+} + N_{\mu^- \leftarrow W^-}} \quad (3)$$

where $N_{\mu^+ \leftarrow W^+}$ and $N_{\mu^- \leftarrow W^-}$ are the measured numbers of positive and negative muons after efficiency correction, respectively. The charge asymmetry is sensitive to the down-to-up-quark ratio in the nucleus, and allows for a reduction or partial cancellation of the uncertainties. In theoretical calculations, the uncertainty on the scale are greatly reduced. On the experimental side, the uncertainties on the tracking and trigger efficiency cancel. As this ratio is computed from the corrected yields and not the cross sections, all uncertainties arising from the luminosity evaluation are vanishing. The lepton charge asymmetry will be measured to complement the cross section analysis and bring more constrains to nPDFs models.

6 Conclusions

The preliminary measurement of the Z-boson production cross section in p–Pb collisions at $\sqrt{s_{NN}}$= 8.16 TeV at large rapidity has been reported. Compared to the previously published results from collisions at $\sqrt{s_{NN}}$= 5.02 TeV, an appreciable increase in the measured yield was observed, allowing for a more precise measurement. Despite this fact, the statistical limitation and the small magnitude of nuclear effects in p–Pb collisions prevent any firm conclusion to be drawn on nuclear modifications. The measured cross sections were indeed found to be in agreement with theoretical calculations both including and excluding nuclear modifications of the PDF. The analysis procedure for the ongoing measurement of the W-boson production cross section and lepton charge asymmetry has been presented as well. As W bosons are more copiously produced, one can expect the precision of the measurement to be high enough in order to constrain nPDFs models.

Acknowledgements

The author would like to thank Hannu Paukkunen, from the EPPS group, and Aleksander Kusina, Fredrik Olness, Tom Tunks, Ingo Schienbein and Karol Kovarik of the nCTEQ project for providing the pQCD calculations.

References

[1] R. Pasechnik and M. Sumbera, *Phenomenological Review on Quark-Gluon Plasma: Concepts vs. Observations*, Universe 3(2017)7, arXiv:1611.01533.

[2] H. Paukkunen and C. Salgado, *Constraints for the nuclear parton distributions from Z and W production at the LHC*, Journal of High Energy Physics 03(2011)071, arXiv:1010.5392.

[3] ALICE Collaboration, *Measurement of Z^0-boson production at large rapidities in Pb–Pb collisions at $\sqrt{s_{\rm NN}}$ = 5.02 TeV*, Physics Letters B 780(2018)372, arXiv:1711.10753.

[4] ALICE Collaboration, *W and Z boson production in p–Pb collisions at $\sqrt{s_{\rm NN}}$ = 5.02 TeV*, Journal of High Energy Physics 02(2017)077, arXiv:1611.03002.

[5] ATLAS Collaboration, *Measurement of Z boson production in Pb+Pb collisions at $\sqrt{s_{\rm NN}}$ = 2.76 TeV with the ATLAS detector*, Physical Review Letters 110(2013)022301, arXiv:1210.6486.

[6] ATLAS Collaboration, *Z boson production in p+Pb collisions at $\sqrt{s_{\rm NN}}$ = 5.02 TeV measured with the ATLAS detector*, Physical Review C 92(2015)044915, arXiv:1507.06232.

[7] LHCb Collaboration, *Observation of Z production in proton-lead collisions at LHCb*, Journal of High Energy Physics 09(2014)030, arXiv:1406.2885.

[8] CMS Collaboration, *Study of W boson production in PbPb and pp collisions at $\sqrt{s_{\rm NN}}$ = 2.76 TeV*, Physics Letters B 715(2012)66, arXiv:1205.6334.

[9] CMS Collaboration, *Study of Z production in PbPb and pp collisions at $\sqrt{s_{\rm NN}}$ = 2.76 TeV in the dimuon and dielectron channel*, Journal of High Energy Physics 03(2015)022, arXiv:1410.4825.

[10] CMS Collaboration, *Study of Z boson production in pPb collisions at $\sqrt{s_{\rm NN}}$ = 5.02 TeV*, Physics Letters B 759(2016)36, arXiv:1512.06461.

[11] ALICE Collaboration, *The ALICE experiment at the CERN LHC*, Journal of Instrumentation 3(2008)S08002.

[12] ALICE Collaboration, *ALICE dimuon forward spectrometer: Technical Design Report*, CERN report: CERN-LHCC-99-022 (1999).

[13] S. Aioli, P. Nason, C. Oleari and E. Re, *A general framework for implementing NLO calculations in shower Monte Carlo programs: the POWHEG BOX*, Journal of High Energy Physics 06(2010)043, arXiv:1002.2581.

[14] T. Sjostran, S. Mrenna and P. Skands, *PYTHIA 6.4 physics and manual*, Journal of High Energy Physics 05(2006)026, arXiv:hep-ph/0603175.

[15] H.L. Lai et al, *New parton distributions for collider physics*, Physical Review D 82(2010)074024, arXiv:1007.2241.

[16] K. J. Eskola, H. Paukkunen and C. Salgado, *EPS09 - a New Generation of NLO and LO Nuclear Parton Distribution Functions*, Journal of High Energy Physics 04(2009)065, arXiv:0902.4154.

[17] R. Brun et al., *GEANT: Detector Description and Simulation Tool*, CERN report: CERN-W-5013, (1994).

[18] K.J. Eskola, P. Paakkinen, H. Paukkunen and C. Salgado, *EPPS16: Nuclear parton distributions with LHC data*, The European Physical Journal C 77(2017)163, arXiv:1612.05741.

[19] S. Dulat et al., *New parton distribution functions from a global analysis of quantum chromodynamics*, Physical Review D 93(2016)033006, arXiv:1506.07443.

[20] K. Kovarik et al., *nCTEQ15: Global analysis of nuclear parton distributions with uncertainties in the CTEQ framework*, Physical Review D 93(2016)085037, arXiv:1509.00792.

[21] M. Cacciari, M. Greco and P. Nason, *The p(T) spectrum in Heavy-Flavour Hadroproduction*, Journal of High Energy Physics 05(1998)007, arXiv:hep-ph/9803400.

Part V

Instrumentation

session chaired by Sabrina SACERDOTI

Introduction to HEP Instrumentation

Sabrina Sacerdoti

Laboratoire Astroparticule et Cosmologie

Abstract — The instrumentation developments necessary to perform measurements in particle physics are extremely varied, as the field itself. In this introduction I will present, in first place, a brief historical overview of the evolution of HEP experiments, then followed by a summary of some of the more widespread technologies used. The aim of this proceeding is to provide some basic examples of how particle physics experiments work, specially those that will be referred to throughout the workshop, as well as to serve as an introduction to the different lines of work presented in this session.

1 Introduction

There is a clear synergy between the new possibilities given by instrumentation developments and the needs that arise from the desire to explore new aspects of the field.

The beginnings of particle physics can be traced down to the end of the 19^{th} century, times when the structure of the atom was being explored. Back then, only signals produced by the action of many particles could be detected. The particle sources were mostly cathode tubes and radioactive elements (radioactivity was discovered by H. Becquerel in 1896), and experimental setups consisted mostly of photographic plates and ionization chambers.

The improvement of these techniques allowed to move on to a period in which physics could be studied at a single particle level. A large number of new experimental setups were proposed during the first half of the 20^{th} century: cloud chambers, photo-multipliers and the bubble chamber being the main ones. In parallel, the particle sources also evolved: from cosmic rays, discovered using cloud chambers around 1910, to nuclear reactors and synchrotrons. The discoveries associated to these technologies are thus based mostly on image analysis. Figure 1 presents the picture corresponding to the discovery of the positron by C.D. Anderson in 1932. The positron is identified by the curvature of its track within a magnetic field. A lead plate was placed in order to reduce the particle's energy and have a better view of its bending direction. One should note that the combination of an active medium, like a supersaturated gas, with an image acquisition system, is still widely used.

Lastly, we move on to the appearance of more complex event reconstruction techniques. There are several important innovations: the widespread introduction of 'electronic' particle detection, time projection chambers and lastly silicon sensors, which were a major development that introduced a new range of possibilities. But equally important was the new take how experiments and measurements should be conducted: the combination of several detection techniques to achieve a more detailed event reconstruction and a better particle identification, accompanied by more complex analysis techniques and sometimes large collaborations.

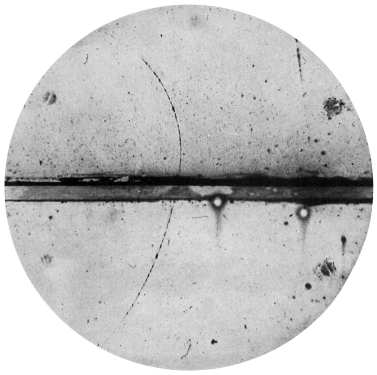

Figure 1: C.D. Anderson discovered the positron in 1932 using a cloud chamber.

2 Miscelaneous concepts

Out of the large zoo of particles know today, only 27 have a lifetime long enough to enable its detection, and actually only 13 that detectors cans try to see: $e^{\pm}$,$\mu^{\pm}$,$\pi^{\pm}$,$K^{\pm}$,K^{0},$p^{\pm}$,n and γ.

Their difference in mass, charge, and ways in which they interact are key for their identification. Charged particles can have multiple interactions within a detector, in the form of ionization, bremsstrahlung, Cherenkov, etc. Hadrons in general will also interact multiple times, with several nuclear interactions. Photons will only interact once, mostly through photoelectric or Compton effect, or pair production. Lastly, neutrinos most of the time escape detection, requiring huge masses of dense material in dedicated detectors. However, nowadays there are numerous specialized detectors that combine a large mass of high density active material with very sensitive detection methods with the

goal to detect the products of the interactions of this elusive particles.

The study of the different ways each type of particle interacts with a material is important, since it allows to model how much energy it will loose as it transverses it. When talking about the thickness of a material, a usual term used is the number of *radiation lenghts* (X_0) transversed. X_0 is defined as the distance in the material after which an incident high energy electron's looses all but $1/e$ of its energy through bremsstrahlung.

The usual way to measure the momentum of a charged particle is through knowledge of its trajectory in a magnetic field. Assuming a mass close to zero and considering that the energy loss due to interactions with the detector is negligible, one can consider that the trajectory of the charged particle in a uniform magnetic field is helical, and thus can be characterized if at least three points are measured. If all points are measured with equal resolution σ_x, one can get the momentum resolution expressed as

$$\frac{\sigma_{p_T}}{p_T} \sim \frac{\sigma_x \, p_T}{n_{\text{hits}}}$$

from where one can tell that the more hits and lower momenta, the better the resolution.

Particle Sources

A large part of the current efforts are focused in the developments happening in accelerators. The Large Hadron Collider at CERN has been, in this sense, a major milestone, having delivered en excellent performance throughout 2 runs of data taking. At Fermilab, works are on the way to install the most powerful neutrino beam yet built. Two lines of work were presented in this session concerning accelerator development. One concerning the work of B. Bai in the context of linear electron accelerators and in the study of injector designs for the electron/positron Future Circular Collider. The second are within the development of TomX and were presented by E. Ergenlik.

One should of course note that numerous experiments use other sources. Many are dedicated to the study of cosmic rays, use nuclear reactors or radioactive sources, while a few have recently begun to exploit another type of signal: gravitational waves. This is the case of the Virgo experiment, for which D. Cohen has presented his work concerning optomechanical parametric instabilities: a source of noise generated in the mirror cavity that reduces the detector's sensitivity.

Signal readout

An equally important part of any experimental setup is the way in which the signals generated by the detector are read out. The requirements set for the data acquisition system can come from different aspects of the experiment: the frequency at which signals will arrive (for example, the time between bunch crossings at the LHC), their expected amplitude (very small or very large), and also the range of amplitude (if the smallest and largest signals expected are too far, a dual system could be needed), the signal to noise ratio, the speed of the signal that will define the necessary sampling rate, etc.

An additional aspect to consider is how the signal will be digitized and transferred for storage. A variety of models of analog to digital converters (ADCs) and time to digital converters (TDCs) have been developed already, and are sometimes even specifically designed for each usage case. The speed at which signals can be sampled and digitized can have a large impact in the performance on the detector. This is why many of the subsystems in the ATLAS and CMS detectors at the LHC are currently upgrading their electronics. One of these projects was presented by E Fortin, concerning the upgrade of the readout electronics of the LAr Calorimenter in ATLAS. Similarly, K.Shchlabo has presented his work related to the development of faster readout electronics to match the increased performance of the iRPCs (improved Resistive PLate Chambers) in CMS.

Detection Technologies used today

Gas detectors

The basic idea behind gaseous detectors is that, when a charged particle transverses some carefully selected gas - or gas mixture - contained within a volume, it will interact with the gas atoms, ionizing them and producing electron/ion pairs. By applying an electric filed, the generated charges will drift towards the electrodes, inducing signals in them that can be collected with the appropriate electronics. A diagram of this process is presented in Fig.2.

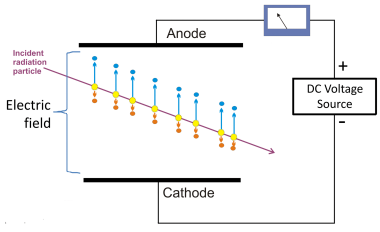

Figure 2: Schematic of the functioning principle of a generic gaseous detector.

Depending on the design of the gas container, the electrodes, the type of gas, etc, different characteristics of the passing particle can be inferred from the measured current. Some detectors, like the Geiger-Muller, have a gas and HV such that a large pulse is generated for each detected particle, thus having a high detection efficiency but no particle identification capabilities, since they cannot measure the energy. Others don't have amplification, thus allowing a direct measurement of the ionization energy but generating very small currents (which can be a challenge to collect with low noise). Examples of these kind are MicroMegas, Gas Electron Multipliers (GEMs) and the before mentioned

RPCs. In addition, with a smart design and placement of the electrodes, they can achieve excellent spatial resolution. Such is the case for MicroMegas which, for example, can achieve a spatial resolution of $\sim 100\mu$m. Lastly, there is a type called proportional counters, in which the gas mixture contains an ionizing gas in which a single ionization avalanche is generated, close to the electrode, and a quenching gas to stop the pulse. The resulting pulse is, as the name indicates, proportional to the energy deposited by the particle. This kind of detector is the most widely used today, in particular in LHC experiments: transition radiation trackers (TRT), monitored drift tubes (MDT), Time Projection Chambers (TPCs), etc.. most of them achieving a resolution in the range of 100μm.

Solid-state detectors

The operational principle of these detectors is very similar to that of a gaseous detector, but with a very important difference: the charged particle transverses a *semiconductor material*. These materials were developed relatively recently, and consist of a crystal, like silicon or germanium, doped so as to control their conductivity. n-type materials will have an excess of electrons, while p-type will have an excess of holes. The properties of n-p junctions are being exploited in a huge variety of devices nowadays, like transistors diodes and LEDs, since there can be light emission from some n-p junctions when subjected to voltage.

The functioning principle of an n-on-p silicon sensor is presented as an example in Fig. 3. The semiconductor material is placed between electrodes which are inversely polarised, so that its volume is depleted. When a charged particle transverses it, the hole/electron pairs drift towards the electrodes, yielding a measurable current as they approach the electrodes. The signal collected is proportional to the intensity of the incident radiation in a well understood way, given that the energy necessary to create an electron/hole pair is well known (i.e. 3.6 eV in silicon).

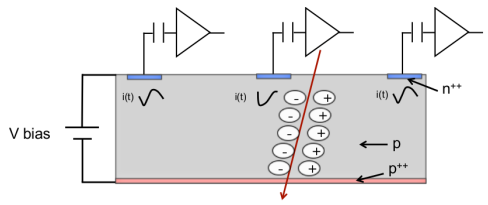

Figure 3: Schematic of the functioning principle of an n-on-p silicon sensor.

This technology has been applied in different geometries, mostly divided into "pixels" and "strips", the first achieving the highest spatial resolution of just $\sim 2\mu$m, but with the disadvantage that a large number of channel readouts are necessary and the implementation of the front end electronics is more complicated. Studies concerning the performance of pixel detectors being developed for the phase-II upgrade of the ATLAS tracking system, ITk, were presented by R. Taibah. Regarding strip sensors, they can achieve lower precision, but are cheaper to implement and easier to read out.

Calorimeters

The aim of a calorimeter detector is to measure the energy of the arriving particle. To this purpose in needs to be able to "stop it", and contain all the products of the interaction between the particle and the detector material. This is usually in the form of a cascade, called a *particle shower*. When the particle is an electron, positron or a photon, it will produced an *electromagnetic shower*, consisting of the photons generated through bremsstrahlung by the e^+/e^-, and the e^+/e^- pairs produced by the photons. The number of particles generated in this process is proportional to the energy of the incident particle. It continues until $E < E_c$, the critical energy which value depends on the material. The calorimeters designed to provide an accurate measurement for this are called electromagnetic calorimeters. Similarly, hadrons produce hadronic showes, and the detectors optimized to measure their energy are hadronic calorimeters.

The design of a calorimeter will not only have to be adequate to the type of particle intended to be detected, but will also depend on which aspect of the measurement is to be prioritized. Concerning this aspect, calorimeters are mostly split into *homogeneous* or *sampling* type. Homogeneous calorimeters are made with a material that is simultaneously dense enough to stop the particles and active so as to emit a detectable signal by interacting with the arriving particle. A schema of what a shower would look like is presented in the top drawing of Fig. 4. A high precision in the measurement of the energy can be achieved in this design, but at the expense of loosing the information of the longitudinal progress of the shower. One of CMSs calorimeters, ECAL [4], follows this idea. It is made of lead tungstate crystals and the light produced is read out by avalanche or vacuum photo diodes connected directly to the crystals.

A different approach is to make a sampling calorimeter, consisting of sandwiches of two materials, by alternating the active material with an absorber. An example of a shower in a sampling calorimeter is presented in the bottom drawing of Fig. 4, where the possibility to measure the progression of the signal is evident, but also the fact that the energy emitted within the absorber is lost. HCAL in CMS [3] has been built like this, and consists of copper absorber plates between which tiles of scintillator plastic have been placed, and whose emitted light is read out using wavelength-shifting fibers. Similarly, ATLAS's Tile calorimeter [1] consists of scintillator plastic tiles places between iron absorbers. Its LAr calorimeter [2] on the other hand uses liquid argon as the active material and has Pb/Steel absorber plates shaped into an accordion to improve the coverage.

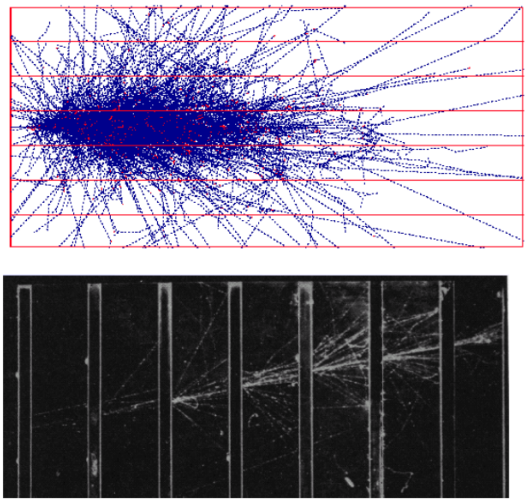

Figure 4: Examples of shower evolution in an homogeneous calorimeter (top) and in a sampling calorimeter (bottom).

3 Conclusions

The technologies for particle detection accumulate a history of around 100 years. They are still advancing, having seen a huge leap in the second half of the 20^{th} century, while still keeping many of the basic principles. A selection of aspects in particle detection has been presented with the aim of introducing the basic of particle detection in general but also the different topics to be discussed within the session. Some very widely used technologies have been omitted, but not for being less important, like Cherenkov detectors or photomultipliers. The rest of the section will address more in detail the different studies mentioned in this proceeding that were presented in the Instrumentation Session of the JRJC 2019.

References

[1] ATLAS tile calorimeter: Technical Design Report, 1996

[2] ATLAS liquid-argon calorimeter : Technical Design Report, 1996

[3] The CMS hadron calorimeter project : Technical Design Report, 1997

[4] The CMS electromagnetic calorimeter project : Technical Design Report

[5] Credit: much of the information and figures were taken from I. Wingerter CERN Summer School slides

Beam optics design for PRAE linac beam lines and FCC-ee injector linac

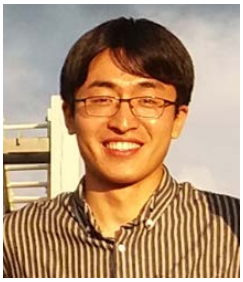

Bowen Bai

Laboratoire de l'accélérateur linéaire, CNRS/IN2P3 & Université Paris-Sud et Paris-Saclay

Abstract — In the last years there has been intense linac electron-accelerator development driven by different community as the X-FEL community, the High Energy Physics (HEP) linear-collider community: ILC and CLIC [1] as well as HEP circular colliders: FCC-ee [2, 3, 4] and the CepC [5] community between others. Furthermore, there are also many other applications from medical field to industry that will use such a linac as main accelerator. In all these studies a high-efficient e-linac with energies from 10-1000 MeV is needed as driver or injector. Even if the linac technology to cope with the performances needed is very well known, an important R&D effort on more compact, simpler, cost-effective, efficient, robust and reliable is still in progress. Here I will present the beam optics design for the beam lines of a multipurpose linac–PRAE and a preliminary introduction to FCC-ee injector linac design

1 Introduction

In this proceeding paper, first I present the two beam lines optics design for PRAE–The Platform for Research and Applications with Electrons, which was considered to be constructed at LAL, in Orsay. PRAE is a multidisciplinary R&D facility gathering subatomic physics, instrumentation, radiobiology and clinical research around a high-performance electron accelerator with beam energies up to 70 MeV, which could be upgraded to 140 MeV in the future. The PRAE accelerator will consist of 2 nC electron bunches produced in a RF gun at 50 Hz, post-accelerated by a S-band linac to 70 MeV and injected into a direct beam line plus one deviated line. The beam line optics has to be as flexible as possible to cope with the different kinds of beam characteristics and operation modes depending on the applications. For the deviated beam line, I will report the complete optics design and performance evaluation of a Very High Energy Electron (VHEE) innovative radiobiology study [6], using Grid mini-beam and FLASH methodologies. The direct beam line design, which is used for the proton radius (ProRad) measurement [7], is also presented.

The second part is about FCC-ee injector linac study. The FCC-ee injector linac accelerates both electron and positron beam up to 6 GeV. The main 6 GeV linac hosts the e^+ source. The positrons are produced with 4.46 GeV e- beam. The FCC-ee positron injector also has to be designed to produce the positron beam with the requested parameters accepted by the DR (Damping Ring). The current scheme is based on the SLC [8]/SuperKEKB [9], in which the electron and the positron beams share the same linacs with a fixed target configuration with a on axis hole as electron beam passage. One of the main drawbacks of this scheme is that the experimental measured positron yield at the end of the linac in SuperKEKB is on the level of 20% (40% design). To get a better performance, we proposed to use a bypass injection option to transfer the electron and positron beams separately. Two bypass proposals are being considered, one using a dogleg and the other using a chicane. The preliminary optics design of the two bypasses is shown here. More work is still in progress, including a dedicated positron linac used to accelerate the positron beam, which will be done in future and is going to be presented in IPAC20.

2 Beam lines design for PRAE

The PRAE accelerator consists of a photo-injector, an acceleration section and two beam lines with the corresponding experimental setups: the subatomic physics in the direct line and the instrumentation and radiobiology platform sharing the deviated line, as shown in Figure 1. The RF gun is located on the left of this figure. The cyan box shows the first HG linac. After the linac, a quadrupole doublet is used to focus the beam. A drift space of about 4 meters is left for a second HG linac which can boost the electron energy to 140 MeV in future. A quadrupole triplet is used to confine the beam as well as allowing to measure the beam emittance. After the triplet, a dogleg with two 30° dipole magnets (pink boxes) are used to deviate the beam following the building constraints and providing a separated area for the radiobiology experiments. The direct line with a magnetic chicane is used for the ProRad experiment.

RF Gun and Linac

A photo-injector has been chosen as the electron source for the purposes of both beam lines: in the radiobiology beam line, the Grid mini-beam requires a low-emittance beam ($5\ mm \cdot mrad$ is assumed) and the proton radius experiment demands the beam with extremely small emittance in the ProRad beam line. The photo-injector consists of a normal conducting RF gun, a drive-laser

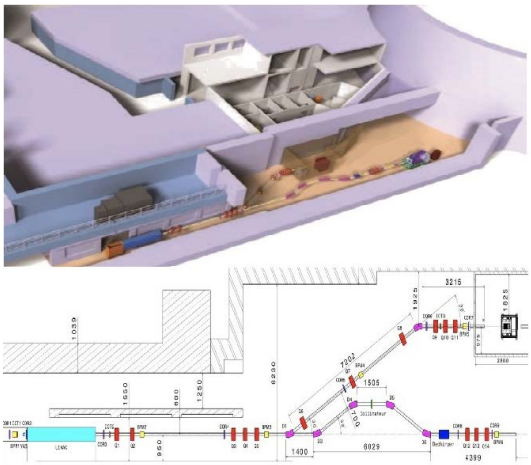

Figure 1: PRAE accelerator layout

and two focusing solenoids. The properties of the RF gun can be seen in the reference [10].

To make the machine more reliable and compact, a High Gradient (HG) S-band linac is chosen. The linac is a 3.47 m long S-band (3 GHz) traveling wave structure, working on the mode $2\pi/3$. The RF design consists of 97-cells (95 regular cells + 2 coupling cells), with a length of 3.47 m. Such structure will provide an energy gain of 65 MeV for an input peak power of 30 MW.

VHEE radiobiology beam line

The radiobiology beam line has been designed with a large flexibility to achieve the beam requirements of the Grid mini-beams and FLASH:

- Grid mini-beam: transverse beam sizes of less than 700 μm with low beam divergence [11, 12].
- FLASH: transverse beam sizes of around 10 mm with a dose of 10 Gy with beam on time 100 ms (5 bunches at 50 Hz), i.e. 100 Gy/s, [13].

In the following, the Grid mini-beam with three different energies (70, 140 and 300 MeV) and the FLASH of 70 MeV are illustrated. For each energy, we first use the program MADX [14] to match the beam line in order to provide proper beam properties. Then the simulated beam from the RF gun and linac will be tracked along the beam line by the program PLACET [15]. The phase space at the end of the beam line are shown for each case. Geant4 [16] is used to simulate the transport of the beam in air and for simulating biological samples water is used.

The Grid Mini-beam Figure 2 shows the optics beam line in the top, the beam envelope along the beam line is less than 2 mm. The phase space at the end of the radiobiology beam line is shown in the bottom. The beam sizes at the end of the beam line are $\sigma x = 207$ μm and $\sigma y = 240$ μm. Similar optics have been calculated for the 140 and 300 MeV energies.

The interaction with the beam with 10 cm of air and 30 cm of water are shown in Figure 3 for 70, 140 and

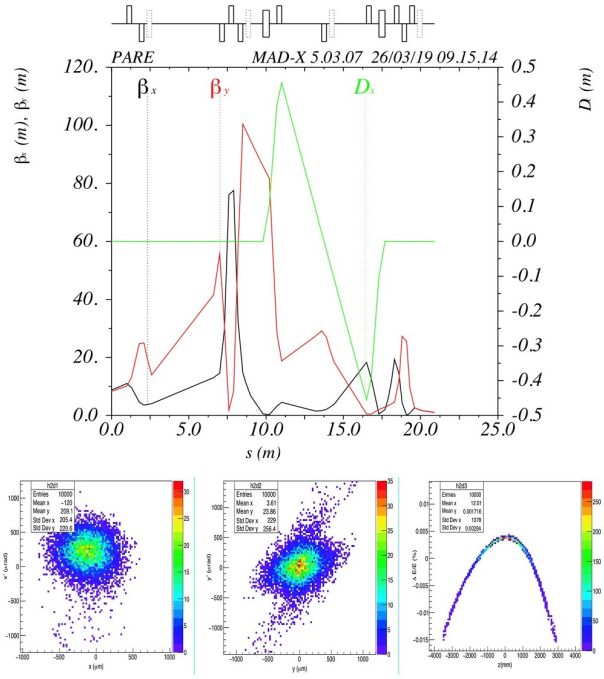

Figure 2: Beam optics and phase space at the end of the beam line, for 70 MeV Grid mini-beam

300 MeV. We could observe that the greater the energy, the deeper the depth of the most intensive energy deposition region. The divergence of the 300 MeV beam at 30 cm water depth is very limited.

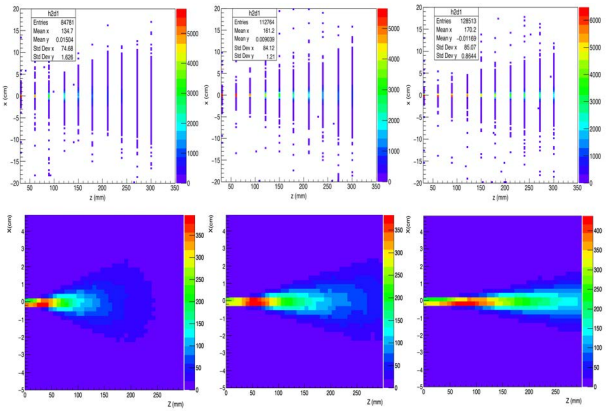

Figure 3: Horizontal beam profile along the longitudinal direction (top) and energy deposition on the x-z plane (bottom) in the water box for 70, 140 and 300 MeV Grid mini-beam respectively.

The FLASH Beam In order to obtain the 10×10 mm transverse beam size, the dispersion from the dipoles dogleg will be used. Two methods are used to generate the FLASH beam. For the first method in the horizontal plane, we can keep the dispersion uncorrected, but in the vertical plane, there is no dispersion generated for a beam without coupling. So the quadrupole in the middle of dogleg is changed to a skew quadrupole, which can couple the horizontal dispersion to the vertical plane. The second method consists of

using the dispersion only in the horizontal plane, generating a large divergence in the vertical plane. The beam optics for the two methods are shown in Figure 4. In a similar way as in the Grid mini-beam, GEANT4 has been used to simulate the interaction with the beam with air and water. In this case an air box of 1 meter and water box of 30 cm are used. The results for a 70 MeV beam are shown in Figure 5.

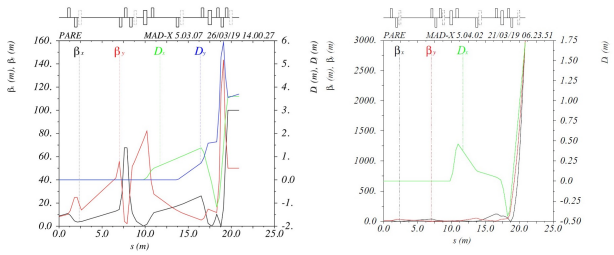

Figure 4: FLASH beam optics for Method 1 (left) and Method 2 (right).

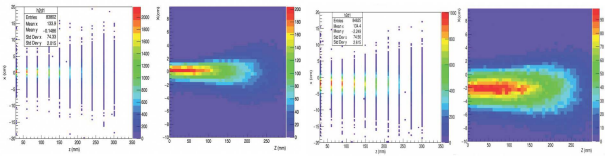

Figure 5: Horizontal beam profile along the longitudinal direction (left) and energy deposition on the x-z plane (right) in the water box for 70 MeV FLASH beam for Method 1 (top) and Method 2 (bottom).

The ProRad beam line

The transverse beam size at the end of the beam line is required to be 200 μm and the beam should reach the beam waist to give less divergence. And the β function along the beam line is required to be smaller than 100 m in order to adapt the beam pipe with radius of 2 cm. Those requirements are matched with MADX. PLACET is used to track the beam until the end of beam line (without collimator). The matched optics and phase space for the ProRad beam line can be seen in Figure 6.

The effect of collimator

A 1 meter long collimator with half aperture of 2 mm in the horizontal plane is put in the middle of the chicane to reduce the energy spread. The comparisons of the beam lines with and without collimator are shown in Figure 7. It can be seen the particles with relative low energies are removed by the collimator. There is about 48% of particles can pass through the collimator and the energy spread for those survived particles is 4.2×10^{-4}. The transverse position distributions are shown in Figure 7. It can be seen that after the collimation, the transverse position distributions still keep

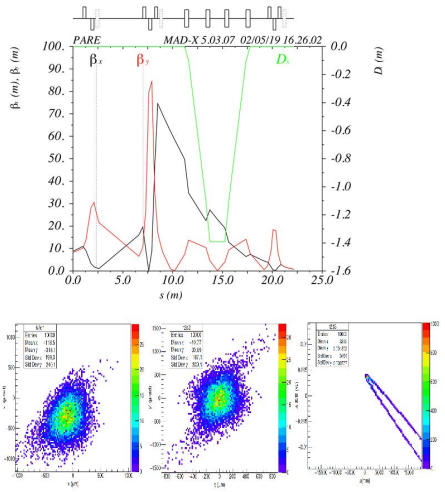

Figure 6: Beam optics and phase space at the end of the beam line for ProRad beam line

symmetric. The central positions are about 200 and 70 μm for x and y plane, respectively. These offsets are coming from the initial beam and can be corrected with some dipole correctors.

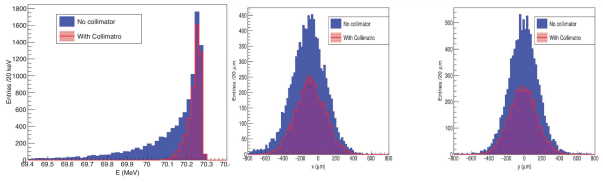

Figure 7: The left figure shows: The comparison of energy between with and without collimator; The two right figures shows: The comparison of transverse distribution between with and without collimator. The left side plot show the distribution of x and the right side plot shows the distribution of y.

3 FCC-ee injector linac design

The FCC-ee is part of a more general study, known as FCC, that comprises three different types of particle collisions: hadron (proton-proton) collisions FCC-hh; the aforementioned electron-positron collisions FCC-ee; and proton-electron collisions FCC-he. The FCC hosted by CERN, is an international collaboration to explore the feasibility of different particle collider scenarios with the aim of significantly increasing the energy and luminosity compared to existing colliders, in the search for new physics.

The injector complex of the FCC-ee comprises a positron/electron linac (for energies up to 6 GeV), a pre-booster synchrotron ring (PBR), accelerating from 6 to 20 GeV, and a full energy booster synchrotron ring (BR), integrated in the collider tunnel. A schematic layout of the injector complex can be seen in the Figure 8. What this paper focuses is the 6 GeV e^+/e^-

injector linac part.

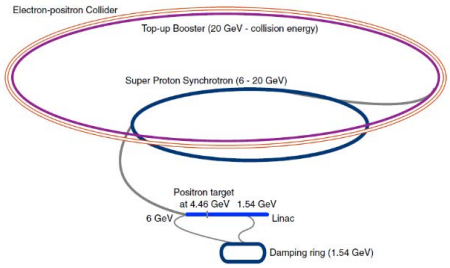

Figure 8: FCC-ee injector complex

As I mentioned in the introduction part above, the current injector scheme for a e^+/e^- collider is based on the SuperKEKB design. But it can't meet the efficiency requirement of FCC-ee. In order to get a better performance and improve the positron generation efficiency, a bypass injection option is proposed to transfer the electron and positron beams separately giving us the possibility to employ a moving target to optimize the thermal loading of the target and the reliability of the entire system. Two bypass proposals are being considered, one using a dogleg (Figure 9 top) and the other using a chicane (Figure 9 bottom). The current work consists of different kinds of bypass designs abd the optics design for a dedicated positron linac which will accelerate the positron beam from 200 MeV to 1.54 GeV. The start-to-end simulation from RF-Gun to positron Damping Ring is followed in the plan.

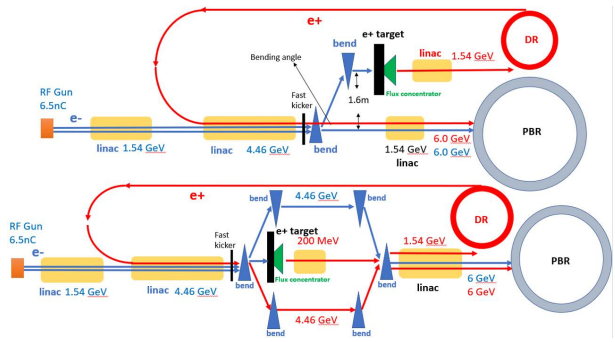

Figure 9: FCC-ee injector bypass

In the new schemes, two RF guns are used to generate two electron beams. One electron beam will be straightly accelerated by electron linac to 6 GeV. The other beam shares the same linac with the first electron beam to 4.46 GeV, and then is bypassed by a dogleg or chicane structure to hit the positron target to produce positrons. Next the yielded positrons will be captured and get primary acceleration to 200 MeV. Afterwards, the collected positrons will be accelerated to 1.54 GeV with a positron linac. The 1.54 GeV positron beam will get a better performance after Damping ring (DR) and gain another 4.46 GeV energy due to the linac acceleration. Finally, the both 6 GeV e^+/e^- beams will be injected into Pre-Booster synchrotron Ring (PBR) for next acceleration.

The 4.46 GeV electron linac is designed by SAD [17], whose beam optics and phase space are shown in Figure 10. The output of 4.46 GeV e- linac is used as the input of dogleg or chicane bypass design. Here I present a preliminary 10° dogleg and chicane transfer line optics design, as shown in Figure 11 and Figure 12, done by MADX and PLACET.

Figure 10: Beam optics (left) and phase space (right) of FCC-ee 4.46 GeV linac

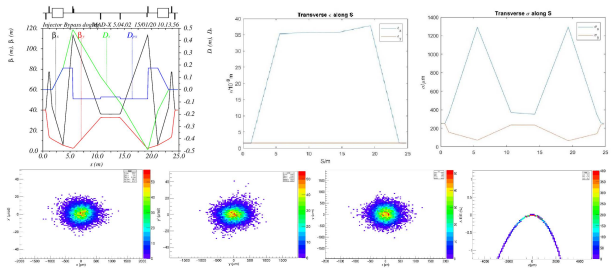

Figure 11: Beam optics (top) and phase space (bottom) of 10° dogleg bypass

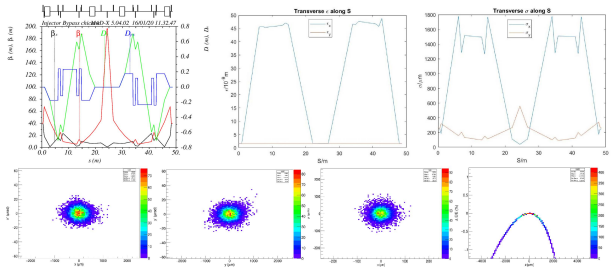

Figure 12: Beam optics (top) and phase space (bottom) of 10° chicane bypass

Different angles of dogleg and chicane studies to cope with target issues are in progress as well as coherent synchrotron radiation and error study. The positron linac used to accelerate e^+ beam to 1.54 GeV is also in design. Those simulation results are planned to be presented in IPAC20 at Caen, in France this May.

4 Conclusion

Beam lines design for PRAE linac and the very preliminary FCC-ee injector linac design are shown in this proceeding paper. More results of the design can be expected in the following few months.

References

[1] THE CLIC CONCEPTUAL DESIGN REPORT, *http://clic-study.web.cern.ch/content/conceptual-design-report*

[2] FCC-ee: The Lepton Collider: Future Circular Collider Conceptual Design Report Volume 2 - FCC Collaboration (Abada, A. et al.) Eur.Phys.J.ST 228 (2019) no.2, 261-623 CERN-ACC-2018-0057, *https://fcc-cdr.web.cern.ch/*

[3] BEAM DYNAMICS SIMULATION IN TWO VERSIONS OF NEW PHOTOGUN FOR FCC-ee ELECTRON INJECTOR LINAC, S.M. Polozov, T.V. Bondarenko, IPAC'17, 1326-1229 (2017).

[4] *http://fccweek2019.web.cern.ch/*

[5] CEPC Conceptual Design Report: Volume 1 - Accelerator - CEPC Study Group arXiv:1809.00285 [physics.acc-ph] IHEP-CEPC-DR-2018-01, IHEP-AC-2018-01, *http://cepc.ihep.ac.cn/*

[6] Y Han et al 2019 J. Phys.: Conf. Ser. 1350 012200

[7] The PRORAD Beam Line Design for PRAE - Faus-Golfe, Angeles et al.

[8] Erickson, R (Apr 2004). SLC Design Handbook (SLAC-R–714). United States

[9] Y. Ohnishi et al., Accelerator design at SuperKEKB, Prog. Theor. Exp. Phys. 2013, 03A011 (2013).

[10] A. Vnuchenko et al., "Start-to-End Beam Dynamic Simulations for PRAE", in Proc. 9th Int. Particle Accelerator Conf. (IPAC'18), Vancouver, Canada, Apr.-May 2018, pp. 495-498. doi:10.18429/JACoW-IPAC2018-MOPML044

[11] Prezado, Y., Deman, P., Varlet, P., Jouvion, G., Gil, S., Le Clec, H. C., Bernard, H., Le Duc, G., and Sarun, S., "Tolerance to dose escalation in minibeam radiation therapy applied to normal rat brain: long-term clinical, radiological and histopathological analysis", Radiat Res 184, pp. 314-321, 2015.

[12] Prezado, Y., Sarun, S., Gil, S., Deman, P., Bouchet, A., and Le Duc, G., "Increase of lifespan for glioma-bearing rats by using minibeam radiation therapy", J Synchrotron Radiat 19, pp. 60-65, 2012.

[13] Montay-Gruel, P., Petersson, K., Jaccard, M., Boivin, G., Germond, J. F., Petit, B., Doenlen, R., Favaudon, V., Bochud, F., Bailat, C., Bourhis, J., and Vozenin, M. C., "Irradiation in a flash: Unique sparing of memory in mice after whole brain irradiation with dose rates above 100Gy/s", Radiother Oncol 124, pp. 365-369, 2017.

[14] Methodical Accelerator Design program, *http://madx.web.cern.ch/madx/*

[15] D. Schulte et al., "PLACET: a program to simulate the drive beams", CERN-PS-2000-028-AE, CLIC-Note-437, CERN, Geneva, Switzerland, 2000.

[16] S. Agostinelli et al., "Geant4 - a simulation toolki", NIM A 506 (2003) 250-303.

[17] SAD, *http://acc-physics.kek.jp/SAD/*

Optomechanical parametric instabilities study for Virgo

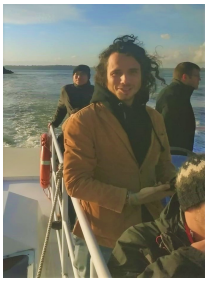

David E. Cohen

Université Paris-Saclay, CNRS/IN2P3, IJCLab, 91405 Orsay, France

Abstract — Increasing the laser power is essential to improve the sensitivity of interferometric gravitational wave detectors. However, optomechanical parametric instabilities can set an upper limit to that power. LIGO experienced this phenomenon in 2015, during the Observing run 1 (O1), for an intra-cavity power of 50 kW when a 15 kHz mechanical mode became unstable under the effect of radiation pressure. The current intracavity power in Virgo (O3: Observing run 3) is about 130 kW, and so far no parametric instability has been observed. Here, we predict the parametric gain for each mechanical modes of the four suspended mirrors of the Virgo configuration. We show preliminary results, which endorse the fact that, to date, mechanical modes up to 70 kHz are unlikely to become unstable.

1 Introduction

Recall of basics and acronyms – A ground-based interferometric gravitational detector such as Virgo [1], LIGO [2], or KAGRA [3] (in the following, the Virgo conventions will be used to label the detector components) is a Michelson interferometer — on Figure 1 is shown such an interferometer in the configuration used for the Virgo Observing run 3 (O3). The mirrors reflecting the beam light back towards the beam splitter (BS) are called END mirrors (E). On the two arms of the interferometer — called North (N) and West (W) — are two extra mirrors called INPUT mirrors (I) creating Fabry-Perot cavities [4], in which the light is stored thus increasing the phase accumulation and improving the detector sensitivity. The interferometer is tuned on the dark fringe, meaning that all the power is reflected back to the laser. Therefore, one additional mirror, the Power Recycling (PR) mirror (see Figure 1), recycles the power reflected from the interferometer.

Parametric instabilities – In 2015, the global LIGO-Virgo network made the first direct detections of gravitational waves coming from compact binary coalescences [5]. Since then, more events have been detected [6]: improvements performed during commissioning phases yielded better detector sensitivities, which allow detection of transient sources that are weaker or located further away. Increasing the laser power traveling within the arms significantly improves the sensitivity, for this reduces the laser quantum phase noise effect dominating the sensitivity in the high-frequency range (above a few hundreds of Hz). However, a nonlinear optomechanical phenomenon that has long been studied [7] – [12], known as optomechanical parametric instabilities (PI), may limit the amount of energy stored in the Fabry-Perot resonator, and thus the interferometer sensitivity.

PI come from the coupling of three modes: a mirror mechanical mode that sets the mirror surface in motion, the fundamental optical mode of an optical cavity (TEM_{00}), and a higher order optical mode (HOM). Photons can be scattered from the TEM_{00} to an HOM through the mechanical mode by annihilating or creating one phonon in this mode. These photons can generate an optical beat note if the difference in frequencies of the two optical modes is equal to the mechanical mode's resonance frequency. This beat note in turn can either damp or increase the mechanical motion via radiation pressure [7]. The latter effect leads to an exponentially growing amplitude of the mechanical mode, which then reaches a plateau after some time. The signal associated with this mirror mechanical excitation would saturate the electronics, hence the control of the interferometer would be lost [13].

Motivation – During the Observing Run 1 (O1), in 2015, LIGO observed PI when a mirror mechanical mode at 15 kHz became unstable, for an intracavity power of 50 kW [13]. Eventually, a similar phenomenon is expected to occur in Virgo, and the purpose of this work is to investigate possible PI in this interferometer. In our simulations, we include measurement uncertainties and possible deviations between the nominal configuration of the detector and the actual one. Current results show that, with an intracavity power of 130 kW (current value for the ongoing O3), one could observe no more than a couple of unstable modes, depending on the radii of curvature (RoC) of the mirrors. Lower quality factors (Q factors) — in agreement with measurements *in situ* — should allow Virgo not to face any PI for the time being, for mechanical modes with frequencies lower than 70 kHz — and, indeed, none of them has been seen experimentally within this range.

2 Numerical approach

The selected approach is the one developed by Evans *et al.* [11]. In this framework, the whole interaction between the three implied modes is seen as a classical feedback system. The resulting gain of the mechanical

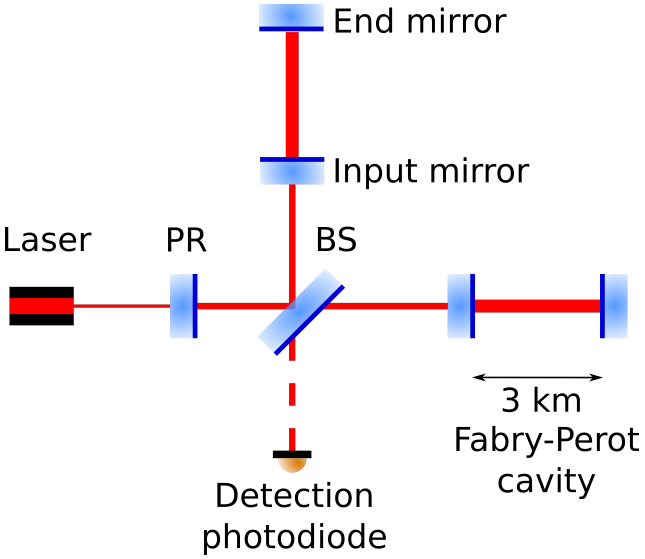

Figure 1: The Virgo O3 configuration. It comprises the Fabry-Perot cavities, and the Power Recycling mirror.

mode m is given by

$$R_m = \frac{8\pi Q_m P_{arm}}{M\omega_m^2 c\lambda} \sum_{n=0}^{\infty} \Re[G_n] B_{m,n}^2 \qquad (1)$$

where Q_m is the quality factor of the mechanical mode m and ω_m its frequency, P_{arm} the intracavity optical power, λ the optical wavelength, M the mirror mass, c the speed of light, G_n is related to the scattered field optical gain of the n^{th} optical mode, and encapsulates the mechanical response, and $B_{m,n}$ is the spatial overlap integral between the three involved modes. A mechanical mode is amplified if $R_m > 0$ and damped if $R_m < 0$. It becomes unstable if $R_m > 1$.

3 Simulations

The simulations have been performed for a Virgo configuration corresponding to that of O3. The parameters for such a configuration are shown in Table 1.

Using these parameters, the mechanical modes (2D shapes, frequencies, and Q factors) are obtained with a Finite Element Method [14]. The optical modes (2D shapes, frequencies, and diffraction losses due to the finite size of the mirrors) are obtained by numerical diagonalisation of the propagation kernel over a cavity round-trip [15]. Not only does it provide the exact diffraction losses as it considers the finite size of the mirror, but it also allows the use of custom shapes to model the mirrors.

The gains of all mechanical modes are calculated from Equation (1). The elaboration of two different programs using the same formalism (from [11], whose outputs were reproduced) validates our results. A sanity check is also performed after each modification of either of the programs, comparing the resonances of a few chosen mechanical modes obtained with Finesse [16].

Table 1: Parameters used for the simulations.

Virgo 03 configuration parameters		
Arm lengths	2999.8	m
RoC NI	1424.56	m
RoC NE	1695	m
RoC WI	1424.58	m
RoC WE	1696	m
Transmittance NI	13750	ppm
Transmittance NE	4.4	ppm
Transmittance WI	13770	ppm
Transmittance WE	4.3	ppm
Transmittance PR	48400	ppm
Round trip loss (TEM_{00})	75	ppm
Distance from BS to NI	6.0167	m
Distance from BS to WI	5.7856	m
Distance from BS to PR	6.0513	m
Mirror mass	42.28	kg
Intracavity power	130	kW
Laser wavelength	1064	nm
Gouy phase of PR cavity	1.8	mrad
Mirror mechanical parameters		
Young modulus	72.248	GPa
Poisson ratio	0.16629	
Density	2201	kg m^{-3}

The RoCs of the four mirrors are altered by thermal effects due to laser absorption. As a consequence, they are not known exactly. However, curvatures of mirrors play a very important role as they set the frequencies of transverse optical modes: a shift in their values thus shifts the frequencies of potentially unstable mechanical modes. That is a first reason why, in the simulation shown on Figure 2 and 3, we scan the end-mirror RoCs around the nominal values. Another reason is that in order to mitigate possible instabilities, a system that enables the tuning of the mirrors' RoCs has been installed on Virgo. It comprises heaters that are around the mirrors: a surface deformation stemming from induced thermal gradients is used to fine tune the RoCs of the arm mirrors. In the Virgo interferometer, we use the end-mirrors heaters for technical reasons.

4 Results

The results shown thereafter on Figure 2 to 5 are as preliminary. The results obtained with the different simulation methods are in a pretty good agreement (chiefly regarding the number of unstable mechanical modes over the whole scanned range), although further refinements are still ongoing.

Figures 2 and 3 respectively show the number of PI and the maximum gain with respect to the radii of curvature of the two end-mirrors. According to the assumed working point position, no PI should be observable at least with the current laser input power of 26 W (which approximately corresponds to an intracavity power of 130 kW). Indeed, over this whole range,

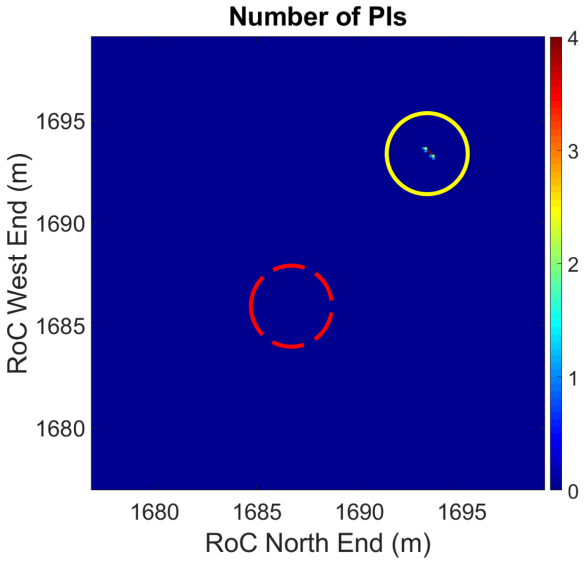

Figure 2: Number of parametric instabilities versus end-mirrors RoCs in the range [1675 m, 1705 m]. The red dashed circle represents the measured AdVirgo working point including its uncertainty. The yellow circle brings out the 12.5156 kHz mechanical mode.

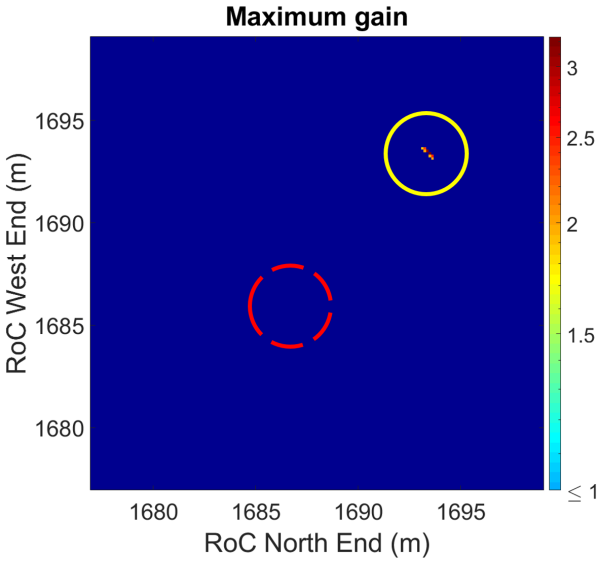

Figure 3: Maximum parametric gain versus end-mirrors RoCs in the range [1675 m, 1705 m]. The red dashed circle represents the measured AdVirgo working point including its uncertainty. The yellow circle brings out the 12.5156 kHz mechanical mode.

only a single mechanical mode could become unstable: the 12.5156 kHz mode. But, this instability is far from the current working point in terms of RoCs, therefore this should not be an issue.

The parametric gain value helps foresee the dynamics of the instability for the e-folding time of an unstable mode given by [13, 17]

$$\tau_{pi} = \frac{\tau_m}{1 - R_m} \tag{2}$$

where $\tau_m = 2Q_m/\omega_m$ is the natural decay time of the mechanical mode. The 12.5156 kHz unstable mode has $R_m = 3.2$, and $Q_m = 4.8 \times 10^6$. This would give rise to an instability growth time constant of about 50 s.

Figure 4 shows the shape of the possible unstable 12.5156 kHz mechanical mode. Figure 5 shows the highest optical mode contributor to the parametric gain of that mechanical mode, with a parametric gain of 2.73, i.e. this mode contributes for about 84 % of the total gain. However, the interesting point is more the fact that the density of instabilities is very low on Figure 2, rather than the exact unstable mechanical mode that comes out from the simulation. Indeed, very small variations of the interferometer's optical parameters do not change the density of instabilities, but change the mechanical modes that become unstable.

A recent campaign of quality factor measurement has highlighted that the quality factors of the real mirrors are lower than expected for the considered mechanical frequencies. As Equation (1) shows, a lower quality factor value reduces the expected parametric gain. This could explain why Virgo did not incur in any parametric instability event during the last years.

5 Conclusions

A simulation campaign has been performed in order to foresee possible parametric instabilities in the Advanced Virgo interferometer. Different simulation codes have been developed to perform this computation and, despite some discrepancies which are still under investigation, they do not forecast any PI event with the current O3 configuration, which is endorsed by the observations up to 70 kHz. On a first iteration, the mirror quality factors extracted from a finite element simulation were used. However, with a following measurement campaign, lower quality factor values have been measured. As a result, all the critical modes that could give rise to an instability are not critical in the present configuration of the interferometer.

After the end of O3, the Advanced Virgo detector will be upgraded in two different phases, called Advanced Virgo + phase I and Phase II, which will respectively lead to the Observing run 4 (O4) and 5 (O5). During the first upgrade, an additional mirror will be included in the optical configuration and the input power will be doubled. Subsequently, the installation of larger END mirrors will be performed, and the optical configuration will be redesigned during the so-called Advanced Virgo + Phase II. In both cases, the optical configuration of the interferometer will be different with respect to the current one, and a new simulation campaign will be performed in order to study the possibility that new parametric instability could arise.

Acknowledgements

This work is being conducted with Annalisa Allocca (INFN Pisa, Pisa, Italy), Gilles Bogaert (Artemis, Nice, France), Thibaut Jacqmin (LKB, Paris, France), and Paola Puppo (INFN Roma, Rome, Italy), within the Virgo Collaboration. We thank Nicolas Arnaud, François Bondu, Marco Romanelli, and Jerôme Degallaix for fruitful discussions. David Cohen is supported by the DIM ACAV+ from the Region Île-de-France.

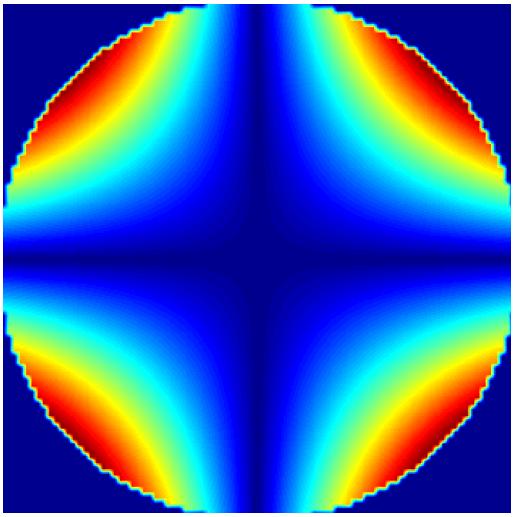

Figure 4: Prospective unstable mechanical mode at 12.5156 kHz, yet far from the working point.

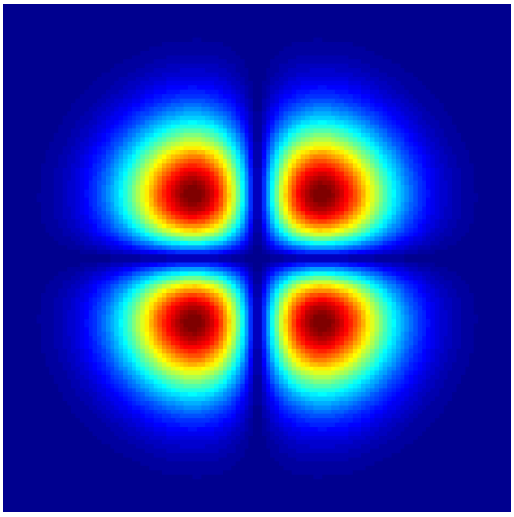

Figure 5: The optical mode contributing the most to the parametric gain of the 12.5156 kHz mechanical mode. The parametric gain resulting from the interaction between this optical mode, the TEM_{00}, and the 12.5156 kHz is 2.73, which represents 84 % of the total parametric gain (3.24).

References

[1] http://www.virgo-gw.eu

[2] https://www.ligo.caltech.edu

[3] https://gwcenter.icrr.u-tokyo.ac.jp/en

[4] H. Kogelnik, L. Tingye, "Laser beams and resonators", *Applied optics*, 5.10, 1550-1567, 1966

[5] B. P. Abbott *et al.*, "Observation of gravitational waves from a binary black hole merger", *Physical review letters* 116.6, 061102, 2016

[6] Abbott, B. P. *et al.*, "GWTC-1: A gravitational-wave transient catalog of compact binary mergers observed by LIGO and Virgo during the first and second observing runs", *Physical Review X* 9.3, 031040, 2019

[7] V. B. Braginsky, S. E. Strigin, S. P. Vyatchanin, "Parametric oscillatory instability in Fabry-Perot interferometer", *Physics Letters A* 287.5-6, 331-338, 2001

[8] W. Kells, E. D'Ambrosio, "Considerations on parametric instability in Fabry-Perot interferometer", *Physics Letters A* 299.4, 326-330, 2002

[9] V. B. Braginsky, S. E. Strigin, S. P. Vyatchanin, "Analysis of parametric oscillatory instability in power recycled LIGO interferometer", *Physics Letters A* 305.3-4, 111-124, 2002

[10] L. Ju *et al.*, "Strategies for the control of parametric instability in advanced gravitational wave detectors", *Classical and Quantum Gravity* 26.1, 015002, 2008

[11] M. Evans, L. Barsotti, P. Fritschel, "A general approach to optomechanical parametric instabilities", *Physics Letters A* 374.4, 665, 2010

[12] S. P. Vyatchanin, S. E. Strigin, "Parametric oscillatory instability in gravitational wave laser detectors", *Physics-Uspekhi* 55.11, 1115, 2012

[13] M. Evans *et al.*, "Observation of parametric instability in Advanced LIGO", *Physical Review Letters* 114.16, 161102, 2015

[14] https://www.ansys.com

[15] H. J. W. Müller-Kirsten, E. Sattel, "Solution of the eigenvalue problem of an integral equation with the help of its associated differential equation applied to the calculation of diffraction losses in confocal resonators", *Journal of mathematical physics* 26.10, 2500-2509, 1985

[16] http://www.gwoptics.org/finesse

[17] C. Blair *et al.*, "First demonstration of electrostatic damping of parametric instability at Advanced LIGO", *Physical review letters* 118.15, 151102, 2017

2D fast timing readout system and hits clustering approach for new generation of Resistive Plate Chambers (RPC)

Konstantin Shchablo

Institut de Physique des Deux Infinis de Lyon

Abstract — We present a new generation of Resistive Plate Chambers (RPC). These chambers will be instrumented with precise timing readout electronics. A thin (0.6 mm) Printed Circuit Board (PCB), 165 cm long, equipped with pickup strips of an average pitch of 0.75 cm is inserted between the two RPC gaseous detectors. The strips are read out from both ends, and the arrival time difference of two signals is used to determine the particle position along the strip. This new signal readout method requested a new approach to clustering data. We developed a new clustering approach based on the principle of the time of arrival information. One of the realizations of this algorithm was tested based on data from a cosmic ray setup.

1 Introduction

The present Resistive Plate Chambers (RPC) have one layer. Designation position a long the chamber for this chamber is realized by three partitions. A combination of modernized gas detectors and new precision timing electronics give a possibility to design an improved RPC (iRPC) where the position could be measured from two-timing measurements of the hit (Fig. 1).

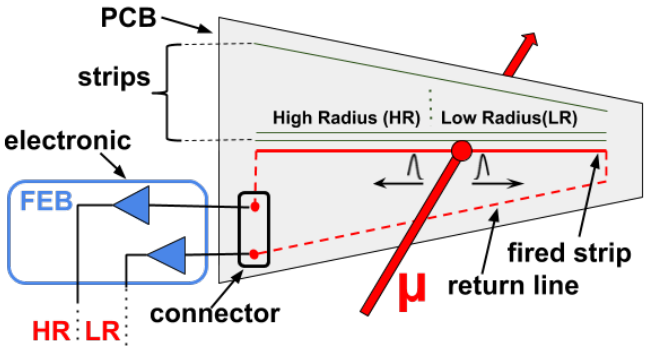

Figure 1: Illustration of the way the iRPC works.

The time of arrival method is one of the straightforward ways to realize the measurement position along the strip (orthogonal). TDoA uses information about the difference of arrival time from both ends of the readout strip. Conception of the proposed method and comparison of the TDoA between the standard readout system is shown in the following scheme (Fig. 2):

We can introduce the definition position and time resolution given the known speed of signal inside strips.

$$Y = \frac{L}{2} - \frac{v \cdot (t_2 - t_1)}{2} \tag{1}$$

Where, Y - position; L - full strip length; v - speed of signal inside strip; t_1 - time of signal arrival in first detector; t_2 - time of signal arrival in second detector;

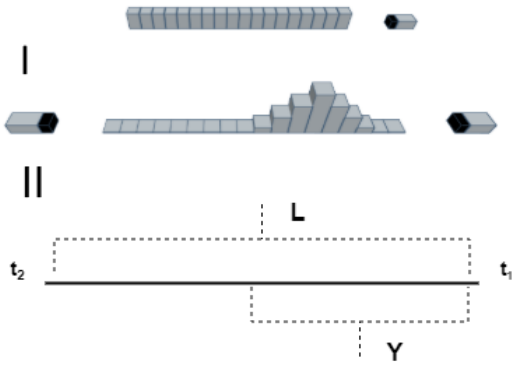

Figure 2: Schematic description of ToDA. I - Readout strip with one end. II - Readout strip with both ends.

$$\sigma(Y) = \frac{v \cdot \sigma(T_2 - T_1)}{2} \tag{2}$$

$\sigma(Y)$ - position resolution; v - speed of signal inside strip; T_2 - time resolution for second detector; T_1 - time resolution for first detector.

2 Scintillator setup

The new RPC includes Front-end Electronics with PETIROC [1] and a Time Digital Converter (TDC) [2]. TDC is providing, for each strip of the chamber, two values of time with a delay between each other. To study performance of detector we used external trigger based on scintillation counters. This trigger will allow us to plot hits profiles for this area. The scheme of the proposed measurement is plotted in fig. 3.

Using the time of the trigger that we mentioned, we can plot the difference between time of arrival and of triggers for the two chamber sides (Fig. 5 and Fig. 5). The time position is determined from the trigger time delay.

Multiplicity of current data is approximately equal

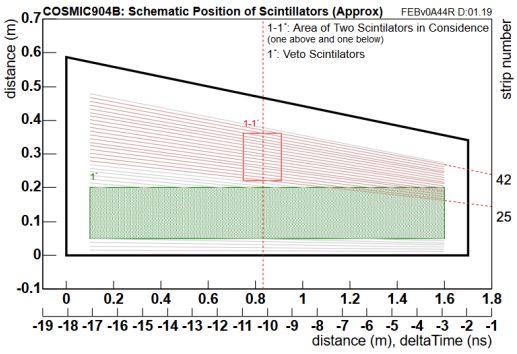

Figure 3: Scheme of the trigger.

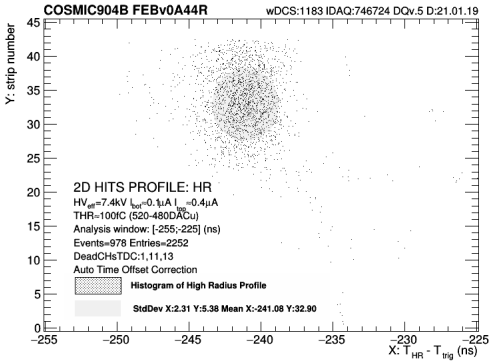

Figure 4: Example of hits profile: High Radius (HR) side.

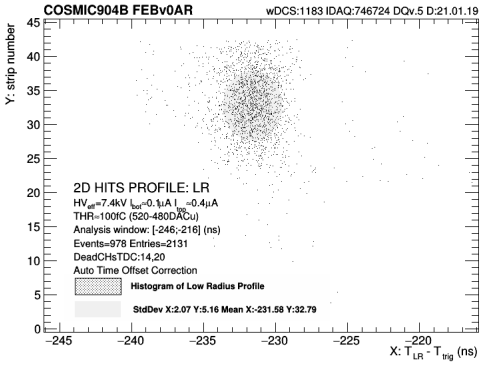

Figure 5: Example of hits profile: Low Radius (LR) side.

to three hits per trigger. This value depends on the geometry of the strip panel and the charge threshold of FEBs. Charge, in turn, depends on the GAP's thickness. It's important to mention that to reconstruct positions from this type of raw data, we have to use clustering.

3 Two-dimensional (2D) clustering algorithm

Our clustering approach is based on grouping all hits from one side, and the opposite side separately. Next, we could associate these clusters. In this case, we will be able to keep all arrived signals. When the chamber fired, all collected information split to the corresponding sides of the detector for two sets. Sets are processing independently in different threads. When the clusters are ready, they will associate on the following step. The output of this clustering could be only associated clusters that will be used for position reconstruction a long the strip. Also, we can keep groups of clusters without a couple from the opposite side that not possible to use for measurements position, but these clusters could be used for the control data.

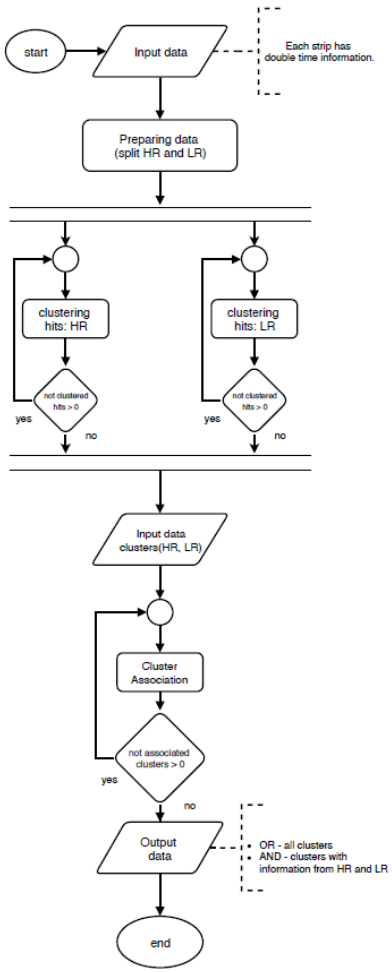

Figure 6: Block scheme of two-dimensional clustering algorithm.

An example of clustering for several scenarios could be shown with the following schematic (Fig. 7). It should be noted that this example is collective for several hits at the same time.

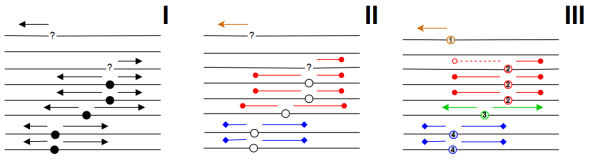

Figure 7: Example of clustering: I - input data; II - High and Low radius clustering; III - result of clustering.

With cluster algorithm we can plot cluster profile. (Fig. 8) Important characterisation for clustering is

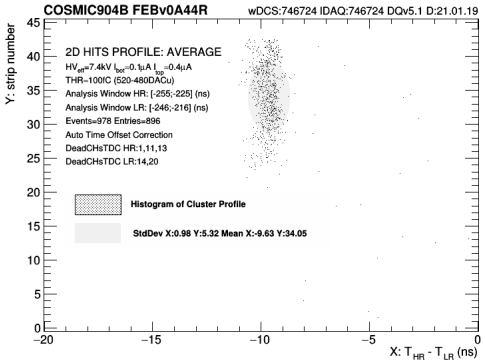

Figure 8: Example of cluster profile

cluster size and number of clusters that can be optimized. We will set only spatial clustering for sides (HR, LR). The thresholds of arrival time set without limitation. This assumption allows us to carry out all optimizations of the limit for the association of a couple of clusters from the chamber sides (Fig. 9 and Fig. 10)

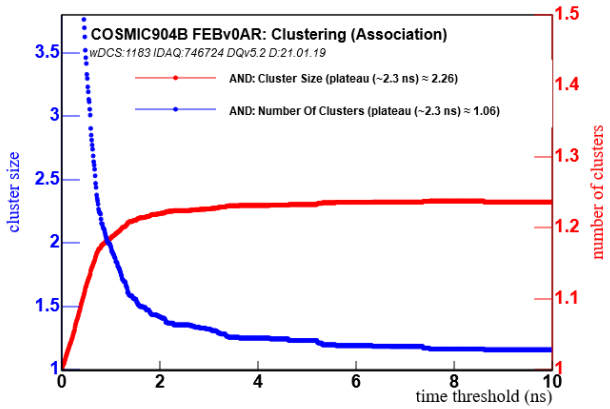

Figure 9: Fine-tuning of the clustering algorithm.

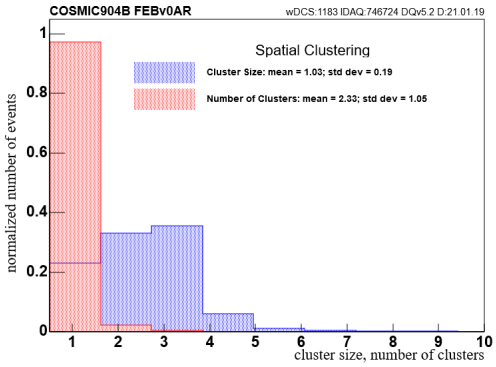

Figure 10: Cluster size and Number of cluster.

We can see clustering stabilization at a level of 1 cluster per event that should be from the given test.

4 Results

We showed one of the possible approaches for clustering data from the new generation of Resistive Plate Chambers with the 2D readout scheme. Data for the fine-tuning algorithm was taken by a setup based on a cosmic ray where the trigger includes two main scintillators, and in addition, one special veto scintillator outside the study area.

References

[1] J. Fleury et al., Petiroc, a new front-end asic for time of flight application, 2013 IEEE Nuclear Science Symposium and Medical Imaging Conference, conference record pp. 15, October 2013

[2] Pan, Weibin, Guanghua Gong and Jianmin Li. âA 20-ps Time-to-Digital Converter (TDC) Implemented in Field-Programmable Gate Array (FPGA) with Automatic Temperature Correction.â IEEE Transactions on Nuclear Science 61 1468 (2014).

Performance of n-in-p planar pixel sensors for ATLAS Inner Tracker to operate at High-Luminosity LHC

Reem H. Taibah

Laboratoire Physique Nucléaire et Hautes Énergies (LPNHE)

Abstract — In view of the High Luminosity LHC upgrade (HL-LHC), the ATLAS experiment plans to replace the current Inner Detector with an all-silicon Inner Tracker system (ITk). ITk will be instrumented with pixel and strip sensors with an n-in-p silicon technology to achieve tracking requirements with radiation hardness and cost efficiency. The paper reports on the performance of thin n-in-p planar pixel sensors produced by FBK-CMM and bump-bonded to the RD53a prototype chip. An overview of 2018-2019 testbeam results of hit efficiencies are given before and after irradiation.

1 Introduction

The Large Hadron Collider (LHC) is planning an upgrade to High-Luminosity LHC in 2026. The collider will operate at an instantaneous luminosity of 7.5×10^{34} cm^{-2}s^{-1}, about 5 times its current value. Increasing the luminosity is directly proportional to the rate of events per collision. Increasing the rate of events will increase the probability of rare events to occur. Therefore, this upgrade allows to extend the search for New Physics. For the ATLAS detector to cope with the harsher environment of events, one major upgrade is the replacement of the Inner Detector with a new all silicon Inner Tracker (ITk) of pixels and strips as shown in figure 1. To maintain the same performance of the

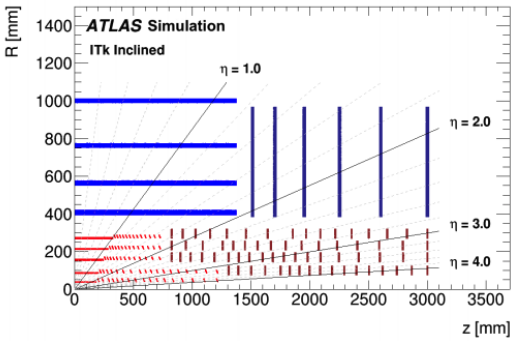

Figure 1: Schematics of one quarter of the layout in r-z axis of ITk including pixel detector (red) and strip detector (blue) covering pseudorapidity angle $\eta = 4$ [1].

current ATLAS detector, there are 3 main requirements for ITk: 1) high granularity by implementing smaller pitch pixels of 50×50 μm^2 or 25×100 μm^2, 2) radiation hardness for planar sensors up 3×10^{15} n_{eq}cm^{-2}[1] and 3) pixels to have hit efficiency $> 97\%$.

[1] n_{eq}: neutron equivalent unit is of particular interest in high energy physics. It is the fluence of 1 MeV neutrons producing the same damage in the material as induced by an arbitrary particle fluence with a specific energy distribution.

2 N-in-p pixel sensors

N-in-p technology is chosen for all ITk silicon sensors. Pixel sensors investigated at LPNHE[2] are produced at the FBK-CMM foundry[3] . The sensor's bulk is doped with Boron atoms and its surface with Phosphorus atoms to create the junction. Sensors are produced in 6" wafers and then diced into bare sensors with dimensions of 11.8 mm high and 20 mm wide to match the size of its designated prototype readout chip the RD53a [2]. To read out signals, sensors are bonded to the readout chip via solder bump balls. Each pixel on the sensor is bump bonded to a pixel on the readout chip. The combination of the silicon sensor bonded to the readout chip produces the hybrid module as shown in figure 2. The hybrid module is then assembled by wire bonds to a Printed Circuit Board (PCB) to enable electrical characterization and calibration of the hybrid module.

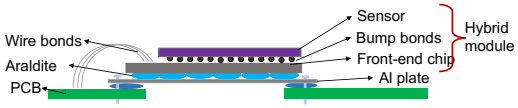

Figure 2: Sketch of a module assembly. A module consist of the hybrid module wire bonded to a PCB.

For the tracking performance at ITk, pixel sensors are required to have pixel size of 50×50 μm^2 or 25×100 μm^2 as shown in figure 3. ITk pixel sensor size is 10 times smaller than what is currently installed in the ATLAS pixel detector. Pixels are grounded via biasing structure to deplete the sensor bulk. The biasing structure can employ a biasing dot that serves 4 neighboring pixels. These sensors are compatible with the RD53a readout chip that is composed of 192 rows and 400 columns to make an array of 76,800 pixels. The RD53a is a prototype chip designed by the RD53 international collaboration [3]. The chip has

[2] http://lpnhe.in2p3.fr/
[3] https://cmm.fbk.eu/

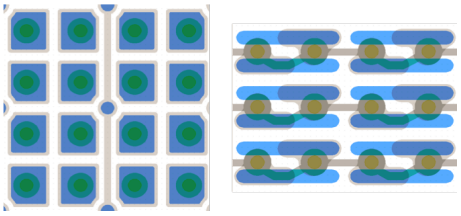

Figure 3: layout for the two types of ITk sensors with pitch size of 50×50 μm^2(left) and 25×100 μm^2(right).

50×50 μm^2 pixel size with the same dimensions of the sensor 11.8×20 mm[2]. For research and development purposes the RD53a chip matrix is divided in 3 regions, each region is equipped with a different analog front-end design or "flavor" to evaluate the performance of the design. Front-end "flavors" are Linear, Differential and Synchronous. Only one front-end will be chosen and passed on to the next production of the chip.

To ensure the quality of the module operation, the electrical properties are measured at each step of the module assembly beginning at wafer level, bare sensor level and module level. To study the module performance, modules are measured in a testbeam setup which provides similar condition as of the HL-LHC using high-energy particle beam. In these conditions the module's efficiency, radiation hardness and tracking performance are investigated.

3 Irradiation

Radiation hardness up to 3×10^{15} $n_{\text{eq}}\text{cm}^{-2}$ is one of ITk requirements for planar pixel sensors. They are irradiated to different fluences to study their performance under real conditions. Modules are measured in testbeam conditions before and after irradiation. Several facilities offer to irradiated devices based on the target fluence. Examples of irradiation facilities include: PS Irrad facility at CERN [4] and Birmingham irradiation facility [5]. Each facility offers different irradiation beam type and specification.

LPNHE modules have been irradiated at the PS Irrad facility at CERN which has 24 GeV proton beam with a 10×10 mm^2 FWHM Guassian beam profile. Given that the irradiation beam has the bi-variate normal profile smaller than the target surface, the procedure results to a non-uniform irradiation throughout the module. The fluence estimate has a 20% uncertainty from measurements and fitting the beam profile from the dosimetetry results of the irradiation. While Birmingham irradiation facility has a beam of 23 MeV with the same dimensions 10×10 mm^2 that uniformly scans the surface of the target which produces a uniform irradiation over the whole module.

4 Module tuning

Tuning is a process of multiple scanning procedures to set the discriminator of the chip at a certain value. The chip has an individual discriminator for each pixel to set the threshold. The tuning process adjusts the per-pixel threshold to have a uniform response of the hybrid. Tuning the RD53a readout chip is performed using the BDAQ53 readout board [6]. Each front-end flavor of the RD53a is tuned separately. The modules are tuned to lowest possible threshold with minimum noise, optimally at about 1000e.

5 Characterisation with high-energy particle beam

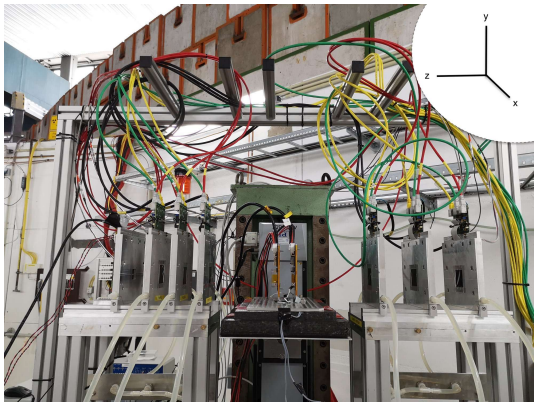

Figure 4: Image of testbeam setup at DESY. Telescope planes are fixed along the beam-z-axis while the DUTs can move upward/downward on the y-axis, inward/outward on the x-axis.

Pixel modules are irradiated, tuned and characterized with a high-energy particle beam to study their performance under conditions of the HL-LHC environment. Testbeam setups are available at CERN providing a particle beam with 120 GeV pions and at DESY providing 1-6 GeV electrons [7]. The measurement period at the testbeam is organised and shared among ITk collaboration.

Characterization setup is shown in figure 4 at the DESY testbeam hall [7]. The setup includes 6 Mimosa telescopes parallel to each other on the z-axis and separated into two arms, upstream and downstream planes. In between the arms the Device Under Test (DUT) box is placed. Modules are mounted in the DUT insulating box to ensure consistent temperature and humidity during measurement. The telescope planes are enclosed by scintillators from both ends for external triggering. The planes are connected to a Trigger Logic Unit (TLU) and the readout system BDAQ53 or Yarr [8] for data collection.

Modules are tuned before measurement and are measured before and after irradiation. Irradiated modules must be kept in low temperature to prevent thermal runaway due to the large level of leakage current in the bulk of the sensor. The DUT box is cooled down using dry ice that brings the temperature to $-50°C$. In the setup shown in figure 4 the electron beam travels through the planes from right to left. The modules can

be positioned so the beam traverses in the center of the measured region. Due to the lower energy particle beam at DESY only 2 modules are mounted and measured simultaneously to minimize the effect of multiple scattering [9]. Whilst at CERN up to 6 modules can be measured simultaneously thanks to the high energy beam.

6 Results

Track reconstruction and analysis

Particle trajectories from the testbeam measurements are reconstructed using the Eutelescope software framework [10]. The software provides the necessary processors to run the full track reconstruction starting from the testbeam raw data files. Tracks are reconstructed following the General Broken Lines model (GBLFit) [11]. The alignment level can be quantified by the residual distributions produced in Eutelescope. The residual is the distance between the hits on the plane and the fitted track of the same plane. The residual width have several contributing effects such as the intrinsic resolution and the multiple scattering effect. The intrinsic binary resolution correlates to the pitch of the sensor by

$$\textit{binary resolution}\ [\mu\text{m}] = \frac{\textit{pitch size}\ [\mu\text{m}]}{\sqrt{12}}. \quad (1)$$

The output file of Eutelescope is analyzed further by Tbmon2 [12]. Tbmon2 is an offline post-reconstruction framework for testbeam data analysis and graphical interface.

Hit efficiency

The hit efficiency is calculated as the number of hits associated to tracks divided by the the no. of reconstructed tracks. ITk sensors require hit efficiency no less than 97%. The hit efficiency is investigated while scanning the bias voltage to deplete the sensor.

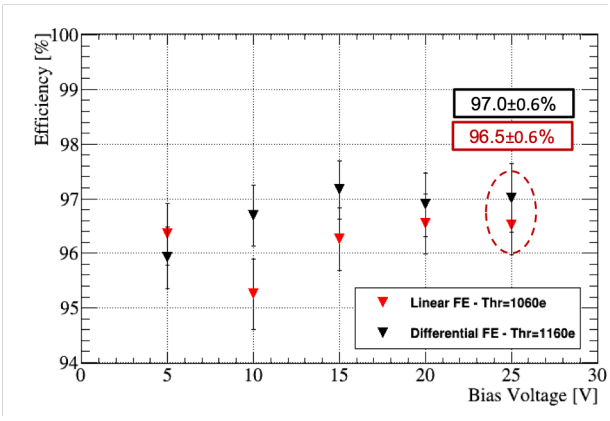

Figure 5: Hit efficiency vs. bias voltage for ITk sensor with $25 \times 100\ \mu\text{m}^2$ pitch size comparing both linear and differential front-ends.

The analysis region is defined by the area of the front-end regions. Figure 5 shows the hit efficiency for a non-irradiated ITk sensor with $25 \times 100\ \mu\text{m}^2$ pitch without biasing dot. Both linear and differential front-ends are measured simultaneously. The linear front-end is tuned to threshold of 1060 e and the differential front-end is tuned to 1160 e. At full depletion the non-irradiated sensor shows hit efficiency of $96.5 \pm 0.6\%$ for the linear front-end and $97 \pm 0.6\%$ for the differential one. Within the uncertainty these values are consistent and compatible with ITk requirements.

The hit efficiency vs. bias voltage is investigated for modules also after irradiation. Figure 6 shows the hit efficiency for the linear front-end for a $50 \times 50\ \mu\text{m}^2$ pitch sensor irradiated at $\Phi = 3.5 \times 10^{15}\ n_{\text{eq}}\text{cm}^{-2}$. The same module is measured at 2 different tuned thresholds; 1400 e and 1180 e. At 500 V the lower threshold value (black plot) achieves an efficiency of $96.8 \pm 0.4\%$ while the at higher tuned threshold (blue plot) the module achieves $95.29 \pm 0.16\%$. Measurement with lower threshold value shows earlier saturation of efficiency at 200 V. Comparing efficiencies for both thresholds at 200V, the lower tuned threshold shows about 15% higher efficiency.

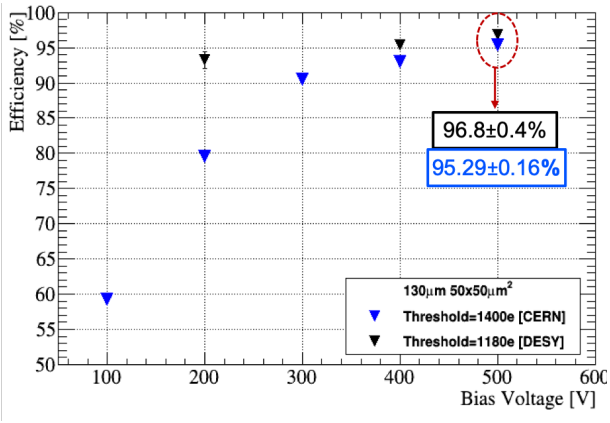

Figure 6: Hit efficiency vs. bias voltage for ITk sensor irradiated to $\Phi = 3.5 \times 10^{15}\ n_{\text{eq}}\text{cm}^{-2}$ with $50 \times 50\ \mu\text{m}^2$ pitch size comparing different tuned threshold values.

After irradiation the hit efficiency can be reduced due to the radiation damage, since trapped charge carriers decrease the hit efficiency. Investigating different irradiation levels for sensor with $25 \times 100\ \mu\text{m}^2$ pitch. The linear front-end has fluence of $\Phi = 3.5 \times 10^{15}\ n_{\text{eq}}\text{cm}^{-2}$ and differential front-end has fluence of $\Phi = 1.3 \times 10^{15}\ n_{\text{eq}}\text{cm}^{-2}$. The module is tuned to threshold of 1300e. As shown in figure 7 at 500V, both irradiation levels can achieve up to 99% within the uncertainty. It is visible at lower bias voltages that at higher fluence the module is much less efficient due to the higher level of irradiation damage. Therefore modules irradiated to lower fluences would achieve higher efficiency and saturates at low bias voltages.

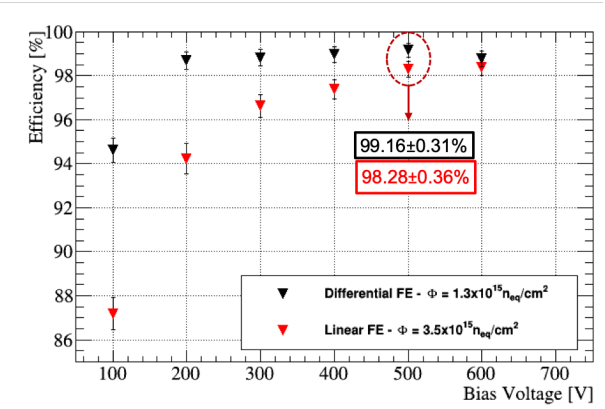

Figure 7: Hit efficiency vs. bias voltage for ITk sensor with 25 × 100 μm^2 pitch size comparing different irradiation levels.

In-pixel efficiency map

The in-pixel efficiency map is the 2D representation of the overall efficiency of each pixel in the sensor folded in one region. Shown in figure 8 is a 2 × 2 folded efficiency map to reveal the pixel geometry and resolve the substructure of the sensor. The figure shows the efficiency map for a 50×50 μm^2 pitch sensor (left) and for 25×100 μm^2 (right) at 500V. The efficiency map for the 50 × 50 μm^2 pitch sensor with biasing structure shows visible hit efficiency loss in the biasing structure region in-between the pixel implants. The biasing dot is n^+ implant that attracts charge and therefore introduces the visible inefficiency. moreover, sensors without biasing structure show more uniform efficiency maps as shown in figure 8 for the 25 × 100 μm^2 pitch sensor. These sensors also achieve higher overall efficiency.

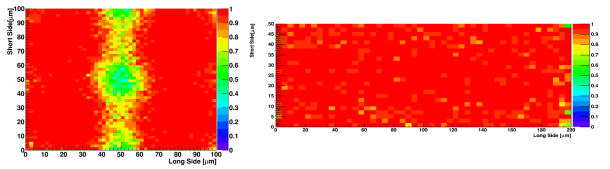

Figure 8: 2×2 in-pixel efficiency map at 500V for both types of ITk sensors 50×50 μm^2 (left) and 25×100 μm^2 (right). These are the in-pixel efficiency map for the same structures in figure 3.

7 Conclusions

The n-in-p sensor technology with 50 × 50 μm^2 or 25 × 100 μm^2 pixel size is chosen as a baseline concept for ITk to cope with HL-LHC environment. The performance study for both types of ITk sensors shows that biasing structure reduces the efficiency of the sensor. For non-irradiated sensors the hit efficiency reaches up to 97%. While for an irradiated 50 × 50 μm^2 pitch sensor similar efficiency for different tuned threshold values at the highest biasing voltage while the sensor with the lower tuned threshold achieves earlier saturation of hit efficiency. For a 25 × 100 μm^2 pitch sensor tuned to 1300e investigating different fluences shows that at high bias voltage they are compatible with ITk requirements achieving efficiency > 97%. Lower irradiation level achieves earlier saturation of efficiency at 200 V due to less damage in the bulk.

Performance studies cumulatively optimize the design and production of the modules. Currently in 2020 the Market Survey phase is on-going to anonymously measure RD53a modules from different production institutes to commission the best suitable production foundry for ITk sensors.

References

[1] ATLAS collaboration, Expected Tracking Performance of the ATLAS Inner Tracker at the HL-LHC, ATL-PHYS-PUB-2019-014.

[2] M.Garcia-Sciveres, The RD53A Integrated Circuit, CERN-RD53-PUB-17-001, 2017.

[3] S.Marconi, Design and optimisation of low power hybrid pixel array logic for the extreme hit and trigger rates of the large hadron collider upgrade CERN-THESIS-2017-400.

[4] F.Ravotti B.Gkotse M.Glaser P.Lima E.Matli M.Moll, A new high-intensity proton irradiation facility at the CERN PS east area, AIDA-CONF-2014-019.

[5] P.Dervan R.French P.Hodgson Marin-Reyes K.Parker J.Wilson M.Baca, Upgrade to the Birmingham Irradiation Facility. AIDA-PUB-2015-013.

[6] Characterization and Verification Environment for the RD53A Pixel Readout Chip in 65nm CMOS, DOI:10.22323/1.313.0084.

[7] The DESY II Test Beam Facility,Nucl. Instr. and Meth. A 922 (2019) 265-286.

[8] T.Heim, YARR - A PCIe based Readout Concept for Current and Future ATLAS Pixel Modules, 2017 J. Phys.: Conf. Ser.898 032053.

[9] Phys. Rev. D 98, 030001 (2018) and 2019 update. M. Tanabashi et al. (Particle Data Group).

[10] H.Perrey, EUDAQ and EUTelescope Software Frameworks for Test Beam Data Aquisition and Analysis, 2014. PoS TIPP2014 (2014) 353.

[11] C.Kleinwort, General Broken Lines as advanced track fitting method, Nucl. Instr. and Meth. A 673, (2012) 107-110.

[12] K.N.Sjobak, Full simulation of a testbeam experiment including modeling of the Bonn atlas telescope and atlas 3D pixel silicon sensors, CERN-THESIS-2010-247.

Part VI

Neutrino Physics

session chaired by Laura ZAMBELLI

Signal and trajectories reconstruction in ProtoDUNE Dual-Phase Liquid Argon TPC

Etienne Chardonnet

University of Paris, CNRS, Astroparticule et Cosmologie, F-75013 Paris, France

Abstract — The Deep Underground Neutrino Experiment (DUNE) is a long-baseline project studying an accelerator-made neutrino beam produced at Fermilab. DUNE consists of two detectors placed in the path of the neutrino beam, one near the source and one at the Stanford Underground Research Facility, at a distance of 1300 km and protected by a 1500 m rock overburden. Fundamental features of neutrino oscillation physics, such as leptonic CP violation and the neutrino mass hierarchy, as well as supernovae and proton decay physics will be studied with high precision during more than 10 years of data taking, starting in 2026. The far detector technology consists of four $60 \times 12 \times 12$ m^3 time-projecting chambers (TPC), each module having 10kt of liquid argon (LAr) fiducial mass. Two designs are currently under study for the far detector : one with only liquid argon (Single-Phase), the other containing a small volume of gaseous argon at the top of the active volume (Dual-Phase). Both designs are currently being tested with $6 \times 6 \times 6$ m^3 prototypes at CERN. Regarding Dual-Phase, all aspects of the detectors have the same size as those for the final far detector except for the drift length (6 m against 12 m). My PhD is centered on the Dual-Phase technology and in particular on the development of signal and trajectory reconstruction algorithms created or adapted for its unique features.

1 Introduction

DUNE is part of a new generation of neutrino experiments aiming to finally measure with a precision above 5σ fundamental neutrino oscillation quantities from the PMNS matrix such as δ_{CP} and the sign of Δm^2_{31}. It is a long-baseline accelerator-based experiment meaning that we will be studying the oscillations of a pure neutrino beam, muon-neutrinos, generated by an accelerator, between a near and a far detector [1]. DUNE will be using a liquid argon time projection chamber technology (LArTPC) first imagined in 1977 for the noble nature, cheapness and density of liquid argon [2]. ICARUS and GLACIER were two crucial experiments regarding LArTPCs respectively demonstrating the feasability of the "Single-Phase" (SP) technology , using only liquid argon, at the tonne-scale [3] and pioneering the concept of large scale "Dual-Phase" (DP),that includes a small volume of gaseous argon, for neutrino studies [4]. Along with having a gigantic active volume, DUNE's detection technique ensures a very high spatial resolution (3 mm) in all 3 dimensions hence allowing to resolve complex neutrino interactions with argon atoms. The Dual-Phase design of LArTPC is being developed alongside with SP in the current prototyping stage ProtoDUNE. ProtoDUNE-DP has started commissioning and taking cosmics data during summer 2019. We now have to demonstrate the viability of the DP technology for it to be chosen as one of the four modules that constitute the DUNE's far detector.

2 DUNE physics

The primary physics program of the DUNE experiment is centered around the measurement of neutrino oscillation parameters. The ν_μ-disappearance is the phenomena where we detect less muon neutrinos in the far detector than in the near detector (they "disappear" along the way). On the other hand, the ν_e-appearance is when we detect more electron neutrinos in the far detector. Those are the two oscillation channels involved in the measurement of θ_{23} (for the former) and δ_{CP} and Δm^2_{31} (for the latter). DUNE's neutrino beam will be able to switch from neutrino mode to anti-neutrino mode which enables to study the CP violation and mass ordering parameters. Thanks to DUNE's very long baseline, neutrinos will travel through the Earth crust long enough to generate a large asymmetry between neutrino and anti-neutrino oscillations caused by neutrinos interactions with matter. In order to perform those measurements it is obviously crucial to have a functioning and stable detector but it is just as important to have optimized signal and trajectory reconstruction algorithms.

We are interested in Charged-Current (CC) neutrino interactions, which gives us the flavor and the directionality of the neutrino. These interactions leave a clear signature in the detector for all three flavors. Tau neutrino appearance is much rarer but will occur in the energy range of DUNE's neutrino beam (0-8GeV) and thus are part of the so called "Ancillary" physics program.

This program includes the study of other accelerator-based neutrino oscillations with the tau neutrinos appearance but also sterile neutrinos and other non-standard interactions. The low detection threshold,

~10 MeV, of the LArTPC makes possible the detection of core-collapse supernova neutrinos which is an event that could happen in the lifetime of the experiment. Due to space constraints, other relevant aspects of the DUNE physics program will not be addressed in this proceeding; more information can be found in Ref [2].

3 A Dual-Phase Liquid Argon TPC

In ProtoDUNE-DP all detector components are the same size as would be used in the final far detector module. One important difference, however, is the drift length, which is 6 m in ProtoDUNE-DP and will be 12 m in the DP far detector module.

After the crossing of a charged particle in the fiducial volume, the ionization electrons are drifted vertically in a fully homogeneous argon active volume towards the segmented anode at the top of the detector by an homogeneous electric field. Before reaching the anode, the ionization electrons are extracted from liquid to gas by a submersed extraction grid. The electron signal is then amplified by the Large Electron Multipliers (LEMs). These are large, 1mm thick squares made of PCB, placed only a few mm above de LAr surface within the ultra pure argon gas. The signal is amplified when the electrons pass through the micro-metric holes that have been drilled through the LEMs, on their way towards the anode. The ionization electrons are amplified by avalanches (Townsend multiplication) occurring in the argon gas in this micro-pattern structure due to the high electric field (30 kV/cm). The amplification is a specific feature of the Dual-Phase design allowing a tunable gain to achieve high Signal-to-Noise ratio and also to counterpart the possible signal loss during the drift of the electrons. The charge is eventually collected on a segmented 2D horizontal readout anode plane, composed of 2 perpendicular collection views sharing equal amounts of charge. The anode plane is situated at the top of the gas volume and fed to the front-end accessible cold electronics to achieve a low noise level. At the bottom of the detector, 8-inch cryogenic PMTs with TPB coatings are placed below the cathode. Their primary objective is to detect scintillation light from the de-excitation of ionized argon atoms. This gives the time of the ionization necessary, when associated with the collection time given by the anode, to reconstruct the absolute vertical position of the interaction and finally the 3D the trajectory of a charged particle.

4 Muon trajectory reconstruction

The fact that we read the ionization signal on only 2 views creates difficulties in the reconstruction. Each view is basically a 2D projection of the interaction. With the current state of reconstruction algorithms, having only two pictures to perform the 3D reconstruction sometimes leads to ambiguous situations.

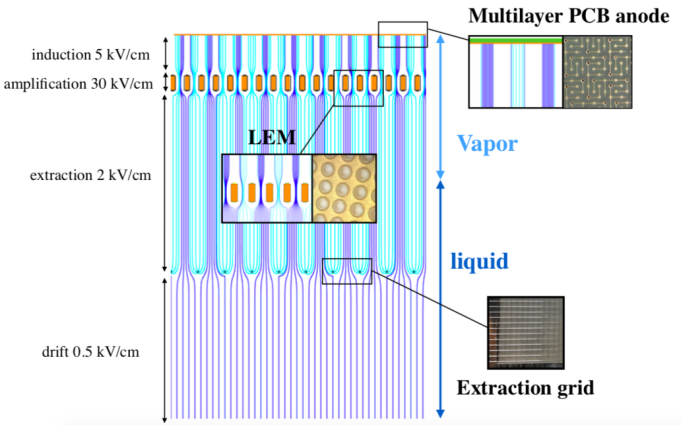

Figure 1: Vertical slice of the Dual-Phase detector. The drift field is applied over 6 m whereas the extraction field is applied in 5 mm of liquid and 5 mm of gas. The amplification and induction fields are generated respectively in the 1 mm-thick LEMs and the 5 mm between the LEMs and the anode.

Around 50k muons have been simulated for this study and reconstructed using Pandora, a multi-algorithm software adapted for the imaging performances of the LArTPC technology [5]. Two situations were found to cause trouble : when muons were travelling horizontally or parallel to one view.

4.1 Horizontality

In the Dual-Phase geometry, the two projections we are working with to reconstruct the event in 3D share the vertical direction. Hence the vertical position (X) is used to match two pixels from each view. When a muon travels horizontally, all pixels in both views have the same vertical position. The reconstructed trajectory has been found to be quite unphysical as depicted in figure 2. The algorithm mismatches two pixels therefore the two corresponding unmatched pixels will be mismatched as well. This creates those wave-looking trajectories **in the horizontal (Y,Z) plane** (which corresponds to the matching plane).

The issue here is that Pandora's view matching algorithm, in addition to looking at the vertical position as the primary reason to match two hits, is performing a fit in order to keep the trajectory smooth in the horizontal plane. In other words it will associates hits such that the trajectory stays smooth. It is possible however to overcome this by putting constraints on the result of the fit and the matching choices.

Two leads are currently being studied :

- Put limits on the trajectory's direction changes.
- Force the matching of hits in the order in which they are stored in the data.

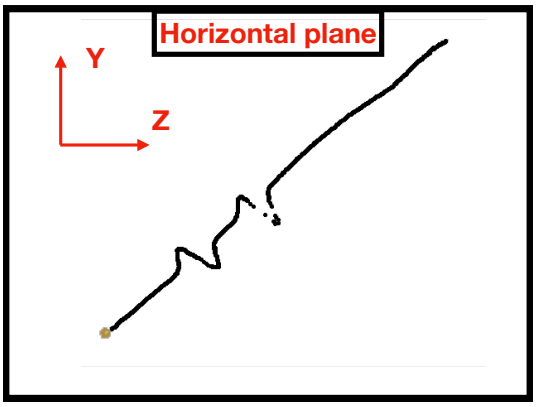

Figure 2: Event display of the reconstructed trajectory of a simulated horizontal muon **in the horizontal plane**. The wavy shapes appearing along the reconstructed muon track are the result of hits mismatching between the two views.

The latter should be more robust when associated with a check on the charge of each hit, thus verifying if the particle isn't going backwards somewhere along the way.

4.2 View parallelism

In the case when muons travel parallel to a view (and are therefore perpendicular to the other view), the ionization signal is collected on the same strip over an extended period of time. The signal waveform, that one has to reconstruct to form one pixel of one view, is strongly modified and the current signal reconstruction algorithm cannot manage to fit its new shape because of how different it is from the usual waveform (Fig.3). We have plotted the reconstruction efficiency as a function of the horizontal angle. We observe a clear drop in efficiency within 10° from the parallel. (Fig.4)

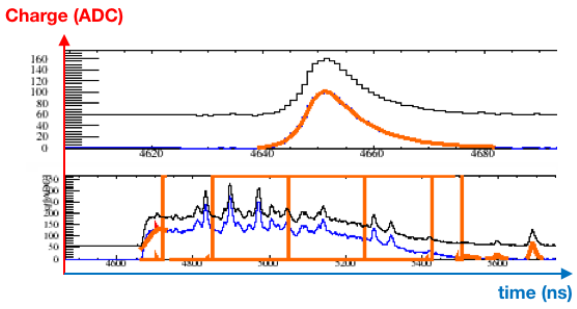

Figure 3: The waveforms are printed as an ADC count versus time. There is one per strip. On top, waveform coming from a non-parallel muon. At the bottom, from a muon parallel to the specific strip. Black bins are the raw signal, orange curve is the fit. An ADC pedestal is also simulated as a 60 ADC offset in the raw signal and has to be removed during the fit in order to obtain the correct charge content of the hit.

The hit waveform reconstruction is performed by fitting the signal with the following function where A,B,C,D and E are fitting parameters and t is the time :

$$f(t) = A\,\frac{e^{\frac{0.4(\,t\,-\,B\,)}{C}}}{1+e^{\frac{0.4(\,t\,-\,D\,)}{E}}}$$

At the time of this writing, when several hits are believed to be superimposed, like in the parallel case, we simply sum fit functions until we obtain a satisfactory χ^2. However this is not sufficient in the presence of waveforms like shown in the bottom of figure 3.

Developments of algorithms using the deconvolution to disentangle the superimposed waveforms have shown promising results and is currently being implemented.

The reconstruction efficiency is plotted as a function of the horizontal angle. We observe a clear drop in efficiency within 10° from the parallel. (Fig.4)

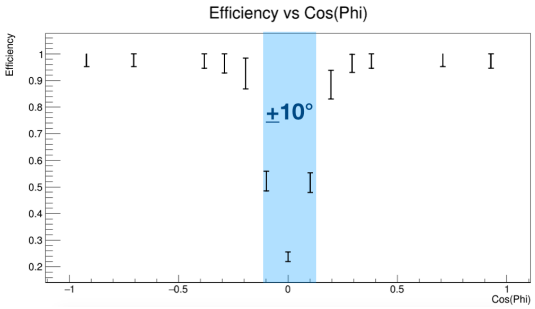

Figure 4: Reconstruction efficiency as a function of the horizontal angle. The efficiency drops drastically when muons are travelling ±10° from parallel to a view (when Cos(Phi)=0).

5 Conclusions

DUNE is a very ambitious experiment that will start taking data in 2026. In the meantime the ProtoDUNEs are being actively studied and in particular the much more recent concept-wise Dual-Phase prototype. We have to demonstrate the feasibility of this technology in terms of stability and reconstruction performances. Concerning the signal analysis, 50k muons have been simulated and the issues related to particles travelling horizontally or parallel to one view have been identified. Horizontal particles makes the view matching difficult to perform due to the hits all having the same vertical position. New algorithms using the charge information are being developed with the help of Pandora's developer. On the other hand, parallel muons are depositing an important amount of charge one the same anode strip over an extended period of time. The current waveform reconstruction algorithms are strongly underperforming on the concerned strips for all muons travelling within 10° from the parallel. Deconvolution has shown promising results on waveforms coming from data of the Single-Phase technology and shall be implemented in the Dual-Phase framework.

References

[1] LBNF and DUNE Conceptual Design Report Volume 2: The Physics Program for DUNE at LBNF (2016) arxiv:1512.06148

[2] C. Rubbia, *The Liquid Argon Time Projection Chamber: A New Concept for Neutrino Detectors*, (1977)

[3] S. Amerio et al., *Design, construction and tests of the ICARUS T600 detector*, Nucl. Instr. Meth. A527 (2004)

[4] A. Rubbia, *Underground Neutrino Detectors for Particle and Astroparticle Science: the Giant Liquid Argon Charge Imaging ExpeRiment (GLACIER)*, (2009) arxiv:0908.1286

[5] The Pandora multi-algorithm approach to automated pattern recognition of cosmic-ray muon and neutrino events in the MicroBooNE detector (2017) arxiv:1708.03135

Light sterile neutrino search with the STEREO experiment at ILL

Loïc-René Labit

Laboratoire d'Annecy de Physique des Particules Université Savoie Mont Blanc, 9 chemin de Bellevue 74940 Annecy

Abstract — During the last decades, reactor neutrino experiments allowed us to characterize the neutrino oscillations, in particular the mixing angle θ_{13} has been precisely measured. However, a 3σ discrepancy between the observed and expected antineutrino flux, known as Reactor Antineutrino Anomaly (RAA), has yet to be solved. This anomaly could be due to the existence of a sterile neutrino state participating in the oscillation. The parameters value that best fit this oscillation are : $\sin^2(2\theta_{new}) = 0.14$ and $\Delta m^2_{41} = 2.4$ eV^2 . The STEREO experiment was designed to test this oscillation hypothesis, by measuring the energy spectrum and flux of the antineutrinos emitted by the compact research reactor core of the Laue-Langevin Institute (Grenoble, France). The detector, segmented in six cells and located at about 10m from the reactor core, allows for a measurement of the energy spectrum at various baselines. The oscillation toward a sterile neutrino would be detected thanks to the different oscillation imprint left in each cell. Ongoing data taking has begun in 2016. In 2018 the STEREO collaboration published its first results excluding a significant part of the parameter space and excluding the RAA best fit with a confidence level of 99%.

1 Introduction

Following the re-evaluation of anti-neutrino spectra from reactor core in 2011 [1, 2]: a 7%, 3σ discrepancy between the measured and the newly predicted flux of anti-neutrino has been found at short baseline. The deficit, known as reactor anti-neutrino anomaly (RAA) could either be the result of underestimated systematics in the prediction or the existence of a light sterile neutrino state. A sterile neutrino state would not interact through weak interaction but would oscillate with the other active flavors. The oscillation toward a sterile neutrino state would result in a baseline and energy dependent distortion of the electronic anti-neutrino energy spectra.

The survival probability of electronic anti-neutrinos at short baseline is given by:

$$P_{\nu_e \to \nu_e}(L,E) = 1 - \sin^2(2\theta_{ee}) \sin^2\left(1.27 \Delta m^2_{41} \frac{L}{E}\right) \quad (1)$$

where E and L are respectively the anti-neutrino energy in MeV and the baseline in meters, θ_{ee} denotes the mixing angle and $\Delta m^2_{41} = m^2_4 - m^2_1$ stands for the difference of the squared eigenvalues of the new mass eigenstate and the first mass eigenstate. The RAA is best explained by an oscillation with parameters: $\sin^2(2\theta_{ee}) = 0.14$, $\Delta m^2_{41} = 2.4eV^2$ [3] for which the maximal amplitude of the distortion is expected to be at baseline below 10m. The survival probability is energy and baseline dependent thus a segmented detector allows for a relative measurement independent from predictions. The STEREO experiment is designed to test the sterile neutrino hypothesis independently of rate or spectral shape predictions.

2 The STEREO experiment

The STEREO detector (Figure 1) is located at the ILL research institute in Grenoble France, at a distance of approximately 10m from the compact research reactor core. The ILL reactor is a compact heavy water reactor core with 58.3 MW nominal thermal power working with 93% ^{235}U enriched fuel. The STEREO detector is a gadolinium (Gd) loaded liquid scintillator detector whose fiducial volume of 2.4m^3 is segmented into 6 identical and optically isolated cells. The target cells are surrounded by a Gd-free outer crown called Gamma Catcher. The whole detector is topped with a water Cerenkov muon veto. The anti-neutrinos are detected via the inverse beta decay (IBD) process:

$$\bar{\nu_e} + p \to e^+ + n$$

A time coincidence search between a prompt signal resulting from the positron annihilation and a delayed signal given by the neutron capture on gadolinium after thermalisation is carried out.

3 Liquid non-linearity response study

While travelling through the liquid scintillator a particle will deposit its energy in the scintillator through ionisation, Compton and photo-electric effects. The excited scintillator molecules relaxe by producing scintil-

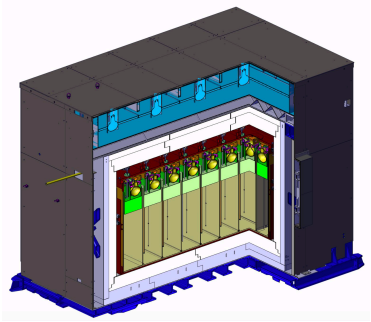

Figure 1: Side view of the STEREO detector: the target is composed of 6 cells filled with Gd-loaded liquid scintillator and surrounded by an Gd-free outer crown. The whole detector is topped by a Cerenkov muon veto

lation photons that are then detected by the photomultipliers. The number of scintillation photons depends on the deposited energy, however this dependence is not linear and can be described by the empirical Birks' law:

$$\frac{\mathrm{d}L}{\mathrm{d}x} = S\frac{\frac{\mathrm{d}E}{\mathrm{d}x}}{1 + K_{Birks} \times \frac{\mathrm{d}E}{\mathrm{d}x}} \qquad (2)$$

where S is the scintillation efficiency (number of scintillation photons by unit of deposited energy), L is the light output (amount of scintillation photon), K_{Birks} is the Birks parameter that characterizes the liquid scintillator and $\frac{dE}{dx}$ is the energy loss by unit of track length, which depends on the energy of the particle. To probe this non-linearity, the STEREO collaboration has a set of radioactive calibration sources with energies ranging between 0.5 and 4.44 MeV:

Sources	^{137}Cs	^{54}Mn	^{65}Zn	^{42}K	^{24}Na	AmBe
E[MeV]	0.66	0.83	1.12	1.52	1.372 2.750	4.44 n

A first study of the non-linearity has been performed in 2017 (Figure 2). It showed a Data-Monte Carlo agreement at the percent level, but large uncertainties are considered.

In order to reduce the uncertainties and check the Data-MC agreement at a subpercent level. We have developed a new strategy: the radioactive source is placed in the neighboring cell to have a better energy separation of the gammas for the multi-gamma source (^{2}4Na) and background mitigation for the AmBe source. An iterative fitting procedure has been set up: A first gaussian fit on a limited range around the maximum of charge is performed $[Q_{max} \pm 1.3\sqrt{Q_{max}}]$ to avoid bias in the peak width due to a potential non-gaussian shape of the peak. The mean and standard deviation evaluated by the first fit are given as initial parameters for the second fit which is performed on an asymmetric range $[Q_1^{mean} - 1.5\sigma; Q_1^{mean} + 3\sigma]$ to avoid bias in the mean due to a non-gaussian tail at low energy. A calibration coefficient (CC) for each source is then computed by taking the mean of the second fit and the average

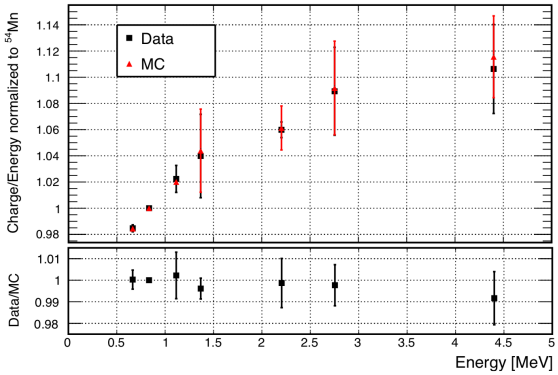

Figure 2: Non-linearity of the liquid scintillator response of the target in 2017[4]. Data and MC points are normalized to the ^{54}Mn. Data-MC ratio is normalized to the ^{5}4Mn ratio.

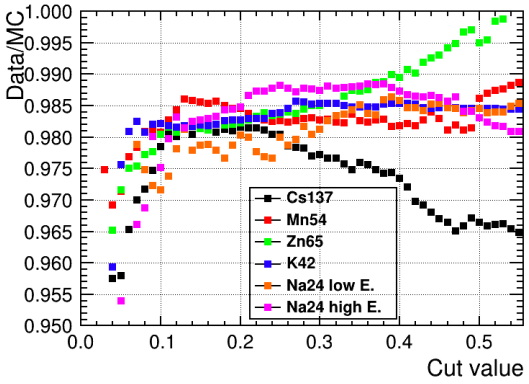

Figure 3: Data to MC ratio of the CC for various isolation cut X.

deposited energy evaluated by MC simulation:

$$CC = \frac{Q^{\mathrm{mean}}}{\langle E_{dep} \rangle}$$

Particular care has been taken to define the isolation cuts: previous cuts asked that neighbour cell have less than about 10% of the amount of charge in the study cell. The new cuts have been set in a flatter regime at 20% of the study cell (Figure 3). In order to evaluate the non-linearity response of the liquid it is important to characterize the high energy regime. The only available source at high energy is the AmBe source whith a gamma of 4.44 MeV, however this source emits simultaneously a gamma and a neutron with an energy between 2 and 8 MeV.

$$\begin{aligned} ^{241}\mathrm{Am} &\rightarrow {}^{237}\mathrm{Np} + \alpha \\ \alpha + {}^{9}\mathrm{Be} &\rightarrow {}^{13}\mathrm{C}^{*} \\ {}^{13}\mathrm{C}^{*} &\rightarrow {}^{12}\mathrm{C}^{**} + n[2-8\ \mathrm{MeV}] \\ {}^{12}\mathrm{C}^{**} &\rightarrow {}^{12}\mathrm{C} + \gamma[4.44\ \mathrm{MeV}] \end{aligned}$$

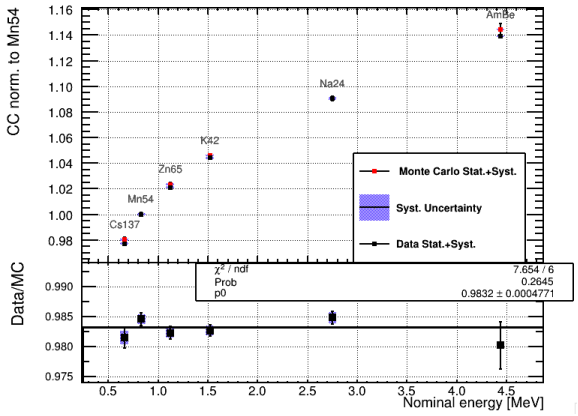

Figure 4: Non-linearity of the liquid scintillator response as resulting from the new analysis strategy. Calibration coefficient are normalized to ^{54}Mn.

During its thermalization, the neutron produce proton recoils before being captured on Gd. The neutron capture on Gd results in a gamma cascade of 2 MeV gammas for a total energy of about 8 MeV. Both proton recoils and Gd cascade gammas can be mistakenly identified as a 4.44 MeV gamma. A simple charge selection around the 4.44 MeV charge peak gives a proportion of background of about 51%. To reduce the proportion of background a time coincidence search strategy has been developed. An event in the study cell with characteristics of a 4.44 MeV gamma is taken as a prompt signal, then in a 50μs window a neutron capture on Gd is searched for in cells as far as possible from the study cell. This strategy bias the sample for events where proton recoils on Gd capture happen further away from the study cell, hence reducing the number of background. The amount of fake events due to n-Gd capture has been shown to reduce from ∼46.5% to ∼15.5% and the amount of fake events due to proton recoils is reduced from ∼5% to ∼4.5%.

	n-Gd events	Proton recoils
Without coincidence	∼46.5%	∼15.5%
With coincidence	∼5%	∼4.5%

For each source, the value of the CC is normalized to the value of the ^{54}Mn one, and the Data to MC ratio is computed. The new study shows a Data-MC agreement of the order of 0.3%, and the systematic uncertainties have been reduced. In addition the results shows that Data of 2017 and 2018 are compatible giving no hint for a change in time in the non-linearity of the liquid response as seen in figure 4.

4 Oscillation analysis

The oscillation analysis is performed on the spectrum shape independently of any reactor prediction. The number of IBD candidates in each energy bin i of cell l ($D_{l,i}$) is compared to the expected value from simulation ($M_{l,i}$). The parameters of interest $\vec{\mu}$ are the oscillation amplitude $\sin^2 2\theta$ and frequency Δ m$^2_{41}$. Nuisance parameters $\vec{\alpha}$ are added to take into account systematic uncertainties. The nuisance parameters include:

- the uncorrelated uncertainty on the normalization α^{NormU}
- the uncorrelated energy scale uncertainty $\alpha^{EScaleU}$
- the correlated energy scale uncertainty (time stability) $\alpha^{EscaleC}$

We introduce an additional normalization parameter Φ_i for each energy bin, but taking the same value in all cells, thus making this analysis independent of the initial choice of predicted spectrum. The following χ^2 is minimized:

$$\chi^2 = \sum_l^{N_{\text{Cells}}} \sum_i^{N_{\text{Ebins}}} \left(\frac{D_{l,i} - \phi_i M_{l,i}(\vec{\mu},\vec{\alpha})}{\sigma_{l,i}}\right)^2 + \sum_l^{N_{\text{Cells}}} \left(\frac{\alpha_l^{\text{NormU}}}{\sigma_l^{\text{NormU}}}\right)^2 + \left(\frac{\alpha_l^{\text{EScaleC}}}{\sigma_l^{\text{EScaleC}}}\right)^2 + \left(\frac{\alpha_l^{\text{EScaleU}}}{\sigma_l^{\text{EScaleU}}}\right)^2 \quad (3)$$

A $\Delta\chi^2$ formalism is used to perform the statistical tests, the $\Delta\chi^2$(Equation 4) is the difference between the χ^2(Equation 3) value obtained with the parameters of interest fixed to a given hypothesis and the χ^2 value obtained for the parameters that describes the best the data sample:

$$\Delta\chi^2 = \chi^2(\theta_H, \Delta m^2_H, \hat{\vec{\alpha}}) - \chi^2(\hat{\theta}, \Delta\hat{m}^2, \hat{\vec{\alpha}}) \quad (4)$$

The probability density function of the $\Delta\chi^2$ for the null-hypothesis (no oscillation hypothesis) is produced by computing the $\Delta\chi^2$ value for the null-hypothesis on many non-oscillated pseudo-data samples (Figure 5). A discovery test is then performed: The $\Delta\chi^2_{expt}$ value for the null hypothesis on the experimental data sample is computed: $\Delta\chi^2_{expt} = 6$. The p-value of the discovery test is the probability to have a Data-model agreement at least as bad as the one observed in the test. A p-value smaller than a critical value α (usually 5%) leads to a discovery at a 1-α confidence level. In our case, the p-value is given by the following equation:

$$\text{p-value} = \int_{\Delta\chi^2_{\text{expt}}}^{\infty} \text{PDF}(\Delta\chi^2) \times \text{d}\Delta\chi^2 \quad (5)$$

The p-value of the discovery test is p-value=0.40, much bigger than the critical value α=5% hence we do not reject the null-hypothesis (Figure 5). The measured spectra are in good agreement with the non-oscillated model (Figure 6). A limit on the potential signal is then computed in the form of an exclusion contour (Figure 7). To produce the exclusion contour a raster-scan method is used and for each hypothesis the $\Delta\chi^2$ is computed for a fixed Δm^2_{41} value on a set of 10000 pseudo-experiments. Finally the RAA best fit is rejected at more than 99% confidence level. An alternative oscillation analysis that has not been discussed here is in preparation and should allow an increase in sensitivity.

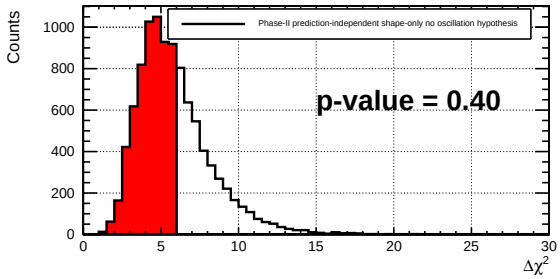

Figure 5: Probability density function of the $\Delta\chi^2$ for the null-hypothesis (no oscillation). The red region represents 1-p-value. The p-value of the discovery test is p=0.40.

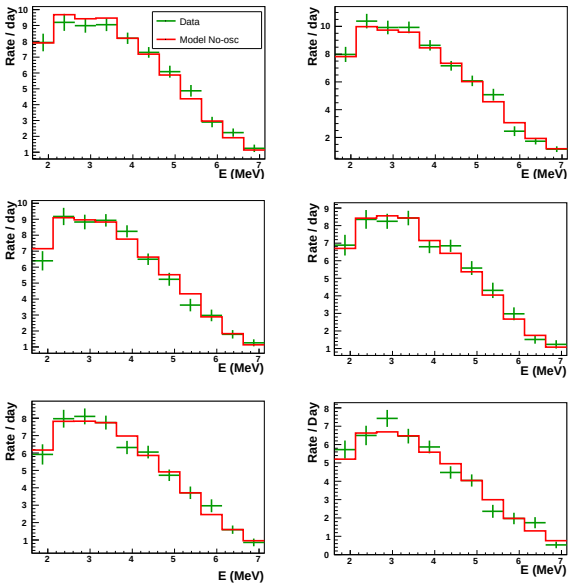

Figure 6: Neutrino Data spectra and non-oscillated simulated spectra for each cells

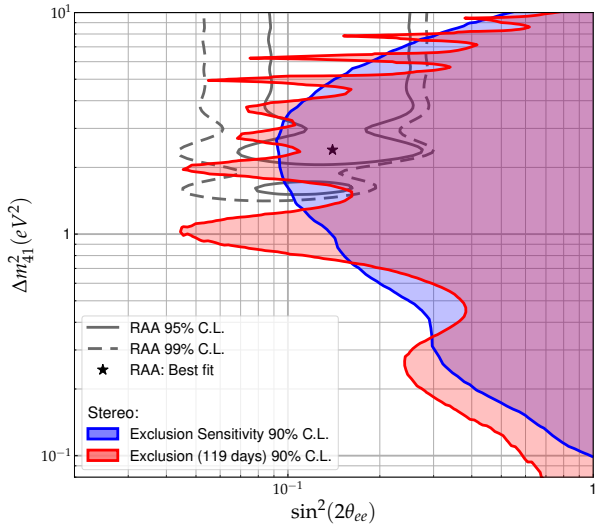

Figure 7: Exclusion and sensitivity contours for the oscillation parameter space. The RAA best fit (star) is excluded at 99% confidence level.

5 Conclusions

New strategies in the determination of the liquid non-linearity response and namely the improvement of the signal to noise ratio of the AmBe source allowed us to characterize the non-linearity at the sub-percent level and check the time stability of the liquid non-linearity. Additionally, a major part of the sterile neutrino oscillation parameter space has already been excluded in particular the RAA best fit has been excluded at 99% confidence level, but data taking is ongoing and the statistics acquired by the end of 2020 should be enough to exclude the remaining favored island in the oscillation parameter space.

References

[1] Determination of antineutrino spectra from nuclear reactors, 2011, Huber et al. Phys. Rev. C84 024617

[2] Improved prediction of the reactor antineutrino spectra, 2011, Mueller et al, Phys. Rev. C83 054615

[3] The reactor antineutrino anomaly, 2011, Phys. Rev. D83 073006

[4] The STEREO experiment, 2018, Journal of Instrumentation 13, 07P07009

Revisiting the modeling of reactor antineutrino spectra

Lorenzo Périssé

Irfu, CEA

Abstract — Nuclear reactors are intense antineutrino ($\overline{\nu}_e$) emitters and are therefore useful sources to study their fundamental properties. Detection of $\overline{\nu}_e$ is usually done through the inverse beta decay process (IBD), where an antineutrino is captured on a proton and then give a neutron and a positron. Past measurements of $\overline{\nu}_e$ flux and spectrum made at different reactor sites have shown significant rate and shape differences from recent models. The origin of these anomalies has been confirmed by last generation experiments measuring the θ_{13} mixing angle, but remains unclear. A possibility to address this issue is to revisit the theoretical models of reactor $\overline{\nu}_e$ spectrum and the associated uncertainty budget. Reactor $\overline{\nu}_e$ are produced by successive β^- decays of neutron-rich fission products originating from the fission of ^{235}U, ^{238}U, ^{239}Pu, ^{241}Pu in the core. The total antineutrino spectrum is then the superposition of thousand of β spectra. One way to model a reactor spectrum is to use the summation method which sums all the β branches listed in modern nuclear databases. A new and preliminary computation of a reactor antineutrino spectrum using this method is presented, using a refined modeling of β^- decay along with a revision of the associated uncertainties. The portion of the spectrum below 1.8 MeV, which is relevant to the study of coherent elastic neutrino-nucleus scattering at reactors, has also been investigated. While fission product spectra can be modified up to 20% with this new computation, the total reactor ($\overline{\nu}_e$) spectrum is barely corrected with subpercent changes.

1 Introduction

There exists two methods to predict reactor $\overline{\nu}_e$ spectra. The summation method (SM) uses available nuclear and fission data to build the reactor spectrum, but faces the incompleteness and missing information of databases. The second method is called the conversion method and is used for state-of-the-art predictions. It consists of fitting a measured electron spectrum using a set of virtual β branches. Converting each virtual β spectrum to its $\overline{\nu}_e$ counterpart, the $\overline{\nu}_e$ spectrum is obtained. In 2011, a new evaluation of reactor $\overline{\nu}_e$ spectra was performed independently by the Saclay group [6] and P. Huber [5]. The comparison of measured $\overline{\nu}_e$ rates of very short baseline experiments with the two new flux predictions led to a $(6 \pm 2.4)\%$ systematic deficit, which was then called the Reactor Antineutrino Anomaly [7]. In addition two other anomalies have been highlighted. A shape difference between the measured reactor $\overline{\nu}_e$ spectra and the expectation has been observed in several experiments including recent ones. This difference manifests mostly in the 4-6 MeV range where the measured shape is not consistent with predictions up to 4σ depending on the experiment [4]. The second one concerns the correlation of reactor $\overline{\nu}_e$ flux with the fuel composition which does not appear to be consistent between the measurements and predictions [1]. Still unexplained, these anomalies may have different origins. Several scenario have been proposed to explain them [4, 8], among which a misprediction and/or an underestimated uncertainty budget.

In order to investigate the origin of these anomalies, the reactor spectrum modeling must be revisited. This article focuses on the SM. The SM can be used to test the conversion method. Tools developed for the SM can also be integrated into the conversion model to improve it. The SM will be first described along with the detail of a reactor spectrum. The improvements brought to the SM are then presented and discussed.

2 Reactor antineutrinos

Study of neutrinos can be properly achieved by using one of the best man-made sources available: nuclear reactors. They emit a huge number of purely electronic antineutrinos and they do not require to be built. Nuclear reactors use turbines to produce electricity from hot steam. The general principle consists in warming up water by inducing fission on immersed fuel material. Reactor fresh fuel consists of uranium dioxide enriched in ^{235}U. Successive neutron captures starting on ^{238}U eventually leads to the production of fissile ^{239}Pu and ^{241}Pu. Hence a reactor core burns ^{235}U and accumulates ^{239}Pu with time, a phenomenon called the burnup process. It is responsible for modifying the reactor core relative proportion of fission products with time. In commercial reactors, more than 99.9% of the thermal power is induced by the fission of ^{235}U, ^{238}U, ^{239}Pu and ^{241}Pu. Each fission produces two unstable fission, sometimes three, a couple of neutrons that sustain the chain reaction, and releases about 200 MeV of energy. Fission products are usually rich in neutrons. They undergo successive β-decays to reach a more stable nucleus, emitting a $\overline{\nu}_e$ with an energy typically ranging from 0 to 10 MeV. On

average, six $\overline{\nu}_e$ are emitted per fission. It follows that for a reactor delivering 1 GW of electric power, one expects an isotropic emission of about 2×10^{20} $\overline{\nu}_e \cdot s^{-1}$ [6]. The gigantic number of $\overline{\nu}_e$ produced, associated to large detectors or short baseline detectors, balance the very low probability of interaction due to the weak interaction, the IBD cross-section being about $\sigma_{IBD} \sim 10^{-42}$ cm^{-2} below 10 MeV. An accurate prediction of a reactor $\overline{\nu}_e$ spectrum requires to know the fission rate evolution of the four main fissioning isotopes, associated to a good knowledge of fission product $\overline{\nu}_e$ spectra.

3 Summation method

The SM uses nuclear data to build a fission spectrum. Using decay data, each fission product's β and $\overline{\nu}_e$ spectra are calculated. At the level of a single β-branch b of a fission product f, the associated β spectrum S_f^b is given by

$$S_f^b(Z_f, A_f, E_{0,f}^b, E) = \underbrace{K_f^b}_{\text{Normalization}} \times \underbrace{\mathcal{F}(Z_f, A_f, E)}_{\text{Fermi function}} \times \underbrace{pE(E_{0,f}^b - E)^2}_{\text{Phase space}} \times \underbrace{C_f^b(E)}_{\text{Shape factor}} \times \text{Corrections} \quad (1)$$

where Z_f and A_f are the daughter nucleus charge and mass numbers, $E_{0,f}^b$ is the endpoint energy of the considered β transition, p and E are the β particle momentum and total energy. This equation comes from the Fermi theory of β-decay. The $\overline{\nu}_e$ spectrum of a transition is directly given by energy conservation, if recoil effects are neglected [5]. It consists in replacing the β energy E by the $\overline{\nu}_e$ energy $E_{\overline{\nu}_e} = E_{0,f}^b - E$, in Eq.1. The normalization factor K_f^b is calculated such that $\int_0^{E_{0,f}^b} \mathrm{d}E\ S_f^b(E) = 1$. The Fermi function specifically accounts for the deceleration of the electron in the Coulomb field created by the Z_f positive charges of a point-like daughter nucleus. It is the leading order QED correction [5]. When considering the Coulomb interaction with the daughter nucleus, the electron has a non-zero probability to have a vanishing momentum which shifts the β spectrum to lower energies and results in physical discontinuities in the $\overline{\nu}_e$ spectra when several branches overlap. The phase space factor is derived from the density of final states accessible to the emitted particles, simply reflecting the sharing of the momentum between the leptons. The shape factor $C_f^b(E)$ is a modification to the Fermi function depending on the forbiddenness of the transitions. The forbiddenness degree of a β transition is a classification based on spin and parity change between the parent and daughter nucleus. The higher the difference in angular momenta and spins between initial and final states, the higher the forbiddenness degree. A high degree of forbiddenness implies a low probability for a transition to happen and a high decay time. For allowed transitions (lowest forbiddenness degree) the shape factor is constant. For forbidden transitions shape factors are polynomials in the electron and neutrino momenta. Some forbidden transitions are too complicated to be computed and are approximated using a lower forbiddenness degree which introduces a shape uncertainty. This is called the ξ approximation. The polynomial coefficients are a special class of functions called Coulomb functions, which are discussed in the next section. The β transitions making a reactor $\overline{\nu}_e$ spectrum are mostly allowed. Among the 6000 transitions of the ^{235}U spectrum, about 69% of them are allowed transitions. Note that the spin and parity of some transitions are not well known, so these transitions are estimated with the lowest possible forbiddenness degree. Various corrections can be applied to the Fermi theory of β-decay, among which only the most important ones are cited: radiative corrections from QED [10, 11], weak current corrections due to the nucleon finite size [12], and lastly the daughter nucleus finite size and its atomic screening bring two more corrections which are discussed in the next section.

The spectrum $S_f(E)$ of a fission product f is given by summing its $n(f)$ β-branches. Let us write B_f^b the decay probability of the transition, or branching ratio, of the b^{th} β-branch of the f^{th} fission product. The fission product β spectrum is then given by,

$$S_f(E) = \sum_{b=1}^{n(f)} B_f^b\ S_f^b(Z_f, A_f, E_{0,f}^b, E) \quad (2)$$

The fission spectra S_k of ^{235,238}U, ^{239,241}Pu are then obtained by summing their respective fission product spectra.

$$S_k(E,t) = \sum_{f=1}^{N_f} \mathcal{A}_f(t)\ S_f(E) \quad (3)$$

where $\mathcal{A}_f(t)$ is the activity at time t. An example is given in Fig.1 showing all the spectra making up the spectrum of ^{235}U. Note that if the reactor is under a reactor burnup equilibrium condition, the β-decay rate are time independent and directly linked to the fission rate. Activities can then be replaced by cumulative fission yields, which combine the activity and the fission product proportion in the reactor core. Fission yields from the JEFF3.1.1 database [13] have been used in this work. The total spectrum emitted per fission is then the sum of the fission spectra, weighted by their fission fraction.

4 Refined β-decay modeling

The basic equation of a β spectrum is obtained from Fermi's theory. It is an effective theory where the weak interaction is not mediated via the W boson but is rather punctual. Several corrections are required to accurately describe a process in this framework, the β-decay being no exception. Here we focus on the

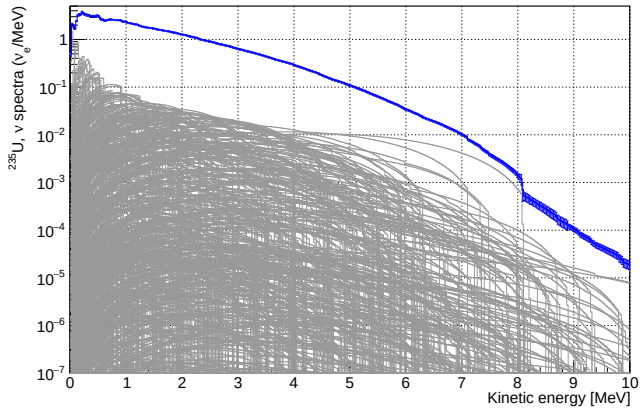

Figure 1: $\overline{\nu}_e$ fission spectrum of ^{235}U obtained with the SM. In grey are displayed all the fission product spectra composing the $\overline{\nu}_e$ spectrum. In blue is the total $\overline{\nu}_e$ spectrum of ^{235}U along its uncertainty.

Coulomb finite size (considering the nucleus as a sphere with radius R instead of point-like) and atomic screening effects. These effects are accounted for by modifying the Coulomb potential used to solve the Dirac equations and to calculate the electron radial wavefunction solutions.These radial solutions are used to compute Coulomb functions, such as the Fermi function or the shape factor coefficients. Hence Coulomb functions are nuclear model dependent.
In previous works, the Fermi function corrections were given by additional terms. In [12, 6] it is introduced with $F_0 \rightarrow F_0(1 - \frac{10}{9}\frac{Z\alpha R}{\hbar c}E)$. In [5], $F_0 \rightarrow F_0 L_0$ is used, where L_0 is a polynomial in Z_f, E and R . The screening correction was either not considered or added through yet another term. While it was checked that these approximations were consistent with one another [5] and that they were reproducing numerical tabulated data of reference from [2], such formulations are not modular and cannot adapt to different nuclear models. In this work the numerical approach presented in [3] has been adopted. Coulomb functions can then be computed for any given nuclear potential. As this computation is very time consuming, they have been tabulated in order to be interpolated with a relative precision of 10^{-4}%. When using the same nuclear model as in [2], the tabulated values of reference are reproduced up to numerical rounding errors. A refined nuclear model has been used in this work, using more recent data for screening [9]. Shape factors are polynomial in the electron and neutrino momentum. For instance the shape factor of a first forbidden transition is $C = p_e^2 + \lambda(p_e)p_\nu^2$ where λ is a Coulomb function. In previous models the λ function was simply set to 1 with no energy dependency. This is called the $\lambda = 1$ approximation. Our computed shape factors differ from the approximated ones especially over 5 MeV. The Fermi function and shape factor for a point-like nucleus are compared to the ones associated to two nuclear models in Fig.2.

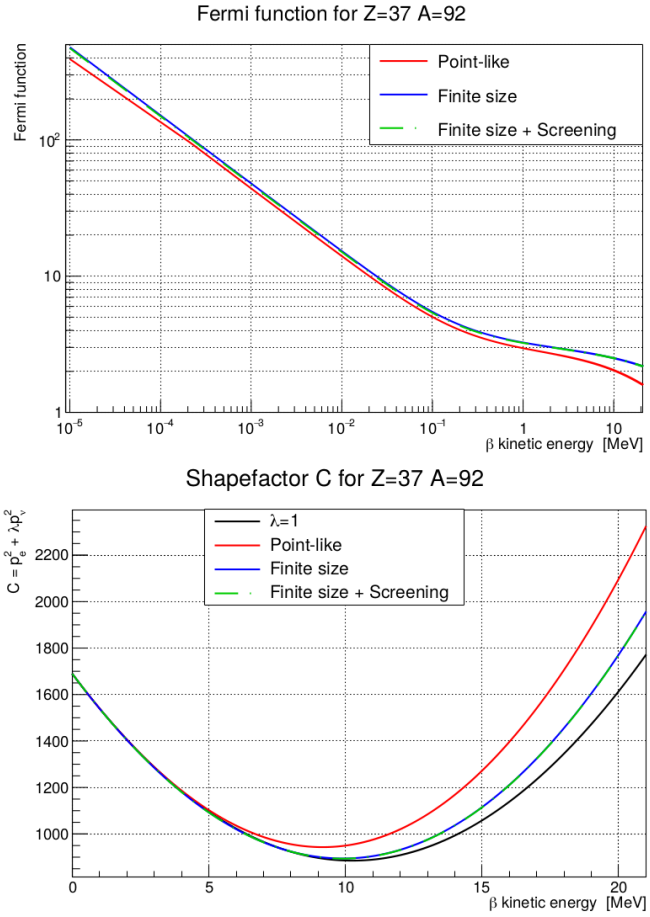

Figure 2: Fermi function and shape factor for different approximations and nuclear models. The nucleus charge and mass numbers are Z=37 and A=92. Red line: the nucleus is point-like. Blue line: the nucleus is spherical with a radius $R \simeq 0.0029A^{1/3} - 0.0024A^{-1/3}$. Green dashed line: the nucleus is spherical and its charge is screened by atomic electrons.

5 Preliminary results

These new corrections are then applied to all fission product spectra. Two models S and S' are compared. They both use the same radiative and weak finite size corrections. S uses the $\lambda = 1$ approximation and the Fermi function form $F_0(1 - \frac{10}{9}\frac{Z\alpha R}{\hbar c}E)$. S' uses exact Fermi functions and shape factors based on our tabulated values for Coulomb functions for an improved nuclear model with finite size and screening. In Fig.3, the effect of the new modeling on the 50 major contributors to the ^{235}U neutrino spectrum are displayed: they vary between a few percent and up to some tens of percent depending on the fission product and the energy. Note that the spectrum normalization is conserved while the shape is modified. Hence, a compensatory effect happens when summing all the contributors. The result is only a subpercent change in the total $\overline{\nu}_e$ spectra: ± 0.1% below 6.5 MeV (where most of the flux in concentrated), with a maximum of -0.8% at 8 MeV as it is seen in Fig.4. Fission spectrum shape is then slightly

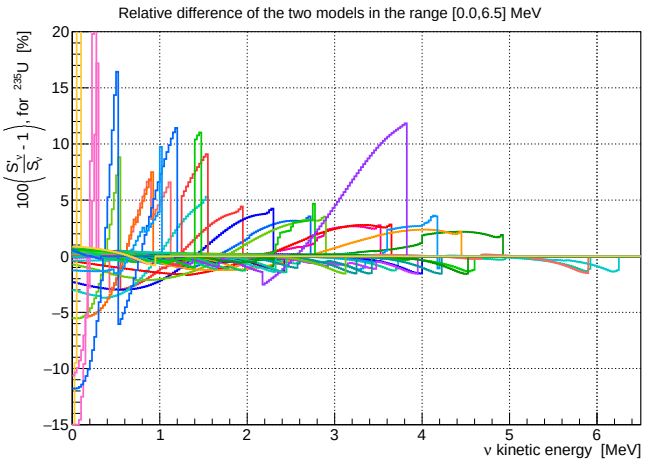

Figure 3: $\overline{\nu}_e$ spectrum relative difference between S and S', for the 50 major contributors to the $\overline{\nu}_e$ flux of ^{235}U.

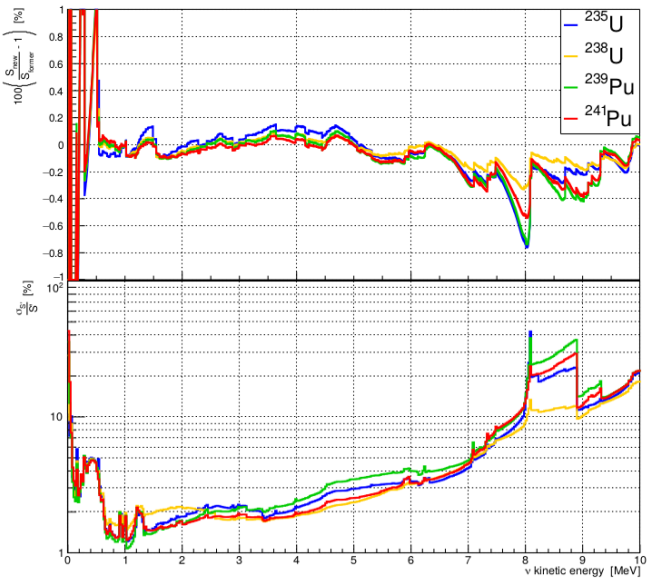

Figure 4: Top: Relative difference between fission spectra build according to the two models S and S'. Bottom: uncertainty envelope associated to the new model S'.

impacted in this new model, but not significantly.
As a preliminary calculation, uncertainties on endpoint energies, branching ratios and fission yields have been propagated to the total $\overline{\nu}_e$ spectrum. Because the fission product spectrum normalization is constrained, the endpoint error plays a role in the branch spectrum shape and anti-correlates some bins of the spectra. This uncertainty is propagated using a Monte-Carlo method while the branching ratio and fission yield errors are propagated analytically, using values from ENSDF and JEFF3.1.1 databases respectively [14, 13]. Correlations between decay data (branching ratios, fission yields) are missing in modern nuclear databases. Hence they were assumed to be null for this calculation. The error envelopes associated to new preliminary spectra are presented along the spectra in Fig.4. Possible branching ratio or fission yield correlations would led to a potentially more important uncertainty budget. Finally, the ξ approximation uncertainty is not considered here.

6 Conclusions

In the context of the observed reactor anomalies, a precise knowledge of the predicted $\overline{\nu}_e$ spectra appears to be of paramount importance. In addition, the upcoming coherent-scattering experiments will require a prediction at low energy that only the SM can provide. The current predictions of reference of reactor $\overline{\nu}_e$ spectrum still relies on multiple approximations and incomplete databases. In this context a new model is being developed, using finer corrections and lifting approximations. This new modeling modifies significantly individual fission products, but the total spectrum shape is impacted to less than 1%. The preliminary uncertainty budget will soon be completed by studying the effect of branching ratio and fission yield correlations, propagating the nuclear model error, and testing multiple scenario to estimate the uncertainty due to the different approximations. This work has been done in the framework of the NEνFAR project, run by the CEA.

References

[1] An et al. (2017), doi: 10.1103/PhysRevLett.118.251801

[2] Behrens and Janecke, Numerical Tables for Beta-Decay and Electron Capture, Springer-Verlag Berlin Heidelberg, 1969

[3] Behrens and Buhring, Electron radial wave functions and nuclear beta-decay, Clarendon press. Oxford, 1982

[4] Hayes et al. (2015), doi: 10.1103/PhysRevD.92.033015

[5] Huber (2011), doi: 10.1103/PhysRevC.84.024617

[6] Mueller et al. (2011), doi: 10.1103/PhysRevC.83.054615

[7] Mention et al. (2011), doi: 10.1103/PhysRevD.83.073006

[8] Mention et al. (2017), doi: 10.1016/j.physletb.2017.08.035

[9] Salvat et al. (1987), doi: 10.1103/PhysRevA.36.467

[10] Sirlin (1967), doi:10.1103/PhysRev.164.1767

[11] Sirlin (2011), doi: 10.1103/PhysRevD.84.014021

[12] Vogel (1984), doi: 10.1103/PhysRevD.29.1918

[13] http://www.oecd-nea.org/dbdata/JEFF/index-JEFF3.1.1.html

[14] https://www.nndc.bnl.gov/ensarchivals/

Part VII

Nuclear Physics

session chaired by Diego GRUYER

Development of an all-in-one methodology that computes neutron activation relying on the capacities of RayXpert, CAD modeling software and Monte-Carlo computations

Nicolas Dray, E. Suraud, P.M. Dinh, C. Dossat, N. Chatry

Laboratoire de Physique Théorique, Université de Toulouse, CNRS, UPS, France / TRAD - Tests & Radiations

Abstract — The generation of neutrons in nuclear installations involves a phenomenon called activation. The neutron activation consists in the creation of radioactive isotopes in materials close to a neutron source. These radioactive isotopes produced in activated materials induce radiation when they decrease which can be harmful for humans. The real issue with neutron activation is that the radioactivity of activated materials can last over decades. The aim of the present work is to create a "press-button" (all-in-one) methodology which would be able to compute the residual dose of neutron activated materials (also known as the shutdown dose rate : SDDR). The prototype code of this methodology would use the functionalities of RayXpert© a CAD and Monte-Carlo software. Nevertheless, estimating the SDDR is really complex as it involves three different time-consuming computations : two Monte-Carlo and and one inventory calculations. In this paper, the method used to compute the SDDR is described. Then the preliminary results are exposed. Finally, future developments are presented.

1 Introduction

In nuclear facilities where neutrons are generated, materials are activated by particles that make nuclear interactions. In particular, neutrons are likely to cause nuclear reactions in matter even at low energy. These interactions generate a phenomenon called neutron activation [1]-[2] : it consists in the appearance of unstable isotopes in materials close to a neutron source. These unstable isotopes generated in activated materials produce radiations when they decay, which can be harmful for humans. Furthermore, these decays can last for periods longer than decades [3]. To carry out maintenance operations in complete safety, to predict how to dismantle a nuclear installation or to define the best way to build a nuclear installation, it is necessary to correctly model the effects due to neutrons.

This modeling is generally carried out in different stages. The first step consists in calculating the neutron flux by the Monte-Carlo method on a sufficiently fine mesh of the real geometry using a code such as MCNP [4]. Then, the calculation of the evolution of the isotopic inventory, which is the number of atoms of each isotope in the material considered, is carried out for each elementary voxel. Finally, the sources of decay are used to propagate the particles resulting from these decays in the geometry. This transport is generally carried out by a Monte-Carlo method and makes it possible to calculate the flux of particles of decay on a mesh superimposed on the geometry. Finally, flux-to-dose conversion factors [5] allow to transform the flux of particles into dose. Transport of the particles is carried out with a Monte-Carlo calculation code and inventory calculation with an isotopic inventory calculation code such as FISPACTII [6]. Such a method, used to estimate the shutdown dose rate (SDDR), is called R2S (Rigorous-Two-Steps) [7]-[8]. The simulation of the SDDR in a nuclear installation where neutrons have been produced is therefore a complicate process requiring at least two Monte-Carlo calculations which are time-consuming in addition to a coupling between different calculation type codes. Moreover, to take care of the neutron flux gradients, it is mandatory to use a mesh superimposed on the model. This allows us to greatly increase the accuracy of the computation. In [9], two different meshes are used in order to compute the intensity of the neutron flux on a fine mesh and the shape of it on a coarse mesh. Then both results are coupled to estimate the flux on the fine mesh. Another process discussed in [10] consists in computing the neutron fluxes for each part of cells enclosed in a voxel to increase the accuracy of the simulation. Also, an adaptive mesh that conforms to geometry is tested in [11] and [12] and has the advantage to perfectly take account of the neutron flux gradients. Finally, Valenza tries to simulate the SDDR with one Monte-Carlo that performs the transport of both the neutrons and the decay particles at the same time but it requires a Monte-Carlo transport beforehand [13].

The aim of the current work is therefore to find an all-in-one methodology which would be able to make all the previous steps in one click. The two Monte-Carlo transports are made with RayXpert [14] Monte-Carlo capacities and the activation is handled by the prototype code currently under evolution. In this article, we first discuss the method used to compute the SDDR. Then, some preliminary results are shown. We finally end by giving some future reflection points.

2 Methodology

There are many methods used to estimate the SDDR of a nuclear installation. In the present work, the R2S method (for Rigorous-Two-Step) is implemented. As previously said, it consists in computing the neutron

flux of a nuclear facility for each voxel of a superimposed mesh. It is mandatory to add a mesh on the geometry because of neutron flux gradients. Indeed, a cell of the geometry can size up over several meters. In this case, one can easily imagine that the neutron flux will not be the same in the part of the cell next to a neutron source as in the part at the opposite. Then, an inventory computation is made for each voxel by considering a user supplied irradiation scenario and by using the neutron flux previously computed for each voxel. Once the inventory is estimated at the time requested for each considered voxel, the transport of the decay particles is made by a Monte-Carlo computation and a map of decay fluxes is obtained on another mesh defined by the user. Finally, flux-to-dose factors are used to convert the fluxes into doses.

In the methodology which is under development, the Monte-Carlo steps are handled by RayXpert© both analogue and non-analogue Monte-Carlo code. Moreover, RayXpert© is able to make a 3D CAD model of the geometry. It is also possible to import model from a step (Standard for the Exchange of Product Data) file. Finally, with RayXpert©, one can in addition superimpose a mesh on the geometry. The mesh type available is only structured cartesian at the moment and the voxel has to be rectangular. An example of the CAD capacity of RayXpert is shown in figure 1. The height of the accelerator presented in this figure is around 2 meters.

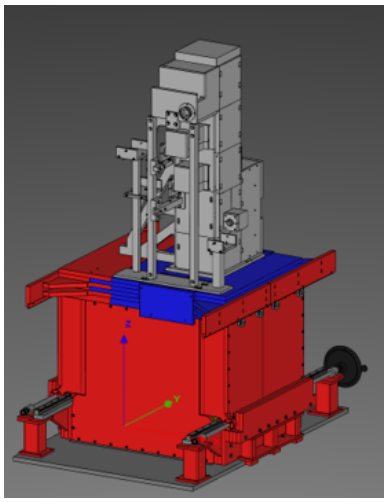

Figure 1: Example of a CAD model of an linear accelerator made with RayXpert©.

For each voxel of the mesh, the inventory computation is made with an internal ordinary differential equation (ODE) solver. This solver is based on a 2 point block backward differentiation formulae (2 point BBDF) [15]. This kind of solver computes the isotopic inventory for the next two steps at the same time. This has the advantage to be more accurate than a solver that computes the solution only for the next step. Moreover, this solver is based on a variable step size in order to minimize the CPU time consumption as there is an inventory computation for each voxel. The performances of the internal ODE solver will be discussed in the next part.

Once the voxel's inventory is computed for the desired time, it has to be converted into a decay source of particles. Then, a Monte-Carlo transport of these decay particles is achieved with RayXpert to compute the particle fluxes on a user defined mesh. This mesh can in principle be different of the mesh used for the inventory calculation. For the moment, this part of the computation is not yet coupled with the inventory calculation but this will be done in the months to come.

3 ODE Solver performances

As said previously, the solver used to compute the isotopic inventory is based on a 2 point BBDF method of order 4. This kind of method is numerically expensive but is necessary for the system of ODE that governs the inventory evolving system under neutron flux. In fact, the inventory system of equations is a "stiff" problem : it could not be solved by using explicit methods such as Runge-Kutta formulae. The stiffness of the system comes from the fact that some isotopes have a half-life less than 1 second and others have a half-life over the century. Therefore, it is compulsory to use the expensive but more stable BBDF method. Two cases have been tested to evaluate the performances of the solver. The first one is the Gear's problem from [16] :

$$\begin{aligned} y_1' &= 998y_1 + 1998y_2 \\ y_2' &= -999y_1 - 1999y_2 \end{aligned}$$

with $y_1(0) = 1$, $y_2(0) = 0$ and $0 \leq x \leq 20$ with the analytic solutions :

$$\begin{aligned} y_1(x) &= 2e^{-x} - e^{-1000x} \\ y_2(x) &= -e^{-x} + e^{-1000x} \end{aligned}$$

The second test case is the inventory evolution system under neutron flux which is actually the problem to solve for the inventory step. The corresponding system is given by :

$$\frac{dN_i(t)}{dt} = -N_i \cdot (\lambda_{i\rightarrow} + \sigma_{i\rightarrow}\Phi) + \sum_{\substack{j=1 \\ j\neq i}}^{n} N_j \cdot (\lambda_{j\rightarrow i} + \sigma_{j\rightarrow i}\Phi)$$

$$N_i(t=0) = N_{i,0}, \forall i \in [1,n]$$

where :

- $N_i(t)$ is the number of nuclei of isotope i
- $N_{i,0}$ is the initial number of nuclei of isotope i
- n is the total number of isotopes available in the database
- Φ is the neutron flux computed from the Monte-Carlo transport for the considered voxel (cm^{-2}/s)
- $\lambda_{i\rightarrow}$ is the decay constant of the isotope i to any of its progeny ($1/s$)

- $\sigma_{i\rightarrow}$ is the total microscopic cross-section of the isotope i with a neutron (barn)
- $\lambda_{j\rightarrow i}$ is the decay constant of the isotope j to the isotope i (1/s)
- $\sigma_{j\rightarrow i}$ is the microscopic cross-section production of isotope i from isotope j when there is a neutron interaction (barn)

The first example, the Gear's problem, was tested both with the internal ODE solver developed for the inventory calculation and with the well known solver of ordinary differential equations LSODE [17]. The value of the solution vector was requested for 10^3 times varying by 2×10^{-2} seconds starting at $t = 0.02$ s. For each time computed, each solution was compared to the analytical solution. Then the relative error η_{rel} obtained was computed with the formulae :

$$\eta_{\text{rel}} = \frac{y(t)_{computed}}{y(t)_{analytical}} - 1$$

We present the maximum value of η_{rel} obtained on the one hand with LSODE and on the other hand with the internal ODE solver, for the first and the second solutions of the Gear's problem in tables 1 and 2 respectively. Both solvers are based on a variable step size process in order to optimize the resolution. Therefore, they need tolerances to control the step size length. The relative and absolute tolerances (resp. $rtol$, $atol$) are defined such that the error δ made by the solver on the solution should not exceed the value $rtol * y_i(t_n) + atol$. In all the computations of the Gear's case, we used $atol = 10^{-16}$. From tables 1 and 2, we can here conclude, according to the tested relative tolerances, that the internal ODE solver outperforms LSODE.

Rel. tol.	$\max(\eta_{\text{rel}})_{intern}$	$\max(\eta_{\text{rel}})_{LSODE}$
10^{-4}	5.50×10^{-5}	215.67×10^{-5}
10^{-6}	1.15×10^{-6}	61.10×10^{-6}
10^{-8}	4.77×10^{-7}	19.89×10^{-7}

Table 1: Maximum value of η_{rel} for the first solution of the Gear's system obtained with the internal ODE solver (column 2) or with LSODE (column 3).

Rel. tol.	$\max(\eta_{\text{rel}})_{intern}$	$\max(\eta_{\text{rel}})_{LSODE}$
10^{-4}	5.50×10^{-5}	215.67×10^{-5}
10^{-6}	1.07×10^{-6}	61.10×10^{-6}
10^{-8}	4.77×10^{-7}	19.89×10^{-7}

Table 2: Maximum value of η_{rel} for the second solution of the Gear's system obtained with the internal ODE solver (column 2) or with LSODE (column 3).

The second test case run was an inventory calculation. For this problem, the initial inventory was composed of 1.075382×10^{22} nuclei of ^{56}Fe with a neutron flux of 6.12572×10^{15} neutrons/cm^2/s. The total irradiation duration considered was 10 years. The results obtained with the new ODE solver were compared to those given by FISPACTII for $Z > 10$ and for a number of nuclei of an isotope greater than or equal to $10^{-4} \times N_{^{56}\text{Fe}}(t = 0)$, where Z is the atomic number of an isotope. We chose these initial conditions so that the results are more easily readable and the number of relevant isotopes is reasonable (as there are for both cases 183 isotopes produced under the conditions of this test). For both FISPACTII and the methodology currently in elaboration, the relative and absolute tolerances used were respectively 10^{-4} and 10^3. Table 3 shows the inventory for FISPACTII and for our code in the second and the third column respectively. The last column shows the absolute value of the relative difference between FISPACTII and RayXpert where FISPACTII is considered as the reference value.

	FISPACTII	RayXpert	Rel. difference
^{47}Ti	2.33E+18	2.28E+18	2.5%
^{48}Ti	1.38E+19	1.36E+19	1.5%
^{49}Ti	2.95E+19	2.90E+19	1.7%
^{50}Ti	2.35E+19	2.28E+19	3.0%
^{49}V	4.43E+18	4.34E+18	2.0%
^{50}V	4.44E+19	4.36E+19	2.0%
^{51}V	1.60E+20	1.57E+20	1.4%
^{51}Cr	4.31E+18	4.25E+18	1.2%
^{52}Cr	7.95E+20	7.88E+20	0.9%
^{53}Cr	6.41E+20	6.39E+20	0.3%
^{54}Cr	1.04E+21	1.05E+21	0.5%
^{53}Mn	3.06E+20	3.05E+20	0.4%
^{54}Mn	3.18E+20	3.19E+20	0.5%
^{55}Mn	2.05E+21	2.06E+21	0.4%
^{54}Fe	3.36E+20	3.32E+20	1.2%
^{55}Fe	9.31E+20	9.27E+20	0.4%
^{56}Fe	4.04E+21	4.05E+21	0.2%
^{57}Fe	3.59E+18	3.42E+18	4.7%

Table 3: Inventory for FISPACTII (second column) and the prototype code (third column) for the second test case, at $t = 10$ years and absolute value of the relative difference associated (fourth column).

Both inventories are in good agreement, with relative differences below 5%. The maximum relative difference is 4.7% for the isotope of ^{57}Fe. Even if this value is much larger than those for the other isotopes, it is nevertheless acceptable. The observed discrepancies can arise from different origins, since many different calculations are performed to obtain the inventory : from the nuclear data used, the numerical approximations made in the codes, the algorithms used in the ODE solvers, etc. It is therefore compulsory to compare the values of FISPACTII and the prototype code with experimental data to determine which code is the most accurate.

4 Further developments

One should keep in mind that the desired value of this computation is the SDDR. So far, we treated all the steps for the computation of an inventory at a requested time. Many steps are still needed to allow the cal-

culation of the SDDR. First, from the inventory, we have to envision a method able to reconstruct the decay sources in order to map the dose. Next, the automatic Monte-Carlo transport of decay particles has to be implemented. Finally some automatic biasing of the Monte-Carlo should be created to accelerate the convergence of the two Monte-Carlo computations as they are the most time consuming steps of the whole process.

5 Conclusions

The SDDR estimation with the R2S method is an expensive process in terms of computational time and numerical resources. It requires two different kinds of calculation (Monte-Carlo and inventory) with two distinct Monte-Carlo calculations. Therefore, automating the whole process is very demanding and cumbersome. The results reported here show that the first Monte-Carlo calculation and the inventory calculation are correctly linked as the inventories of FISPACTII and the prototype code are in good agreement. Once again, on the basis of the test cases explored in this work, the ODE solver implemented for this methodology performs as good as, and sometimes better than, LSODE. Still, more tests are needed to confirm that these steps correctly compute the inventory. One of these tests will be to compare the inventory computed either with FISPACTII or with the prototype code to experimental data. This comparison will be performed in the months to come. Finally, estimating the SDDR through an automatic process relying on the capacities of RayXpert calls for further developments, the latter being currently under preparation. This will offer to the community a unique tool for a readily estimate of the SDDR.

References

[1] S.P. Murarka (2001). Encyclopedia of Materials: Science and Technology. Neutron Activation Analysis

[2] L. Hamidatou(2019). Overview of Neutron Activation Analysis. DOI: 10.5772/intechopen.85461

[3] M.B. Chadwick & al. (2011). ENDF/B-VII.1 Nuclear Data for Science and Technology: Cross Sections, Covariances, Fission Product Yields and Decay Data. Nuclear Data Sheets, Volume 112, Issue 12, Pages 2887-2996, https://doi.org/10.1016/j.nds.2011.11.002

[4] C.J. Werner & al. (2018). MCNP6.2 Release Notes. LA-UR-18-20808

[5] ANSI/ANS-6.1.1 Working Group, M.E. Battat. (1977). American National Standard Neutron and Gamma-Ray Flux-to-Dose Rate Factors. ANSI/ANS-6.1.1- (N666), American Nuclear Society, LaGrange Park, IL, p. 1977

[6] J.-Ch. Sublet and al. (2017). FISPACT-II: An Advanced Simulation System for Activation, Transmutation andMaterial Modelling. Nuclear Data Sheets 139, p. 77-137

[7] Y. Chen & al. (2001). Rigorous MCNP Based Shutdown Dose Rate Calculations: computational scheme, verification calculations and application to ITER. Forschungszentrum Karlsruhe, Interner Bericht , IRS Nr. 2/01, FUSION Nr. 166

[8] L. Petrizzi & al. (2003). Two computational approaches for Monte-Carlo based shutdown dose rate calculation with applications to the JET fusion machine.

[9] M. Majerle & al. (2012). Verification and validation of the R2Smesh approach for the calculation of high resolution shutdown dose rate distributions. Fusion Engineering and Design, Volume 87, Issues 5-6, Pages 443-447

[10] P. Sauvan & al. (2016). Development of the R2SUNED Code System for Shutdown Dose Rate Calculations. IEEE Transactions on Nuclear Science, vol. 63, no. 1, pp. 375-384

[11] A. Turner & al. (2014). Comparison of Shutdown Dose Rate Results using MCNP6 Activation Capability and MCR2S. ARP-097

[12] T. Eade & al.(2015). MCR2S unstructured mesh capabilities for use in shutdown dose rate analysis. Fusion Engineering and Design Volume 100, Pages 321-333

[13] Valenza & al. (2001). Proposal of shutdown dose estimation method by Monte Carlo code. Fusion Engineering and Design. 55. 411-418. 10.1016/S0920-3796(01)00188-0.

[14] C. Dossat (2017). RayXpert Manuel Utilisateur. TRAD/DL/DOS/RAYXPERT/CD/110412 Rev13

[15] M. B. Suleiman & al. (2013). A new variable step size block backward differentiation formula for solving stiff initial value problems. International Journal of Computer Mathematics, 90:11, 2391-2408, DOI:10.1080/00207160.2013.776677

[16] C.W. Gear (1971). Numerical Initial Value Problems in Ordinary Differential Equations. Prentice Hall, Inc., Upper Saddle River

[17] Alan C. Hindmarsh. (1980). LSODE and LSODI, two new initial value ordinary differential equation solvers. SIGNUM Newsl. 15, 4 (December 1980), 10-11. DOI:https://doi.org/10.1145/1218052.1218054

Part VIII

Standard Model

session chaired by Reina CAMACHO TORO

Measuring quantum interference in the off-shell Higgs to flour leptons process with Machine Learning

Aishik Ghosh

Université Paris-Saclay, CNRS/IN2P3, IJCLab, 91405 Orsay, France

Abstract — The traditional machine learning approach to optimize a particle physics measurement breaks down in the presence of quantum inference between the signal and background processes. A recently developed family of physics-aware machine learning techniques that rely on the extraction of additional information from the particle physics simulator to train the neural network could be adapted to a signal strength measurement problem. The networks are trained to directly learn the likelihood or likelihood ratio between the test hypothesis and null hypothesis values of the theory parameters being measured. We apply this idea to a signal strength measurement in the off-shell Higgs to four leptons analysis for the Vector Boson Fusion production mode from simulations of the high energy proton-proton collisions at the Large Hadron Collider. Promising initial results indicate that a model trained on simulated data at different values of the signal strength outperforms traditional approaches in the presence of quantum interference.

1 Introduction

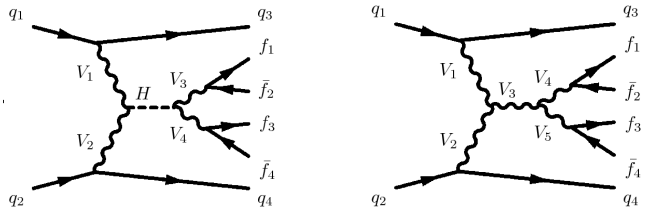

(a) Signal: Higgs from Vector Boson Fusion

(b) Background: Vector Boson Scattering

Figure 1: Feynman Diagrams of the processes under study, (a) signal Higgs diagram, (b) interfering background diagram

The Heisenberg uncertainty principle of quantum mechanics ($\sigma_E \sigma_t \geq \frac{\hbar}{2}$) allows particles to become "virtual", with a mass going far away from the one described by special relativity's mass-energy equivalence formula $E^2 - |\vec{p}|^2 c^2 = m_0^2 c^4$ (where the energy E is given in terms of the rest mass m_0 and momentum $\vec{p}$ of the particle and c is the speed of light in vacuum). They and are refereed to as "off-shell" particles. Quantum mechanics also prescribes that given an initial and final state, all possible intermediate states can and will occur, and they may interfere with one another.

A study of the off-shell Higgs boson decaying to two Z bosons that decay to four leptons (henceforth referred to as "offshell h4l"), such the 2018 study [2] in the ATLAS Collaboration [1] is one of the most interesting studies in high energy particle physics because it allows to break certain degeneracies between the Higgs couplings, and constrain the Higgs width (under certain model dependent assumptions) that cannot be disentangled by an on-shell measurement alone. An update to the previous ATLAS study using the entire Run2 data will have develop innovative methodology to deal with quantum interference between the Higgs Feynman diagram (referred to as "signal") and other standard model processes (referred to as "background"). While the previous round used simple cuts to define the region of interest, we investigate a recently developed family of physics-aware machine learning techniques to improve the sensitivity of such an analysis. The two main diagrams studied here are shown in Figure 1. Other signal and background processes will be included in future studies. The objective of the analysis is to measure the "signal strength", μ, of the signal, which is a proxy for measuring how strongly the Higgs interacts with other fields. Interestingly, the usual notion that the signal strength corresponds to the ratio of the observed in data to the expected in Monte Carlo simulation signal yield breaks down in the presence of quantum interference.

This study is performed with data simulated with `MadGraph5_aMC` [3], `Pythia 8` [4] and `Delphes 3` [5].

2 Machine Learning in a signal strength measurement

Traditionally, in analyses without quantum interference, one can train a machine learning classifier (such as a Boosted Decision Tree) to separate the signal and background samples (referred to as "events") that are simulated separately, and under the assumption that it is an optimal classifier, due to the Neyman-Pearson lemma [6], one can get the likelihood ratio [7] between a test hypothesis and the null hypothesis from the output of the classifier. The output of the classifier can be used for a fit to measure the signal strength, μ, optimally. In the presence of quantum interference, this strategy is no longer optimal. Figure 2 shows how a physics variable (the invariant mass of the four leptons) that is

usually good for a Higgs to four leptons analysis cannot distinguish between $\mu = 0$ and $\mu = 4$, however a different variable, the pseudo-rapidity (angular) difference between the two jets, can break the degeneracy in this case. The figure also shows that for the standard model (SM) value of the signal strength ($\mu = 1$), the total expected number of events is fewer than in the background only ($\mu = 0$) case. Figure 3 is a sketch of how the expected number of events scales with μ, demonstrating that a deficit is expected near the SM value ($\mu = 1$), while an excess is expected at high values of μ. In fact it is the "signal-like" background events (background events with kinematic properties similar to events in an unphysical signal-only simulation) that diminish in number in the presence of signal Feynman diagrams in the simulation. A machine learning strategy that is optimal not only at the SM value but at all other values of μ could be expected to improve the sensitivity of this analysis.

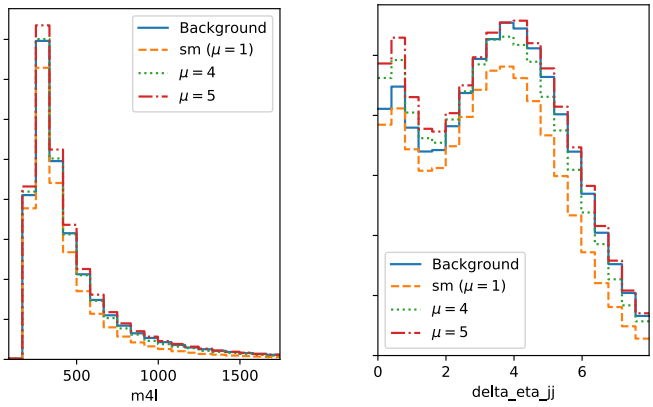

(a) m_{4l} (GeV) (b) $\Delta\eta_{jj}$

Figure 2: Distributions of (a) invariant mass of the four leptons, (b) difference between the pseudo-rapidity of the two jets

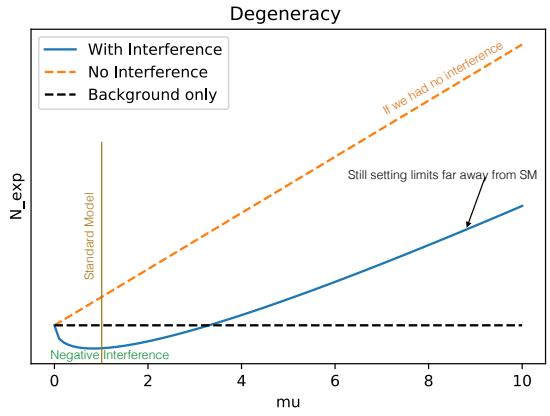

Figure 3: Sketch of extrapolation of the expected number of events observed as a function of signal strength μ, up to an arbitrary normalization. Exact numbers not directly comparable to Figure 2

3 Madminer based Likelihood-Free Inference

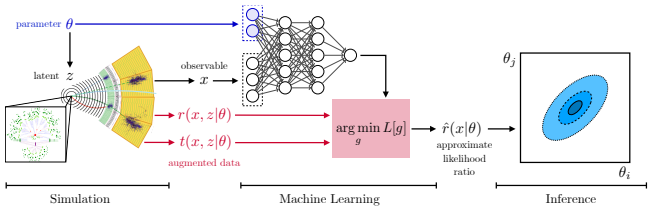

Figure 4: Schematic overview of the family of techniques investigated [9]

A family of machine learning algorithms have recently been developed [8, 9, 10, 11] that are at the intersection of machine learning, probabilistic programming, statistics and particle physics phenomenology. The techniques rely on the extraction of additional information from the simulator to train neural networks that directly learn the likelihood/likelihood ratio between a test hypothesis value of a theory parameter and the null hypothesis value. Figure 4 is schematic diagram of the algorithm from the authors of these techniques. This is well suited for a measurement in the Effective Field Theory (EFT) Framework [12], where the theory parameters come from an EFT Lagrangian. However, such an algorithm would also be beneficial for a signal strength measurement in the context of interference, by avoiding the need to define "signal" and "background" class labels, or tuning the model only at a fixed value of μ. The extra information extracted from the simulators is only required to train the networks but not required at inference time.

We try to adapt these techniques for a signal strength measurement, even though μ is not a theory parameter of the Lagrangian but rather a representation of various theory parameters that determine the strength of Higgs coupling to other fields.

The additional information extracted from the simulator involves 're-weighting' each event from the event-generator (the part of the simulation that numerically computes the Quantum Field Theory calculations for the given Lagrangian to generate parton level data, in this case, `MadGraph5_aMC`) to other values of the theory parameter. This means finding the probability of having observed a particular event if the true value of the theory parameter was something else. The 'weight' of an event roughly corresponds to the probability of observing it. By having the weights for each event at different parameter points, one can 'morph' [8] the events to generate a dataset for any desired parameter point. Morphing in the case of a Vector Boson Fusion produced Higgs process where the Higgs decays to four leptons, is similar to a fourth order polynomial fit. Thus, having weights for each event at five different parameter points is sufficient to morph it to any other parameter point. In this technique, the individual events remain unchanged, but their weights are adjusted so that the overall distributions are correct for

the given parameter point. Morphing to points where the physics is very different would make the value of the weights extreme, therefore simulation still needs to be done at several points. The distribution of effective number of events is given in Figure 5a, where $N_{effective} = \frac{\sum weights}{max(weights)}$ (as defined in [8]). Interestingly, since the destructive interference is maximal near the SM point, there are very few 'signal-like' events at that point, therefore the events generated at the SM do not morph well to nearby points which require at least a few 'signal-like' events (indicated by the sharply falling $N_{effective}$ in green). The full simulation in-

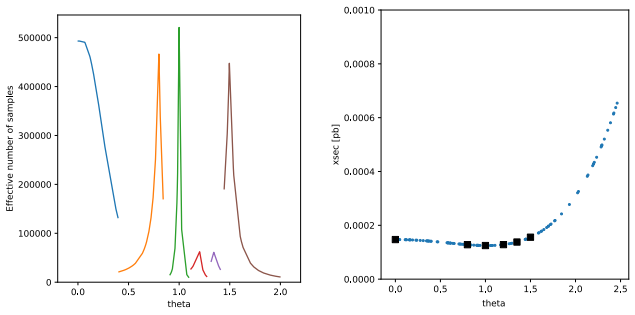

(a) (b)

Figure 5: (a) Effective number of events for different values of $\theta = \mu^{\frac{1}{4}}$ events are generated at benchmark points $\theta = 0, 0.8, 1, 1.5$ and a few additional events at additional benchmark points $\theta = 1.2, 1.35$. For a new point, events are morphed from the nearest benchmark point. (b) Cross Section as a function of θ, the validation point at 1.35 matches the fitted morphing prediction shown in blue

cludes parton showering (with `Pythia 8`) and the detector response (with `Delphes 3`), resulting in the observables that are recorded for data analysis. From the above mentioned setup, the 'joint-likelihood ratio', $r(x, z|\mu_0, \mu_1) = \frac{p(x,z|\mu_0)}{p(x,z|\mu_1)}$ (the parton-level likelihood ratio, where x are the observables, z the parton level information) can be calculated from the weights of each event for two different hypotheses, μ_0 and μ_1, and the 'joint score', $t(x, z|\mu) = \Delta_\mu \log p(x, z|\mu)$, can also be calculated from the morphing setup for any μ. The authors of [8] show that training a neural network to regress these quantities from the observables is effectively solving a calculus of variations problem of finding the true likelihood ratio $r(x|\mu_0, \mu_1)$ and score $t(x|\mu)$, marginalizing out the unobserved history of the events. The likelihood ratio can directly be used for inference, and the score can be binned and used as a locally optimal observable that is sensitive to μ.

Out of the two models investigated in this study, the first, "SALLY" (**S**core **A**pproximates **L**ikelihood **L**ocally), is trained on the joint-score at the SM point, $t(x, z|\mu_{SM})$, whereas the second, "ALICES" (**A**pproximate **L**ikelihood with **I**mproved **C**ross-entropy **E**stimator and **S**core), is in addition trained on the joint-likelihood ratio, $r(x, z|\mu_{SM}, \mu_1)$ for various test hypotheses, μ_1 (both developed by [9]). The latter is therefore aware of how the physics changes at parameter points far away from the SM, whereas the former is only aware of how the physics changes are the local neighbourhood of the SM.

4 Dataset

The dataset was generated with `MadGraph5_aMC` [3], `Pythia 8` [4] and `Delphes 3` [5], requesting $pp \to jjzz$ processes with the z decaying to ee or $\mu\mu$. Minimal preselection cuts were applied, apart from a requirement of at least 2 jets and 4 leptons. The observables used to train the network were the four momentum of the final state objects, energy and pseudo-rapidity (η) of the sum of all visible objects, missing transverse momentum and its azimuthal angle (ϕ), dijet invariant mass and angle differences, invariant mass of the four leptons system as well as the total number of leptons and jets. The distribution of all observables is given in Figure 6.

5 Results

Some preliminary results are shown in Figure 7 to compare a traditional 1-dimensional histogram fitting approach with two "physics-aware" neural network approaches to measure μ on two Asimov (i.e. representative) test datasets. At inference time, the inputs of the ALICES neural network, for a given event, are the measured observables of the event, as well as the hypothesis being tested (i.e. one particular value of μ). The output of the network is the likelihood ratio between the test hypothesis and the null hypothesis ($\mu = 1$). The output for all events in the test dataset for a given test hypothesis is converted into a single p-value (which represents here the probability of obtaining data at least as extreme as the test dataset, assuming that the test hypothesis is correct), and the entire process is redone for the same test dataset with a new test hypothesis (new value of μ). The p-values for the histogram techniques is calculated using multi-binned Poisson likelihood with the normalized histogram of particular physics variable (such as the invariant mass of the four leptons). SALLY performs better than traditional physics variables near the SM value ($\mu = 1$) as anticipated (see Figure 7b), but quickly deteriorates far away from it, performing not much better than the traditional technique for a test dataset generated with $\mu = 4$ (Figure 7a). ALICES, however, is aware of physics in the entire range of μ, and therefore more confidently excludes wrong values of μ for both the test dataset generated at the SM and the one generated at $\mu = 4$. It is the best technique at breaking the degeneracy near $\mu = 0$ in Figure 7a. The 1σ limits from ALICES is consistently better than all other techniques for Asimov test datasets generated at any point of μ in this study. However, it should be noted that total cross section information was not used in the p-value scan because the dominant $q\bar{q} \to ZZ$ background has not been included in this study, and it is expected to have a major contribution to how the total cross section affects the results.

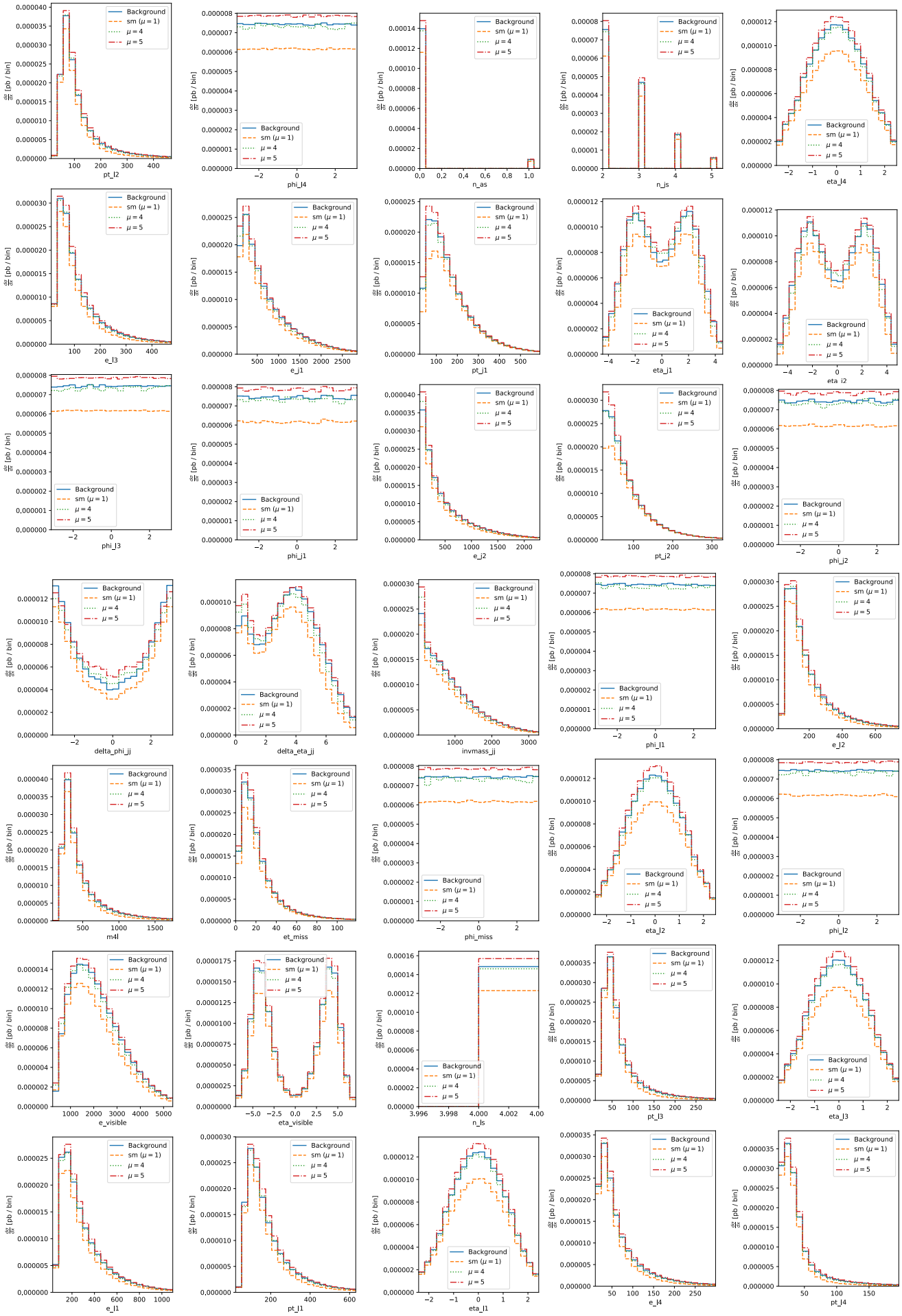

Figure 6: Distributions of all observables used in this study at $\mu = 0, 1, 4, 5$

6 Conclusions

A first study was performed to investigate a new family of machine learning algorithms that could be used for the off-shell Higgs to four leptons analysis in the ATLAS experiment at CERN. These techniques leverage the use of very accurate simulators in particle physics, to extract additional information that is very useful in learning the likelihood ratio between a test hypothesis and the null hypothesis. They also avoid the need to define 'true class labels', a concept that is ill-defined in the presence of quantum interference between signal and background processes.

The results demonstrate a considerable improvement in performance using the new machine learning technique compared to traditional histogram methods, however, a study with a true ATLAS experiment baseline, as well as the inclusion of all other signal and background processes has yet to be performed. The study was performed only for the Vector Boson Fusion produced Higgs process, which interferes with Vector Boson Scattering process in the high mass off-shell regime. The dominant $q\bar{q} \to ZZ$ background as well as $gg(\to H) \to ZZ$ processes need to be included for a full study.

Using such techniques in a full ATLAS analysis for the first time, including all the systematic uncertainty checks and combination of results, is an enormous effort. Additionally, the ATLAS software will need to be modified to extract and propagate the additional information from the simulator through the entire analysis chain. Statistical inference tools will also need to be updated to handle a network that is parameterized on the hypothesis being tested. The pyhf [13] package is expected to support such inference in the very near future.

Successfully adapting the ATLAS software infrastructure and developing strategies to harmonise uncertainty studies will allow integrating these tools into the ATLAS framework, thereby opening the door to various other applications of machine learning based likelihood-free inference, such as in Effective Field Theory studies, in the ATLAS experiment.

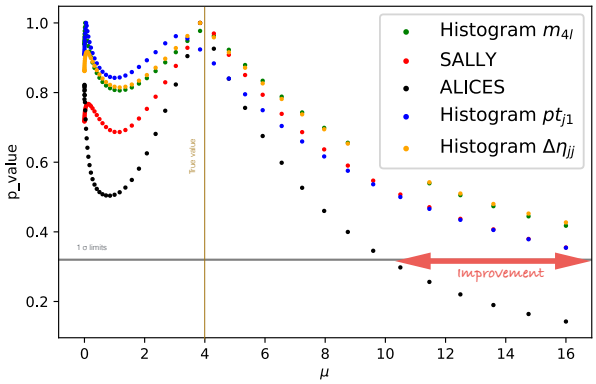

(a) p-value scan with Asimov test dataset generated at $\mu = 4$

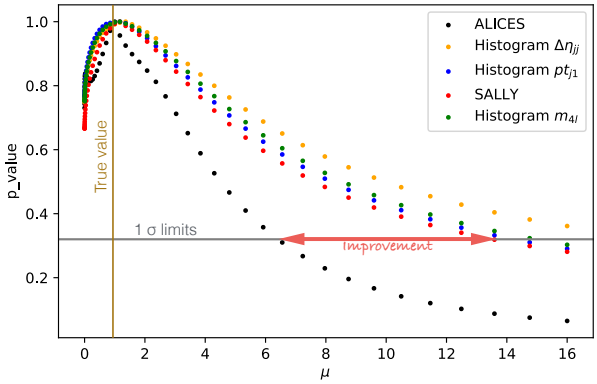

(b) p-value scan with Asimov test dataset generated at SM

Figure 7: p-values scans for Asimov test dataset generated at (a) $\mu = 4$ and (b) standard model ($\mu = 1$) for a luminosity of 36 fb^{-1} where the true value is indicated with the golden vertical line and the 1σ limit threshold indicated by the grey horizontal line

References

[1] ATLAS Collaboration. The ATLAS Experiment at the CERN Large Hadron Collider. *JINST*, 3:S08003, 2008.

[2] Morad Aaboud et al. Constraints on off-shell Higgs boson production and the Higgs boson total width in $ZZ \to 4\ell$ and $ZZ \to 2\ell 2\nu$ final states with the ATLAS detector. *Phys. Lett.*, B786:223–244, 2018.

[3] J. Alwall, R. Frederix, S. Frixione, V. Hirschi, F. Maltoni, O. Mattelaer, H. S. Shao, T. Stelzer, P. Torrielli, and M. Zaro. The automated computation of tree-level and next-to-leading order differential cross sections, and their matching to parton shower simulations. *JHEP*, 07:079, 2014.

[4] Torbjorn Sjostrand, Stephen Mrenna, and Peter Z. Skands. A Brief Introduction to PYTHIA 8.1. *Comput. Phys. Commun.*, 178:852–867, 2008.

[5] J. de Favereau, C. Delaere, P. Demin, A. Giammanco, V. Lemaître, A. Mertens, and M. Selvaggi. DELPHES 3, A modular framework for fast simulation of a generic collider experiment. *JHEP*, 02:057, 2014.

[6] Neyman Jerzy, Pearson Egon Sharpe, and Pearson Karl. On the problem of the most efficient tests of statistical hypotheses. *Philosophical Transactions of the Royal Society of London. Series A, Containing Papers of a Mathematical or Physical Character*, 231:289–337, 02 1933.

[7] M Neal, Radford. Computing Likelihood Functions for High-Energy Physics Experiments when Distributions are Defined by Simulators with Nuisance Parameters. 2008.

[8] Johann Brehmer, Kyle Cranmer, Gilles Louppe, and Juan Pavez. A Guide to Constraining Effective Field Theories with Machine Learning. *Phys. Rev.*, D98(5):052004, 2018.

[9] Johann Brehmer, Kyle Cranmer, Gilles Louppe, and Juan Pavez. Constraining Effective Field Theories with Machine Learning. *Phys. Rev. Lett.*, 121(11):111801, 2018.

[10] Johann Brehmer, Felix Kling, Irina Espejo, and Kyle Cranmer. MadMiner: Machine learning-based inference for particle physics. 2019.

[11] Johann Brehmer, Gilles Louppe, Juan Pavez, and Kyle Cranmer. Mining gold from implicit models to improve likelihood-free inference. 2018.

[12] D. de Florian et al. Handbook of LHC Higgs Cross Sections: 4. Deciphering the Nature of the Higgs Sector. 2016.

[13] M. Feickert L. Heinrich, G. Stark. diana-hep/pyhf: v0.1.2, July 2019.

Forward jet vertex tagging in ATLAS using the particle flow algorithm

Anastasia Kotsokechagia

Laboratoire de l'Accelerateur Lineaire (LAL)

Abstract — The rejection of forward jets originating from additional proton–proton interactions (pile-up) is crucial for a variety of physics analyses at the LHC, including Standard Model measurements and searches for physics beyond the Standard Model. This note presents a method for tagging forward jets originating from pile-up interactions using the ATLAS particle flow algorithm. The overall pile-up rejection power observed in POWHEG + PYTHIA8 simulated events for jets with transverse momentum between 20 and 60 GeV, is 34% and 51% with an efficiency of 87% and 76% respectively for selecting hard-scatter jets.

1 Introduction

In order to enhance the capability of experiments to discover physics beyond the Standard Model, the Large Hadron Collider (LHC) operates at the conditions yielding the highest possible integrated luminosity. As a result, the collisions of proton bunches result not only in large transverse-momentum transfer proton–proton (pp) interactions, but also in additional collisions within the same bunch crossing, primarily consisting of low-energy quantum chromodynamics (QCD) processes. Such additional pp collisions are referred to as in-time pile-up interactions. In addition to in-time pile-up, there exists another class of pile-up originating from energy deposits in the ATLAS calorimeter from the previous and following bunch crossings with respect to the analyzed event and is referred to as out-of-time pile-up. In this note, in-time and out-of-time pile-up are referred to collectively as pile-up (PU).

In Ref. [1] it was shown that pile-up jets can be effectively removed using track and vertex information with the jet-vertex-tagger (JVT) algorithm. A limitation of the JVT discriminant used by the ATLAS Collaboration is that it can only be used for jets within the coverage[1] of the tracking detector, $|\eta| < 2.5$, whereas ATLAS can reconstruct jets out to the full range of the calorimeter, $|\eta| < 4.5$. The rejection of pile-up jets in the forward region, here defined as $2.5 < |\eta| < 4.5$, is crucial to enhance the sensitivity of key analyses such as the measurement of Higgs boson production in the vector-boson fusion (VBF) process, single top studies, vector-boson scattering (VBS) processes, and in general any analysis that requires jets in the forward region [2, 3, 4, 5]. For this purpose, a technique was developed in ATLAS [6] that allows the identification and rejection of pile-up jets beyond the tracking coverage of the inner detector. Topological correlations among particles originating from a pile-up interaction are exploited to extrapolate the jet-vertex-tagger, using track and vertex information, to the forward region in order to identify and reject pile-up jets beyond the coverage of the tracking detector. In the following, this technique is referred as the forward jet-vertex-tagger (fJVT) algorithm. In this note, the development and performance of the fJVT algorithm using particle flow jets is presented for the first time in ATLAS. In Run 1 of the LHC, the ATLAS experiment used either solely the calorimeter or solely the tracker to reconstruct hadronic jets and soft particle activity. The vast majority of analyses utilized jets that were built from topological clusters of calorimeter cells (topo-clusters) [7]. These jets were then calibrated to the particle level using a jet energy scale (JES) correction factor [8, 9, 10, 11, 12]. For the final Run 1 jet calibration and the beginning of Run 2, this correction factor also took into account the tracks associated with the jet, as this was found to greatly improve the jet resolution [8]. Particle flow introduces an alternative approach, in which measurements from both the tracker and the calorimeter are combined to form the signals, which ideally represent individual particles. The energy deposited in the calorimeter by all the charged particles is removed. Jet reconstruction is then performed on an ensemble of "particle flow objects" consisting of the remaining calorimeter energy and tracks which are matched to the hard interaction. More details on the particle flow algorithm in ATLAS can be found in Ref. [13].

2 Monte Carlo Samples

Dijet events produced from collisions at $\sqrt{s} = 13$ TeV are simulated with the PYTHIA8 [14] event generator. Besides the generated primary collision, a set of additional, pile-up, interactions are overlaid for each event. Both the effect of in-time as well as out-of-

[1] ATLAS uses a right-handed coordinate system with its origin at the nominal interaction point (IP) in the center of the detector and the z-axis along the beam pipe. The x-axis points from the IP to the center of the LHC ring, and the y-axis points upward. Cylindrical coordinates (r, ϕ) are used in the transverse plane, ϕ being the azimuthal angle around the beam pipe. The pseudorapidity is defined in terms of the polar angle θ as η = -ln tan(θ/2).

time pile-up is simulated using minimum-bias events generated with Pythia8 to reflect the pile-up conditions during the 2017 data-taking period with a mean number of overlaid interactions of ∼39, using the A3 tune [15] and the NNPDF23LO [16] PDF set. A sample of Z bosons decaying into a pair of opposite charge muons, produced with jets (() + jets) is generated with Powheg + Pythia8 [17] interfaced with the AZNLO tune [18] and the CTEQ6L1 [19] PDF set. All generated events are processed with a detailed simulation of the ATLAS detector response, based on Geant 4 [20], and subsequently reconstructed and analyzed in the same way as the data.

3 Object Reconstruction and events selection

Vertices and tracks

The reconstructed primary vertex with the largest $\sum p_{\mathrm{T}}^2$ of constituent tracks is defined to be the hard scatter primary vertex in each event, as described in Ref. [6]. To avoid the convolution of the results of this study with the selection efficiency of the primary vertex, the reconstructed primary vertex z-coordinate is required to be within 0.1 mm ($|\Delta z| < 0.1$ mm) of the position of the true hard-scatter interaction. Tracks originating from the hard-scatter primary vertex are required to have $|z_0 \sin(\theta)| < 2$ mm, where z_0 is the distance of closest approach of the track to the hard-scatter primary vertex along the z-axis. All tracks are required to have $p_{\mathrm{T}} > 0.5$ and to satisfy quality criteria designed to reject poorly measured or fake tracks. Tracks are assigned to primary vertices based on the track-to-vertex matching resulting from the vertex reconstruction. Tracks that are not matched to any vertex are not considered.

Inputs to jet reconstruction

The particle flow (PFlow) jet reconstruction algorithm is employed in this study. In particle flow, a cell-based energy subtraction algorithm is applied in order to remove overlaps between the momentum and energy measurements made in the inner detector and calorimeters, respectively.

The inputs to the jet reconstruction are the PFlow objects, which are the ensemble of positive energy topo-clusters surviving the energy subtraction step of the PFlow algorithm, within $|\eta| < 2.5$, and the selected tracks that are matched to a primary hard-scatter or pile-up vertex. Prior to jet-finding, the topo-cluster η and ϕ are recomputed with respect to the primary vertex (PV) position, rather than the detector origin.

Outside the geometrical acceptance of the tracker, $|\eta| > 2.5$, only the calorimeter information is available. Hence, in the forward region, the topological clusters, formed from calorimeter cells with significant energy depositions, are used as inputs to jet reconstruction.

Jets

Jets are reconstructed using the anti-k_t algorithm [21] as implemented in [22], with a radius parameter of $R = 0.4$. The inputs to are the particle flow objects discussed above. After jets are built, a sequence of corrections are applied to calibrate the jets to the particle-level energy scale, as described in Ref. [12]. The calibrated jets are required to have a $p_{\mathrm{T}} > 20$ and are divided into two categories: those with $|\eta| < 2.5$, in order for most of their charged particles to be within the tracking coverage (central jets), and those with $|\eta| > 2.5$ (forward jets).

Jets built from particles in the Monte Carlo generator event record ("truth particles") are also considered. Truth-particle jets are reconstructed using the anti-k_t algorithm with a radius parameter of $R = 0.4$ from stable[2] final-state truth particles from all interactions (hard scatter and in time pile-up).

The simulation studies in this note require an additional classification of the reconstructed jets into two categories: hard-scatter and pile-up jets. Jets are labeled as hard-scatter (HS) if a truth-particle hard-scatter jet with $p_{\mathrm{T}} > 10$ is found within $\Delta R < 0.3$[3]. Jets are labeled as pile-up jets if no truth-particle hard-scatter jet with $p_{\mathrm{T}} > 10$ is found within $\Delta R < 0.6$. The pile-up jets are further divided into two categories: the QCD pile-up jets originating from a single QCD process, occurring in a single pile-up interaction, and the stochastic pile-up jets that include particles associated with both pile-up interactions in the event, without a single prevalent source [6].

Muons

Muons are built from an inner detector track (for $|\eta| < 2.5$) and a muon spectrometer track. Muons are required to satisfy $p_{\mathrm{T}} > 10$ as well as reconstruction quality and isolation criteria [23]. A veto on cosmic-ray muons is also applied. For selecting the events, two muons of opposite charge are further required, such that their invariant mass lies within the Z boson mass[4].

4 Forward JVT for particle flow jets

The forward JVT algorithm employs momentum conservation in order to tag a forward PFlow jet. First, central jets are reconstructed for every pile-up vertex i[5] and the relevant energy calibration is applied. This "per-vertex" jet reconstruction is required by the particle flow algorithm, and is different with respect to the

[2] Truth particles are considered stable if their decay length $c\tau$ is greater than 1 cm. A truth particle is considered to be interacting if it is expected to deposit most of its energy in the calorimeters; muons and neutrinos are considered to be non-interacting.

[3] Angular distance is measured in units of $\Delta R = \sqrt{(\Delta\phi)^2 + (\Delta\eta)^2}$.

[4] $|\mathrm{m} - \mathrm{m}_Z| < 25$ GeV.

[5] The positive-energy topo-clusters (described in Sec. **??**) are treated inclusively for all vertices here.

fJVT algorithm applied to calorimeter jets, for which calorimeter jets are reconstructed "per-event" and then matched to vertices [6]. Following the particle flow jet reconstruction and calibration, the QCD pile-up jets are distinguished from stochastic pile-up jets in the central region. For this, the $R^i_{p_{\mathrm{T}}}$ discriminant is used in the central region:

$$R^i_{p_{\mathrm{T}}} = \sum_{\mathrm{trk}} \frac{p_{\mathrm{T}}^{\mathrm{trk}}(\mathrm{PV}_i)}{p_{\mathrm{T}}^{\mathrm{jet}}} \tag{1}$$

defined as the scalar p_{T} sum of the tracks that are associated with the jet and originate from the pile-up vertex i divided by the fully calibrated jet p_{T}. QCD pile-up jets are expected to have the majority of the tracks associated to them originating from the same pile-up vertex (PV_i), and thus have large values of $R^i_{p_{\mathrm{T}}}$. Tracks associated with stochastic pile-up jets are not likely to originate from the same pile-up vertex, thus yielding small $R^i_{p_{\mathrm{T}}}$ values[6]. A value of $R^i_{p_{\mathrm{T}}}$ greater than 0.1 is chosen to optimally reject stochastic pile-up jets. Subsequently, a cut of JVT < 0.2, as described in Ref. [6], is applied in order to ensure that hard-scatter central jets are not taken into account. The efficiency of the JVT cut is very high, rejecting 98.8% of the hard-scatter central jets. The missing transverse momentum per vertex i ($\mathbf{p}^{\mathrm{miss}}_{\mathrm{T},i}$) is then calculated as

$$\begin{aligned}\mathbf{p}^{\mathrm{miss}}_{\mathrm{T},i} = -\Big(& \sum_{\text{jets, } p_{\mathrm{T}}^{\mathrm{jet}}>20} \mathbf{p}_{\mathrm{T}}{}^{\mathrm{jet}} \\ & + \sum_{\text{tracks, } p_{\mathrm{T}}^{\mathrm{jet}}<20} \mathbf{p}_{\mathrm{T}}{}^{\mathrm{track}} \\ & + \sum_{\text{tracks, jets fail } R^i_{p_{\mathrm{T}}} \text{ cut}} \mathbf{p}_{\mathrm{T}}{}^{\mathrm{track}} \Big)\end{aligned}$$

where the components correspond to:

- The vector sum of all the central jets with transverse momentum $p_{\mathrm{T}}^{\mathrm{jet}} > 20$,
- The vector sum of the tracks transverse momentum for the jets with $p_{\mathrm{T}}^{\mathrm{jet}} < 20$,
- The vector sum of the tracks transverse momentum of the tracks associated to the jets that were rejected with the $R^i_{p_{\mathrm{T}}}$ cut at the previous step of the algorithm.

Finally, for every forward jet, the normalized projection of $\mathbf{p}^{\mathrm{miss}}_{\mathrm{T},i}$ on the direction of the forward jet,

$$\mathrm{fJVT}_i = \frac{\mathbf{p}^{\mathrm{miss}}_{\mathrm{T},i} \cdot \mathbf{p}_{\mathrm{T}}{}^{\mathrm{fj}}}{|\mathbf{p}_{\mathrm{T}}{}^{\mathrm{fj}}|^2} \tag{2}$$

is computed. The final forward JVT (fJVT) discriminant is then defined as

$$\mathrm{fJVT} = \max_i(\mathrm{fJVT}_i) \ . \tag{3}$$

[6] Note that all the stochastic pile-up jets seen are due to the positive-energy topo-clusters participating in the jet reconstruction.

For a forward pile-up jet, it is expected that its energy will be balanced by the $\mathbf{p}^{\mathrm{miss}}_{\mathrm{T},i}$ leading to fJVT values close to 1. On the contrary, this effect is not present at the case of hard-scatter forward jets, resulting in fJVT values closer to 0. Therefore, a forward jet is tagged as pile-up if its fJVT value is above a given threshold ($\mathrm{cut}_{\mathrm{fjvt}}$).

The fJVT discriminant has been trained using a simulated dijet MC sample, in a leading truth jet p_{T} range of 60 to 160 GeV, and validated using a simulated $Z(\rightarrow)$ + jets MC sample.

5 Results

fJVT discriminant with particle flow jets

The fJVT discriminant for forward jets is shown in Fig. 1 for $30 < p_{\mathrm{T}}^{\mathrm{jet}} < 40$ and $40 < p_{\mathrm{T}}^{\mathrm{jet}} < 50$. The fJVT value for pile-up jets tends to be smaller than those of hard-scatter jets, offering a powerful discriminant.

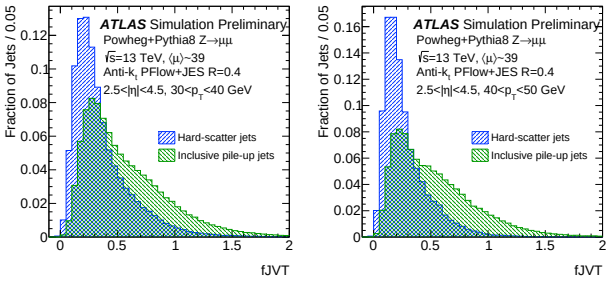

Figure 1: fJVT distributions for hard-scatter (blue) and pile-up (green) forward jets with $30 < p_{\mathrm{T}}^{\mathrm{jet}} < 40$ (left) and $40 < p_{\mathrm{T}}^{\mathrm{jet}} < 50$ (right).

Performance

For a given fJVT cut value, where fJVT$<$ $\mathrm{cut}_{\mathrm{fjvt}}$, the hard-scatter and pile-up efficiencies are defined as:

$$\varepsilon_{\mathrm{HS}} = \frac{\mathrm{N}(\mathrm{jets}^{\mathrm{matched}}_{\mathrm{HS}}, \ \text{with fJVT}< \mathrm{cut}_{\mathrm{fjvt}})}{\mathrm{N}(\mathrm{jets}^{\mathrm{matched}}_{\mathrm{HS}})} \ , \tag{4}$$

and

$$\varepsilon_{\mathrm{PU}} = \frac{\mathrm{N}(\mathrm{jets}^{\mathrm{matched}}_{\mathrm{PU}}, \ \text{with fJVT}< \mathrm{cut}_{\mathrm{fjvt}})}{\mathrm{N}(\mathrm{jets}^{\mathrm{matched}}_{\mathrm{PU}})} \ , \tag{5}$$

where $\mathrm{N}(\mathrm{jets}^{\mathrm{matched}}_{\mathrm{HS}})$ is the number of jets matched geometrically to truth jets coming from the hard-scatter vertex, and $\mathrm{N}(\mathrm{jets}^{\mathrm{matched}}_{\mathrm{PU}})$ is the number of jets that are not matched geometrically to truth jets and are therefore considered to be pile-up jets. The pile-up jet efficiency as a function of the hard-scatter jet efficiency, while varying the fJVT cut value (fJVT$<$ $\mathrm{cut}_{\mathrm{fjvt}}$), is plotted in Fig. 2 for four p_{T} regions. The performance of the fJVT discriminant improves as p_{T} increases. For an fJVT cut value of 0.53 (0.72), hard-scatter efficiencies of 76% (87%) are achieved, yielding pile-up efficiencies of 49% (66%) for forward jets with $20 < p_{\mathrm{T}} < 60$.

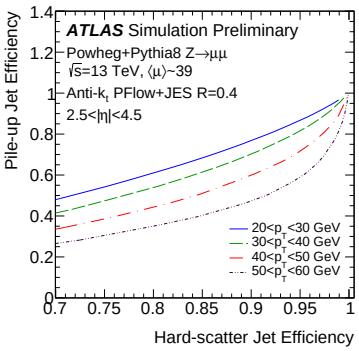

Figure 2: Efficiency for pile-up jets in simulated events as a function of the efficiency for hard-scatter jets for different jet p_{T} ranges. For a standard value of hard-scatter jet efficiency the pile-up jet efficiency is improving with p_{T} since pile-up effects are less dominant in higher p_{T} bins.

The dependence of the hard-scatter and pile-up efficiencies on the forward jet p_{T} is shown in Fig. 3. As expected, the probability of mis-labeling a forward hard-scatter jet as pile-up is higher in the low p_{T} bins, yielding to lower hard-scatter jet efficiencies. In Fig. 4, the hard-scatter and pile-up jet efficiencies are plotted as a function of the number of primary vertices ($\mathrm{N_{PV}}$) for two forward jet p_{T} regions. A dependency of the hard-scatter jet efficiency on the $\mathrm{N_{PV}}$ is observed as expected.

The performance was also evaluated using the dijet sample, and for a fixed hard-scatter jet efficiency the background rejection was compatible within a relative 5%.

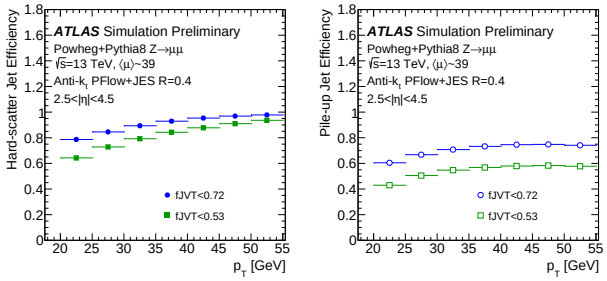

Figure 3: Hard-scatter (left) and pile-up (right) jet efficiency as a function of forward jet p_{T} for simulated events.

6 Conclusions

Forward JVT (fJVT) is a technique developed for the suppression of pile-up jets in the forward region. In this note, the development and performance of this technique using particle flow jets is presented for the first time in ATLAS. The method exploits the correlation of the transverse momentum of QCD pile-up jets in the transverse plane between central and forward region of the detector, introducing a technique of tagging pile-up

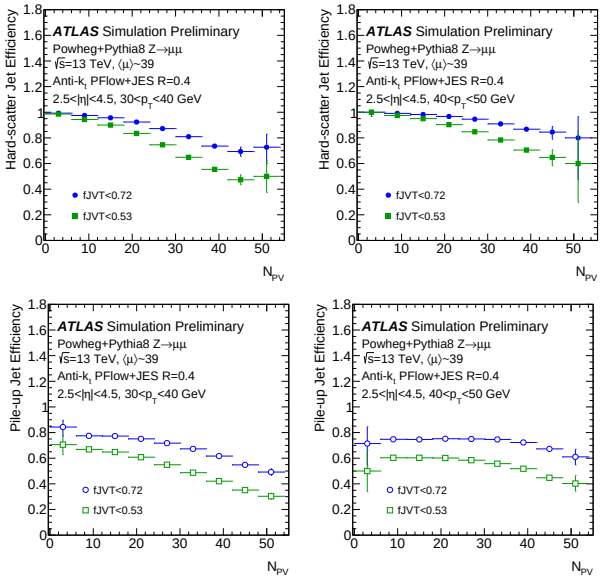

Figure 4: Efficiency in simulated events as a function of N_{PV} for hard-scatter forward jets with $30 < p_{\mathrm{T}} < 40$ (top left), $40 < p_{\mathrm{T}} < 50$ (top right), and for pile-up forward jets with $30 < p_{\mathrm{T}} < 40$ (bottom left), and $40 < p_{\mathrm{T}} < 50$ (bottom right).

jets beyond the coverage of the tracker. In samples with Pythia8 pile-up simulation, the technique reduces the overall forward pile-up jet rate by 51% and 34% for hard-scatter efficiencies of 76% and 87%, respectively. The hard-scatter efficiency depends on the jet p_{T}, and a dependence on the number of reconstructed primary vertices is observed as expected. Forward JVT provides the capability for pile-up suppression at high pseudo-rapidity in ATLAS, and has been extended for the first time to be usable with the particle flow reconstruction of jets.

References

[1] ATLAS Collaboration. Performance of pile-up mitigation techniques for jets in pp collisions at $\sqrt{s} = 8$ TeV using the ATLAS detector. Eur. Phys.J. C76(2016) 581, arXiv:1510.03823 [hep-ex]

[2] ATLAS Collaboration. Measurements of the Higgs boson production, fiducial and differential cross sections in the 4ℓ decay channel at $\sqrt{s} = 13$ TeV with the ATLAS detector. ATLAS-CONF-2018-018, 2018

[3] ATLAS Collaboration. Measurement of Higgs boson production in association with a $t\bar{t}$ pair in the diphoton decay channel using 139 fb1 of LHC data collected at $\sqrt{s} = 13$ TeV by the ATLAS experiment. ATLAS-CONF-2019-004, 2019

[4] ATLAS Collaboration. Search for large missing transverse momentum in association with one top-quark in protonâproton collisions at $\sqrt{s} = 13$ TeV with the ATLAS detector. JHEP (2018), arXiv:1812.09743 [hep-ex]

[5] ATLAS Collaboration. Observation of electroweak production of a same-sign W boson pair in association with two jets in pp collisions at $\sqrt{s}$ = 13 TeV with the ATLAS detector. (2019), arXiv:1906.03203 [hep-ex]

[6] ATLAS Collaboration. Identification and rejection of pile-up jets at high pseudorapidity with the ATLAS detector. Eur. Phys. J. C77(2017) 580,arXiv:1705.02211 [hep-ex],Erratum: Eur. Phys. J. C77(2017) 712.

[7] ATLAS Collaboration. Topological cell clustering in the ATLAS calorimeters and its performance in LHC Run 1. Eur. Phys. J. C77(2017) 490,arXiv:1603.02934 [hep-ex]

[8] ATLAS Collaboration. Jet global sequential corrections with the ATLAS detector in protonâproton collisions at $\sqrt{s}$ = 8 TeV . ATLAS-CONF-2015-002, 2015

[9] ATLAS Collaboration. Data-driven determination of the energy scale and resolution of jets reconstructed in the ATLAS calorimeters using dijet and multijet events at $\sqrt{s}$ = 8 TeV . ATLAS-CONF-2015-017, 2015

[10] ATLAS Collaboration. Monte Carlo Calibration and Combination of in-situ Measurements of Jet Energy Scale, Jet Energy Resolution and Jet Mass in ATLAS. ATLAS-CONF-2015-037, 2015

[11] ATLAS Collaboration. Determination of the jet energy scale and resolution at ATLAS using Z/γ-jet events in data at $\sqrt{s} = 8$ TeV . ATLAS-CONF-2015-057, 2015

[12] ATLAS Collaboration. Jet energy scale measurements and their systematic uncertainties in protonâproton collisions at $\sqrt{s}$ = 13 TeV with the ATLAS detector. Phys. Rev. D96(2017) 072002, arXiv:1703.09665 [hep-ex]

[13] ATLAS Collaboration. Jet reconstruction and performance using particle flow with the ATLAS Detector. Eur. Phys. J. C77(2017) 466, arXiv:1703.10485 [hep-ex]

[14] T. Sjöstrand et al. An Introduction to PYTHIA8.2. Comput. Phys. Commun.191(2015) 159,arXiv:1410.3012 [hep-ph]

[15] ATLAS Collaboration. The Pythia 8 A3 tune description of ATLAS minimum bias and inelastic measurements incorporating the DonnachieâLandshoff diffractive model. ATL-PHYS-PUB-2016-017, 2016

[16] R. D. Ball et al. Parton distributions with LHCdata. Nucl. Phys. B867(2013) 244, arXiv:1207.1303 [hep-ph]

[17] S. Alioli, P. Nason, C. Oleari, and E. Re. NLOvector-boson production matched with shower in POWHEG. JHEP07(2008) 060, arXiv:0805.4802 [hep-ph]

[18] ATLAS Collaboration. Example ATLAS tunes of Pythia8, Pythia6 and Powheg to an observable sensitive to Z boson transverse momentum. ATL-PHYS-PUB-2013-017, 2013

[19] J. Pumplin et al. New generation of parton distributions with uncertainties from global QCD analysis. JHEP07(2002) 012, arXiv:hep-ph/0201195

[20] S. Agostinelli et al. GEANT4: A Simulation-toolkit. Nucl. Instrum. Meth. A506(2003) 250

[21] M. Cacciari, G. P. Salam, and G. Soyez. The anti-ktjet clustering algorithm. JHEP04(2008) 063,arXiv:0802.1189 [hep-ph]

[22] M. Cacciari, G. P. Salam, and G. Soyez. FastJetUser Manual. Eur. Phys. J. C72(2012) 1896,arXiv:1111.6097 [hep-ph]

[23] ATLAS Collaboration. Muon reconstruction performance of the ATLAS detector in protonâproton collision data at $\sqrt{s} = 13$ TeV . Eur. Phys. J. C76(2016) 292, arXiv:1603.05598 [hep-ex]

Towards the first observation of the simultaneous production of four top quarks with the ATLAS detector

Lennart Rustige

LPC Clermont Ferrand / Université Clermont Auvergne / TU Dortmund

Abstract — This contribution belongs to the field of high energy particle physics (HEP), which is the part of physics dealing with the question: "What are the fundamental building blocks of nature and how do they interact?". In order to introduce the main topic, a broad overview is given of the theoretical models and the experimental and statistical tools needed.

1 Introduction

The theoretical framework of this field is called the standard model of particle physics (SM), which is a powerful framework resulting in very precise predictions and it has been tested and validated in a large variety of different experiments over the course of its existence.
Even though the SM already covers a very broad spectrum in HEP, a few major phenomena, such as gravity or dark matter, are not yet accounted for. To incorporate these processes not yet described by the SM, is one of the goals of beyond standard model (BSM) theories.

Seeing that there are a plethora of possibly valid BSM theories, it is the task of experimentalists to find and study processes that have a differently predicted outcome for the SM or BSM theories, which would allow for a verification or falsification of the corresponding models.
Among such processes, those involving a top quark play an important role due to the quark's elevated mass and its corresponding short decay time, which inhibits the forming of compound states for this particle. Within this group of top quark related processes, a particularly interesting process is the simultaneous production of four top quarks, since it involves a very high center-of-mass energy, since it has not yet been observed and because the probability of occurrence predicted by the SM and BSM theories differ enormously.

2 Particle Physics

The field of particle physics covers phenomena from the currently smallest directly measurable lengths of about 10^{-18}m to sizes at the scale of the (visible) universe of about 10^{26}m. Its objective is to study the most fundamental building blocks of the universe, i.e. particles, to determine their interactions and to describe those in a comprehensive model called the standard model (SM). Following that the sizes of those building blocks are very small and that their interactions happen at speeds comparable to the speed of light, the mathematical description used for such a comprehensive model is quantum field theory (cf. Figure 1). The SM is built around the idea of gauge symmetries, which makes it a very elegant and powerful model and it has been tested and verified in countless experiments to date.

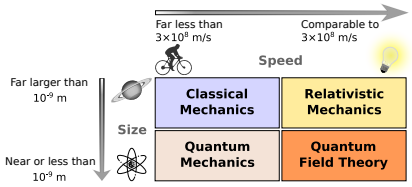

Figure 1: Classification-scheme of modern physics fields in dependence of speed and size. [1]

The SM comprises a series of fundamental particles, a quick overview of which can be found in Figure 2. Among those, bosons represent the force-carriers of three of the four fundamental forces, i.e. the electromagnetic, the weak and the strong interaction, and the Higgs mechanism. Additionally, it comprises six quarks that carry an electric and a color charge, and which can be further grouped into up- and down-like quarks and into three different families. Finally, leptons are included which can be grouped into electrically charged and neutral leptons and into three families.

As indicated above, only three of the four fundamental forces are included in the SM, leaving out gravitation. In addition, the SM is currently not able to fully describe the matter/anti-matter asymmetry observed in the universe and it also currently does not include mechanisms neither for dark matter nor for dark energy. This leads to the need for BSM theories that can be probed by experimentalists.

3 Challenges and Experimental Setup

The main challenge in particle physics is the fact that in most cases the measurements are very indirect

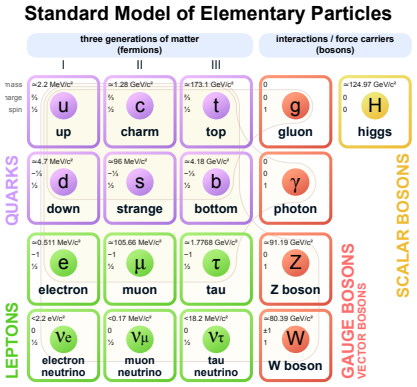

Figure 2: Table of fundamental particles described by the standard model of particle physics. [1]

and only the decay products of the particles and interactions under study are available. Given that the underlying principles of quantum mechanics yield probability based predictions, the only viable interpretations in this field are through statistical methods.
In more applied terms, the reader could be interested in the search of $H \rightarrow bb$. The only measurable quantity would then be the two b-quarks coming from the Higgs boson. On the other hand, two b-quarks could be produced in a series of other processes, most notably gluon-gluon fusion, where two gluons fuse to one virtual gluon, which then decays into a pair of b-quarks. The task of the reader is then to design an experiment and a statistical test that would allow for discrimination of the sought-after Higgs decay against all the other possible production mechanisms and to give a level of confidence on this conclusion.

In the full analysis chain, the most important tool to achieve this are Monte Carlo (MC) simulations, that combine the community's current understanding of the processes involved in a probabilistic simulation based on random numbers. It often is a sophisticated comparison between the results that are anticipated by the simulation and the results that are actually measured.

The actual measurements in this field come from particle colliders, or in the case of this contribution from the Large-Hadron-Collider (LHC) situated approximately 100 m beneath the franco-swiss border near Geneva. The LHC is a proton-proton circular collider at 27 km circumference and it currently runs at an unprecedented center-of-mass energy of $\sqrt{s} = 13\,\text{TeV}$. There are four major experiments at four different interaction points of the LHC, i.e. where the clock- and anticlockwise proton beams may be brought to collision, the largest of which is called ATLAS.

4 Four Top Quarks

The top quark was first discovered in 1995 [3][4] and it has since become one of the major particles of interest in the HEP community for a number of reasons. One of the reasons is that the top quark is the heaviest particle of the SM and considerably heavier than all the other quarks (cf. Figure 3). This large mass results in a decay time that is shorter than the time needed to form a compound state (called hadronization), so that the processes under study are not so much biased by this effect. Another very interesting fact is that its interaction with the Higgs boson, expressed as the Yukawa coupling y_t, is very close to 1, indicating a special role of the top quark in the electroweak symmetry breaking that gives rise to the Higgs boson.

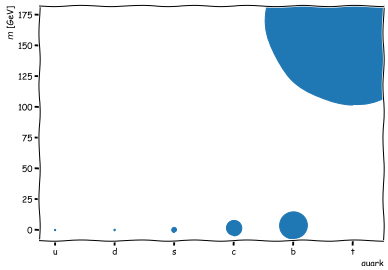

Figure 3: Masses of the six known quarks

As mentioned in the introduction, one of the current goals of experimentalists in HEP is to search for processes that have a different predicted outcome between the SM and BSM theories. One such process is the simultaneous production of four top quarks, which is of particular interest, firstly because it involves four times the heaviest particle leading to a very energetic event. Secondly, it is interesting because the accumulated data by the ATLAS experiment may soon be enough to observe this process given the SM hypothesis for the first time.

The theoretical prediction of the production cross-section, i.e. a measure of the probability of this process taking place, of the process $pp \rightarrow t\bar{t}t\bar{t}$ at next-to-leading order in quantum-chromo-dynamics and the electroweak sector is $\sigma(pp \rightarrow t\bar{t}t\bar{t}) = 11.97\,\text{fb}$ [2]. To put this into perspective, previous analyses at the ATLAS and CMS experiments set upper limits to the production cross-section at a 95 % confidence level at 49 fb [5] and 33 fb [6], respectively, using a data set corresponding to an integrated luminosity of $L \approx 36\,\text{fb}^{-1}$.

In order to measure the production cross-section of this process, the decay probabilities, called branching ratios, of the top quark need to be taken into account, seeing that only the decay products are measurable within the experiment. The top quark decays in almost 100 % of the cases into a W-boson and a b-quark.

The b-quark may then directly interact with the detector, here, directly means that the decay products of a bound state interact with the detector, whereas the W-boson further decays into a quark/anti-quark pair ($\sim 60\,\%$ probability) or into a charged lepton and a neutrino ($\sim 30\,\%$ probability, excluding the τ-lepton). The decay of the top quark resulting in a quark/anti-quark pair and a b-quark is often denoted hadronic decay (h), whereas the decay of the top quark into a charged lepton, a neutrino and a b-quark is denoted leptonic decay (ℓ).
Given that there are four top quarks that decay and that they have no order, there are 5 different decay channels: $hhhh$, $hhh\ell$, $hh\ell\ell$, $h\ell\ell\ell$ and $\ell\ell\ell\ell$. For this analysis there is a further split where there are two leptonic and two hadronic decays, depending on whether the two charged leptons in the final state have the same electric charge (SS) or an opposing electric charge (OS). The all-hadronic decay ($hhhh$) is not considered for this analysis even though it makes up a large share of the produced four-top events ($\sim 31\,\%$), because it is extremely difficult to separate the signal from background, i.e. other processes that yield the same set of particles interacting with the detector. With the same argument, not the decay channel with the largest BR, $hhh\ell$, has had the highest sensitivity in previous analyses, but the $hh\ell\ell$ SS and $h\ell\ell\ell$ channels. The proportions of all the possible decay channels are found in Figure 4.

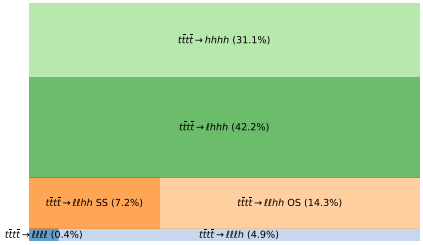

Figure 4: Branching ratios of four top quark decays. h meaning "hadronic" decay of a top and ℓ representing the "leptonic" decay of a top

There are two main background categories for the $hh\ell\ell$ SS (SS) and $h\ell\ell\ell$ (ML) channels. The instrumental backgrounds that come from processes that would not normally result in a similar set of final state particles (particles measurable by the detector) as the signal, but do so because of errors in the measurement, hardware or software related or both, and the physics backgrounds which are simply other possible processes that result in a similar set of final state particles as the signal.

In order to determine whether or not a signal is observed in the available data set, a profile likelihood fit using the MC simulation and measured data is applied. In this fit there is a particular parameter of interest (in this case the signal strength of the four top quark production) and a large series of other free parameters some of which may be constrained or determined by auxiliary measurements, being fully independent analyses or coming from regions in the phase space particularly suited to isolate the impact of these parameters called control regions. A schematic of what a signal region (most important for determining the parameter of interest) and a control region may look like is shown in Figure 5.

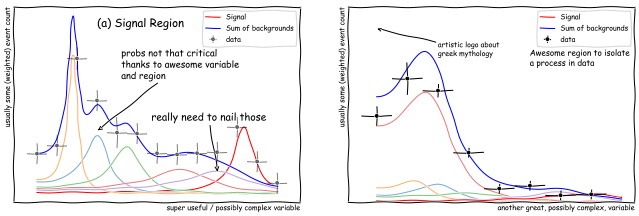

Figure 5: Schematic of a possible signal region (left) and a control region (right)

5 Reconstruction

The next step after discovering the simultaneous production of four top quarks will be to investigate its properties. In order to do so, the four top quark system needs to be reconstructed, i.e. the measured final state particles need to be combined in the correct way to yield the four-vectors of each of the produced and subsequently decayed top quarks.

Not only is this the logical next step, but algorithms that reconstruct the four top quark system may be used to further discriminate the signal from background even before this signal is discovered.

To probe the feasibility of the reconstruction of the four top quark system, a study is conducted using the KLFitter [7] tool with a likelihood that corresponds to the $hhh\ell$ decay of the system.

The major difficulty of the $hhh\ell$ decay is that it results in 10 jets, 1 lepton and 1 neutrino in the final state, where all possible permutations of the 10 jets, i.e. $10! = 3,628,800$ permutations are tested for every collision event (simulated or real). Another challenge with the standard approach in KLFitter is that all final state particles at parton level, i.e. before detector reconstruction effects, need to be correctly reconstructed by the experiment's software. Currently, this is only the case for about 0.06% of collision events that have already been loosely pre-selected to fit the $hhh\ell$ decay (cf. Figure 6).

In principle, the tool could handle the case where additional jets are reconstructed, but since that would further worsen the combinatorial payload, this case is omitted during this study.

The large number of viable permutations can be significantly reduced by using two approaches. First, b-

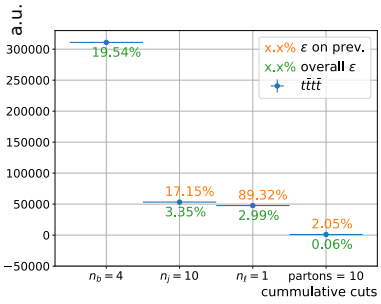

Figure 6: Collision event selection efficiencies of a four top quark MC sample after a loose pre-selection. The last bin corresponds to the selection used in the four top system reconstruction study

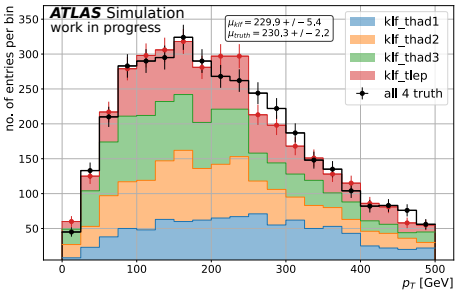

Figure 8: Transverse momentum p_T distributions of the reconstructed top quark system (colored) and the simulated top quark system at parton level (black).

tagging can be used, which identifies jets originating from a b-quark, and second the fact that ordering between light jets, i.e. all jets that originate from quarks that are lighter than the b-quark, is not important for the calculation of four-vectors. The former restricts the permutations under the hypothesis that a top quark decay results in exactly one b-quark so that any permutation that would match two b-tagged jets to one top quark can be dismissed. The latter restricts the number of permutations because the reconstructed four-vector of a W-boson is calculated by summing the four-vectors of two jets, which is a commutative operation. A summary of those two techniques is given in Figure 7. Applying these techniques reduces the number of viable permutations from $3,628,800$ to just 360.

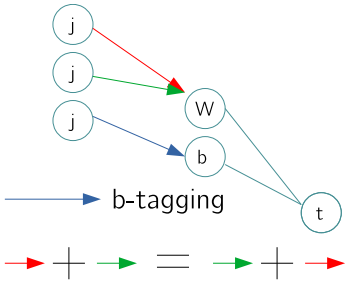

Figure 7: Schematic of the two approaches to reduce the number of possible jet permutations.

As a result of this study, it could be shown that the reconstruction using KLFitter works well given the caveat that currently this should only be applied to a fraction of all collision events. Figure 8 shows the agreement between the transverse momentum p_T distribution of the reconstructed top quarks (colored areas) and the simulated top quarks (black) at parton level, indicating a successful reconstruction procedure.

6 Summary

This contribution broadly introduces the topic of particle physics as a whole and the search for the simultaneous production of four top quarks in detail to the general public. As such, the general approach for searches conducted using data from the ATLAS experiment is laid out, followed by a description of the challenges faced in the case of the search for four top quarks, i.e. it is very rare $\sigma(pp \to t\bar{t}t\bar{t}) = 11.97\,\text{fb}$ [2] and there are a series of detector and physics related backgrounds that need to be controlled or estimated. Finally, a very promising outlook is given by presenting a study that uses the KLFitter tool to reconstruct the four top quark system, which yields good results.

References

[1] Creative Commons, Wikimedia

[2] Frederix et al., *Large NLO corrections in $t\bar{t}W^{\pm}$ and $t\bar{t}t\bar{t}$ hadroproduction from supposedly subleading EW contributions*, JHEP 02(2018) 031

[3] D0 Collaboration, *Observation of the Top Quark*, Phys. Rev. Lett. 74, 2632

[4] COF Collaboration, *Observation of Top Quark Production in $p\bar{p}$ Collisions with the Collider Detector at Fermilab*, Phys. Rev. Lett. 74, 2626

[5] ATLAS Collaboration, *Search for four-top-quark production in the single-lepton and opposite-sign dilepton final states in $p\bar{p}$ collisions at $\sqrt{s} = 13\,TeV$ with the ATLAS detector*, Phys. Rev. D 99, 052009 (2019)

[6] CMS Collaboration, *Search for the Production of Four Top Quarks in the Single-Lepton and Opposite-Sign Dilepton Final States in Proton-Proton Collisions at $\sqrt{s} = 13\,TeV$*, JHEP 1911 (2019) 082

[7] Erdmann et al., *A likelihood-based reconstruction algorithm for top-quark pairs and the KLFitter framework*, Nucl. Instrum. Meth. (2014)

Part IX

Theoretical Physics

session chaired by Andreas GOUDELIS

Theoretical Physics Session Introduction

Andreas Goudelis

Laboratoire de Physique de Clermont (UMR 6533), CNRS/IN2P3, Univ. Clermont Auvergne, 4 Av. Blaise Pascal, F-63178 Aubière Cedex, France

Abstract — In this introductory talk we briefly discuss two topics that will be elaborated upon in more detail during the "Theoretical Physics" session: Lattice Quantum ChromoDynamics and Dark Matter. Our aim is to introduce the topics in a pedagogical and accessible manner, focusing on some conceptual issues rather than on mathematical rigour.

1 Introduction

Theoretical physics is a vast, ever-evolving (and, needless to say, wonderful!) field. It addresses topics as diverse as the origins of the Universe, the elementary constituents of matter, the structure of atoms, crystals and semiconductors, the mathematical foundations of physical laws and so on. Basically, it is half of physics - the other half being, of course, experimentation. Being such a broad subject, theoretical physics is not completely straightforward to define. I think that it is, however, fair to say that it generically involves three key elements.

The first element is *abstraction*. In theoretical physics we typically try to reduce physical systems down to simpler (often idealized) ones, and the physical laws that theorists formulate are typically deduced from (and intended to apply to) more than just one single physical phenomenon: the second law of theormodynamics, perhaps the most iron-clad law that we know of, does not only apply to refrigerators extracting heat from their interior, it applies to nearly any real-world (or even remotely realistic) physical system that we can think of. Secondly, despite its reputation theoretical physics aims at developing a *qualitative understanding* of the physical world surrounding us. Put simply, we are not just interested in writing down equations and computing numbers, we are equally interested in understanding what these equations mean and in developing some sort of intuition about them. This becomes all the more relevant – and challenging – in relativistic and/or quantum mechanical systems, which involve phenomena that often evade our simple everyday perception. Last but not least, yes, theoretical physics also aims at developing a *quantitative description* of physical phenomena, by defining mathematical objects in order to describe the properties of physical systems and establishing relations among them.

In this short presentation we will introduce, in a brief – and mostly qualitative – manner, the two topics that will be discussed by the speakers that follow in this session: Lattice Quantum ChromoDynamics and Dark Matter. Our goal is by no means to provide an exhaustive presentation of these two subjects. They are both extremely active areas of research and any such effort would not make them justice. Instead, we will focus on some conceptual issues that will hopefully render what follows more understandable.

2 Lattice Quantum Chromodynamics

The world of microscopic, relativistic physics is described by the mathematical framework of quantum field theory. In this picture, particles are described as excited states of fields, operator-valued functions of spacetime. The interactions between such fields can be encoded by a very important mathematical object called *Lagrangian*. Consider, for example, a real scalar field ϕ. The most general Lagrangian that we can write down with such a limited field content and involving up to four fields in each term reads

$$\mathcal{L} = (\partial_\mu \phi)(\partial^\mu \phi) - \frac{m^2}{2}\phi^2 + \frac{a}{3!}\phi^3 + \frac{\lambda}{4!}\phi^4 \qquad (1)$$

where m is the mass of ϕ and a and λ are constants, with a having units of mass and λ being dimensionless. The first two terms in the RHS of this equation correspond to the kinetic and the mass term for the ϕ field, respectively. The third and fourth term, in turn, describe the way through which three or four fields interact with each other. Note that the reason for not writing down higher-order terms involving, *e.g.*, five fields, is related to a more subtle property of quantum field theories called renormalizability which is, loosely speaking, related to the question of up to what energy scale our theory holds.

The Standard Model of particle physics is described by a similar, albeit slightly more involved, framework: each species of known elementary particles is also described by a dedicated quantum field, and their interactions are described by a – considerably lengthier – Lagrangian. The strong interactions, in particular, concern a subset of the known elementary particles: the gluons, which are the (spin-1) carriers of the strong force and the quarks, which are the (spin-1/2) matter fields that participate, along with the gluons, in pro-

cesses mediated by these interactions. The underlying theory is called Quantum ChromoDynamics (QCD).

Employing a bit of hiddsight, let us also point out that the "constants" appearing in a Lagrangian are actually not exactly constant. For example, the strength of most interactions varies with energy and, in particular, the strong coupling constant becomes large at low energies.

So how do we compute measurable quantities? In quantum physics observables are represented by operators. Quantities such as cross-sections, decay rates etc can be calculated as expectation values of such operators. The basic object that we (often, silently) employ when computing these expectation values is the so-called *path integral*. In particular, the expectation value of an operator $\mathcal{O}$ is

$$\langle \mathcal{O} \rangle \propto \int \mathcal{D}\phi \; e^{i \int d^4x \mathcal{L}[\phi]} \; \mathcal{O}[\phi] \tag{2}$$

where $\mathcal{L}[\phi]$ (the Lagrangian) and $\mathcal{O}[\phi]$ are generalizations of ordinary functions (called *functionals*) and $\int \mathcal{D}\phi$ denotes integration over a functional space. The theory behind such expressions can be found in numerous excellent textbooks on quantum field theory, *e.g.* [1, 2]. Long story short, the path integral is an integral over all field configurations as well as all spacetime points.

From the previous, it would seem that we possess a perfectly well-defined framework to compute physical observables in relativistic quantum mechanics. The problem is that, in the general case, we do not actually know how to compute such objects[1].

In particle physics, two solutions are envisaged. Let's consider an even simpler Lagrangian than the one in Eq.(1) as

$$\mathcal{L} = (\partial_\mu \phi)(\partial^\mu \phi) - \frac{m^2}{2}\phi^2 + \frac{\lambda}{4!}\phi^4 \; . \tag{3}$$

The first two terms represent the "free part" of the Lagrangian whereas the last term encodes all the interactions (in this case, the interaction of four ϕ fields with each other). If we assume that the parameter λ is small, then we can separate the free from the interacting part in Eq.(2), calculate the free part (this is something that we do know how to do), Taylor-expand the exponential involving the interacting part[2] and end up with ordinary integrals that we know how to compute. This is the approach of perturbation theory, which can be used, *e.g.*, to compute the hard part of Drell-Yan production at the Large Hadron Collider (LHC).

But what if the parameter λ is not small? In particular, we already mentioned that the QCD coupling constant can become sizable at low-energies. In this case, we can no longer rely on perturbation theory since our Taylor expansion will not converge as we compute higher and higher orders. When λ (or any coupling) becomes strong, we have to figure out a way to actually calculate the functional integral itself. The main, if not the only, method that we dispose of in order to do so is lattice quantum field theory and, in the case of QCD, lattice QCD (LQCD).

The idea behind LQCD is to discretize the problem: first, we discretize the spacetime coordinates by defining a lattice of finite volume. Then, we properly define matter fields (fermions) to live on the lattice sites and link them together with interactions (gauge fields)[3]. Thirdly, we numerically (Monte-Carlo) integrate a discretized version of the path integral and, finally, take care in order to properly recover the continuum limit.

This approach finds a very large number of applications, ranging from flavor physics (e.g. calculating hadronic form factors), low-energy QCD (gaining insight to the phenomenon of confinement), physics Beyond the Standard Model (technicolor) and so on. In Letizia Parato's talk, we will see how LQCD can play an essential role in computations concerning a very important observable of high-energy physics, the anomalous magnetic moment of the muon.

3 Dark matter

Let us, now, change subjects rather abruptly and switch to a topic that lies at the intersection between particle physics and cosmology. Since more than two decades, compelling evidence has convinced us that the Universe contains much more matter than we previously thought. In Fig.1 we present three such pieces of evidence. In the top panel, we show the rotation curve of the galaxy NGC 6503, taken from [3], *i.e.* the orbital speed of stars as a function of their radial distance from the galaxy's center. The actual observations are represented by the black dots, whereas the dashed and dotted lines correspond to what we would expect from General Relativity based on the luminous matter in that galaxy, in the form of the galactic disk and gas respectively. The observations clearly do not match the predictions, which implies that either the laws of gravitation fail in some environments, or that there is some additional amount of matter in the galaxy that remains obscure to us. The first approach corresponds to approaches falling in the realm of modified gravity. The latter, to dark matter. Indeed, by adding an appropriate component of non-luminous matter (according to the dotted-dashed line), it is perfectly possible to reproduce the observed rotation curve (solid line). In the middle panel of Figure 1 we present a second observation that has consolidated the existence of dark matter: the Bullet Cluster (figure taken from [4]). The Bullet Cluster is a galaxy cluster consisting of two sub-clusters

[1] Additional complications concerning the rigorous mathematical foundations of path integrals fall well beyond the scope of this short presentation.

[2] This description is quite schematic. In reality, there are more rigorous methods from functional analysis that are employed.

[3] Note that this step, which we mention here rather lightly, is highly non-trivial. As an example, let us remind that fermions and vectors (gauge bosons) are defined with respect to the properties of the Lorentz group. However, by discretizing spacetime we have explicitly broken Lorentz invariance! Thankfully, there are well-defined schemes in order to define these objects over a discrete spacetime and obtain meaningful results.

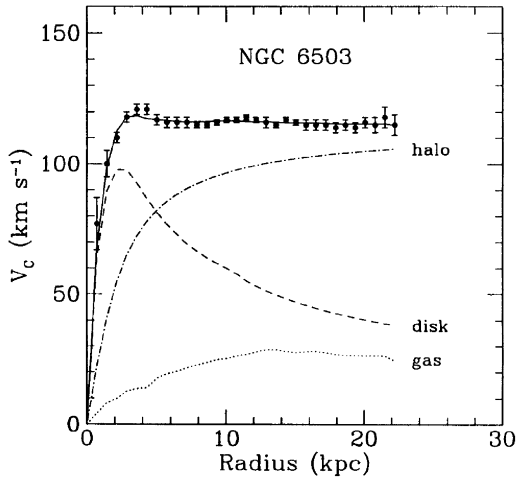

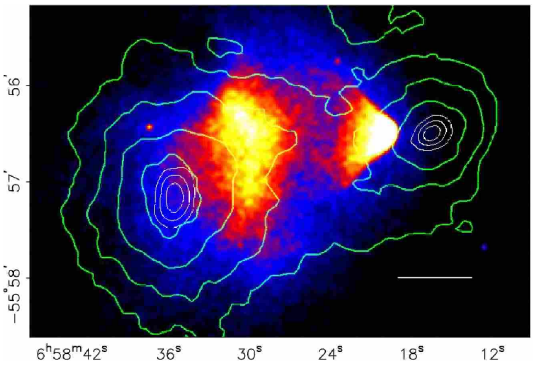

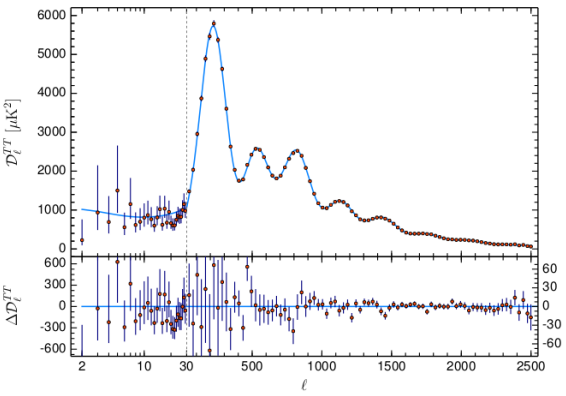

Figure 1: Evidence for dark matter. Top panel: the rotation curve of NGC 6503, taken from [3]. Middle panel: the bullet cluster, taken from [4]. Bottom panel: the CMB temperature power spectrum, taken from [5]. For explanations see text.

that collided with each other in the far past. The different colorings correspond to the places at which most of the visible matter in the clusters can be found (brighter regions correspond to a higher density). However, the Cluster's mass can also be reconstructed via gravitational lensing, resulting in the distribution represented by the green contours. Clearly, the bulk of each cluster's mass lies further away than one would think by merely observing the luminous components. In other words, the mass content of the two clusters appears to be dominated by a component that does not absorb or emit light, dark matter. On should note that, unlike in the case of galactic rotation curves, modified gravity theories are not as successful at explaining such observations. The final, and perhaps most crucial, piece of evidence for the existence of dark matter, is the Cosmic Microwave Background, the temperature power spectrum of which is presented in the bottom panel of Figure 1, taken from [5]. Providing a full overview of CMB physics goes beyond the scope of this short presentation. Put simply, it is known since long that our Universe is permeated by an almost perfect blackbody spectrum microwave radiation. Sattelites such as WMAP and Planck measure the small anisotropies that are present in this Cosmic Microwave Background which, among other things, can be used to extract information about the amount of baryonic ("ordinary") and non-baryonic (dark) matter in the Universe.

The take-home message is that the existence of dark matter is today extremely well-grounded, thanks to the existence of multiple pieces of evidence at different scales. However, as one may have noticed already, all the relevant evidence relies on gravitational interactions. Gravity, however, does not provide much insight on the microscopic, particle nature of dark matter. So what do we know about dark matter? Well, we do know a few things:

1. It gravitates (that's how we know it exists).
2. It's electrically neutral (otherwise we would have seen it).
3. It must be quite cold, *i.e.* it can't be relativistic (the reason stems from structure formation arguments). This means that it cannot be made up of ordinary neutrinos, because then it would be relativistic.
4. It must be stable on cosmological timescales (otherwise it would have decayed away).
5. It constitutes about 85% of the total matter content of the Universe. This last piece of information is extracted from CMB analyses.

Note that the combination of points 2, 3 and 4 implies that dark matter cannot be made up of Standard Model particles: today, dark matter constitutes one of the strongest pieces of evidence for the existence of physics beyond the Standard Model. Given this situation, there are two extremely important questions concerning dark matter: first, can we explain its

abundance in the Universe as inferred from the CMB? Second, can we detect it non-gravitationally? Interestingly, as we will briefly sketch, the two questions may actually be interconnected.

Let's start with the question of the origins of dark matter by noting that, as we know, the Universe expands. At early cosmic times, its total matter-energy content was the same as today but it was much denser (since its size was smaller) and hotter (*i.e.* its temperature was higher). Let's assume that at first, the Universe only contained Standard Model particles and that the Dark Matter particles χ, which for simplicity we take to be heavier than all the SM particles, were pair-produced and pair-annihilated through processes of the type

$$\mathrm{SM} + \mathrm{SM} \leftrightarrow \chi + \chi \ . \tag{4}$$

The dark matter annihilation rate scales as $n_\chi^2 \langle \sigma v \rangle$, *i.e.* it is larger when the Universe is dense and the dark matter annihilation cross section is large. The evolution of the dark matter number density (number of particles per unit of comoving volume) for strong enough DM-SM interactions (say, of comparable strength as the weak force) is shown by the solid lines in Figure 2, which we have adapted from [6]. In this figure, we can see the evolution of the dark matter abundance as a function of inverse temperature (i.e. time flows towards the right). We can roughly distinguish three phases. At early enough times, even if the initial dark matter abundance was zero, dark matter quickly equilibrated with the SM particles, so its abundance remained constant with time and equal to its equilibrium abundance (Bose-Einstein or Fermi-Dirac). As the Universe expanded, its temperature dropped and dark matter could no longer be produced from annihilations of SM particles. Then, dark matter started annihilating away into SM particles and its density started dropping exponentially, following an equilibrium distribution until the Hubble expansion rate became larger than the DM annihilation rate. After this point, both directions of Eq.(4) closed down and the comoving number density of dark matter became constant. This picture, which dominated dark matter physics for more than two decades, is called "thermal freeze-out". It is not the only mechanism that has been proposed in order to explain the DM abundance in the Universe, though. If, instead, we assume that dark matter only interacts extremely weakly with the visible sector then, starting from a negligible initial density, dark matter particles can be slowly produced from annihilations of SM particles without annihilating back (because n_χ remains small throughout the cosmic evolution), until its production becomes kinematically disfavoured due to cosmic cooling. This picture has been dubbed the "freeze-in" mechanism. In both cases, for appropriate choices of the DM mass and its interaction strength with the Standard Model, it is possible to match the DM abundance in the Universe as inferred from the CMB.

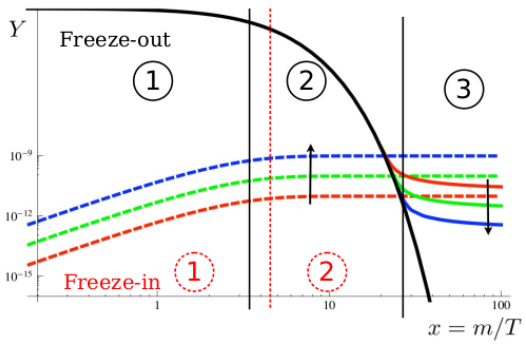

Figure 2: Evolution of the dark matter abundance as a function of $x \equiv m_\chi/T$ for freeze-out (solid lines) and freeze-in (dashed lines). The numbers in circles delineate different phases in the evolution. Figure adapted from [6].

So, how do we hope to detect dark matter? In the case of freeze-in, due to the fact that dark matter is required to interact only very weakly with the Standard Model particles, devising detection strategies becomes slightly tricky. Broadly speaking, many freeze-in models predict *e.g.* the existence of long-lived particles that could be produced at the Large Hadron Collider and decay with a macroscopic lifetime into DM along with visible objects. In the case of freeze-out, where these interactions are required to be more sizeable, we can actually draw inspiration from the processes that were responsible for setting the final DM abundance in the first place: if dark matter particles can be pair-produced at sufficient rates from annihilations of SM particles, then we could hope to produce them at the LHC, in association with ordinary visible objects (e.g. a jet from initial state radiation) and obtain signatures like jet(s)+MET. The inverse reaction, dark matter annihilation into SM particles could take place in today's Universe at observable rates, especially in places with a high concentration of DM particles such as the centres of galaxies (where typically the gravitational wells are the deepest). This detection strategy is called Indirect Detection and will be the topic of Celine Armand's talk. Finally, if instead of considering pair-production or pair-annihilation of DM particles we consider elastic scattering of a dark matter particle off ordinary ones, then we could hope to observe such scattering events as nuclear or electron recoils in appropriate low-background detectors. This detection technique, which is called Direct Detection, will be the topic of Ali Mjallal's talk.

4 Conclusions

From the previous presentation I hope that a few things become clear. Theoretical Physics is far from a mere mental exercise. Even in its most speculative forms, it is *physics*, *i.e.* it studies and tries to make sense out of the physical world. Moreover, it is not only interesting, but also useful: we already saw (and this will become even clearer during the session) that Lattice QCD computes quantities that are crucial for experi-

mental searches. Dark matter physics proposes new experimental signatures that can give rise to new ideas for experiments. The Higgs boson and gravitational waves were predicted long before they were actually discovered in experiments. Lastly, think of all the theoretical input that goes into some of the most commonly used numerical tools in experimental physics such as GEANT. Long story short, whether you're a theorist or an experimentalist, you should care about theoretical physics. Because theoretical physics is great, and theoretical physicists are cool! I hope you'll enjoy the session.

References

[1] M. E. Peskin and D. V. Schroeder, "An Introduction to quantum field theory", Addison-Wesley

[2] M. Srednicki, "Quantum field theory", Cambridge University Press

[3] K. Freese, EAS Publ. Ser. **36** (2009) 113 doi:10.1051/eas/0936016 [arXiv:0812.4005 [astro-ph]].

[4] D. Clowe, M. Bradac, A. H. Gonzalez, M. Markevitch, S. W. Randall, C. Jones and D. Zaritsky, Astrophys. J. **648** (2006), L109-L113 doi:10.1086/508162 [arXiv:astro-ph/0608407 [astro-ph]].

[5] N. Aghanim *et al.* [Planck], [arXiv:1807.06209 [astro-ph.CO]].

[6] L. J. Hall, K. Jedamzik, J. March-Russell and S. M. West, JHEP **03** (2010), 080 doi:10.1007/JHEP03(2010)080 [arXiv:0911.1120 [hep-ph]].

Dark Matter searches towards the WLM dwarf irregular galaxy with H.E.S.S.

Celine Armand, for the H.E.S.S. collaboration

Laboratoire d'Annecy de Physique des Particules & Laboratoire d'Annecy-le-Vieux de Physique Théorique , Univ. Grenoble Alpes, Univ. Savoie Mont Blanc, CNRS, 74000 Annecy, France

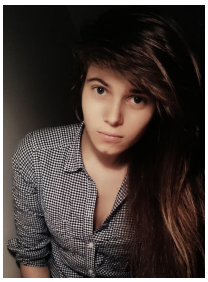

Abstract — In the indirect dark matter (DM) detection framework, the DM particles would produce some signals by self-annihilating and creating standard model products such as γ rays, which might be detected by ground-based telescopes. Dwarf irregular galaxies represent promising targets for the search for DM as they are assumed to be dark matter dominated systems at all radii. These dwarf irregular galaxies are rotationally supported with relatively simple kinematics which lead to small uncertainties on their dark matter distribution profiles. In 2018, the H.E.S.S. telescopes observed the irregular dwarf galaxy Wolf-Lundmark-Melotte (WLM) for a live time of 19 hours. These observations are the very first ones made by an imaging atmospheric Cherenkov telescope toward this kind of object. We search for a DM signal looking for an excess of γ rays over the background in the direction of the WLM galaxy. We present the first results obtained on the velocity weighted cross section for DM self-annihilation as a function of DM particle mass.

1 Introduction

Dark matter represents 85% of all matter in the Universe, affecting the formation of large scale structures, influencing the motion of galaxies and clusters, and bending the path of light. Yet, we do not know much about its nature and properties.

In the early Universe, dark matter particles such as the WIMPs (Weakly Interacting Massive Particles) are assumed to have been in full thermal equilibrium with the standard model (SM) particles at sufficiently high temperatures. Since the particle density is high, they can easily interact with one another. As the Universe expands, it gets less dense and cools down, which makes the interactions between particles less likely and the particle abundance freezes-out. Thus, dark matter particle annihilation is greatly suppressed but a relic density remains and dark matter particles still annihilate and may be observable in rich and dense regions such as dwarf galaxies or the Galactic center. Dark matter would then send some indirect signals by pair-annihilating and creating SM products, which might be detected. Among these particles used as probes for indirect dark matter searches are γ-rays. High-energy γ rays offer several advantages: they are not deflected by the Galactic magnetic field, so that their source can be well localized in the sky. In addition, γ rays do not undergo as much attenuation as the charged particles while propagating. This allows us to point directly our γ-ray telescopes to the sources to look for signals reaching the Earth.

The differential γ-ray flux (in $\gamma \cdot \mathrm{m}^{-2} \cdot \mathrm{s}^{-1} \cdot \mathrm{GeV}^{-1}$) produced by dark matter annihilation in dwarf galaxies, assuming WIMPs are Majorana particles, is written as:

$$\frac{d\Phi_\gamma}{dE} = \frac{1}{2}\frac{\langle\sigma v\rangle}{4\pi m_\chi^2}\,\frac{d\Phi_{PP}}{dE}\,J \qquad (1)$$

with $\dfrac{d\Phi_{PP}}{dE}$ given by

$$\frac{d\Phi_{PP}}{dE} = \sum_f B_f \frac{dN_\gamma^f}{dE_\gamma} dE_\gamma \qquad (2)$$

and J by

$$J = \int_{\Delta\Omega}\int_{\mathrm{los}} \rho^2_{\mathrm{DM}}(r(s,\alpha_{\mathrm{int}}))ds d\Omega'. \qquad (3)$$

The first term is the normalization containing the DM mass m_χ and its annihilation cross section averaged over the velocity distribution $\langle\sigma v\rangle$. The second term is defined as the particle physics factor $d\Phi_{PP}/dE$ which encloses the differential spectrum dN_γ^f/dE_γ of each annihilation channel f weighted by their branching ratio B_f. These differential spectra correspond to the number of γ rays emitted per annihilation per energy range. The last term is called the *astrophysical J factor* describing the amount of dark matter annihilations occurring within the sources. This component holds the dark matter density profile ρ_{DM} squared, as a function of the distance r from the center of the galaxy. The distance is defined in terms of line-of-sight s and integration angle α_{int}, extending from the center of the dwarf towards the outer region. The squared density is then integrated along the line of sight (los) and over the solid angle $\Delta\Omega$. The solid angle corresponds to the field of view over which γ-ray telescopes (e.g. H.E.S.S.) observe the sky. This proceeding focuses on a new kind of target to probe dark matter: dwarf irregular galaxies. Dwarf irregular galaxies (dIrrs) are very promising targets as they possess a J factor in the order of $\sim 10^{17}$ $\mathrm{GeV}^2.\mathrm{cm}^{-5}$. So far 36 of them have been optically observed within a distance of 11 Mpc and an extension of their halo of $0.3 < \theta_{\mathrm{halo}} < 3$. These objects are rotationally supported with relatively simple kinemat-

ics. They are assumed to be dark matter dominated objects at all radii, even in their central part [1]. dIrrs offer the advantage to have well-constrained rotation curve which leads to an actual measured J factor (not a prediction) with very small uncertainties. Another property of these dwarf galaxies is their star-forming region, below 0.1, at their center. The HAWC experiment published a study of irregular galaxies [1] and set limits on the DM annihilation cross section using these galaxies. In 2018, the H.E.S.S. experiment observed one these dIrrs called WLM (Wolf-Lundmark-Melotte) which makes H.E.S.S. the first IACT (Imaging Air Cherenkov Telescopes) to observe this new kind of sources.

H.E.S.S. is a Cherenkov telescope array located in central Namibia in the Khomas Highland plateau area, at around 1,800 meters above sea level. The original array consists of 4 small-sized telescopes (CT1-4) with 12-meter reflectors. Each of these reflectors is made of hundreds of spherical mirrors, concentrating the faint flashes on a camera installed in the focal plane of the telescope. These telescopes detect brief flashes of Cherenkov radiation generated by very high energy γ rays of $\sim$ 100 GeV up to $\sim$ 100 TeV. In 2012, a fifth, 28-meter telescope (CT5) was added to the array with an improved camera allowing detection at a lower threshold of $\sim$ 30 GeV.

2 Properties of WLM

WLM is a dwarf irregular galaxy located at (l = 75.86, b = -73.62) at 1 Mpc from the Milky Way. It possesses a star-forming region at its center and is isolated from other astrophysical sources. This dwarf possesses excellent HI data with a smooth HI distribution and a well-measured photometry and stellar kinematics [4] [5] with an extension of its halo of $r_{\rm halo} = 49.4$ kpc ($\theta_{\rm halo} = 2.89$). WLM is rotationally supported with no significant non-circular motions in the gas. A smooth rotation curve of this galaxy can then be derived, which is well-constrained from these measurements, and implies WLM is DM dominated [4].

3 DM distribution

The DM distribution in WLM can be well represented by a coreNFW profile [5] that writes:

$$\rho_{\rm coreNFW(}{}_{r)} = f^n(r)\rho_{\rm NFW}(r) + \frac{f^{n-1}(r)(1-f^2(r))}{4\pi r^2 r_c} \times M_{\rm NFW}(< r). \quad (4)$$

This new profile takes into account the history of the stellar component within the galaxy which is still active and impacts the DM distribution. $\rho_{\rm NFW}$ is the original NFW profile, $M_{\rm NFW}$ is the mass of the galaxy at some radius r and f^n is responsible for generating a shallower density profile at radii $r < r_c$, with r_c being the core radius and where n is a coefficient tied to the total star formation time. Fitting the results of an MCMC on the coreNFW profile parameters, we derive a J factor of $\log_{10} J(\mathrm{GeV}^2.\mathrm{cm}^{-5}) = 16.6 \pm 0.037$ (Fig. 1) based on the DM profile derived in [5]. WLM represents a very promising target among the dIrrs as it possesses one of the highest J factor with extremely small uncertainties compared to those of some other dIrrs (eg. Aquarius).

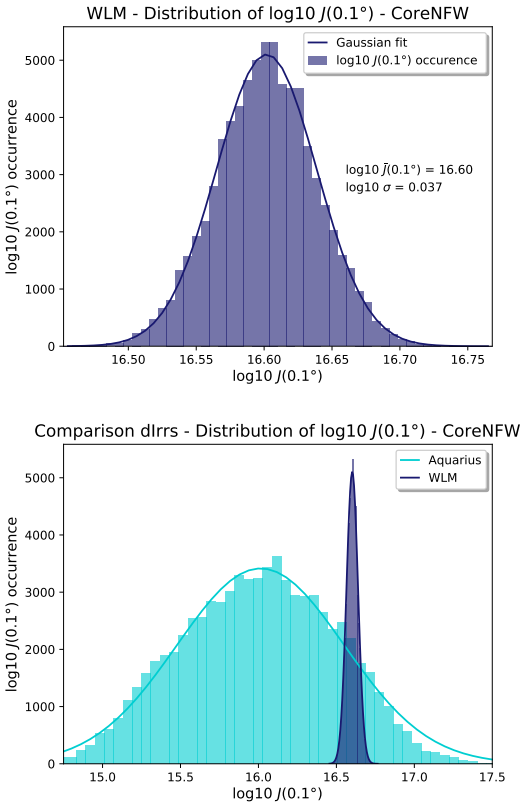

Figure 1: Histograms and fits (solid lines) of the results of the MCMC on the coreNFW profile parameters [5] for a ROI (Region of Interest) of 0.1. **Top:** Distribution of the J factor for WLM. The nominal J factor and its uncertainties are the mean and σ values respectively of the fit. **Bottom:** Comparison of the J factor of WLM and Aquarius and their uncertainties on J. This comparison shows WLM has a larger J factor with smaller uncertainties than Aquarius.

4 Observations and data analysis

In 2018, H.E.S.S. collected about 19 hours of data towards WLM with an offset of 0.5 and 0.8. We perform the analysis of this dataset in order to identify a potential signal from DM. As the signal-to-noise ratio gives a maximum at an extension of 0.08, this analysis is performed over a ROI of 0.1, which corresponds to the point-like source treatment in H.E.S.S. We use the Mono standard configuration which only includes the events detected by the CT5 telescope.

The analysis gives the number of γ-ray-like events detected in the ON region, where the signal is expected,

and the OFF region to compute the background noise. The ON region corresponds to a disk of 0.1 angular radius in the direction of the source while the region OFF is defined according to the multiple-OFF method. This method allows the estimation of the residual background and the measure in the ON region simultaneously so that both are performed in the same conditions of observation and is described in [3]. As the ON region and all the OFF regions combined cover a different area, the acceptance corrected exposure ratio α is also provided which renormalizes the OFF region to the ON region area. From the analysis, we also obtain the γ excess and its significance σ. Table 1 summarizes the results of the analysis. We can conclude from it that no significant excess in the signal region has been observed towards WLM.

$N_{\rm ON}$	$N_{\rm OFF}$	α	Live hours	γ excess	σ
1677	26726	16.24	18.6	31.2	0.7

Table 1: Data analysis results of WLM. $N_{\rm ON}$ and $N_{\rm OFF}$ are the number of events detected in the ON and OFF regions, α is the acceptance corrected exposure ratio, the live hours give the observation time, γ gives the excess detected and the standard deviation σ the significance of the excess.

This result can also be seen in the significance map (Fig. 2) where no excess is observed in the ROI.

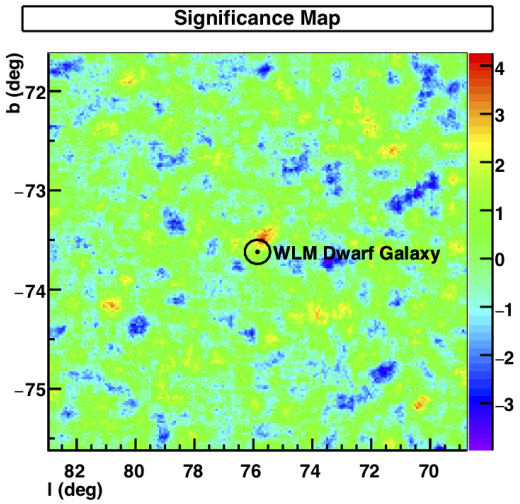

Figure 2: Significance map showing no excess in the ROI.

5 Statistical analysis and upper limits

A loglikelihood ratio test is performed on the data in order to constrain DM and set some upper limits on the DM annihilation cross section.
The total likelihood function contains two terms, a product of a Poisson likelihood $\mathcal{L}^{\mathcal{P}}{}_i$ on the events of all energy bins and a log-normal distribution $\mathcal{L}^{\mathcal{J}}$ of the J factor. This expression is written as

$$\mathcal{L} = \Pi^i \mathcal{L}_i^P(N_{S_i}, N_{B_i}|N_{ON}, N_{OFF}, \alpha) \cdot \mathcal{L}^J(J|\bar{J}, \sigma). \quad (5)$$

For an energy bin i, the likelihood function $\mathcal{L}^{\mathcal{P}}{}_i$ of the event counts is the product of two Poisson likelihoods, one for each of the ON and OFF regions:

$$\mathcal{L}^{\mathcal{P}}{}_i = \frac{(N_{S_i}+N_{B_i})^{N_{\rm ON_i}}}{N_{\rm ON_i}!}\exp\left[-(N_{S_i}+N_{B_i})\right] \times \frac{(\alpha N_{B_i})^{N_{\rm OFF_i}}}{N_{\rm OFF_i}!}\exp\left[-\alpha N_{B_i}\right] \quad (6)$$

where N_{S_i} and N_{B_i} are the number of signal events and background events respectively for a given energy bin i and α is the ratio of the solid angles of the ON and OFF regions. In order to take into account the uncertainty on the J factor in our analysis, we introduce a log-normal distribution in the construction of our total likelihood function $\mathcal{L}$ which is given by

$$\mathcal{L}^J = \frac{1}{\sqrt{2\pi}\sigma_J J}\exp\left[-\frac{(\log_{10} J - \log_{10} \bar{J})}{2\sigma_J^2}\right]. \quad (7)$$

where J is the true value of the J factor and $\bar{J}$ the value of the observed J factor with its uncertainty σ_J. We perform a loglikelihood ratio test on the total likelihood L to set upper limits at 95% C.L. on the annihilation cross section $\langle\sigma v\rangle$ based on the method [6].
If the test statistics TS is less than 2.71, then the null hypothesis $\mathcal{H}_0$ is valid at 95% C.L., whereas if TS is greater than 2.71, $\mathcal{H}_0$ is rejected. This criterion is used to set the upper limits on $\langle\sigma v\rangle$.

6 Results

As no significant excess has been found towards WLM in the ROI, upper limits on the DM annihilation cross section $\langle\sigma v\rangle$ at 95% C.L. vs. the DM mass are computed using the log-likelihood ratio method for the $b\bar{b}$, $\tau^+\tau^-$, W^+W^- and Z^+Z^- annihilation channels (fig. 3). Each annihilation channel is treated individually which corresponds to a branching ratio of $B_f = 100\%$ and all the spectra are simulated using Pythia [2]. We also include the uncertainties on J as a nuisance parameter in our analysis which makes the derivation of the upper limits more conservative. Figures 3 show the upper limits obtained for all these annihilation channels with the solid lines being the observed limits, the dashed lines the mean expected limits and the dark (resp. light) bands representing the 1 σ (resp. 2 σ) uncertainty bands. The mean expected limits and 1-2σ containment bands are derived from a sample of 100 Poisson realizations of the background events in the ON and OFF regions. The mean expected limits corresponds to the mean of the distribution of $\log_{10}\langle\sigma v\rangle$ on these 100 Poisson realizations and the uncertainty bands are given by the standard deviation of this distribution.
The observed upper limits on $\langle\sigma v\rangle$ at 95% C.L. reach

the magnitude of $\langle\sigma v\rangle \sim 10^{-20}$ cm^3.s^{-1} in the quark and boson annihilation channels at a DM mass of 1 TeV. They improve by an order of magnitude in the leptonic annihilation channel with a $\langle\sigma v\rangle \sim 10^{-21}$ cm^3.s^{-1} at 1 TeV.

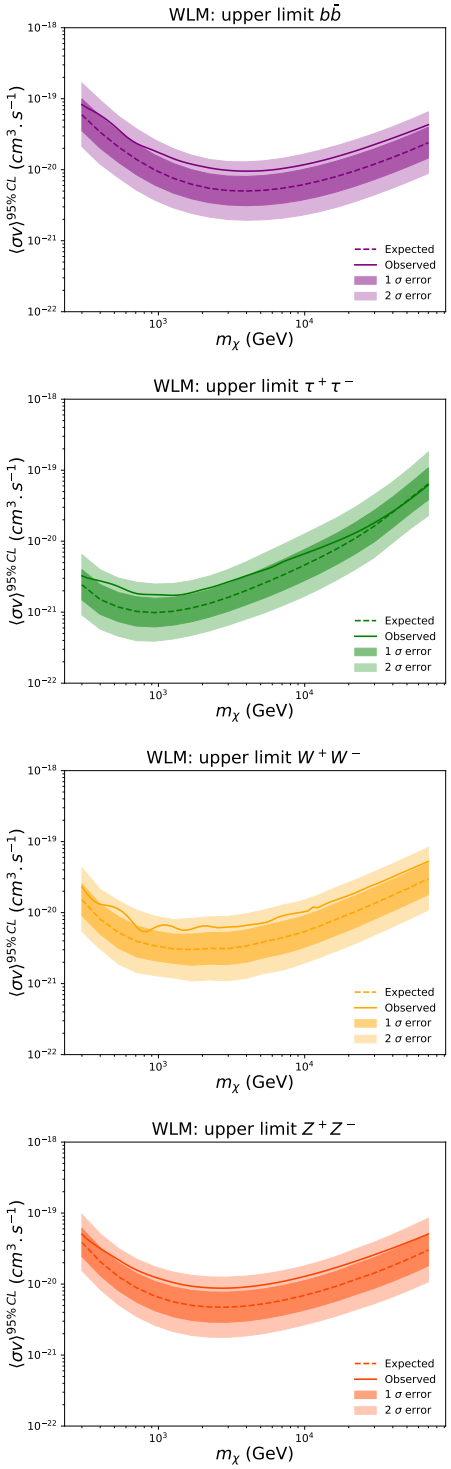

Figure 3: Upper limits on the annihilation cross section $\langle\sigma v\rangle$ at 95% C.L. for WLM, in the $b\bar{b}$, $\tau^+\tau^-$, W^+W^-, Z^+Z^- annihilation channels. These upper limits include the uncertainties on the J factor. The solid lines are the observed limits, the dashed lines the mean expected limits and the dark (resp. light) bands are the 1 σ (resp. 2 σ) containment bands.

7 Conclusions

With its recent 19 hour observations towards WLM, H.E.S.S. is the first IACT experiment to observe a dwarf irregular galaxy to search for DM annihilation signals. As no detection of a significant signal has been made in the ROI, upper limits on the annihilation cross section at 95% C.L. have been derived for many individual annihilation channels with a branching ratio of $B_f = 100\%$. In the case of a continuum spectrum, the most constraining limits are given by the $\tau^+\tau^-$ channel with a $\langle\sigma v\rangle \sim 10^{-21}$ cm^3.s^{-1} at a DM mass of 1TeV. The upper limits derived in this work improve of a factor of 10 to almost 100 compared to those obtained by the HAWC experiment [1].

Acknowledgements

We thank Francesca Calore, LAPTh Annecy, for the useful discussions on the theoretical part of this study, as well as Justin Read, University of Surrey, for his insight about the dark matter distribution of WLM. The support of the Namibian authorities and of the University of Namibia in facilitating the construction and operation of H.E.S.S. is gratefully acknowledged, as is the support by the German Ministry for Education and Research (BMBF), the Max Planck Society, the German Research Foundation (DFG), the Helmholtz Association, the Alexander von Humboldt Foundation, the French Ministry of Higher Education, Research and Innovation, the Centre National de la Recherche Scientifique (CNRS/IN2P3 and CNRS/INSU), the Commissariat à l'énergie atomique et aux énergies alternatives (CEA), the U.K. Science and Technology Facilities Council (STFC), the Knut and Alice Wallenberg Foundation, the National Science Centre, Poland grant no. 2016/22/M/ST9/00382, the South African Department of Science and Technology and National Research Foundation, the University of Namibia, the National Commission on Research, Science Technology of Namibia (NCRST), the Austrian Federal Ministry of Education, Science and Research and the Austrian Science Fund (FWF), the Australian Research Council (ARC), the Japan Society for the Promotion of Science and by the University of Amsterdam. We appreciate the excellent work of the technical support staff in Berlin, Zeuthen, Heidelberg, Palaiseau, Paris, Saclay, Tübingen and in Namibia in the construction and operation of the equipment. This work benefited from services provided by the H.E.S.S. Virtual Organisation, supported by the national resource providers of the EGI Federation.

References

[1] S. H. Cadena *et al.* [HAWC Collaboration], PoS ICRC **2017**, 897 (2018) doi:10.22323/1.301.0897 [arXiv:1708.04642].

[2] M. Cirelli *et al.*, JCAP **1103**, 051 (2011) Erratum: [JCAP **1210**, E01 (2012)] doi:10.1088/1475-

7516/2012/10/E01, 10.1088/1475-7516/2011/03/051 [arXiv:1012.4515].

[3] D. Berge, S. Funk and J. Hinton, Astron. Astrophys. **466**, 1219 (2007) doi:10.1051/0004-6361:20066674 [astro-ph/0610959].

[4] J. Read and I. Iorio, G., Agertz, et al. Mon. Not. Roy. Astron. Soc. **462**, 3628 (2016) doi:10.1093/mnras/stw1876 [arXiv:1601.05821v2].

[5] J. I. Read, M. G. Walker and P. Steger, Mon. Not. Roy. Astron. Soc. **484**, 1401 (2019) doi:10.1093/mnras/sty3404 [arXiv:1808.06634].

[6] G. Cowan, K. Cranmer, E. Gross and O. Vitells, Eur. Phys. J. C **71**, 1554 (2011) Erratum: [Eur. Phys. J. C **73**, 2501 (2013)] doi:10.1140/epjc/s10052-011-1554-0, 10.1140/epjc/s10052-013-2501-z [arXiv:1007.1727].

[7] M. L. Ahnen *et al.* [MAGIC and Fermi-LAT Collaborations], JCAP **1602**, no. 02, 039 (2016) doi:10.1088/1475-7516/2016/02/039 [arXiv:1601.06590].

Recasting Direct Detection Limits Within micrOMEGAs And Implication For Non-Standard Dark Matter Scenarios

Ali Mjallal

LAPTh, Univ. Grenoble Alpes, USMB, CNRS, 9 Chemin de Bellevue, F74940 Annecy, France

Abstract — Direct detection experiments obtain 90% upper limits on the cross sections for point-like Dark Matter interaction with nucleons for fixed cosmological parameters. In this paper, we discuss a possibility to extend these limits to models with arbitrary cosmological parameters, interactions via a light t-channel mediator and millicharged DM. We analyse recent results of Xenon-1T, PICO-60 and DarkSide-50.

1 Introduction

Searches for dark matter (DM) through direct detection experiments have been pursued actively for decades [1, 2, 3, 4, 5, 6, 7]. However, none of the experiments have found a "confirmed" signal for DM, thus could only set upper limits on the DM elastic scattering cross-section of nucleons. For DM masses above roughly 6 GeV, the best limits are currently obtained by Xenon-1T [1]. As for lower masses, the best limits are obtained from DarkSide [3] and CRESST [5]. These limits are generally obtained assuming an interaction through a mediator with a mass much larger than the typical momentum exchange, equal proton and neutron spin-independent (SI) cross-section and for a specific choice of cosmological parameters, see Eq. (4). Our goal is to reinterpret the 90% limits obtained by the experimental collaborations within their specific framework and apply them to a wider set of DM models and DM velocity distributions using micrOMEGAs [8, 9]. We first describe our reconstruction of the exclusion limits from the Xenon-1T and PICO-60 [4] direct detection experiments. Then, we use these results to place constraints on the spin dependent (SD) DM-nucleon cross section, and to obtain the limits for the case of a light mediator, for a different DM velocity distribution and millicharged DM.

2 Direct detection experiments

In this section we analyse Direct Detection (DD) experiments in order to predict their response to any arbitrary recoil energy signal initiated by DM. We first review the standard formulas for detection rates. DM particles have velocities about $v_0 = 0.001c$. Thus, the transferred momentum in DM-nucleus collision cannot exceed $q_{max} = 2v_0 M_A \approx 200$ MeV and can be neglected for heavy mediators. In this case the DM-nucleus elastic scattering cross section is given by

$$\sigma^{SI} = \frac{4}{\pi}\mu_{\chi A}^2 A^2 \lambda^2 \tag{1}$$

where λ is the DM-nucleon amplitude and we assume equal proton and neutron amplitudes.
The recoil energy distribution of nuclei A produced by SI interaction in a detector with mass $\mathcal{M}_{det}$ and exposure time T reads [8, 11]

$$\frac{\mathrm{d}N_A^{SI}}{\mathrm{d}E} = T\mathcal{M}_{det}\frac{\rho_{\mathrm{DM}}}{2M_\chi \mu_{\chi A}^2}\sigma^{SI}F^2(E)\int_{\sqrt{\frac{EM_A}{2\mu_{\chi A}^2}}}^{\infty}\frac{f(\vec{v})}{v}\mathrm{d}\vec{v} \tag{2}$$

where $f(\vec{v})$ is the DM velocity distribution in the detector rest frame, $F(E)$ is the nuclear form factor and $\mu_{\chi A}$ is the reduced mass given by

$$\mu_{\chi A} = \frac{M_\chi M_A}{M_\chi + M_A} \tag{3}$$

where M_χ is the DM mass. Direct detection experiments set limits on σ^{SI} after analysing the number of registered events and using background estimations. All experiments use the same assumption about the DM local density, $\rho_{\mathrm{DM}} = 0.3$ GeV/cm^3, and the DM velocity distribution, a Maxwell distribution with parameters

$$\mathrm{v}_{\mathrm{Earth}} = 232 \text{ km/s} \ , \ \mathrm{v}_{\mathrm{Rot}} = 220 \text{ km/s} \tag{4}$$

where $\mathrm{v}_{\mathrm{Earth}}$ is the velocity of the Earth in the galactic frame, $\mathrm{v}_{\mathrm{Rot}}$ is the local circular speed in the Milky Way [11] and with an escape velocity $\mathrm{v}_{\mathrm{Esc}} = 544$ km/s .

2.1 Simplified approach for interpreting the Xenon-1T exclusion

To repeat exactly the Xenon-1T analysis, we would need detailed information on events distribution, background estimation and the relevant nuisance parameters for all points of event space. Since we have incomplete information, we assume that there is some effective subspace of the total space of events where after applying cuts the probability to register a DM event is $p_{\mathrm{eff}}(E)$. If no signal events were observed, then the likelihood function for the signal recoil events distribu-

tion $\frac{\mathrm{d}N}{\mathrm{d}E}$ reads

$$L = e^{-\mathcal{L}\int_0^{Emax}\left(p_{\rm eff}(E)\frac{\mathrm{d}N}{\mathrm{d}E}+\frac{\mathrm{d}B}{\mathrm{d}E}\right)\mathrm{d}E} \quad (5)$$

where $B\,(E)$ is the background distribution and $\mathcal{L}$ is the exposure. The maximal likelihood is reached for zero DM signal and the p-value corresponding to a given signal is

$$p_{val} = \frac{L}{L_{max}} = e^{-\mathcal{L}\int p_{\rm eff}(E)\frac{\mathrm{d}N}{\mathrm{d}E}\mathrm{d}E} \quad (6)$$

The Xenon-1T collaboration [10] provides the values of the 90% excluded cross sections σ_{90}^{SI}, that can be use to infer the corresponding $\frac{\mathrm{d}N^{90}}{\mathrm{d}E}$. Using these data we can recover $p_{\rm eff}$ by solving the equation below

$$\mathcal{L}\int p_{\rm eff}\frac{\mathrm{d}N^{90}}{\mathrm{d}E}\mathrm{d}E = log\,(10) \quad for\ 6 \leq M_\chi \leq 1000\ \text{GeV}$$

We use our extracted acceptance $p_{\rm eff}$ shown in Fig.1 to

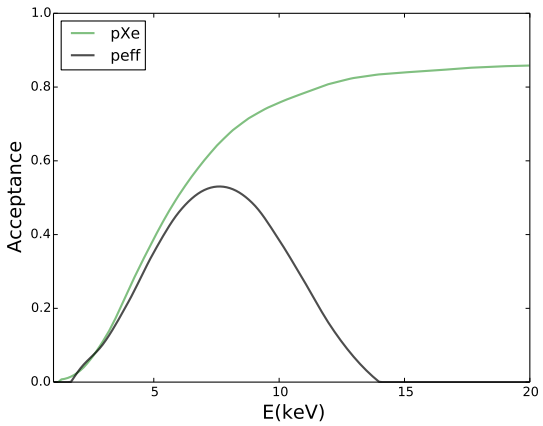

Figure 1: The extracted acceptance function $p_{\rm eff}\,(E)$ compared to the Xenon-1T acceptance pXe before applying cuts.

reconstruct the 90% SI limits obtained by Xenon-1T. Note that both acceptances are in good agreement at low energies. We find an excellent agreement between Xenon-1T 90% excluded cross sections and our reconstruction, see Fig.2. The maximal difference is roughly 10% and is reached for $M_{\rm DM} = 20$ GeV.

2.2 PICO-60

PICO [4] is a Bubble Chamber experiment. As a detector material PICO uses C_3F_8, with 1167 kg-day exposure at a threshold of 3.3 keV and 1404 kg-day at 2.45 keV. After an Acoustic Parameter cut, PICO sees 3 candidate events. PICO expects 1.25 background events from multi-bubble events, 0.12 single bubble events from photons and 0.1 events from neutrinos. Thus, the expected background is 1.47 events. To reconstruct the PICO SI exclusion curve, we assume that the efficiency is a smoothly increasing function with a threshold of 1.6

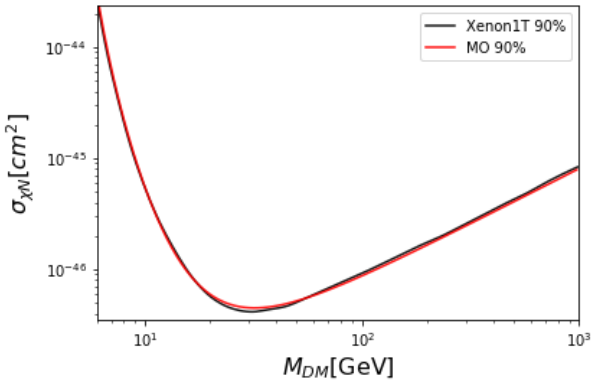

Figure 2: The 90% exclusion cross section for SI interaction by Xenon-1T (black) compared with the 90% exclusion obtained with $p_{\rm eff}$ using micrOMEGAs (red). Note that $M_{\rm DM} \equiv M_\chi$.

keV which reaches 100% far from threshold. Our reconstruction of the PICO SI exclusion limits is shown in Fig.3 using both a Likelihood and a Feldman-Cousins approach. The latter leads to an excellent agreement for all masses while the former is more conservative. More details can be found in [15].

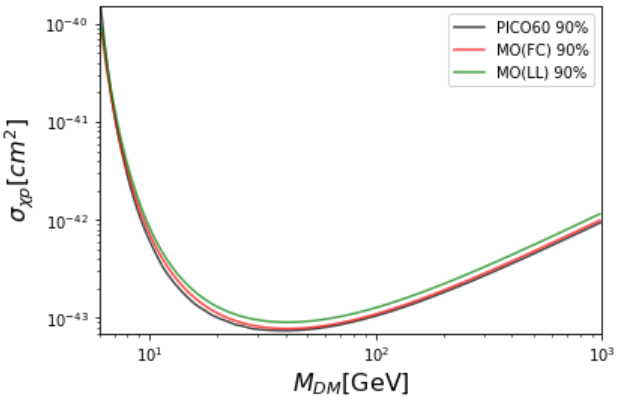

Figure 3: Comparison of PICO SI 90% excluded cross section with our reconstructions which use Likelihood and Feldman-Cousin statistical formulas.

We have also reconstructed the 90% limits obtained by DarkSide-50 experiment using the experimental data provided by the collaboration [3].

3 Applications

In this section we give examples on how to exploit our reconstruction of the limits obtained by DD experiments to get new limits and check the dependence on cosmological parameters. We use simplified models for illustration.

3.1 Spin dependent interactions

In general SD and SI interactions lead to very similar recoil energy spectra. Thus, the 90% SD limits can be

obtained using the efficiency derived for SI interactions. In Fig.4, we show the 90% limits for SD on proton for PICO. For this we use the form factors defined in [12].

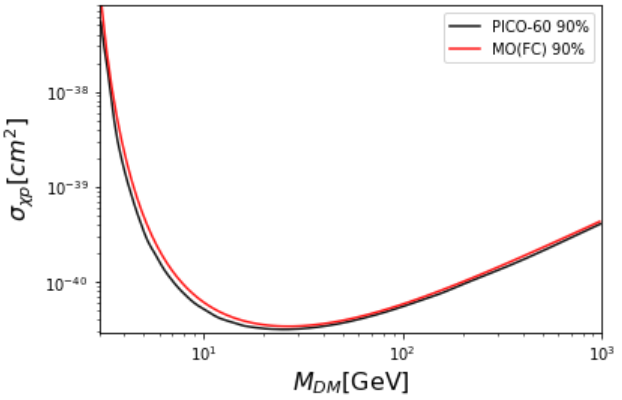

Figure 4: Comparison of PICO original result with our reconstruction.

3.2 Case of a light mediator

We consider a simplified model, consisting of a new gauge boson Z' with pure vector couplings to the standard model fermions and a Dirac fermion DM candidate. The interaction Lagrangian is given by

$$\mathcal{L}_{int} = -g_\chi Z'_\mu \bar{\chi}\gamma^\mu \chi - \sum_f g_f Z'_\mu \bar{f}\gamma^\mu f \qquad (7)$$

When the DM-nucleon interactions are due to the exchange of a light mediator in the t-channel, the standard formula that relates the DM-nucleon cross section with the recoil energy distribution cannot be applied. Indeed it rests on the assumption that the mass of the mediator is much larger than the square-root of the Mandelstan variable $t = -2M_A E_R$, where E_R is the nucleus recoil energy and M_A the mass of the recoiling nucleus. For the typical minimal recoil energy in Xenon-1T, $E_R \approx 2$ keV and $M_{Xe} \approx 130$ GeV, we have $t = -(22\ \text{MeV})^2$. So for light mediators, $\mathcal{O}(100\ \text{MeV})$ or lighter, we can no longer neglect t. In this case, the standard formula of recoil energy distribution is modified to

$$\frac{\mathrm{d}N_A^{m_M}}{\mathrm{d}E} = \frac{m_M^4}{\left(m_M^2 + 2M_A E\right)^2} \frac{\mathrm{d}N_A^{std}(\sigma_0)}{\mathrm{d}E} \qquad (8)$$

where N_A^{std} is the standard expression for the number of recoil events in the case of a point-like interaction, m_M is the mass of the t-channel mediator and σ_0 is the cross section for DM-nucleon elastic scattering for very small momentum transfer. Note that σ_0 is actually inversely proportional to m_M^4. In Fig. 5, we present the 90% limits on the parameters of the Z' Portal model for two cases. The plot shows the limits in case of a light mediator ($M_{Z'} = 1$ MeV), here $g = g_f g_\chi$.

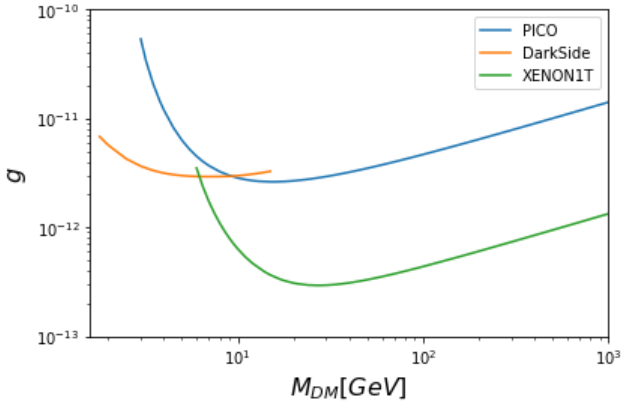

Figure 5: 90% excluded cross section provided by DD experiments in case of light mediator ($M_{Z'} = 1$ MeV).

We observe that Xenon-1T can probe very small couplings, $\mathcal{O}(10^{-12})$. These correspond to typical couplings in models with feebly interacting massive particle (FIMP), more details in [15].

3.3 Dependence of excluded cross section on cosmological parameters

Experimental collaborations obtain their limits assuming a Maxwell velocity distribution for DM with parameters given in Eq. (4). However new data suggest that our stellar halo lies in a strongly radially anisotropic population, the 'Gaia Sausage'. Therefore a new velocity distribution of DM called 'SHMpp' has been proposed in [13]. It is described as

$$f(v) = (1-\eta) f_{Maxwell}(v) + \eta f_S(v) \qquad (9)$$

where η is the DM density in the Sausage and f_S is the velocity distribution of the 'Gaia Sausage' which is a function of the anisotropy β. The SHMpp velocity distribution is defined by 5 parameters

$$\rho_{\text{DM}} = 0.55 \pm 0.17\ \text{GeV/cm}^3$$

$$\text{v}_{\text{Rot}} = 233 \pm 3\ \text{km/s}$$

$$\text{v}_{\text{Esc}} = 580 \pm 63\ \text{km/s}$$

$$\beta = 0.9 \pm 0.05$$

$$\eta = 0.2 \pm 0.1$$

In Figure 6, we show the dependence of the 90% limits obtained by Xenon-1T on the choice of the DM velocity distribution in the $(M_{\text{DM}}, M_{Z'})$ plane. We have used maximum values within the 1 σ range of v_{Rot}, v_{Esc} and ρ_{DM} for the curve underlined as SHMpp-max-values. The strongest dependence on the velocity distribution is observed for small DM mass. We obtain the largest increase in the value of $M_{Z'}$ excluded for $M_{\text{DM}} \approx 6$ GeV (80%). The main reason behind this behavior is the different values of ρ_{DM} used. For larger values of ρ_{DM} we can probe smaller cross sections, which implies higher values of $M_{Z'}$.

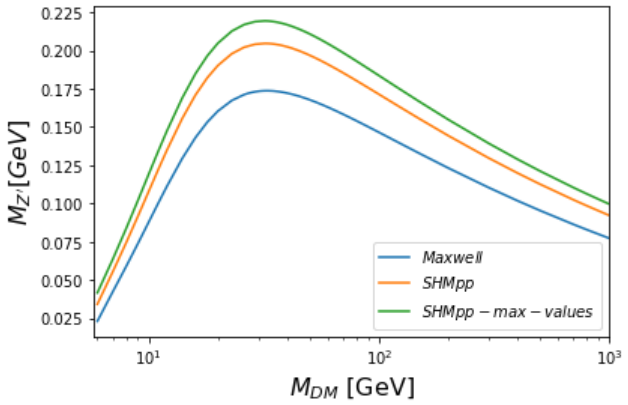

Figure 6: 90% exclusion cross-section for Xenon-1T for different velocity distributions.

3.4 Millicharged Dark Matter

We consider a simple model of millicharged DM. It consists of the SM plus an extra abelian gauge field (A'_μ) that couples to a massive Dirac fermion (ψ) and that mixes with the SM hypercharge through the kinetic term,

$$\mathcal{L} = \mathcal{L}_{SM} - \frac{1}{4}A'_{\mu\nu}A'^{\mu\nu} + i\bar{\psi}\left(\partial\!\!\!/ + ie'A\!\!\!/' + iM\right)\psi - \frac{k}{2}A'_{\mu\nu}B^{\mu\nu}$$

where $k << 1$ and M is the mass of ψ which is a DM candidate. By redefining this new gauge boson ($A'_\mu \to A'_\mu - kB_\mu$), we get

$$\mathcal{L} = \mathcal{L}_{SM} - \frac{1}{4}A'_{\mu\nu}A'^{\mu\nu} + i\bar{\psi}\left(\partial\!\!\!/ + ie'A\!\!\!/' - ike'B\!\!\!/ + iM\right)\psi$$

We observe that DM couples to the photon and so it acquires a charge $q_{\rm DM} = ke'\cos\theta_\omega$.
The photon can be treated as a light mediator, thus allowing to write the energy distribution as in Eq. (8) with $m_M << 2M_A E$. Here

$$\sigma_0 = 16\pi\alpha_{EM}^2 q_{DM}^2 \frac{\mu_{\chi p}^2}{m_{ph}^4} \tag{10}$$

is the DM-proton elastic scattering cross section. Note that m_{ph}^4 cancels out in Eq. (8).
All DD experiments are realised deep underground. Since millicharged DM can lose energy before it reaches the detector because of its interaction with rocks, we also get an upper limit on the DM millicharge $q_{\rm DM}$. The main process of energy loss is the elastic scattering of DM particles with atomic nuclei. The cross section read [14]

$$\frac{\mathrm{d}\sigma}{\mathrm{d}\cos\theta_{cm}} = 2\pi\left|\frac{2\mu}{q}\int_0^\infty V(r)\, r\sin rq\mathrm{d}r\right|^2 \tag{11}$$

where μ is the reduced mass of the colliding particles and q is the momentum transfer. For nucleus charge screened by electrons, we have

$$V(r) = \frac{q_{\rm DM}Z_A e}{r}e^{-r/R_A} \tag{12}$$

where

$$R_A \sim 0.8853 Z_A^{1/3}\frac{1}{m_e\alpha} \tag{13}$$

is the atomic radius. Integrating Eq. (11), one can get the formula for the energy loss of a millicharged DM particle in an elastic collision with an atomic nucleus $< E_{lost}\sigma_{\chi A} >$. Then for a DM particle passing through the Earth we have

$$\frac{\mathrm{d}E_\chi}{\mathrm{d}x} = -\sum_{A\in\mathrm{Earth}}\langle E_{lost}\sigma_{\chi A}\rangle n_A \tag{14}$$

where n_A is the number density of the element A in the Earth. The condition that the faster DM with velocity $v = \mathrm{v_{Esc}} + \mathrm{v_{Earth}}$ will reach the detector located at a depth H with velocity large enough to pass the detector's energy threshold E_{tr} leads to a linear equation on q_{DM}^2

$$\int_{E_{max}}^{E_{min}}\frac{\mathrm{d}E_\chi}{\mathrm{d}E_\chi/\mathrm{d}x} = H \tag{15}$$

where $E_{min} = \frac{E_{tr}M_D M_\chi}{4\mu_{\chi D}^2}$, $E_{max} = \left(\mathrm{v_{Esc}} + \mathrm{v_{Earth}}\right)^2 M_\chi/2$, M_D is the mass of the detector's atom and $\mu_{\chi D}$ is the corresponding reduced mass. In Figure 7, we present the upper and lower limits on the DM's millicharge $q_{\rm DM}$ from Xenon-1T.

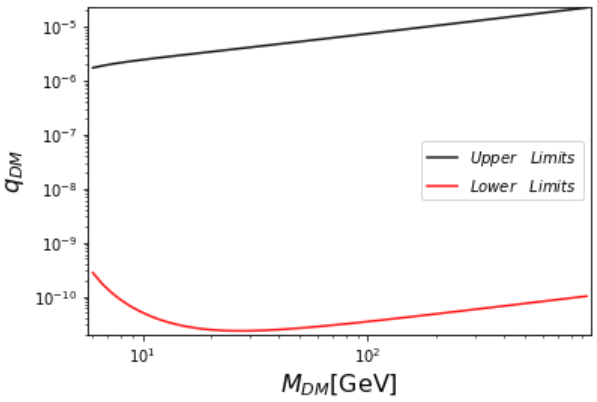

Figure 7: 90% upper and lower limits on DM's millicharge extracted from Xenon1T.

4 Conclusions

micrOMEGAs has a new module that allows one to impose direct detection limits on a variety of DM models, such as models with one or two WIMP/FIMP Dark Matter candidates, models with a light mediator and millicharged DM. It also allows to study these limits for different DM velocity distribution and different nuclear form factors. Direct detection experiments that are currently included in micrOMEGAs are: Xenon-1T, PICO-60, DarkSide-50 and CRESST3.

References

[1] E. Aprile et al. Dark Matter search results from a one tonnexyear exposure of XENON1T. 2018.

[2] E. Aprile et al. Constraining the spin-dependent WIMP-nucleon cross sections with XENON1T. *Phys. Rev. Lett.*, 122(14):141301, 2019.

[3] P. Agnes et al. Low-mass Dark Matter search with the DarkSide-50 Experiment. *Phys. Rev. Lett.*, 121(8):081307, 2018.

[4] C. Amole et al. Dark Matter search results from the complete exposure of the PICO-60 C_3F_8 Bubble Chamber. *Phys. Rev.*, D100(2):022001, 2019.

[5] F. Petricca et al. First results on low-mass Dark Matter from the CRESST-3 experiment. 2017.

[6] Jingkai Xia et al. PandaX-2 Constraints on spin-dependent WIMP-nucleon effective interactions. *Phys. Lett.*, B792:193-198, 2019

[7] R. Agnese et al. Search for low-mass Dark Matter with CDMSlite using a profile likelihood fit. *Phys. Rev.*, D99(6):062001, 2019

[8] G. Belanger, F. Boudjema, A. Pukhov, and A. Semenov. Dark Matter direct detection rate in a generic model with micrOMEGAs 2.2. *Comput. Phys. Commun.*, 180:747-767, 2009.

[9] Genevieve Belanger, Fawzi Boujema, Andreas Goudelis, Alexander Pukhov, and Bryan Zaldivar. micrOMEGAs5.0: Freeze-in. *Comput. Phys. Commun.*, 231:173-186, 2018.

[10] E. Aprile et al. Effective field theory search for high-energy nuclear recoils using the XENON100 dark matter detector. *Phys. Rev.*, D96(4):042004, 2017.

[11] J. D. Lewin and P. F. Smith. Review of mathematics, numerical factors, and corrections for dark matter experiments based on elastic nuclear recoil. *Astropart. Phys.*, 6:87-112, 1996.

[12] A. Liam Fitzpatrick, Wick Haxton, Emanuel Katz, Nicholas Lubbers, and Yiming Xu. The effective field theory of Dark Matter direct detection. *JCAP*, 1302:004, 2013.

[13] N. Wyn Evans, Ciaran A. J. O'Hare, and Christopher McCabe. Refinement of the standard halo model for Dark Matter searches in light of the Gaia Sausage. *Phys. Rev.*, D99(2):023012, 2019.

[14] L. D. Landau and L. M. Lifshitz. *Quantum Mechanics Non-Relativistic Theory, Third Edition: Volume 3.* Butterworth-Heinemann, 3 edition, January 1981.

[15] G. Belanger, A. Mjallal and A. Pukhov. In Progress.

Leading hadronic contribution to the muon magnetic anomaly from lattice QCD

Letizia Parato

Aix Marseille Univ, Université de Toulon, CNRS, CPT, Marseille, France

Abstract — Anomalous magnetic moments have guided the evolution of quantum field theory ever since its earliest stages, serving both as a stringent test of the theory at increasingly higher levels of precision and as a possible window to new physics. After decades of perfect agreement, the measured muon magnetic moment (which is known to a precision of about 0.5 parts per million both from theory and experiment) now deviates from the theoretical expectation by around 3.5σ. In order to accentuate or resolve this discrepancy, an experiment at Fermilab is currently underway and is aiming to improve the precision of the measurement to 0.14 ppm. But the theoretical calculation has to be improved as well. The largest source of error are low energy hadronic contributions, that can be evaluated either via a phenomenological approach or ab initio, directly from the standard model Lagrangian, using lattice QCD. We will see how lattice QCD can be used to compute the leading hadronic contribution to the muon magnetic moment: the one induced by hadronic vacuum polarization.

1 Introduction

The anomalous magnetic moment of the muon, a_μ, is one of the most precisely measured quantities in particle physics. The comparison between its measurement and theoretical expectation provides, at the same time, a severe test of the mathematical framework underlying the Standard Model (SM) and a possible path to new physics.

Short history of a_μ [1, 2, 3] – By definition, the anomalous magnetic moment is $a_\ell = (g_\ell - 2)/2$, where g_ℓ is the g-factor (or gyromagnetic ratio) of a lepton $\ell = e, \mu, \tau$. The g factor appeared in physics around 1925[1]. Earlier that year, Goudsmit and Uhlenbeck [4] postulated that an electron has an intrinsic angular momentum $\mathbf{S}$ with $S_z = \pm\hbar/2$. In analogy with classical electromagnetism where a circulating current due to an orbiting particle of electric charge e and mass m induces a magnetic dipole moment $\boldsymbol{\mu}_L = \frac{e}{2mc}\mathbf{L}$, with $\mathbf{L} = m\mathbf{r} \times \mathbf{v}$ the orbital angular momentum, they associated to the spin $\mathbf{S}$ an intrinsic angular momentum $\boldsymbol{\mu}_S = \frac{e}{2mc}\mathbf{S}$. However, some inconsistencies in the experimental results led Back and Landé to question whether $\boldsymbol{\mu}_S$ couples to a magnetic field in the same way as $\boldsymbol{\mu}_L$. In other words, rewriting $\boldsymbol{\mu}_S = g\frac{e}{2mc}\mathbf{S}$, the question was: does g actually equal 1 as for the orbital gyromagnetic ratio or not? The experimental analysis was inconclusive, so when Pauli formulated his quantum mechanical treatment of the electron spin in 1927, g was left as a free parameter. Just a year later Dirac presented his quantum relativistic theory of the electron, making the unexpected prediction $g = 2$. The first unambiguous experimental confirmation of Dirac's prediction was given by Kinster and Houston in 1934 [5]. Still, the error was quite large and it took 20 more years to establish that g actually exceeds Dirac's expectation by about 0.12%. In 1948 Kusch and Foley [6] published the first precision determination of the electron magnetic moment, $g_e = 2.00238(10)$ (i.e. $a_e \simeq 0.00119$). Meanwhile, with the development of renormalization techniques, Dirac's theory was evolving into quantum electrodynamics (QED). In 1948 Schwinger showed [7] that the anomaly comes from loop corrections to the QED-vertex and computed the leading-order contribution to a_ℓ:

$$a_\ell^{\mathrm{QED}(1)} = \frac{\alpha}{2\pi} \simeq 0.00116 \tag{1}$$

The agreement between Schwinger's evaluation and Kusch and Foley's result was a great success for QED and a key step to establish QFT as the correct framework on which to build a more comprehensive model of fundamental interactions. Today, the whole structure of the SM has to be taken into account in a prediction of a_μ in order to match the current experimental precision.

The reason why a_e and a_μ are still drawing many physicists' attention is that – as theoretical and experimental techniques improved – a tension between SM prediction and measurement started to appear for both a_e and a_μ. Today there is a -2.4σ discrepancy between a_e^{SM} and a_e^{exp} and a 3.5σ discrepancy between a_μ^{SM} and a_μ^{exp}. The latter is one of the most promising signals for new physics and deserves to be investigated further.

Why is a_μ special – e, μ, τ have identical properties, except for their masses and lifetimes. This poses some experimental limitations. For example tau leptons are too short-lived ($\tau_\tau = 3 \times 10^{-15} s$) for a_τ to be measured with present technologies.

• Electrons have infinite lifetime and exist in atoms, so a_e can be measured via spectroscopy of atoms in magnetic fields. An alternative approach, developed by Crane et al. [8], inspired the method later used to

[1] The subscript e is implicit until 1936 (discovery of muons).

measure a_μ. The most recent measurement is [9]

$$a_e^{\text{exp}} = 1159652180.73(28) \times 10^{-12}. \quad (2)$$

• The muon's lifetime is small ($\tau_\mu = 2 \times 10^{-6} s$), but large enough to allow relativistic muons to be stored in a magnetic ring for a sufficiently long time. Also, muons are easy to polarize and it is easy to measure their polarization at the moment they decay. So a_μ can be measured with high precision. The latest measurement dates back to 2006 and was performed by experiment Muon E821 at BNL[10]:

$$a_\mu^{\text{exp}} = 11659208.9(6.3) \times 10^{-10} \quad (3)$$

We see that a_e is about 2200 times more precisely measured than a_μ. However, as pointed out in [11], a_ℓ has a m_ℓ^2/Λ^2 dependence on Λ characterizing the scale of new physics. The masses of charged leptons are $m_e = 0.511$ MeV, $m_\mu = 105.66$ MeV, and $m_\tau = 1776.86$ MeV. This implies that a_μ is about $m_\mu^2/m_e^2 \sim 4 \times 10^4$ more sensitive to new physics than a_e. Ultimately, a_μ turns out to be a better monitor for new physics than a_e.

Measuring a_μ – The new Muon g-2 (E989) experiment is currently taking data at Fermilab. It aims to reduce the experimental uncertainty down to 140 ppb (improving E821's precision by a factor 4). A second experiment is planned at J-PARC that aims to bring uncertainty below 100 ppb. The former exploits the same method used in BNL's experiment (the magnetic ring is actually the same) and it is expected to publish first results in the next months. Muon g-2/EDM at J-PARC will use a new method, with a ultra-cold muon beam stored in a compact magnet. In the standard method (Figure 1) a proton beam is directed on a target to produce pions, which then decay as $\pi^+ \to \mu^+ + \nu_\mu$. Because of parity violation and helicity conservation, muons are highly polarized, with magnetic moment directed along the direction of the flight axis. Muons are then injected into a uniform magnetic field $\mathbf{B}$ where they execute relativistic cyclotron motion with angular frequency $\boldsymbol{\omega}_c = \frac{e\mathbf{B}}{m_\mu c\gamma}$. At the same time, the muons' spins undergo Larmor precession with angular frequency $\boldsymbol{\omega}_s$. The observable we are interested in is

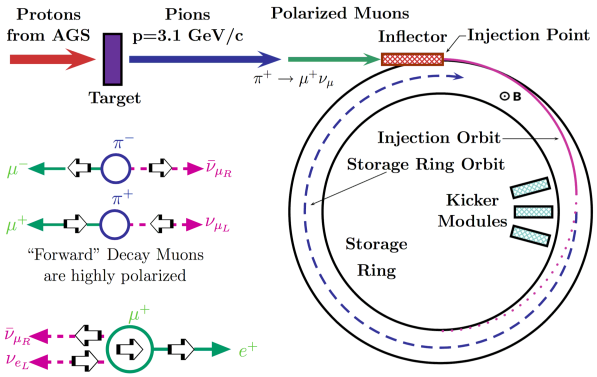

Figure 1: Sketch of BNL E821 experiment

$\omega_a = \omega_s - \omega_c$, that is

$$\boldsymbol{\omega}_a = \frac{e}{m_\mu c}\left[a_\mu \mathbf{B} - \left(a_\mu - \frac{1}{\gamma^2 - 1}\right)\frac{\mathbf{v} \times \mathbf{E}}{c^2}\right] \quad (4)$$

The second term deflects muons from the horizontal plane of the ring so it has to be eliminated. In Fermilab's experiment, the focusing system requires $\mathbf{E} \neq 0$: the solution is to take $1/(\gamma^2 - 1) = a_\mu$, i.e. $\gamma = 29.3$ or $E_{\text{magic}} = 3.098$GeV. In J-PARC's experiment, the cold beam doesn't need any focusing system, so $\mathbf{E}$ can be set to zero. After some time the muon decays as $\mu^+ \to \nu_e + \bar{\nu}_\mu + e^+$. Each positron keeps its parent-muon's polarization, which can be measured, along with the positron's energy, by calorimethers placed all along the ring. The decay rate follows the model

$$N(E,t) = N_0(E)e^{-\frac{t}{\gamma\tau_\mu}}\left[1 + A(E)\sin(\omega_a t + \phi(E))\right]$$

where $A(E)$ is a known energy-dependent asymmetry factor and the desired ω_a appears as a fit parameter. Finally $a_\mu = \frac{\omega_a m_\mu c}{eB}$.

Computing $\mathbf{a_\mu}$ [1, 12] – We want to understand how a_μ naturally emerges from the SM Lagrangian. In particular, we are interested in the motion of a lepton $\ell = e, \mu, \tau$ in a static and homogeneous magnetic field, $A_\mu^{\text{cl}} = (0, \vec{A}^{\text{cl}})$. The S-matrix element for the scattering from A^{cl} is

$$i\mathcal{M}(2\pi)(q^0) = -ie\bar{u}(p')\Gamma^\mu(p',p)u(p) \cdot \tilde{A}^{\text{cl}}(q) \quad (5)$$

where $q = p' - p$, and $\tilde{A}_\mu^{\text{cl}}$ is the Fourier transform of A_μ^{cl}. Poincaré invariance and parity conservation in electromagnetic interactions, and the Dirac equations $\not{p}u(p) = mu(p)$ and $\bar{u}(p)\not{p} = m\bar{u}(p)$ imply that Γ^μ takes the form $\Gamma^\mu(p',p) = A\gamma^\mu + B(p'^\mu + p^\mu) + C(p'^\mu - p^\mu)$, with A, B, and C depending only on scalars (i.e. q^2 and masses). C must be zero or the Ward identity $q_\nu\Gamma^\nu = 0$ wouldn't apply. Finally, using the Gordon identity, Γ^μ can be written as

$$\Gamma^\mu(p,p') = F_1(q^2)\gamma^\mu + \frac{i\sigma^{\mu\nu}q_\nu}{2m}F_2(q^2) \quad (6)$$

where F_1 and F_2 are two form factors that depend on q^2 and masses. Mind that (6) holds only when both sides are sandwiched between $\bar{u}(p')$ and $u(p)$. Replacing (6) in (5) and taking the non relativistic limit in the specific case of a slowly varying (i.e. $q \to 0$) electrostatic field $A^{\text{cl}}(x) = (\phi(x), 0)$, one can identify $F_1(0)$ with the electric charge in units of e, therefore $F_1(0) = 1$. A similar calculation with a homogeneous magnetic field $A^{\text{cl}}(x) = (0, \mathbf{A}^{\text{cl}}(x))$ proves that

$$g_\ell = 2[F_1(0) + F_2(0)] = 2F_1(0) + 2 \quad (7)$$

$$a_\ell = F_2(q^2 = 0) \quad (8)$$

At tree level, $\Gamma^{\mu,(0)} = \gamma^\mu$, meaning $F_2^{(0)} = 0$. Thus a_ℓ depends only on higher order contributions to Γ^μ. Note that the conservation of electric charge implies $F_1(0) = 1$ at every order in perturbation theory.

State of the art of SM predictions – We split

$a_\mu^{\rm SM}$ into three contributions:

$$a_\mu^{\rm SM} = a_\mu^{\rm QED} + a_\mu^{\rm EW} + a_\mu^{\rm Had} \tag{9}$$

• $a_\mu^{\rm QED}$ includes all photonic and leptonic e, μ, τ loops; it is given in perturbation theory by an expansion in α. The coefficients have been computed up to 5 loops [14]:

$$\begin{aligned} a_\mu^{\rm QED} &= \tfrac{\alpha}{2\pi} + 0.765857425(17)\left(\tfrac{\alpha}{\pi}\right)^2 \\ &+ 24.05050996(32)\left(\tfrac{\alpha}{\pi}\right)^3 + 130.8796(63)\left(\tfrac{\alpha}{\pi}\right)^4 + \\ &+ 752.2(1.0)\left(\tfrac{\alpha}{\pi}\right)^5 + ... \\ &= 116584718.92(0.03) \times 10^{-11} \end{aligned} \tag{10}$$

The error is dominated by the uncertainty in α, whose best estimate, $\alpha^{-1} = 137.035999046(27)$, was obtained via the recoil frequency of Cs atoms [13].
• $a_\mu^{\rm EW}$ collects all loop contributions involving at least one of $W^\pm, Z$ and the Higgs. At two loops, $a_\mu^{\rm EW}$ is found to be [14].

$$\begin{aligned} a_\mu^{\rm EW} &= \mathcal{O}\left(\tfrac{G_\mu m_\mu^2}{8\sqrt{2}\pi^2}\right)\left(1 + \mathcal{O}\left(\tfrac{\alpha}{\pi}\right) + ...\right) \\ &= (194.81(.01) - 41.2(1.0) + \mathcal{O}(.1)) \times 10^{-11} \\ &= 153.6(1.0) \times 10^{-11} \end{aligned} \tag{11}$$

The 3-loops contribution to $a_\mu^{\rm EW}$ hasn't been evaluated completely yet, but we know that is of order $\mathcal{O}(10^{-12})$.
• $a_\mu^{\rm Had}$ can be separated into a leading-order (LO) contribution and higher-order contributions. The first corresponds to the LO hadronic vacuum polarization (HVP) contribution, the others include next-to-leading-order (NLO) HVP contribution, the light-by-light (LbL) contribution, NNLO-HVP, etc. Grouping all higher-order contributions under the label N(N)LO [14],

$$\begin{aligned} a_\mu^{\rm Had} &= a_\mu^{\text{LO-HVP}} + a_\mu^{\text{N(N)LO-Had}} \\ &= [6939(40) + 19(26)] \times 10^{-11} \end{aligned} \tag{12}$$

There are two ways to calculate the HVP contribution: from first principles via lattice QCD, or via dispersion relation, which requires the knowledge of the R-ratio $R = \frac{\sigma(e^+e^- \to \text{hadrons})}{\sigma(e^+e^- \to \mu^+\mu^-)}$ from experimental data. At the moment the latter (phenomenological method) gives the most precise result for $a_\mu^{\text{LO-HVP}}$ (the one listed above), but lattice QCD is catching up rapidly.
• Summing all the SM contributions we get [14]

$$a_\mu^{\rm SM} = 116591830(1)(40)(26) \times 10^{-11} \tag{13}$$

where the errors are due to the EW, Had-LO, and Had-N(N)LO, respectively.

Tension between theory and experiment – The difference between (3) and (13) amounts to

$$\Delta a_\mu = a_\mu^{\rm exp} - a_\mu^{\rm SM} = 261(63)_{\rm exp}(48)_{\rm th} \tag{14}$$

Experimental and theoretical errors are comparable, therefore the error on $a_\mu^{\rm SM}$ has to be reduced by a factor 4 in order to match the precision expected by E989 and Muon g-2/EDM. In particular this means reducing the error on $a_\mu^{\rm Had}$ which accounts for more than 98% of the total theoretical error. We will see in next section how $a_\mu^{\text{LO-HVP}}$ can be computed using lattice QCD.

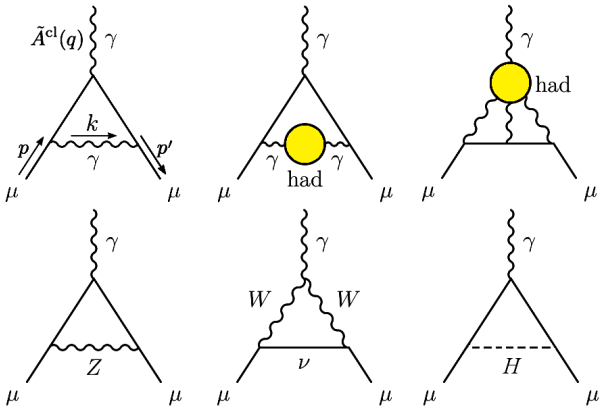

Figure 2: Representative diagrams contributing to $a_\mu^{\rm SM}$. Top: first order QED (Schwinger term), lowest-order hadronic vacuum polarization, hadronic light-by-light. Bottom: the three lowest-order weak contributions.

2 LO-HVP on the lattice

Lattice QCD is a regularization of QCD. The regularization is performed by enclosing spacetime in a finite and discrete four-dimensional euclidean box of size $L^3 \times T$ and elementary step (lattice spacing) a, thus getting rid of IR and UV divergences. The euclidean action, $\mathcal{S}_E$, has to be discretized as well. There is no unique way to do so. The important thing is that $\mathcal{S}_E$ is recovered when taking the limit for $a \to 0$. The QCD partition function on the lattice looks like

$$\mathcal{Z} = \int \prod_{\mu,x} \mathrm{d}U_\mu(x) \det(D[M]) e^{-\frac{\beta}{3}\sum_P \Re\mathrm{Tr}\,(1-U_P)} \tag{15}$$

where $U_\mu(x)$ is the gauge field, $\det(D_x[M])$ contains all the information about fermions, $\frac{\beta}{3}\sum_P \Re\mathrm{Tr}\,(1-U_P)$ is the Wilson gauge action (a lattice version of the Yang-Mills gauge action), and the parameter β is connected to the strong coupling, $\alpha_s = g^2/4\pi$ by $\beta = 6/g^2$. $\mathcal{Z}$ in (15) is similar to the partition function of a statistical, discrete system in the canonical ensemble. Therefore, to compute it we can use all the methods available in statistical mechanics, included Monte-Carlo (MC) simulations. The key point of this approach and the reason it works for QCD, is that – as known from asymptotic freedom – the strong coupling runs to a fixed point where $g^2 = 0$ as the energy scale is increased: picking $1/a$ as our energy scale, it means $\lim_{a\to 0} g^2 = 0$, but also, conversely, $\lim_{g^2\to 0} a = 0$. In short, there is a way to recover the continuum limit $a \to 0$ by simply tuning $\beta \to \infty$ in the MC simulation. Since it is not possible to perform a simulation at $\beta = \infty \leftrightarrow g^2 = 0$ (it would be like expecting a statistical system to evolve at zero temperature), the procedure is to measure a

chosen observable O at different values of β (as big as possible in the limit of available CPU time), link each β to its respective value of a, fitting the data $O_i(a_i)$ to a polynomial $O_i = c_0 + c_1 \cdot a^2 + \mathcal{O}(a^4)$ (this behavior is suggested by the renormalization group), and extracting the continuum limit c_0. To fully recover QCD, finite-volume corrections have to be added to the continuum extrapolation c_0. A final remark: in order to give a physical meaning to lattice prediction, we have to fix the parameters of QCD to their physical value. In our case, all the observables depend on four parameters: a (which is a stand-in for α_s), $m_{ud} = m_u = m_d$ (we work in the chiral limit), m_s and m_c (3rd generation quarks are not included: their contribution is much smaller than our statistical error). a is set by w_0 [15], i.e $a = w_0^\phi/(w_0^{\text{lat}}/a)$ where w_0^ϕ is the physical value in fm and (w_0^{lat}/a) is the corresponding lattice value expressed in units of a. The quark masses are set such that the meson masses, m_π, m_K and m_{η_c} take their physical value.

Defining LO-HVP on the lattice [19] –. The lowest-order HVP contribution to the anomalous magnetic moment of the muon can be written as [16, 17]

$$a_\mu^{\text{LO-HVP}} = \alpha^2 \int_0^\infty \frac{\mathrm{d}Q^2}{Q^2} w\left(\frac{Q^2}{m_\mu^2}\right) \hat{\Pi}(Q^2) \tag{16}$$

where $w(r) = (r + 2 - \sqrt{r(r+4)})^2/\sqrt{r(r+4)}$ and $\hat{\Pi}(Q^2) = \Pi(Q^2) - \Pi(0)$ is the renormalized scalar polarization function. We define

$$C_{\mu\nu}(t) = \frac{1}{e^2} \int \mathrm{d}^3x \langle j_\mu(x) j_\nu(0)\rangle \tag{17}$$

$$= C_{\mu\nu}^{ud}(t) + C_{\mu\nu}^{s}(t) + C_{\mu\nu}^{c}(t) + C_{\mu\nu}^{\text{disc}}(t) \tag{18}$$

where $j_\mu/e = \frac{2}{3}\bar{u}\gamma_\mu u - \frac{1}{3}\bar{d}\gamma_\mu d - \frac{1}{3}\bar{s}\gamma_\mu s + \frac{2}{3}\bar{c}\gamma_\mu c$. The four terms in (18) correspond to different observables on the lattice. $C_{ii}^f(t)$ allows us to compute $\hat{\Pi}(Q^2)$; the two are related by (see [18])

$$\hat{\Pi}^f(Q^2) = \int_0^\infty \mathrm{d}t \left[t^2 - \frac{4}{Q^2}\sin^2\left(\frac{Qt}{2}\right)\right] \frac{\sum_{i=1}^3 \Re C_{ii}^f(t)}{3} \tag{19}$$

where $f = ud, s, c, \text{disc}$. Inserting (19) to (16), performing the integral over Q^2 up to $Q^2_{\text{max}} \ll 2\pi/T$, replacing the integral in t with a sum in steps of a from $t = 0$ to $t = T/2$, replacing $\frac{1}{3}\sum_i C_{ii}^f(t)$ with its discretized, finite-volume version $C_L^f(t) = (a^3/3)\sum_i \sum_{\vec{x}} \langle j_i(x) j_i(0)\rangle$, and averaging $C_L^f(t)$ with $C_L^f(T-t)$ (the lattice has periodic boundary conditions), we get to

$$a_{\mu,f}^{\text{LO-HVP}}[Q < Q^2_{\text{max}}] = \lim_{a\to 0} \lim_{L,T\to\infty} \times$$
$$\times\, \alpha^2 \frac{a}{m_\mu^2} \sum_{t=0}^{T/2} W\left(tm_\mu, Q^2_{\text{max}}/m_\mu^2\right) \Re C_L^f(t) \tag{20}$$

where $W(\tau, x_{\text{max}}) = \int_0^{x_{\text{max}}} \mathrm{d}x\, w(x) \left(\tau^2 - \frac{4}{x}\sin^2\frac{\tau\sqrt{x}}{2}\right)$. For each $f = ud, s, c, \text{disc}$, (20) has to be completed by $a_{\mu,f}^{\text{LO-HVP}}[Q \geq Q^2_{\text{max}}]$, evaluated in perturbative QCD.

3 Analysis and results

Fitting procedure – After computing (20) on a number N of different ensembles (lattices with different $a, L, T, m_{ud}, m_s, m_c$), one has to fit the N measurements and pick the value corresponding to $a = 0$ and physical meson masses $m_\pi, m_K, m_{\eta C}$. There are many adjustments that can be implemented in the fit model:
- Q-cuts (Q^2_{max} above which pQCD is used),
- a-cuts (minimum a that an ensemble must have to be included in the fit),
- t-cuts (C_L^f becomes noisy as t increases: the sum of data over t in (20) can be replaced by the average between an upper and a lower bound above a certain t_c),
- choice of functional form for over a-dependence,
- interpolation of results to physical values of the quark masses.

The final result is a weighted average of the extrapolation resulting from all the different procedures (weighted by the procedure's χ^2 via the AIC method).

Additional challenges – The scale setting method has to be carefully developed because the error on the determination of a propagates with a factor ~ 2 in a_μ. Strong-isospin breaking effects have to included. Standard methods to evaluate finite-volume corrections help but are not sufficient to reach the envisaged precision.

Results – Our collaboration (BMW) is now updating the results obtained in [19]. Since the analysis is still still being finalized, only the last published results will be showed. BMW-17 [19] is consistent with both phenomenology and the "no new physics" scenario. Today, the picture from lattice QCD is still not conclusive. Whatever lattice will tell us in the future, the question remains why the $a_\mu^{\text{LO-HVP}}$ obtained via phenomenology is inconsistent with "no new physics", supposing that the upcoming E989 result confirms the previous measurements. In summary, we have to wait just few more months to know if a_μ will be a confirmed hint of new physics or just the umpteenth validation of the SM.

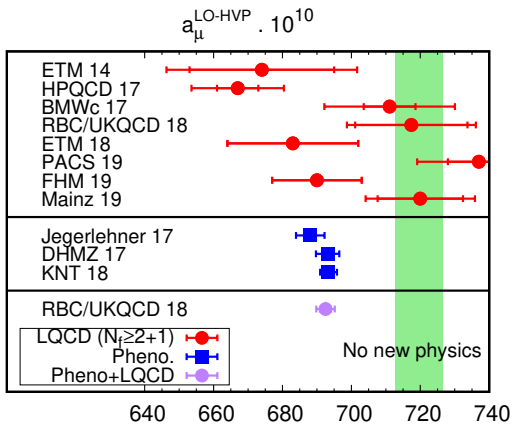

Figure 3: Comparison between lattice and phenomenology predictions of $a_\mu^{\text{LO-HVP}}$ by various collaborations.

References

[1] F. Jegerlehner, *The Anomalous Magnetic Moment of the Muon*, 2nd ed. (Springer, Berlin, 2017).

[2] S.-I. Tomonaga and T. Oka, *The Story of Spin* (University of Chicago Press, Chicago, 1998).

[3] S.S. Schweber, *QED and the Men Who Made It: Dyson, Feynman, Schwinger, and Tomonaga* (Princeton Univ. Press, Princeton, NJ, 2011).

[4] S. Goudsmit, G. E. Uhlenbeck, Nature **117**, 264-265 (1926)

[5] L. E. Kinster, W. V. Houston, Phys. Rev. **45**, 104 (1934)

[6] P. Kusch, H. M. Foley, Phys. Rev. **72**, 1256 (1947)

[7] J. S. Schwinger, Phys. Rev. **73**, 416 (1948)

[8] W. H. Luisell, R. W. Pidd, H. R. Crane, Phys. Rev. **94**, 7 (1954)

[9] D. Hanneke, S. Fogwell, and G. Gabrielse Phys. Rev. Lett. **100**, 120801 (2008)

[10] G. W. Bennett *et al.* (Muon g-2 Collaboration), Phys. Rev. D **73**, 072003 (2006)

[11] V.B. Berestetskii, O.N. Krokhin and A.X. Klebnikov, Zh. Eksp. Teor. Fiz. **30**, 788 (1956)

[12] M. E. Peskin and D. V. Schroeder, *An Introduction to quantum field theory*, (Addison-Wesley, Reading, USA, 1995)

[13] R.H. Parker *et al.*, *Science* Vol. **360**, Issue 6385, pp. 191-195 (2018)

[14] M. Tanabashi *et al.* (Particle Data Group), Phys. Rev. D **98**, 030001 (2018) and 2019 update.

[15] Borsányi, S., Dürr, S., Fodor, Z. *et al.*, "High-precision scale setting in lattice QCD". J. High Energ. Phys. 2012, **10** (2012).

[16] E. de Rafael, "Hadronic Contributions to the Muon g-2 and Low-Energy QCD", Phys. Lett. **B 322**, 239-246 (1994)

[17] T. Blum, "Lattice Calculation of the Lowest-Order Hadronic Contribution to the Muon Anomalous Magnetic Moment", Phys. Rev. Lett. **91**, 05 (2001)

[18] D. Bernecker and H. B. Meyer, "Vector Correlators in Lattice QCD: Methods and applications," Eur. Phys. J. A **47**, 148 (2011)

[19] Sz. Borsanyi, Z. Fodor, C. Hoelbling, T. Kawanai, S. Krieg, L. Lellouch, R. Malak, K. Miura, K. K. Szabo, C. Torrero, and B. C. Toth (Budapest-Marseille-Wuppertal Collaboration), "Hadronic Vacuum Polarization Contribution to the Anomalous Magnetic Moments of Leptons from First Principles", Phys. Rev. Lett. **121**, 022002 (2018)